ANL/OTM/CR--1

DE93 011639

INSTANTANEOUS ENGINE FRICTIONAL TORQUE, ITS COMPONENTS AND PISTON ASSEMBLY FRICTION

FINAL REPORT

Contract No. 73072401

Submitted by:

N.A.Henein

Center for Automotive Research
College of Engineering
Wayne State University
Detroit, Michigan, 48202

Edited by:

Fred A. Nichols

Argonne National Laboratory

Submitted to:

United States Department of Energy,
Office of Transportation Materials-Tribology Project
and Argonne National Laboratory

ACKNOWLEDGEMENT

The author acknowledges the effort of many graduate students, in the Center for Automotive Research at Wayne State University, who carried on the major part of the work described in this report. In particular the efforts of the following individuals are acknowledged: Apostolos Fragoulis who received his Ph.D. degree in 1988, Stanley Marek who is about to complete his Ph.D. dissertation and Shenggiang Huang who is currently working on his Ph.D. dissertation. Mr. Angelo Nichols of Applied Computer Engineering Co. developed the data acquisition system. Ms. Samar Soliman helped in the error analysis of the pressure transducers. The help of the Machine Shop at Wayne State University is greatly appreciated.

The technical support and guidance of Dr. Fred Nichols, Dr. George Fenske and Dr. Allan Michaels of Argonne National Laboratory were instrumental in directing the course of this investigation and reaching its conclusions. The time and the effort made by Dr. Fred Nichols in editing this report is greatly appreciated.

TABLE OF CONTENTS

Nomenclature

ABDC	after bottom dead center
BBDC	before bottom dead center
BDC	bottom dead center
BHP	brake horse power
BMEP	brake mean effective pressure, Pa
cp	crankshaft pin
CAD	crank angle degrees
C.R.	compression ratio
d	bore, m
EVO	exhaust valve opens
FHP	friction horse power
FMEP	friction mean effective pressure, Pa
F_B	reaction force from balance weight, N
F_{B1x}	reaction force on the crankshaft journal, in the x direction, N
F_{B2x}	reaction force on the crankshaft journal, in the x direction, N
F_{B1y}	reaction force on the crankshaft journal, in the y direction, N
F_{B2y}	reaction force on the crankshaft journal, in the y direction, N
F_C	reaction force from the camshaft gear, N
F_{cpx}	reaction force on the connecting rod from the crankshaft in the x direction, N
F_{cpy}	reaction force on the connecting rod from the crankshaft in the y direction, N
F_{cr}	connecting rod force determined by strain gage measurement, N
F_f	frictional force experienced by the piston, N

F_{pr} net force resulting from cylinder gas pressure and crankcase pressure, N

F_{ppx} reaction force on the piston pin in the x direction, N

F_{ppy} reaction force on the piston pin in the y direction, N

FSO full scale output

F_w cylinder wall reaction force, N

IHP indicated horse power

IFT instantaneous friction torque (same as M_{IFT}), Nm

IMEP indicated mean effective pressure, Pa

IVC inlet valve closes

I_B mass moment of inertia of the balance weight about its axis of rotation, kgm^2

I_{crn} mass moment of inertia of the crankshaft about its axis of rotation, kgm^2

I_{flw} mass moment of inertia of the flywheel about its axis of rotation, kgm^2

I_{ro} total rotating mass moment of inertia, kgm^2

l stroke, m

I_{cr} mass moment of inertia of the connecting rod about its center of gravity, kgm^2

L connecting rod length, m

L_1 distance from center of gravity of connecting rod to piston pin, m

L_2 distance from center of gravity of connecting rod to crankshaft pin, m

L_{c1} distance from connecting rod small end to location of center of mass of the connecting rod part above strain gages, m

L_f flywheel position , m

L_{B1} position of crankshaft journal, m

L_{B2} position of crankshaft journal, m

m_{c1} mass of the connecting rod part above strain gages, kg

m_{cr}	mass of the connecting rod, kg
m_{crn}	mass of the crankshaft, kg
m_p	mass of the piston including rings and the pin, kg
M_{cp}	frictional torque from crankshaft pin, Nm
M_{pp}	frictional torque experienced by connecting rod from piston pin, Nm
M_B	frictional torque due to balance weight bearings, Nm
M_{B1}	frictional torque in main bearing, Nm
M_{B2}	frictional torque in main bearing, Nm
M_{CB}	frictional torque due to camshaft bearings, Nm
M_I	torque due to inertia of reciprocating and rotating parts, Nm
M_{IFT}	torque due to frictional forces, Nm
M_L	torque due to load on engine, Nm
M_O	torque necessary to drive the oil pump, Nm
M_P	torque due to gas pressure, Nm
M_{VP}	frictional torque due to engine valves and fuel pump, Nm
pp	piston pin
P	cylinder gas pressure, Pa
P_{peak}	peak cylinder gas pressure, MPa
r	crankshaft radius, m
r_B	radius of crankshaft gear driving the balance weight, m
$\bar{r}$	crankshaft center of gravity position, m
$\bar{r}_B$	balance weight center of gravity, m
RPM	revolution per minute
TDC	top dead center
V	volume, m^3
W_B	weight of the balance weight, N

W_{c1}	weight of the connecting rod part above strain gages, N
W_{cr}	weight of the connecting rod, N
W_{crn}	weight of the crankshaft, N
W_{flw}	weight of the flywheel, N
W_p	weight of the piston including rings and the pin, N
x_{c1}	location of the center of mass of the connecting rod part above strain gages along x axis, m
x_{cr}	connecting rod center of gravity position along x axis, m
x_p	piston pin position along x axis, m
y_{cr}	connecting rod center of gravity position along y axis, m
δ	piston pin offset, m
ω	angular velocity, rad/s
θ	crank angle, degrees
φ	connecting rod angle, degrees
λ	r/L, dimensionless
λ_o	δ/L, dimensionless
λ_1	L_1/L, dimensionless
λ_2	L_2/L, dimensionless

ABSTRACT

The overall goal of this report is to document the work done to determine the instantaneous frictional torque of internal combustion engine by using a new approach known as (P-ω) method developed at Wayne State University. The emphasis has been to improve the accuracy of the method, and apply it to both diesel and gasoline engines under different operating conditions. Also work included an investigation to determine the effect of using advanced materials and techniques to coat the piston rings on the instantaneous engine frictional torque and the piston assembly friction.

The errors in measuring the angular velocity, ω, have been determined and found to be caused by variations in the divisions within one encoder,encoder-to-encoder variations, misalignment within the encoder itself and misalignment between the encoder and crankshaft.

The errors in measuring the cylinder gas pressure, P, have been determined and found to be caused by transducer-to-transducer variations, zero drift, thermal stresses and lack of linearity.

The ability of the (P-ω) method in determing the frictional torque of many engine components has been demonstrated. These components include valve train, fuel injection pump with and without fuel injection, and piston with and without different ring combinations. The emphasis in this part of the research program has been on the piston-ring assembly friction.

The effects of load and other operating variables on IFT have been determined. The motoring test, which is widely used in industry to measure engine friction has been found to be inaccurate. The errors have been determined at different loads.

Coating the piston rings has been found to reduce the piston-assembly friction at all operating conditions. This, in turn reduced the IFT of the whole engine.

INTRODUCTION

Combustion engines are the major power sources for transportation systems on land, sea and air, and for power generation. The U.S. consumption of oil by the transportation sector alone accounts for about 67% of the total U.S. oil consumption [reference 1]. The reciprocating engines represent the majority of combustion engines used in transportation. Any reduction in frictional losses would result in significant savings in crude oil consumption, dependence on foreign oil imports, the economy, and the federal deficit.

Engine manufactures are interested in reducing frictional losses in order to meet the Cooperative Fuel Economy Standards, and some emission standards. A low friction engine is not only an economical engine but can be a less polluting engine than another similar engine having higher frictional losses. While many approaches have been made to reduce the frictional losses in engines, by design modifications, [2-5] or by lubricating oil modifications [5-10], no changes or modifications were made to accurately measure the frictional losses in engines, over the last 50 years.

This report deals with a new approach known as (P-ω) method to determine the instantaneous frictional torque of the whole engine as a system under real life conditions and different driving modes including transient modes of acceleration and deceleration.

The information given in this report is the result of a program which has been in progress at Wayne State University, Center for Automotive Research over the last seven years. The research support was from U.S. Tank Automotive Command, Warren, Michigan, National Science Foundation and the Department of Energy's ECUT Program and the Argonne National Laboratories. Argonne National Laboratories sponsored this program during the last three years.

The new method developed to determine the total instantaneous frictional torque in reciprocating combustion engines and compressors was published in reference [11]. The application of the method to single cylinder and multicylinder engines under the transient conditions of starting, acceleration and deceleration was published in reference [12]. The error analysis of the method due to angular velocity measurements was published in reference [13]. The error analysis of the method due to pressure measurements was published in reference [14]. The effect of load and other operating parameters on IFT was published in reference [15]. The work done to determine the instantaneous frictional torques in different components of a single cylinder diesel engine was published in reference [16].

This report contains all the information needed for the reader to follow the progress of the work in this program at Wayne State University on engine friction. More details may be obtained from the references cited earlier.

Currently the work is still in progress in our laboratories, to improve the accuracy of the method and to apply it to multicylinder gasoline and diesel engines. The scope of the research program is being extended to cover a new method to measure microscopic and macroscopic wear in the cylinder bore at the top ring reversal point. Another program, sponsored by industry, has started to investigate wear in methanol fueled gasoline engines.

The report is divided into 10 chapters.

CHAPTER 1: METHODS TO MEASURE FRICTIONAL LOSSES IN RECIPROCATING COMBUSTION ENGINES

1.1 AVERAGE FRICTIONAL LOSSES

Four methods have been used over the last 50 years to measure the total average frictional torque of internal combustion engines. These are the motoring test, Willan's method, Morse's method and the indicated work method. These methods are described in the following sections. A new method known as (P-ω) method, to measure the instantaneous frictional torque is also described.

1.1.1 MOTORING TEST

In this widely used method the engine is motored by an electric dynamometer and the torque developed is measured. The results obtained do not represent the true frictional torque because during motoring the cylinder pressures are quite different from the pressures with combustion. The difference is great during the expansion stroke where in a fired engine the pressures are much higher than in a motored engine. In a motored engine the gas pressure at any piston position in the expansion stroke is lower than that in the compression stroke. This drop in pressure is caused by the heat transfer and blow-by losses. A lower cylinder gas pressure results in lower frictional losses due to the following:

i- lower back pressures on the compression rings
ii- lower side thrust on the piston skirt
iii- lower loads on the main engine bearings and connecting rod bearings.

The absence of combustion during motoring reduces the rate of heat transfer from the gases to the walls and causes a drop in

temperature of the walls and lubricating oil film. This causes the running clearance of the piston and the viscosity of the lubricating oil film to increase. Also, the motoring test does not account for the effect of blowby on the oil film and the frictional losses.

1.1.2 WILLAN'S METHOD

The rate of fuel consumption is plotted against the torque produced by the engine at a constant speed as shown in Figure 1.1. The best fitting line is drawn and extrapolated to the zero fuel consumption line. The intercept on the negative side of the torque is considered equal to the frictional torque. Therefore, the measured frictional torque is for no-load conditions and is subject to the extrapolation errors.

1.1.3 MORSE'S METHOD

This method is suitable for multicylinder engines and cannot be used for single cylinder engines. To measure the frictional torque at any speed, the engine is run at this speed under steady state with all n cylinders firing, point a in Figure 1.2. One cylinder is misfired which causes a drop in the total engine torque and speed, as a result of n-1 cylinders firing and one motored. This state is represented by point b. To bring the speed back to its original value the load on the engine is reduced, as shown by point c. The difference between the torques at points a and c is considered equal to the indicated torque of the misfired cylinder. The procedure is repeated for the rest of the cylinders. The total frictional torque of the engine is obtained from the difference between the total indicated torque of all the cylinders and the brake torque of the engine. The frictional torque calculated by this method is for the motored engine without combustion. The errors in this method are explained under the motoring test.

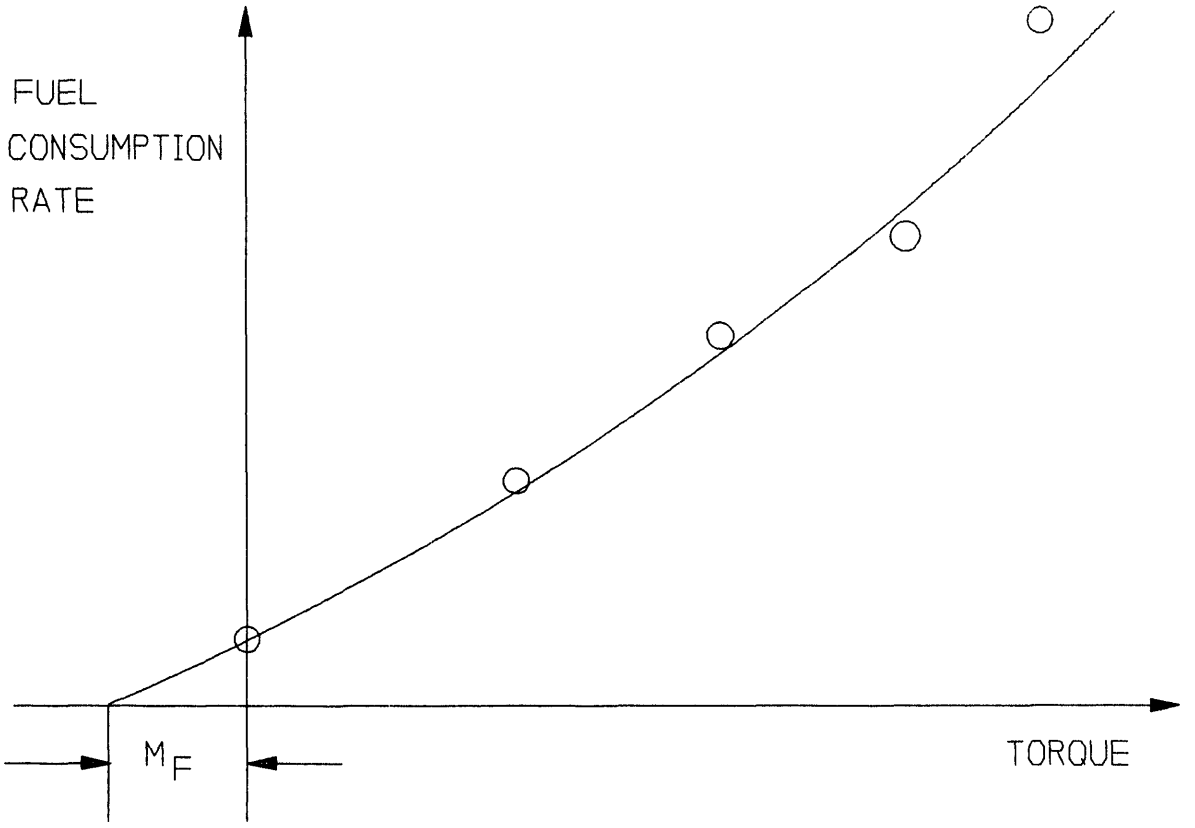

Figure 1.1. Willan's method to determine total engine torque

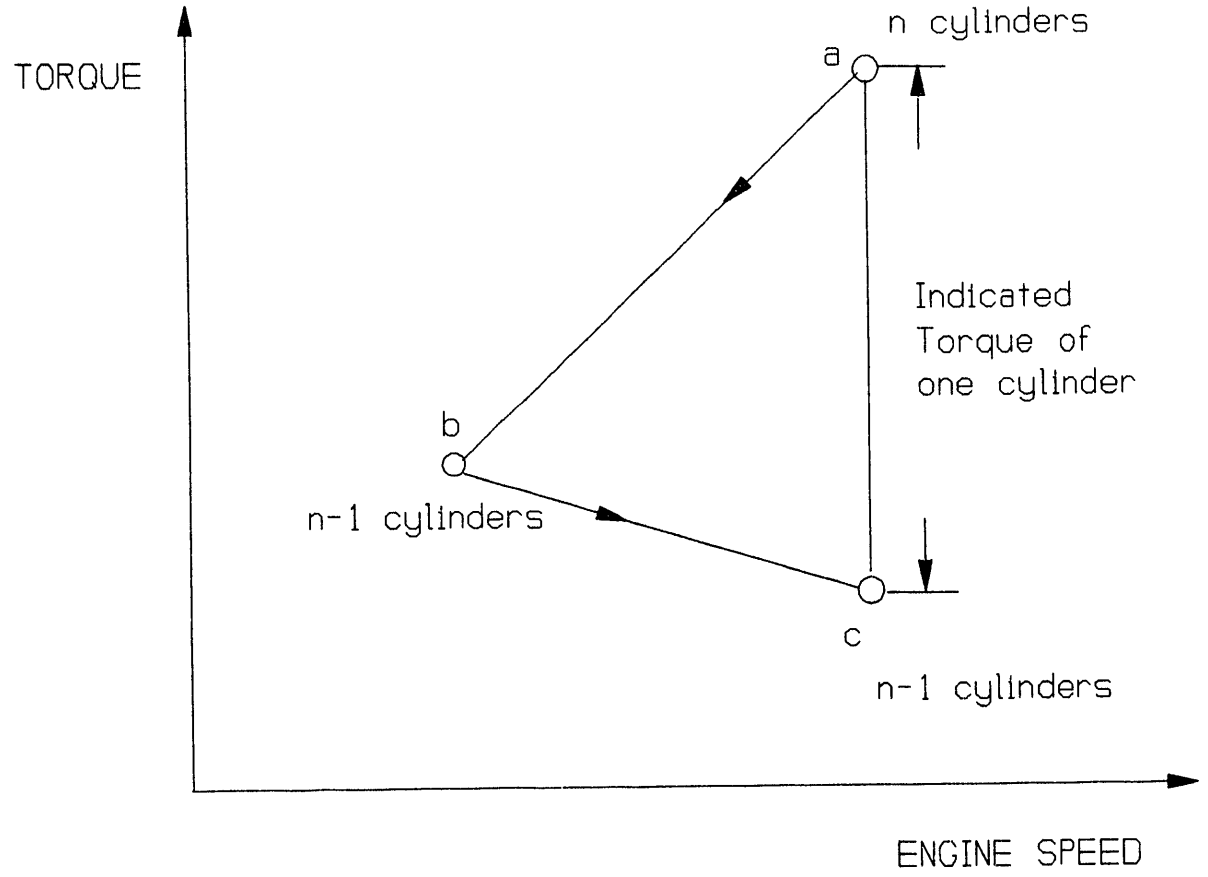

Figure 1.2. Morse's method to determine indicated torque for one cylinder in a multicylinder engine

1.1.4 INDICATED WORK METHOD

In this method the indicated work done by the gases on the piston is calculated from:

$$W=\oint PdV \tag{1.1}$$

The pressure in the cylinder is measured by a pressure transducer. The net work from the engine is measured by dynamometer. The power to overcome the frictional losses is calculated from:

$$FHP=IHP-BHP \tag{1.2}$$

where FHP = friction horse power,
IHP = indicated horse power,
BHP = brake horse power.

This is the most accurate method for determining the total average power to overcome the frictional losses under steady engine rotating speeds. This method cannot be used under transient engine rotating speeds and is subject to the errors caused by the cycle-to-cycle variations and cylinder-to-cylinder variations in the gas pressure.

1.2 TIME DEPENDENT FRICTIONAL TORQUE

1.2.1 THE (P-ω) METHOD FOR INSTANTANEOUS FRICTION MEASUREMENT

All the four techniques described earlier measure the time-averaged frictional torque. While many methods are available to measure the time-dependent frictional forces in some engine components, no technique is known to measure the instantaneous total frictional losses of the engine as a system.

The (P-ω) method was developed at Wayne State University [11]. This method is based on the fact that all the torques acting on the crankshaft should be in equilibrium at any point during the cycle. Figure 1.3 shows the different torques acting on the engine.

$$M_{IFT}=M_P-M_L-M_I \qquad (1.3)$$

where M_{IFT} =Instantaneous Friction Torque,
M_P =Instantaneous Torque due to cylinder gas force,
M_L =Instantaneous Torque due to the load on the engine,
M_I =Instantaneous Torque due to the inertia of the moving parts of the engine.

This method was improved over the years at Wayne State University and applied successfully to a single cylinder diesel engine [12, 16, 15] and gasoline engine. Currently, this method is being applied on multicylinder diesel and gasoline engines.

The following are the main advantages of the (P-ω) method:

1- It is the only method to determine IFT in reciprocating

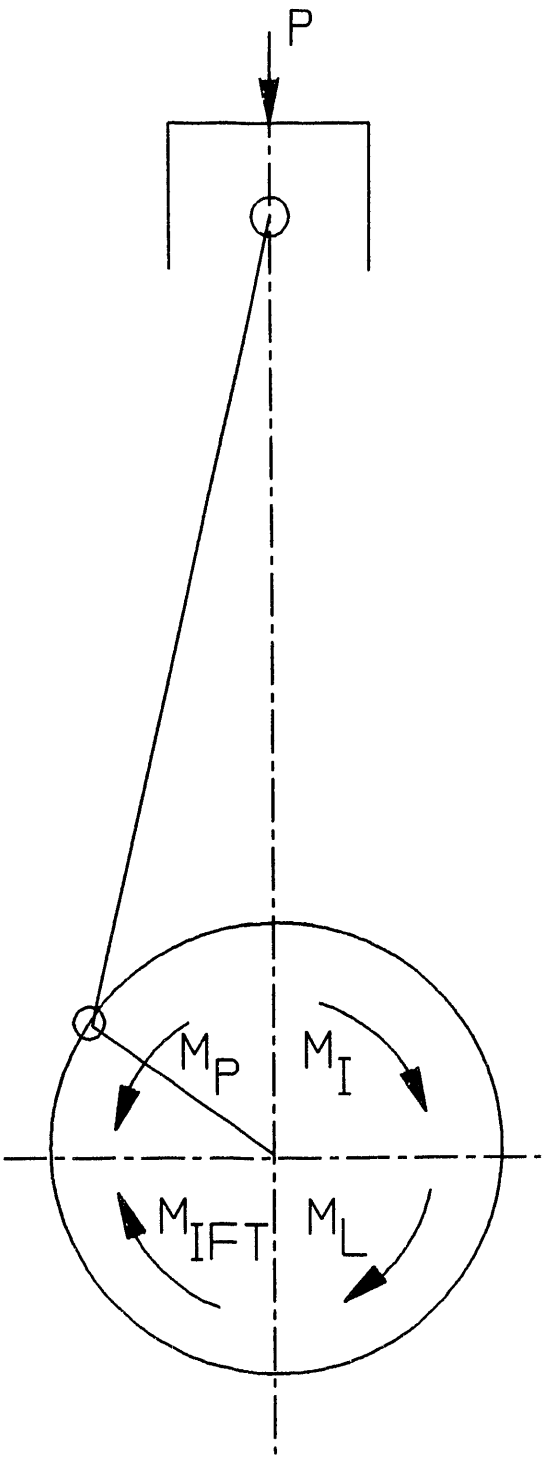

Figure 1.3. (P-ω) method

engines used in land transportation , power generation, marine applications and some airplanes.

2- It is the only method to determine IFT in reciprocating compressors used for compressed air, gas and refrigerants.

3- It determines IFT non-invasively.

4- It determines IFT under different loads and speeds with the engine operating under steady state.

5- It is the only method to determine IFT under the transient states of acceleration and deceleration.

6- Its accuracy is not subject to errors caused by cycle-to-cycle variations, which are common in gasoline engines.

CHAPTER 2: THEORETICAL ANALYSIS

2.1 ENGINE KINEMATICS

A slider crank mechanism, shown in Figure 2.1, consists of a crank with a radius r and a connecting rod with a length L. Distance L is equal to sum of two values L_1 and L_2 which represent distances from center of gravity of the connecting rod to both ends. The location of the piston in the cylinder, its velocity and acceleration are calculated as functions of crank angle θ. Piston location is represented by distance x_p from crankshaft center of rotation (point O) to piston pin position (point pp). Piston pin offset δ, crankshaft center of gravity $\bar{r}$, connecting rod center of gravity position x_{cr}, instantaneous connecting rod angle φ are self-explanatory on Figure 2.1. Note that θ is defined as positive in the counterclockwise direction when φ positive in clockwise direction.

Based on the above definitions the following equations can be written:

$$x_p = r\cos\theta + L\cos\varphi \tag{2.1}$$

$$x_{cr} = x_p - L_1\cos\varphi = r\cos\theta + L_2\cos\varphi \tag{2.2}$$

$$y_{cr} = L_1\sin\varphi - \delta \tag{2.3}$$

where $L = L_1 + L_2$,

$\theta = \omega t$,

ω = angular velocity,

t = time.

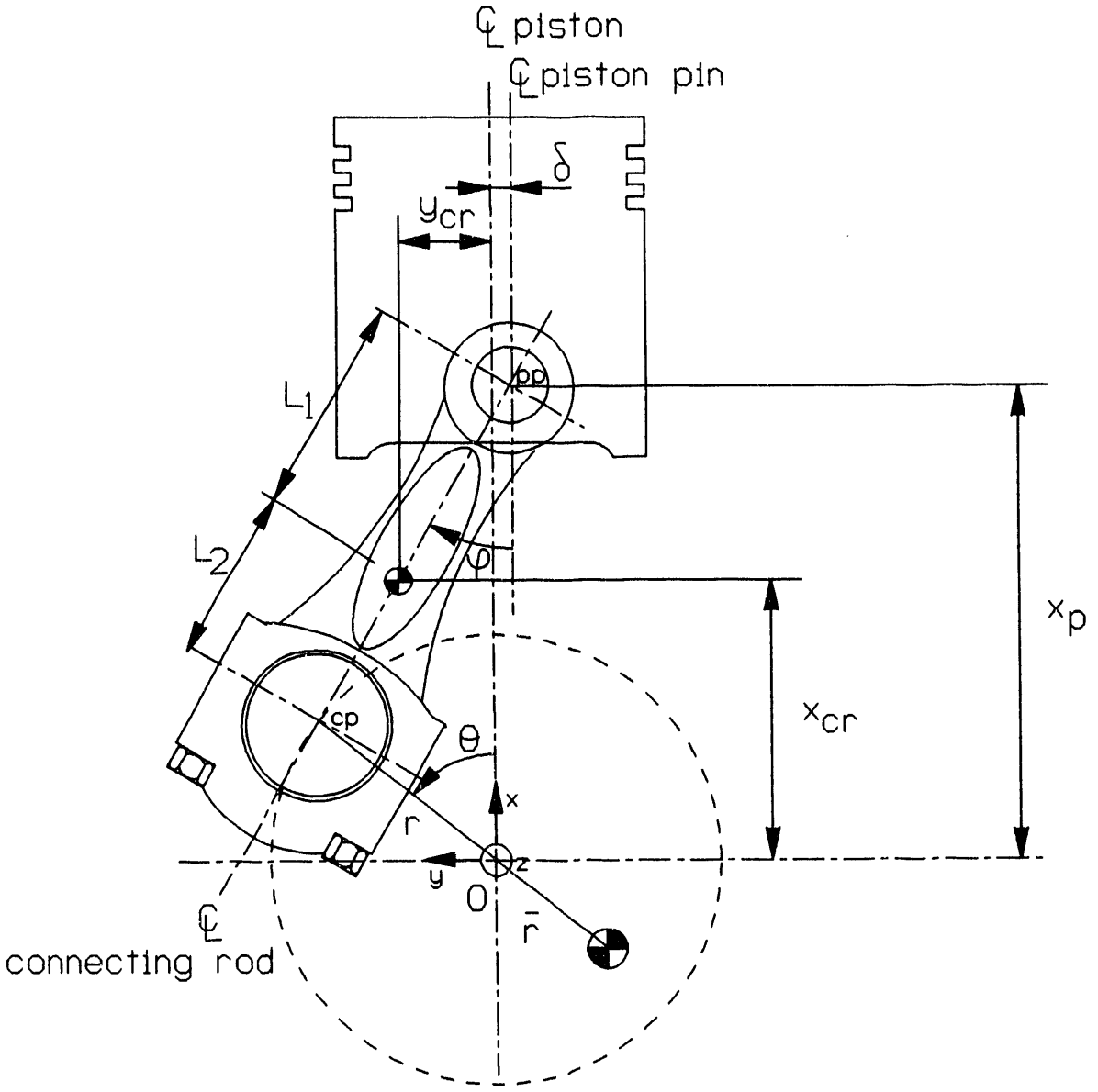

Figure 2.1. Engine diagram

Since

$$r\sin\theta = L\sin\varphi - \delta \tag{2.4}$$

then

$$\sin\varphi = \lambda\sin\theta + \lambda_0 \tag{2.5}$$

$$\cos\varphi = \sqrt{1-(\lambda\sin\theta+\lambda_0)^2} \tag{2.6}$$

where $\lambda = r/L$ and $\lambda_0 = \delta/L$

The velocity and acceleration of the piston are the first and second time derivatives of the piston position. The position, velocity and acceleration of the connecting rod center of gravity can be derived in a similar way. If θ' represents engine angular velocity ω and θ'' represents the engine angular acceleration, the first and second derivatives of equations (2.1), (2.2) and (2.3) can be written as:

$$x_p' = -r\sin\theta\theta' - L\sin\varphi\varphi' \tag{2.7}$$

$$x_p'' = -r\cos\theta(\theta')^2 - r\sin\theta\theta'' - L\cos\varphi(\varphi')^2 - L\sin\varphi\varphi'' \tag{2.8}$$

$$x_{cr} = x_p' + L_1\sin\varphi\varphi' \tag{2.9}$$

$$x''_{cr}=x''_p+L_1(\cos\varphi(\varphi')^2+\sin\varphi\varphi'') \tag{2.10}$$

$$y'_{cr}=L_1\cos\varphi\varphi' \tag{2.11}$$

$$y''_{cr}=L_1(-\sin\varphi(\varphi')^2+\cos\varphi\varphi'') \tag{2.12}$$

from equation (2.5)

$$\varphi'=\frac{\lambda\cos\theta\theta'}{\cos\varphi} \tag{2.13}$$

$$\varphi''=\frac{\lambda}{\cos\varphi}(\cos\theta\theta''-\sin\theta(\theta')^2)+\frac{\sin\varphi}{\cos\varphi}(\varphi')^2 \tag{2.14}$$

It is customary to represent each of the above variables as a function of engine geometry, angle θ, θ' and θ'', but this is unnecessary since all calculations are done by using a computer. Having input values for θ, θ' and θ'', calculating $\sin\theta$ and $\cos\theta$, and using equations (2.5), (2.6), (2.13) and (2.14) to solve for $\sin\varphi$, $\cos\varphi$, φ' and φ'', equations (2.7)-(2.12) can be easily solved.

2.2 ENGINE DYNAMICS

Figure 2.2 shows the piston with the external forces acting on it. Neglecting the frictional forces between the rings and ring grooves, the equations describing the piston motion are:
x-axis:

$$F_{ppx}-F_{pr}-W_p+F_f(-sgnx_p')=m_px_p'' \tag{2.15}$$

y-axis:

$$F_w-F_{ppy}=0 \tag{2.16}$$

where F_{ppx} =reaction force on the piston pin in the x direction,
F_{ppy} =reaction force on the piston pin in the y direction,
W_p =weight of the piston including rings and the pin,
m_p =mass of the piston including rings and the pin,
F_{pr} =net force resulting from cylinder gas pressure and crankcase pressure,
F_w =cylinder wall reaction force, assumed to be acting in line with the piston pin axis,
F_f =frictional force experienced by the piston. Direction of this force depends on sign of piston velocity vector x_p'

$$sgn\ x_p'=\frac{x_p'}{|x_p'|}=\begin{cases}+1 & if\ x_p'\ positive\\ -1 & if\ x_p'\ negative\end{cases} \tag{2.17}$$

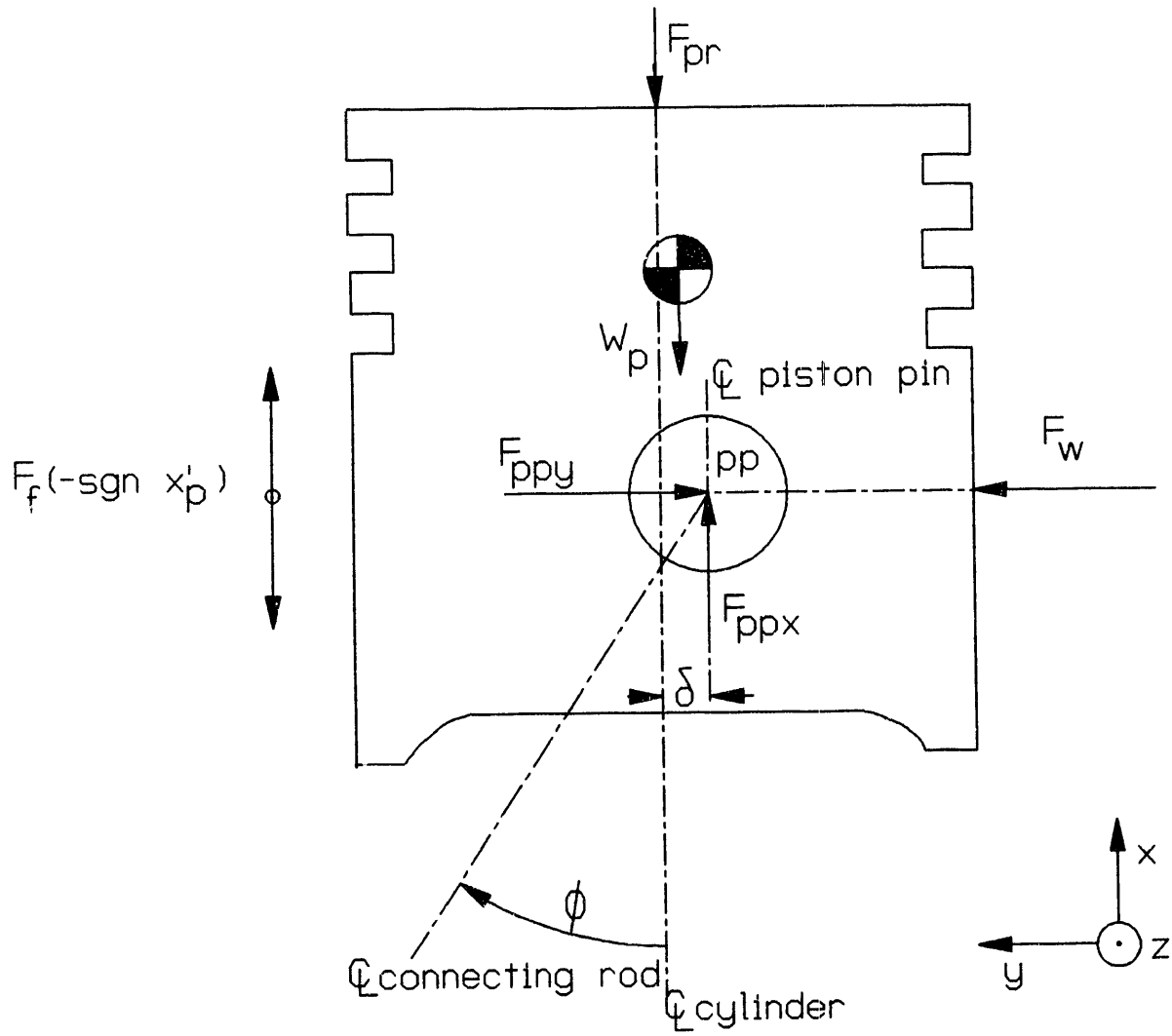

Figure 2.2. Free body diagram of piston

Figure 2.3 shows the connecting rod with the forces acting on it.

The equations of motion are given by:

x-axis:

$$F_{cpx}-F_{ppx}-W_{cr}=m_{cr}x''_{cr} \tag{2.18}$$

y-axis:

$$F_{ppy}-F_{cpy}=m_{cr}y''_{cr} \tag{2.19}$$

Moment O_{cr}:(positive in counterclockwise direction)

$$F_{ppy}L_1\cos\varphi+F_{cpy}L_2\cos\varphi-F_{ppx}L_1\sin\varphi-F_{cpx}L_2\sin\varphi+ \\ +M_{pp}sgn\varphi'+M_{cp}=-I_{cr}\varphi'' \tag{2.20}$$

where W_{cr} =connecting rod weight,
m_{cr} =connecting rod mass,
F_{cpx}=reaction force on the connecting rod from the crankshaft in the x direction,
F_{cpy}=as above in the y direction,
M_{pp} =frictional torque experienced by connecting rod from piston pin. Its direction depends on sign of φ' ,
M_{cp} =frictional torque from crankshaft pin (always positive),
I_{cr} =mass moment of inertia of the connecting rod about its center of gravity.

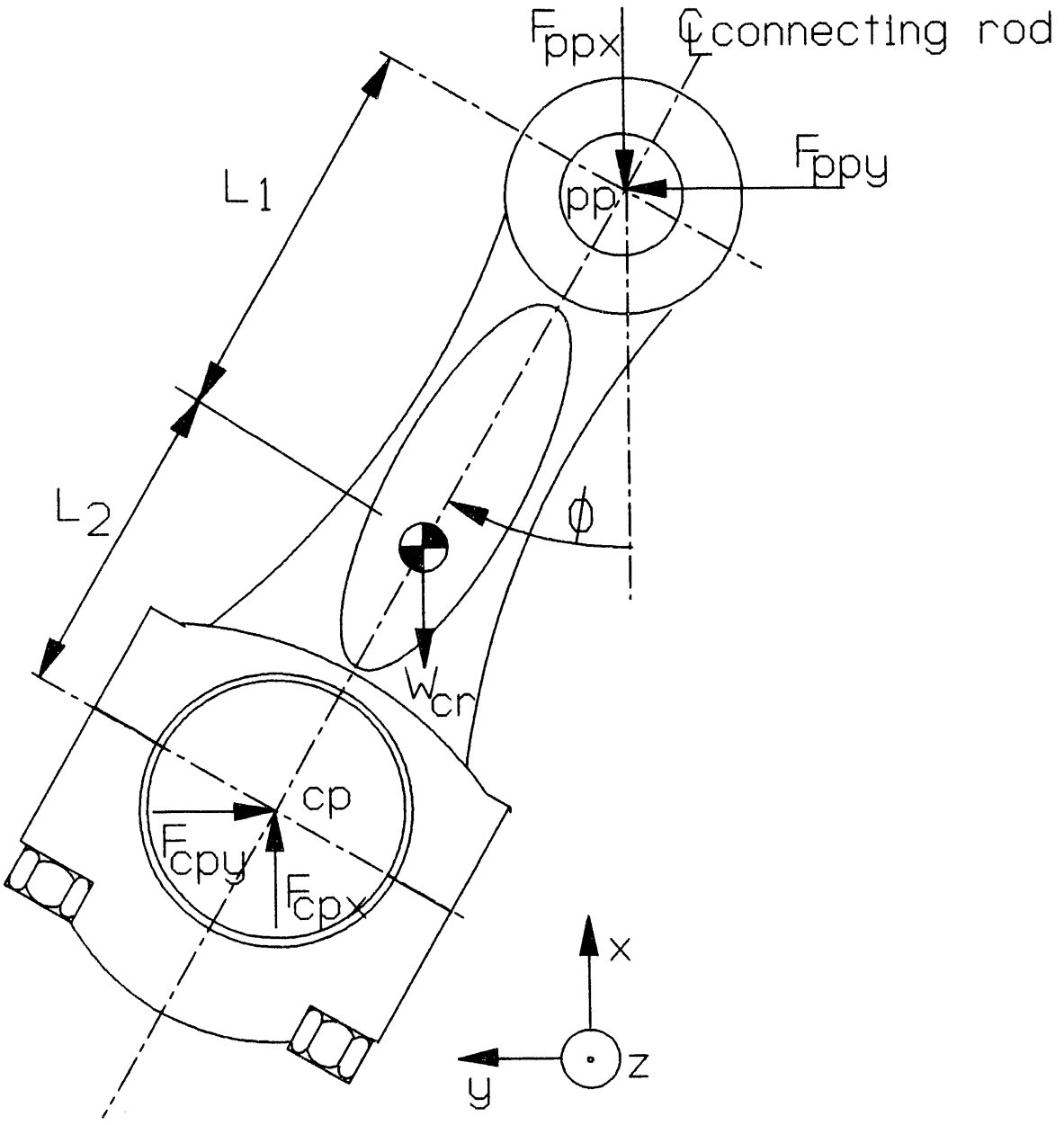

Figure 2.3. Free body diagram of connecting rod

Figure 2.4 and 2.5 show the flywheel-crankshaft system, for which the equations of motion are:

x-axis:

$$F_{B1x}+F_{B2x}-F_{cpx}-W_{flw}-W_{crn}=m_{crn}\bar{r}(\theta')^2\cos\theta+m_{crn}\bar{r}\theta''\sin\theta \qquad (2.21)$$

y-axis:

$$F_{cpy}-F_{B1y}-F_{B2y}-F_B=m_{crn}\bar{r}(\theta')^2\sin\theta-m_{crn}\bar{r}\theta''\cos\theta \qquad (2.22)$$

moment x:

$$F_{B1y}L_{B1}-F_{B2y}L_{B2}=0 \qquad (2.23)$$

moment y:

$$W_{flw}(L_f+L_{B1})-F_{B1x}L_{B1}+F_{B2x}L_{B2}=0 \qquad (2.24)$$

moment z:

$$F_{cpx}r\sin\theta+F_{cpy}r\cos\theta-W_{crn}\bar{r}\sin\theta-F_Br_B+ \\ -M_{cp}-M_{B1}-M_{B2}-M_O-M_L=I_{flw}\theta''+I_{crn}\theta'' \qquad (2.25)$$

where F_{B1x}, F_{B2x}, F_{B1y}, F_{B2y} =reaction forces on the crankshaft journals,

W_{flw} =weight of the flywheel,

W_{crn} =weight of the crankshaft,

m_{crn} =mass of the crankshaft,

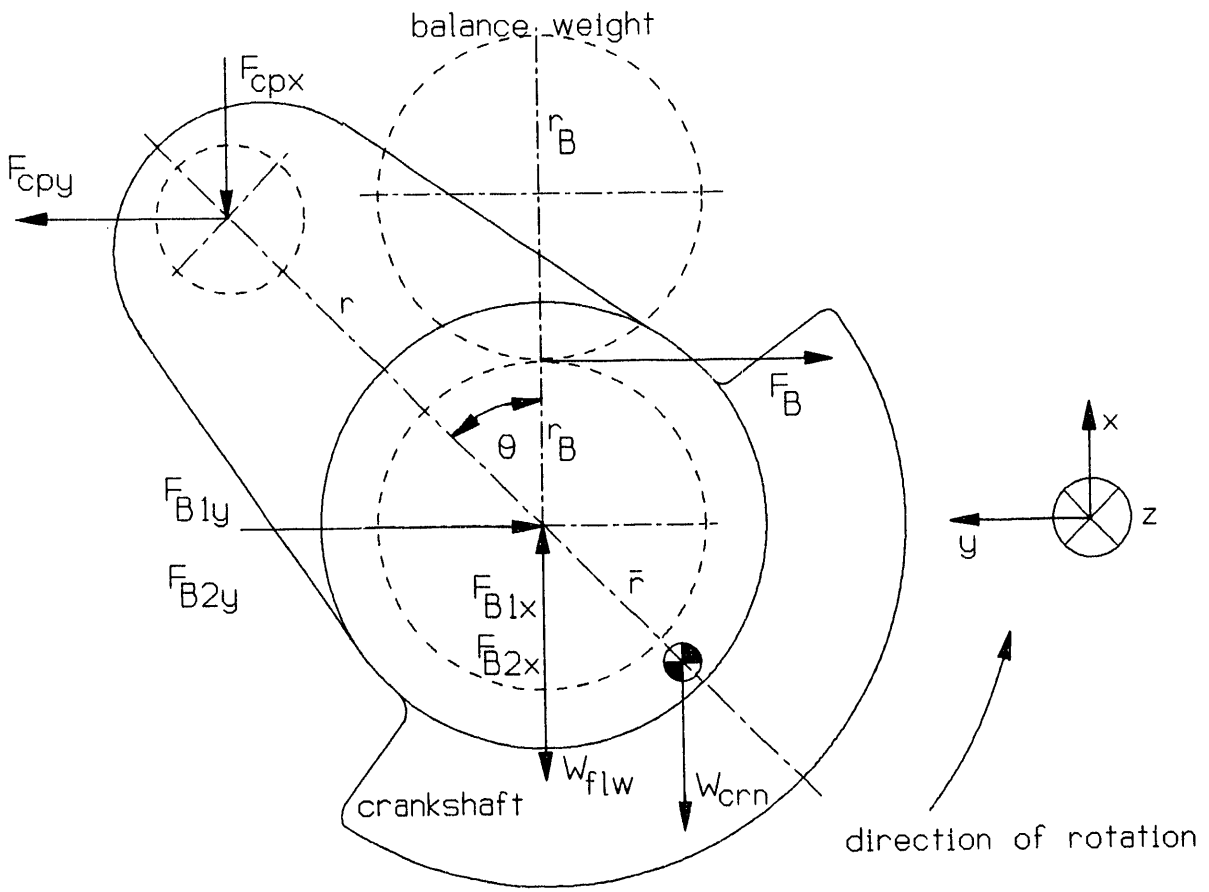

Figure 2.4. Free body diagram of crankshaft

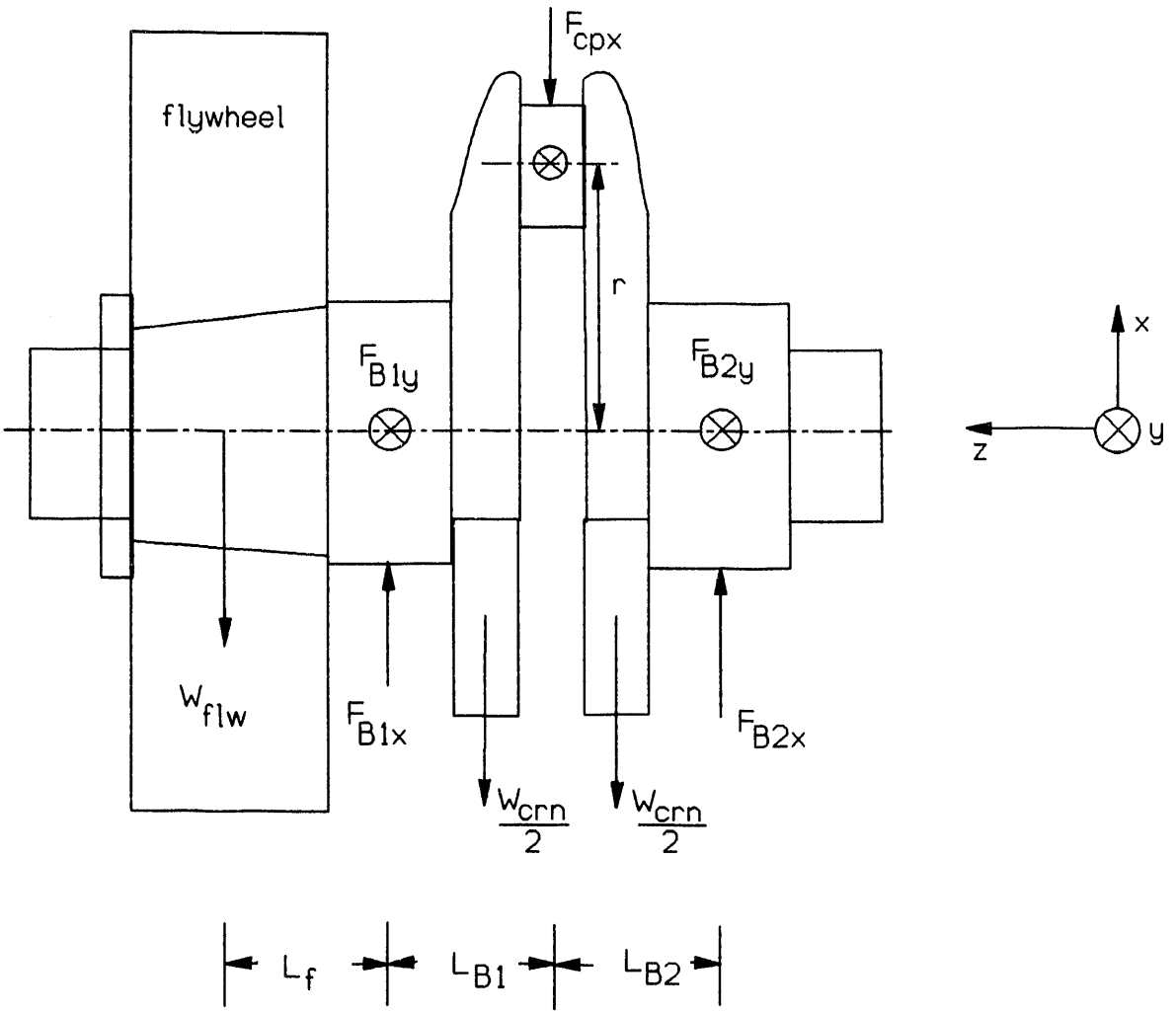

Figure 2.5. Free body diagram of crankshaft

L_f, L_{B1}, L_{B2} =position of crankshaft journals and flywheel,

M_{B1}, M_{B2} =frictional torque in main bearings,

M_L =loading torque on the engine,

F_B =reaction force from balance weight,

r_B =radius of crankshaft gear driving the balance weight, or radius of gear on balance weight shaft,

I_{flw} =mass moment of inertia of the flywheel about its axis of rotation,

I_{cm} =mass moment of inertia of the crankshaft about its axis of rotation,

M_O =torque necessary to drive the oil pump.

Figure 2.6 shows the balance weight. Equation of motion : moment z:

$$W_B\overline{r}_B\sin\theta - F_B r_B + M_B + F_C r_B = I_B(-\theta'') \qquad (2.26)$$

where W_B =weight,

$\overline{r}_B$ =center of gravity,

M_B =frictional torque due to bearings of the balancing weight shaft,

I_B =moment of inertia,

F_C =reaction force from the camshaft gear.

Figure 2.7 shows the camshaft. Equation of motion :

moment z:

$$2F_C r_B - M_{CB} - M_{VP} = I_C\frac{1}{2}\theta'' \qquad (2.27)$$

where M_{CB}, M_{VP} =frictional torques due to bearings, valves, fuel pump,

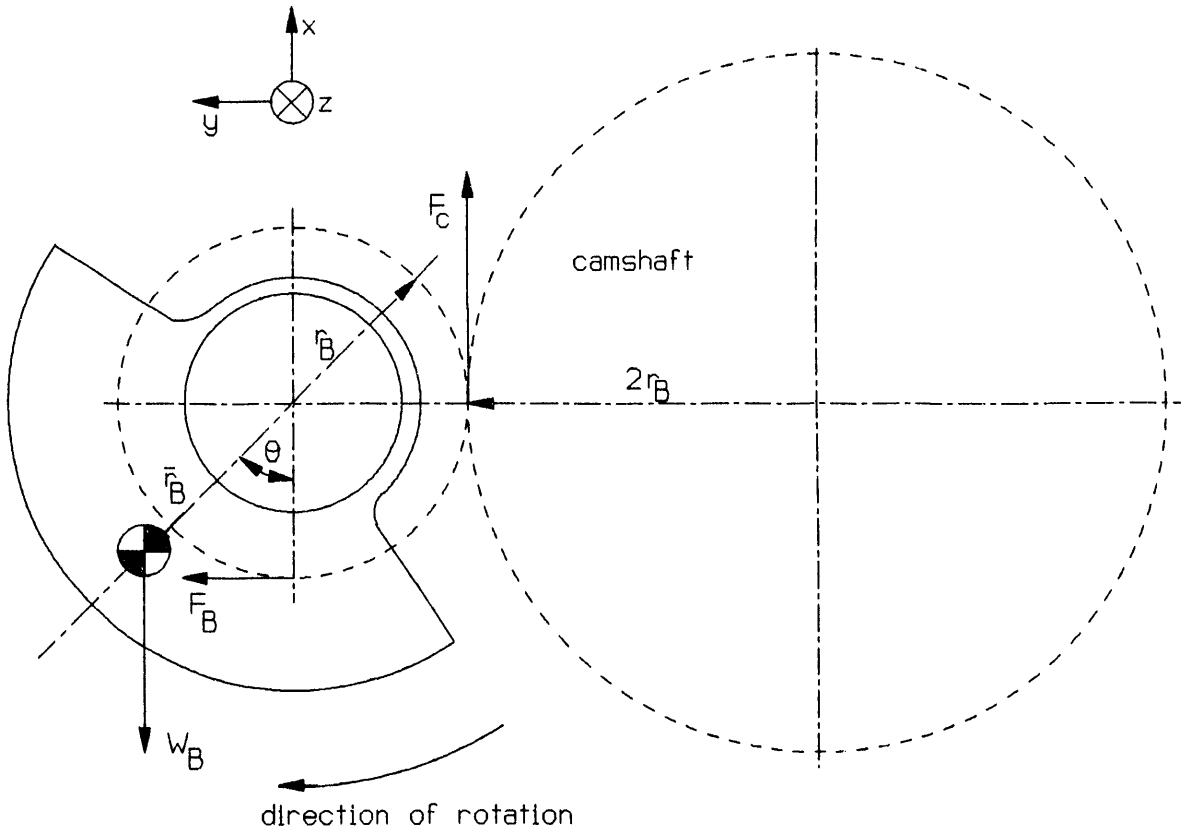

Figure 2.6. Free body diagram of balance weight

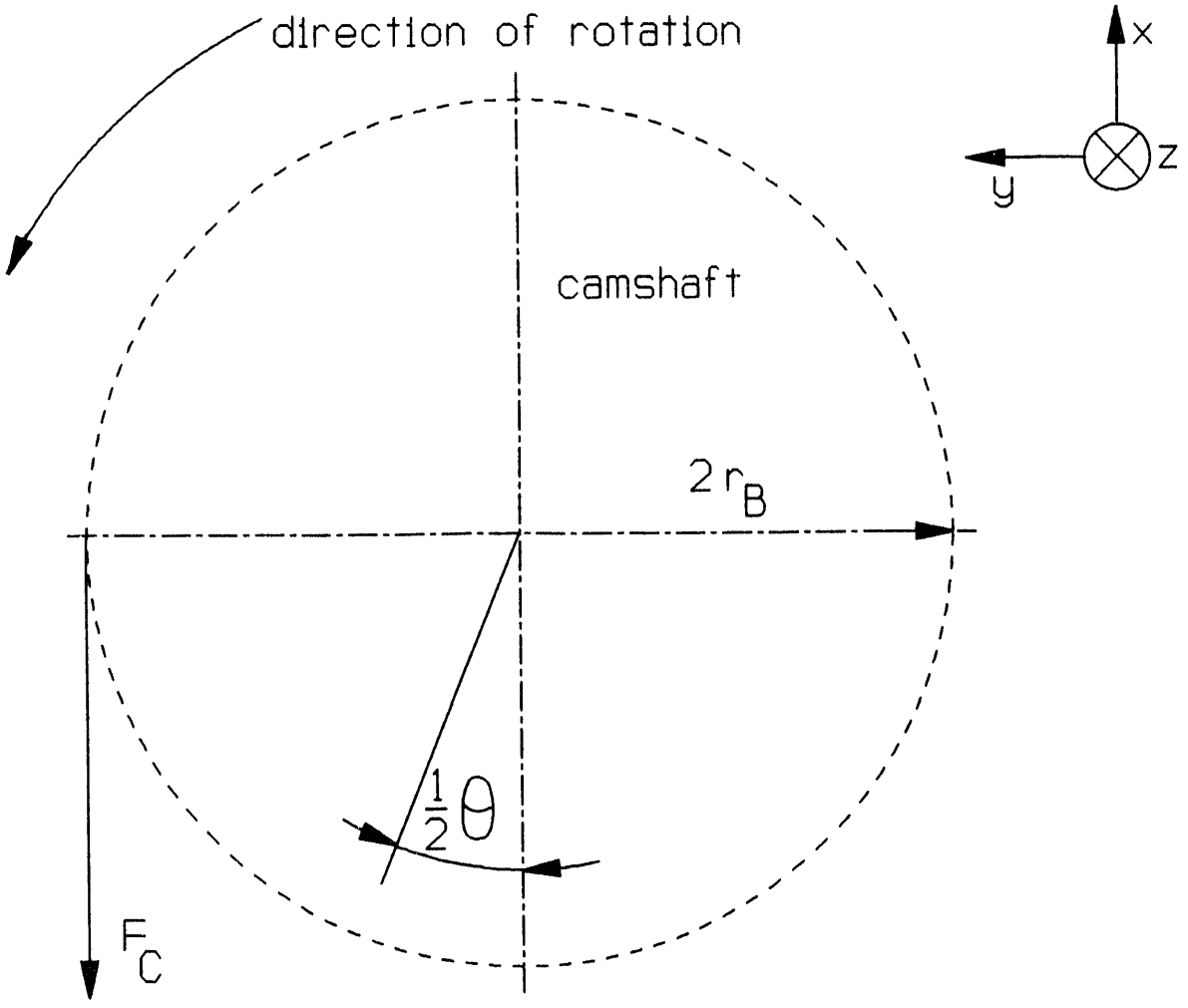

Figure 2.7. Free body diagram of camshaft

I_c =camshaft moment of inertia.

Note that diameter of camshaft gear is twice the size of the balance weight gear.

Combining equations (2.25) (2.26) and (2.27) leads to

$$\begin{aligned} &F_{cpx}r\sin\theta+F_{cpy}r\cos\theta-W_{crn}\bar{r}\sin\theta-W_B\overline{r_B}\sin\theta \\ &-M_{cp}-M_{B1}-M_{B2}-M_O-M_L-M_B-\frac{1}{2}M_{CB}-\frac{1}{2}M_{VP}= \\ &I_{flw}\theta''+I_{crn}\theta''+I_B\theta''+\frac{1}{4}I_C\theta''=I_{ro}\theta'' \end{aligned} \tag{2.28}$$

where I_{ro} =total rotating moment of inertia (not including the rotating part of connecting rod).

If we eliminate F_{ppx}, F_{ppy}, F_{cpx}, F_{cpy} from equations (2.15), (2.18), (2.19), (2.20) and (2.28), and group all the frictional torques reduced to crankshaft axis of rotation on one side of the equation we can write

$$\begin{aligned} M_{IFT}=&I_{ro}\theta''+I_{cr}\frac{\lambda\cos\theta}{\cos\varphi}\varphi'' \\ &-(m_{cr}x_{cr}''+W_{cr})\,r\,(\sin\theta+\lambda_2\frac{\sin\varphi}{\cos\varphi}\cos\theta) \\ &+m_{cr}y_{cr}''\lambda_1 r\cos\theta \\ &-(m_p x_p''+W_p)\,r\,(\sin\theta+\frac{\sin\varphi}{\cos\varphi}\cos\theta) \\ &+W_{crn}\bar{r}\sin\theta+W_B\overline{r_b}\sin\theta \\ &-F_{pr}r\,(\sin\theta+\frac{\sin\varphi}{\cos\varphi}\cos\theta) \\ &+M_L \end{aligned} \tag{2.29}$$

where $\lambda_1=L_1/L$, $\lambda_2=L_2/L$.

Equation (2.29) is the main part of the (P-ω) method for Instantaneous Frictional Torque (IFT) measurement.

2.3 FORCES ACTING ON CONNECTING ROD

Now consider the case where the force acting on the point along the connecting rod is known, by measurement with strain gages. Figure (2.8) shows connecting rod with strain gages attached to it. Strain gages divide connecting rod into two parts. Only equations of motion of the part above strain gage location are necessary to determine frictional forces of the piston assembly.

x-axis:

$$F_{cr}\cos\varphi - F_{ppx} - W_{c1} = m_{c1}x''_{c1} \qquad (2.30)$$

From the equation (2.15) we obtain

$$F_f(-sgn\ x'_p) = m_p x''_p + F_{pr} + W_p - F_{ppx} \qquad (2.31)$$

Eliminating F_{ppx} from (2.30) and (2.31)

$$F_f(-sgn\ x'_p) = m_p x''_p + m_{c1}x''_{c1} + F_{pr} - F_{cr}\cos\varphi + W_p + W_{c1} \qquad (2.32)$$

where F_{cr} =connecting rod force determined by strain gage measurement,

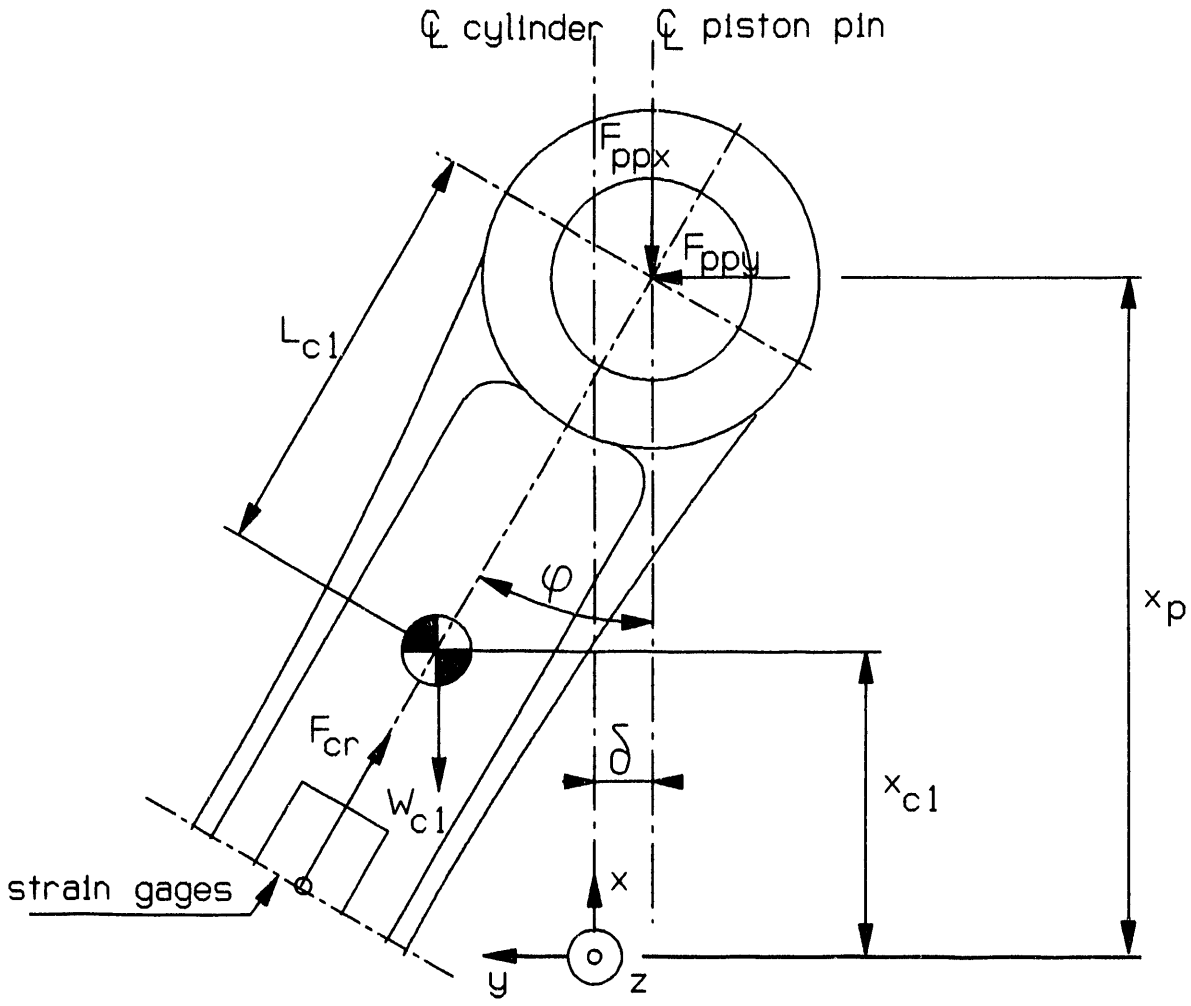

Figure 2.8. Free body diagram of connecting rod (upper part)

W_{c1} =weight of the connecting rod part above strain gages,

m_{c1} =mass of the above,

x_{c1} =location of the center of mass,

$$x_{c1}=x_p-L_{c1}\cos\varphi \tag{2.33}$$

where L_{c1} =distance from connecting rod small end to location of center of mass of the part mentioned above.

In order to calculate the Instantaneous Frictional Torque - IFT (eq 2.29) and Instantaneous Frictional Piston Force - IFPF (eq 2.31) a computer program has been written in C language. Choice of C language instead of FORTRAN was dictated by C portability, ease of graphics implementation, PC hardware control and execution code speed.

Required inputs for computer calculation are:

1. Cylinder pressure data
2. Crankcase pressure data
3. Loading torque signal if any
4. Connecting rod strain gage signal if piston frictional force calculation is required
5. Shaft encoder signal

In addition to above, information about engine part dimensions, masses and inertias is required as equations (2.1) through (2.31) indicate. It was clear from the very beginning that

accuracies of the pressure measurement and angular velocity were the most important factors to reduce errors in calculations. Other input signals also play important roles, but nevertheless those two are the most crucial.

CHAPTER 3: EXPERIMENTAL SETUP AND INSTRUMENTATION

3.1 ENGINES

Most of the experimental work was done on a single cylinder Deutz diesel engine. Some experiments were conducted on a single cylinder Honda gasoline engine. The following are the specifications of the engines.

DEUTZ-MAG F1L 210D DIESEL ENGINE

Number of cylinders	:	1
Bore	:	9.5 cm
Stroke	:	9.5 cm
Working principle	:	Four-stroke Diesel, direct injection, air-cooled
Compression ratio	:	17:1
Inlet valve opens	:	23° before TDC
Inlet valve closes	:	63° after BDC
Exhaust valve opens	:	63° before BDC
Exhaust valve close	:	23° after TDC

Figures 3.1, 3.2 and 3.3 show views of the Deutz engine.

HONDA ATC 250 ES GASOLINE ENGINE

Number of cylinders	:	1
Bore	:	7.45 cm
Stroke	:	5.73 cm
Working principle	:	Four-stroke Gasoline, air-cooled
Compression ratio	:	9:1
Inlet valve opens	:	8° before TDC
Inlet valve closes	:	35° after BDC
Exhaust valve opens	:	40° before BDC
Exhaust valve close	:	5° after TDC

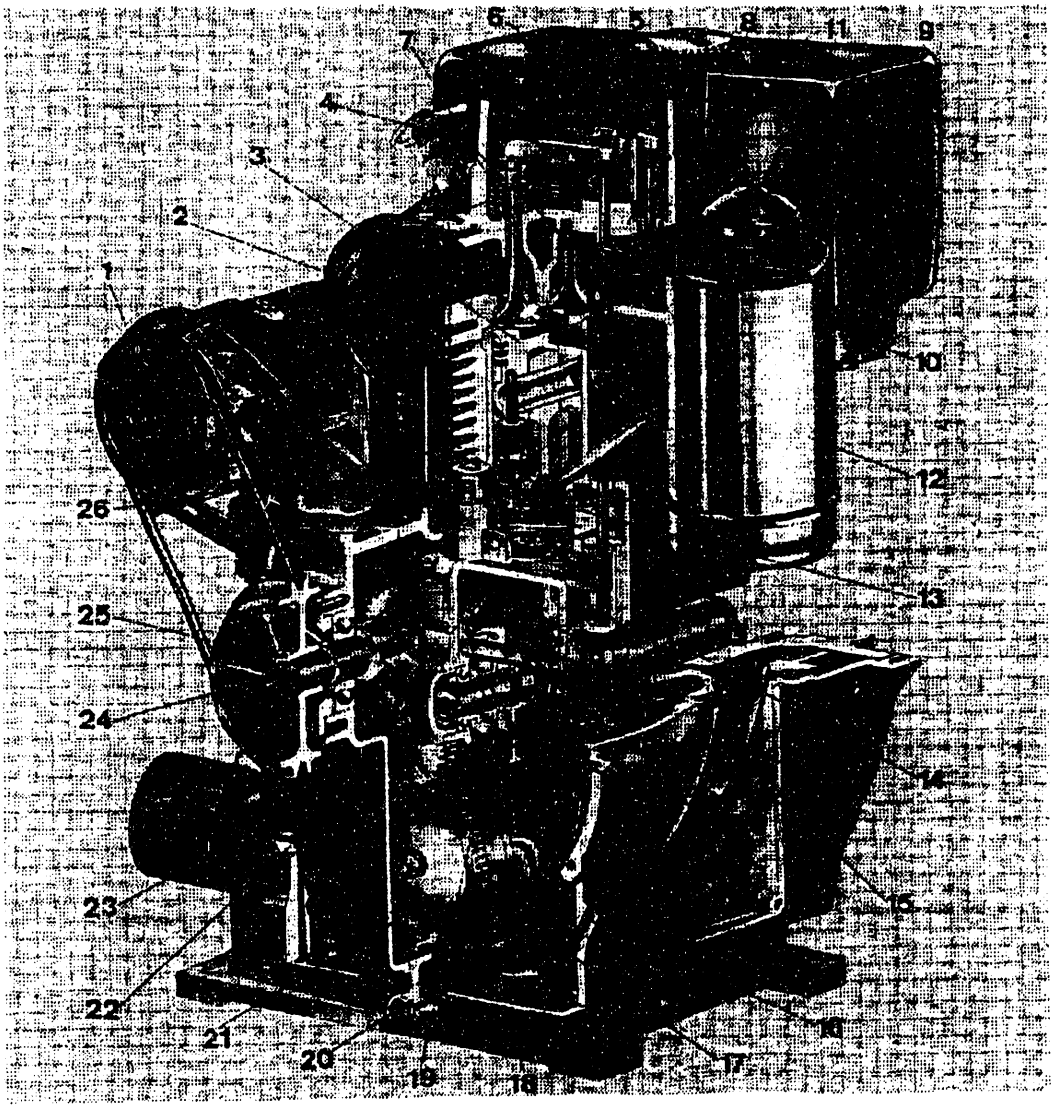

Figure 3.1. Assembled Deutz diesel engine view

1.Three-phase generator
2.Exhaust silencer
3.Piston
4.Injector nozzle
5.Rocker arm
6.Oil filter neck
7.Valves
8.Cylinder head
9.Fuel tank
10.Fuel filter
11.Protective cap
12.Oil bath air-cleaner
13.Injection pump
14.Crankshaft
15.Flywheel blower
16.Lube oil dipstick
17.Oil intake pipe
18.Oil pan
19.Camshaft
20.Oil drain plug
21.Oil pump
22.Oil pressure switch
23.Lube oil filter
24.Mass balancing shaft
25.V-belt pulley
26.Cylinder

Items 1, 2, 25 are not installed on the engine

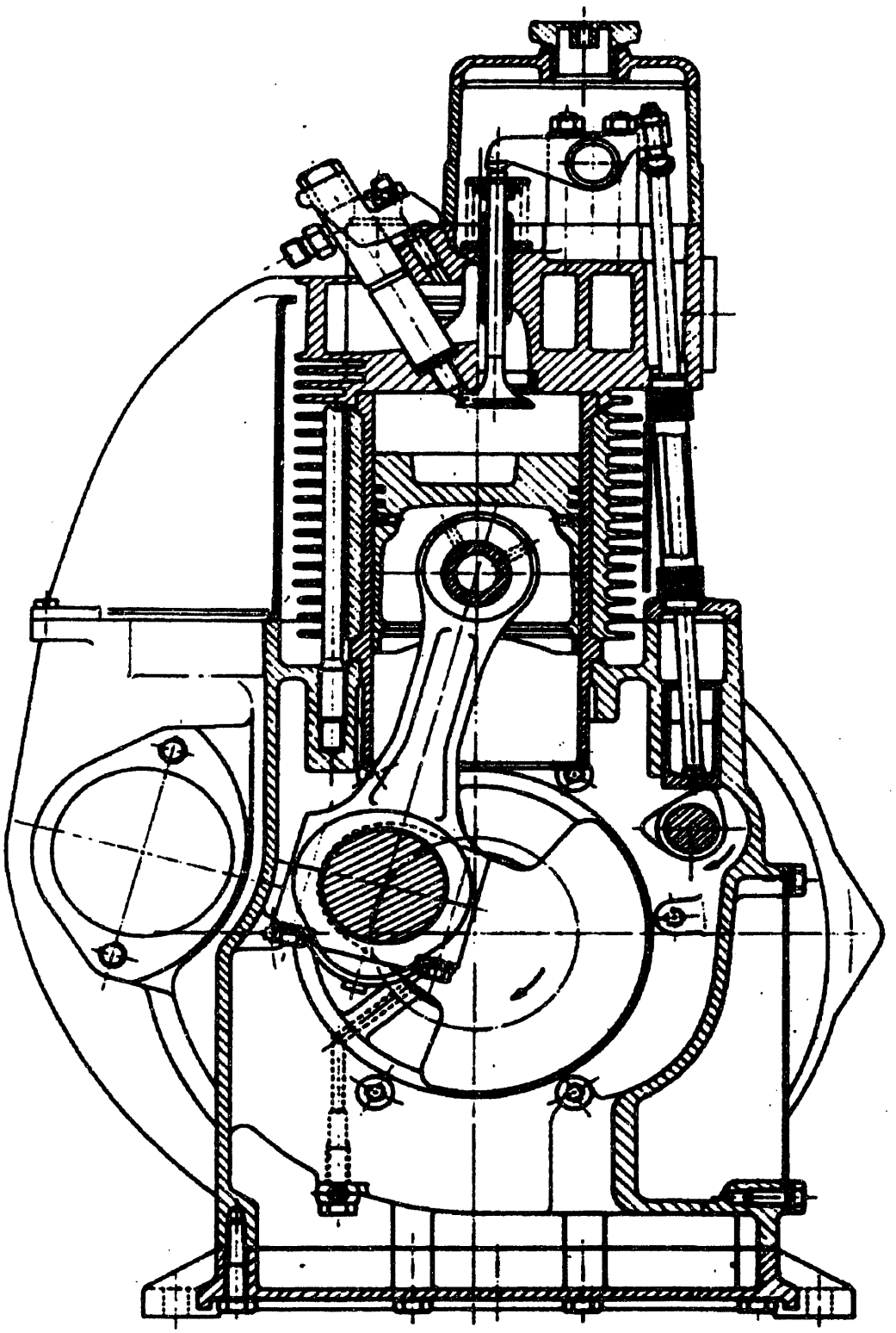

Figure 3.2. Deutz diesel engine cross section

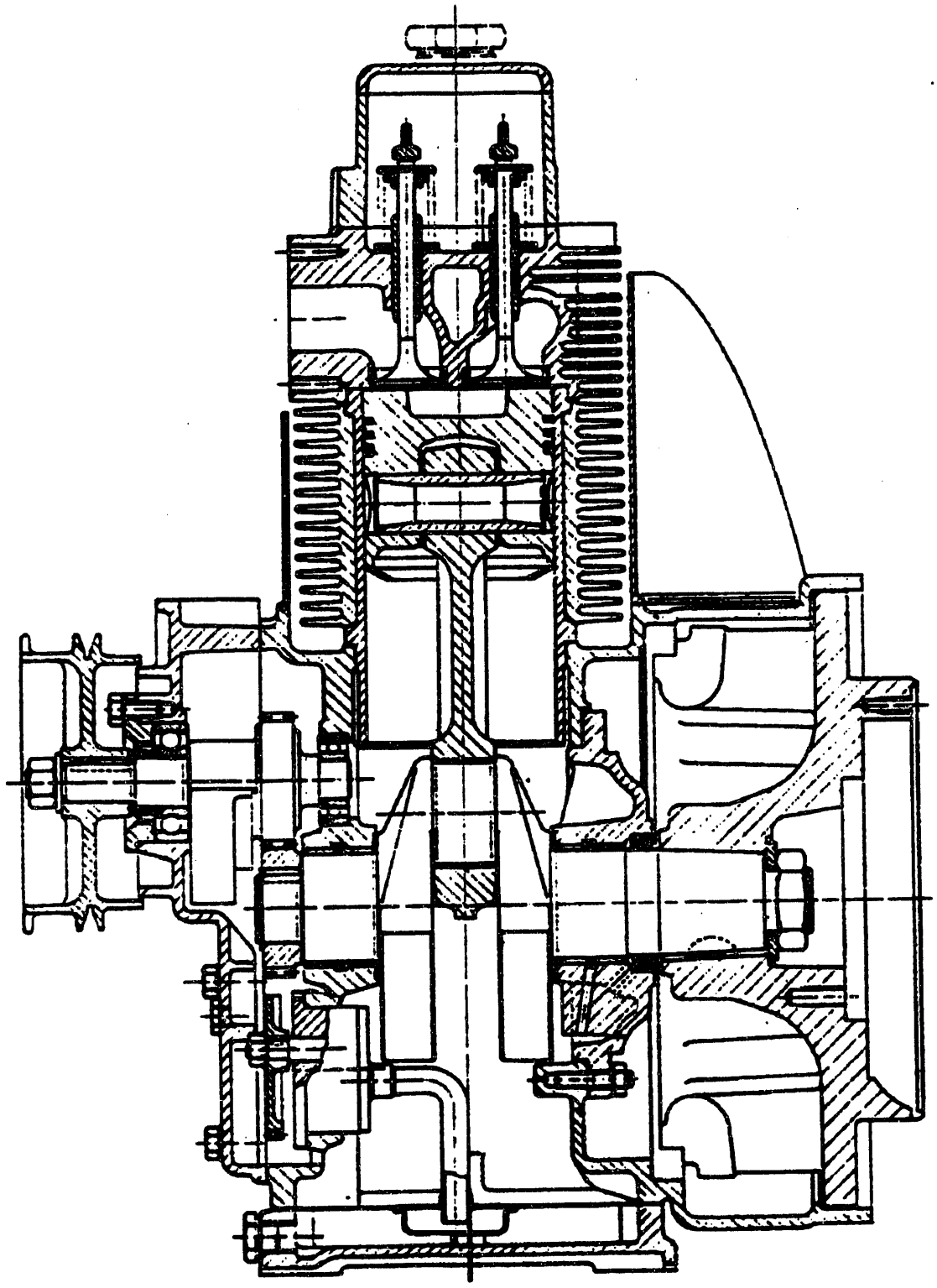

Figure 3.3. Deutz diesel engine longitudinal section

3.2 INSTRUMENTATION

3.2.1 CRANK ANGLE, ANGULAR VELOCITY AND ANGULAR ACCELERATION

The crankshaft position with respect to its position when the piston is at its Top Dead Center, defined as the crank angle, constitutes the most fundamental measurement of the (P-ω) method since every component of the friction equations (2.29) and (2.31) is expressed as a function of it. Its measurement was accomplished by the use of digital shaft encoders. A fair amount of time was spent to analyze errors associated with different shaft encoders, as reported in chapter 4 and published in reference [13]. At present time a BEI hollow shaft encoder mounted on the flywheel is used. It has 0.05 degrees resolution (BEI Model 5VL674HAZ). This shaft encoder has a 2 inch diameter opening in the middle, which provides access to load the engine from the flywheel side.

At present, work is in progress to use an angular accelerometer to measure the crankshaft acceleration.

3.2.2 CYLINDER GAS PRESSURE

Cylinder gas pressure was measured by a quartz pressure transducer installed in the cylinder head. A low range pressure transducer was mounted in the engine crankcase.

Errors in the measurements of the cylinder gas pressure result in errors in calculating the frictional losses and other performance parameters in combustion engine. These errors are explained in chapter 5, and in reference [14].

The pressure transducers were calibrated according to the manufacturers' specifications, on a dead-weight tester, Ashcraft tester model 1305D. The calibration was always performed on the

specific transducer-amplifier combinations.

The dead-weight tester was modified by adding a heating device to allow the calibration of the pressure transducers while mounted at elevated temperatures similar to the cylinder head temperature.

*** DEAD-WEIGHT TESTER MODIFICATION:**

Figure 3.4 shows the modified dead-weight tester with the heating element. The temperature of transducer, calibrating oil and mounting was varied and reached a maximum of 350°C.

*** EFFECT OF FLAME ON THE RESPONSE OF PRESSURE TRANSDUCERS:**

Figure 3.5 shows a rotating disk-device developed in our laboratories to simulate the thermal stresses in the transducer in the presence of the combustion flames. A basic principle behind such a device is that the transducer is mounted above a rotating disk with a hole in it and is exposed to a burner flame below. The frequency of exposure to the flame was adjusted to be equal to the frequency of the flame in an actual engine. This device was able to screen the performance of different designs of transducers and determine their responses to the thermal stresses. Also there have been performed other kinds of tests in order to choose the best transducer for our purposes. Those tests and their findings will be presented later. Finally an AVL Model QC41B-X gold plated pressure transducer was chosen for combustion pressure measurement and a KISTLER Model 206 PIZOTRON® low-range pressure transducer, for crankcase pressure measurement. KISTLER dual-mode amplifier Model 5004 was used for both transducers.

3.2.3 MASS MOMENTS OF INERTIA MEASUREMENT

Accurate determination of the mass moments of inertia is important for an accurate determination of the instantaneous

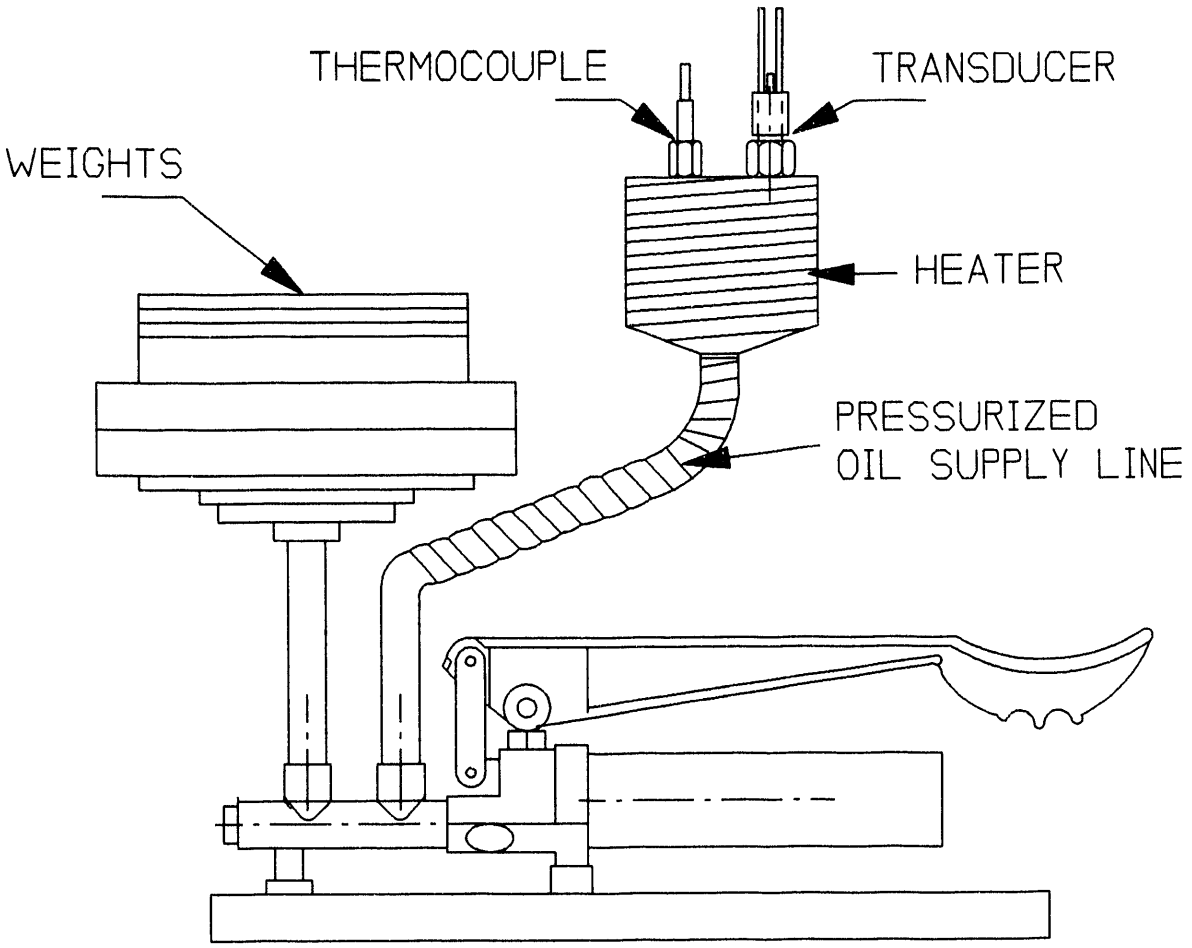

Figure 3.4. Dead-weight calibrator

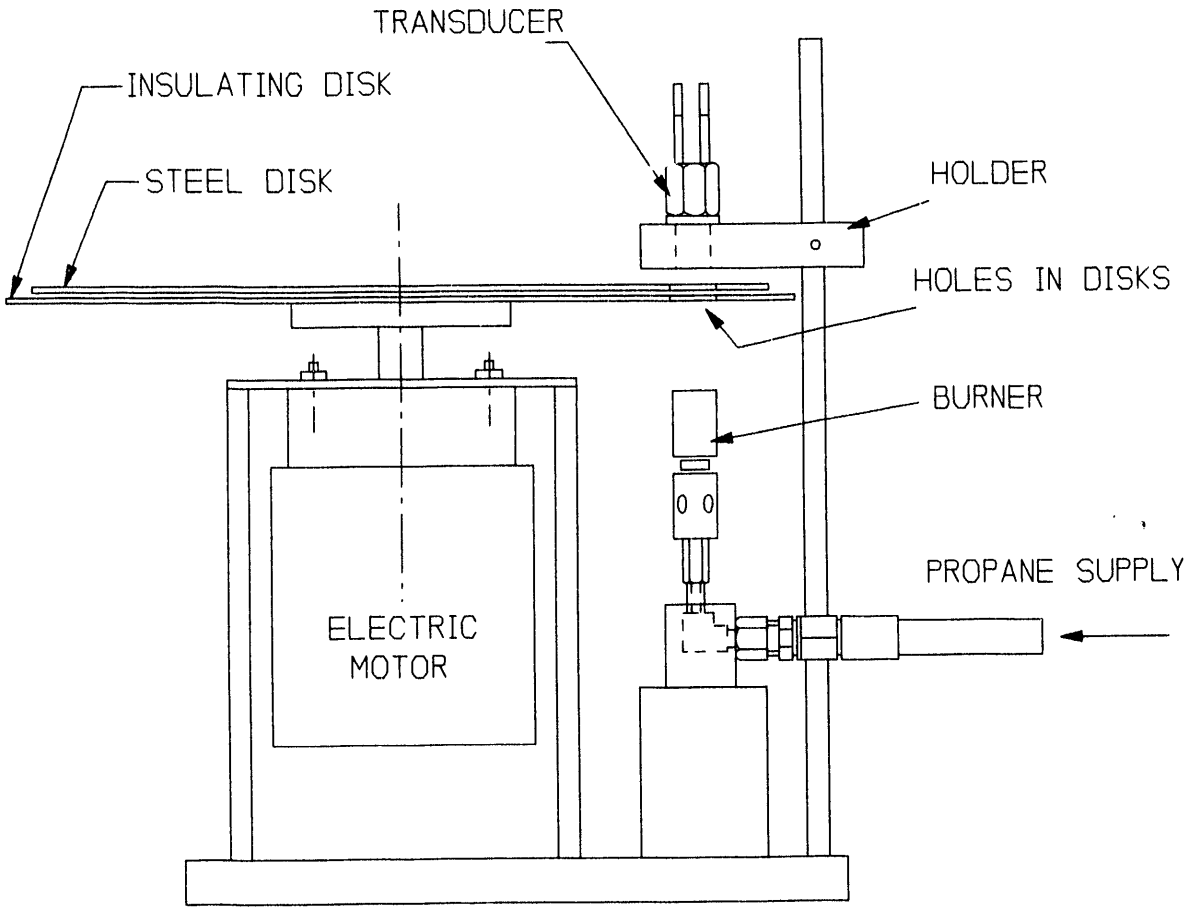

Figure 3.5. Rotating-disk device

frictional torque. Originally, inertia measurements were conducted on Ford Motor Company's torsional-pendulum test rig. Since continuous modifications were made to the engine, there was a need for an alternative. Also the engine's flywheel was too heavy and its inertia had to be measured instead of being calculated from drawings. The alternative solution was an inertia table which was built at Wayne State University. Figure 3.6 shows the design of the inertia table. The principle of operation is based on the fact that inertia is proportional to the frequency of free oscillation.

The inertia table has three major components.

1. Rotating circular table to put engine parts on.
2. Practically frictionless spring (Bendix FREE-FLEX® Model 5053-800)
3. Optical pick-up to measure the frequency of table oscillations.

The signal from the optical pick-up was fed into the frequency meter. The time for 10 full periods was measured and the average calculated. Every measurement could be reproduced to 0.001 second.

Initially the inertia table was calibrated with geometrically simple models made out of steel. Inertia of such pieces could be accurately calculated by knowing weights and dimensions. Samples were chosen to be similar in weight, but simpler in dimensions, and therefore approximately having the same inertias as the different engine parts. Figure 3.7 shows the calibration curve of the inertia table.

The inertia table has proven to be a very accurate and useful instrument. Inertia measurements of all engine parts which were not modified were reproduced and found in agreement with the original measurements done at Ford Motor Co.

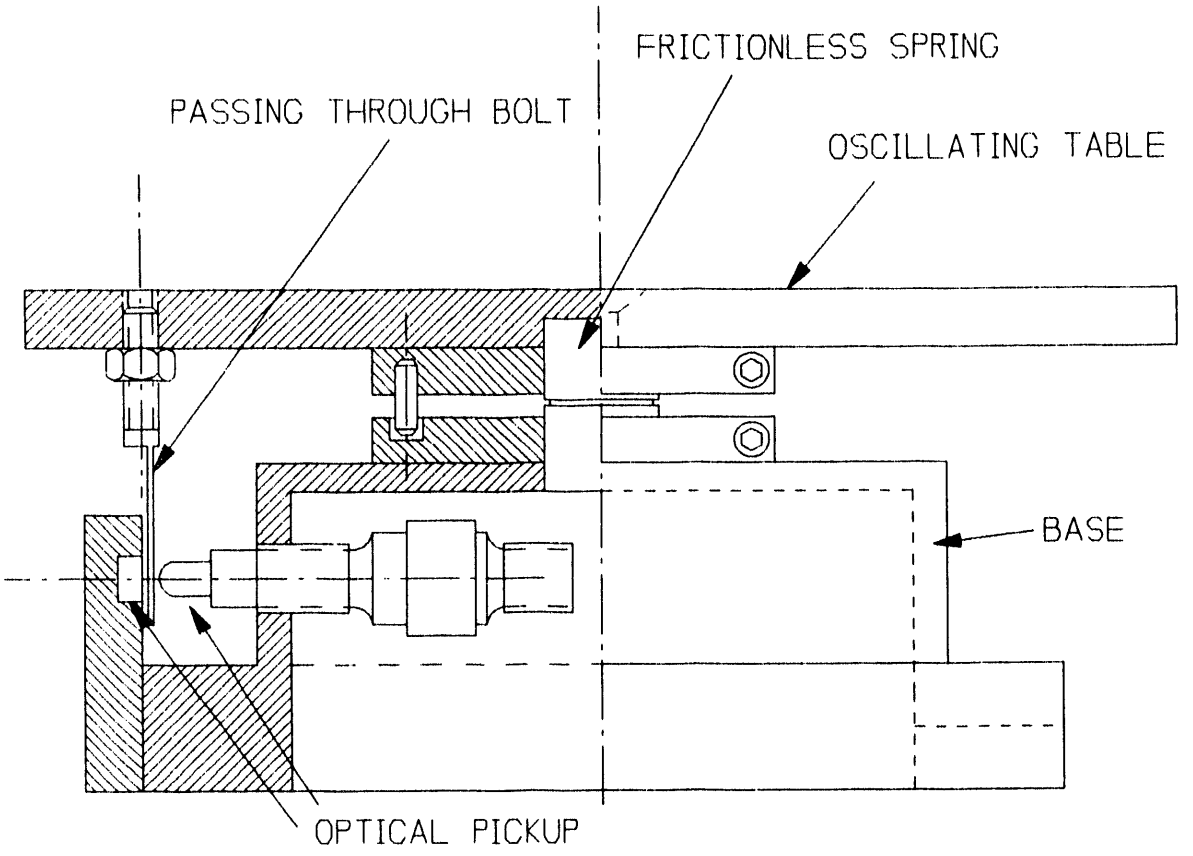

Figure 3.6. Inertia table

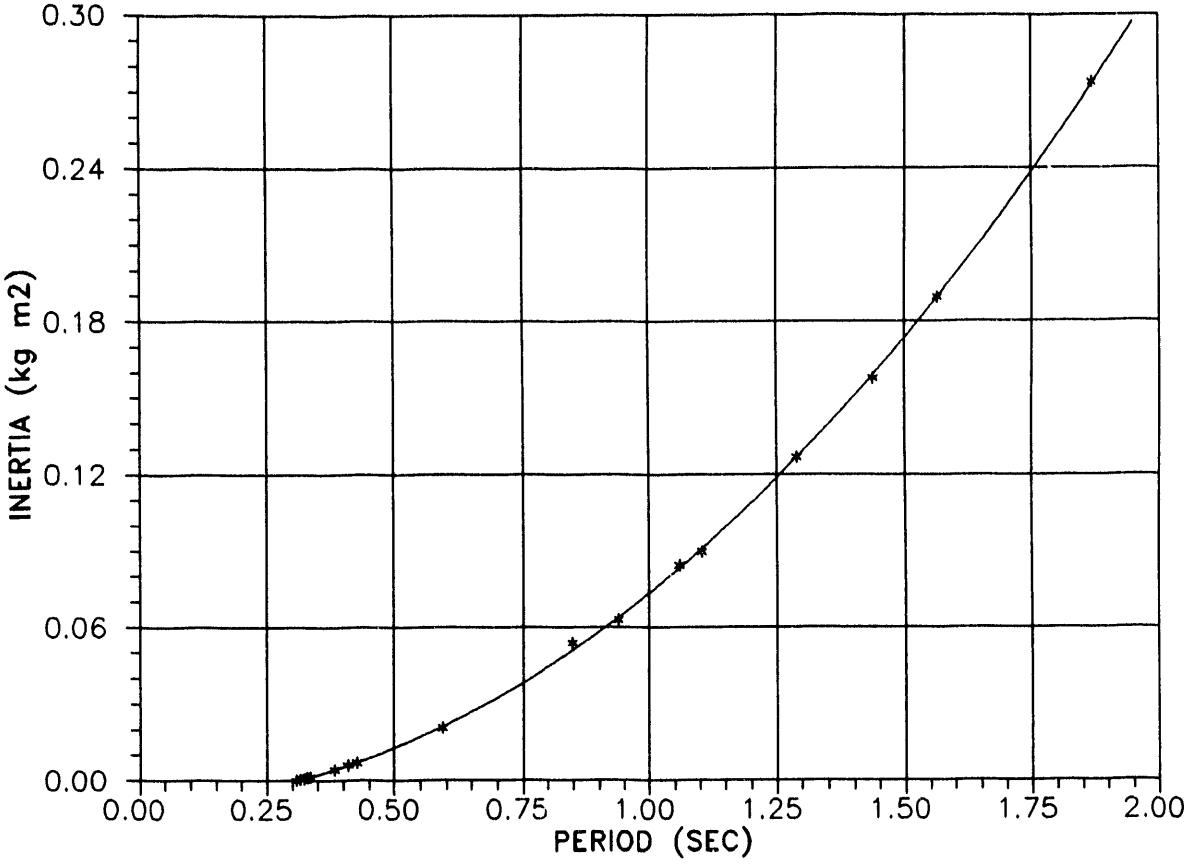

Figure 3.7. Inertia table calibration curve

3.2.4 MEASUREMENT OF CONNECTING ROD FORCE

The connecting rod was instrumented with Micro Measurements resistance type strain gages number WK-06-062TT-350. The mounting surfaces on the connecting rod were machined to provide a uniform, symmetrical cross-section. Gages were applied to the neutral axis of the connecting rod and compensated for bending and temperature variations by means of the orientation of the gages in the Wheatstone bridge circuit. Since gages were located on a point along the connecting rod axis of symmetry, half of the gage was in tension whereas the other half was in compression when there was a bending moment. Temperature compensation was achieved by locating gages as close together as possible in order to subject all of them to the same temperature. High temperature conductance of the connecting rod alloy was very helpful in satisfying that condition. A T type OMEGA thermocouple was mounted next to the strain gages to monitor temperature. The calibration was performed by Eaton Co. and showed excellent linearity and thermal compensation. Also for every run when data were taken we always performed a dynamic calibration of the strain gage and compared it to the static calibration. During every thermodynamic engine cycle when valve openings overlap at TDC engine gas pressure is very close to atmospheric. The inertia forces acting on the connecting rod are known at every point per cycle. By examining closely the strain gage signal, there is a noticeable point where frictional forces of the piston assembly change direction. At that point it can be assumed that those forces are close to zero. Therefore at that point we can equate the strain gage signal with a known valve.

Figure 3.8 shows the modification made to the engine in order to obtain connecting rod force data.

A grasshopper linkage was used to conduct wires from strain gages to the MEASUREMENT GROUP signal conditioning amplifier Model 2310.

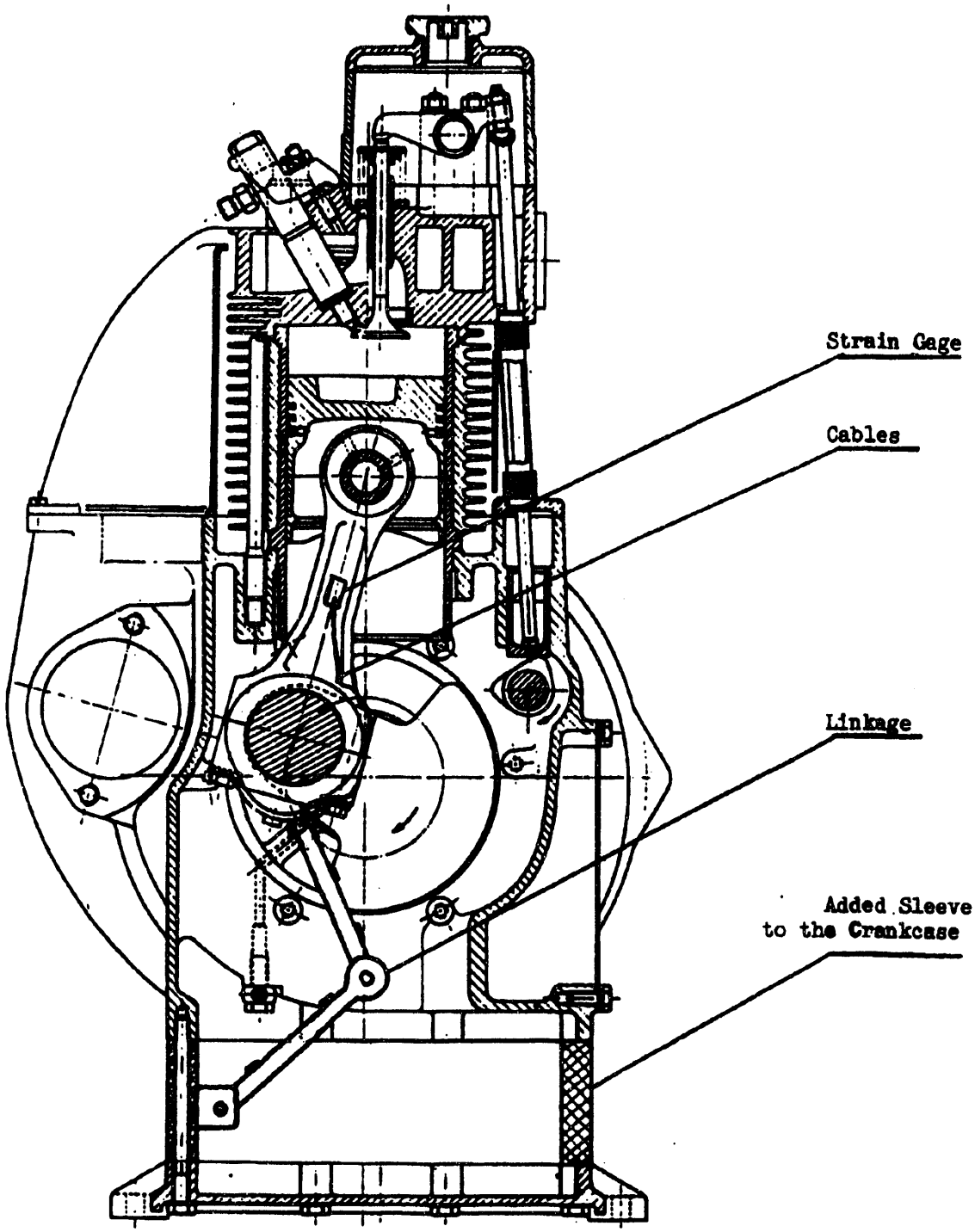

Figure 3.8. Engine modification

CHAPTER 4: ERROR ANALYSIS OF ANGULAR VELOCITY MEASUREMENTS

4.1 BACKGROUND

Errors in the measurement of the angular velocity were first detected after examining figure 4.1. This figure shows two levels of sudden oscillations in ω, oscillations of low amplitude of about 0.25 rad/sec which occur throughout the cycle, and oscillations of high amplitudes which reach about 1 rad/sec. The latter occur at discrete points in the cycle such as points a, b, c and d. Since there is no process in the thermodynamic cycle or engine operation which would produce such a sudden change in ω, attention was drawn to the accuracy of the shaft encoder.

Figure 4.2 shows traces for the cylinder pressure during idling and the corresponding instantaneous angular velocity, for two different runs. The difference between the two sets of traces is that the initial angular position of the shaft encoder was shifted relative to the other position by about 240 degrees. It is noticed that the high amplitude oscillations, or noise, have also been shifted relative to the engine top dead center, by 240 degrees. This experiment indicated clearly the existence of errors in the shaft encoder caused by variations.

The errors in the angular velocity measurements produce errors in the angular acceleration and the calculated inertia torque. The angular acceleration was calculated from

$$\omega' = \frac{d\omega}{dt} = \frac{1}{2}\frac{d\omega^2}{d\theta} \qquad (4.1)$$

$$\omega = \frac{\Delta\theta}{\Delta t}$$

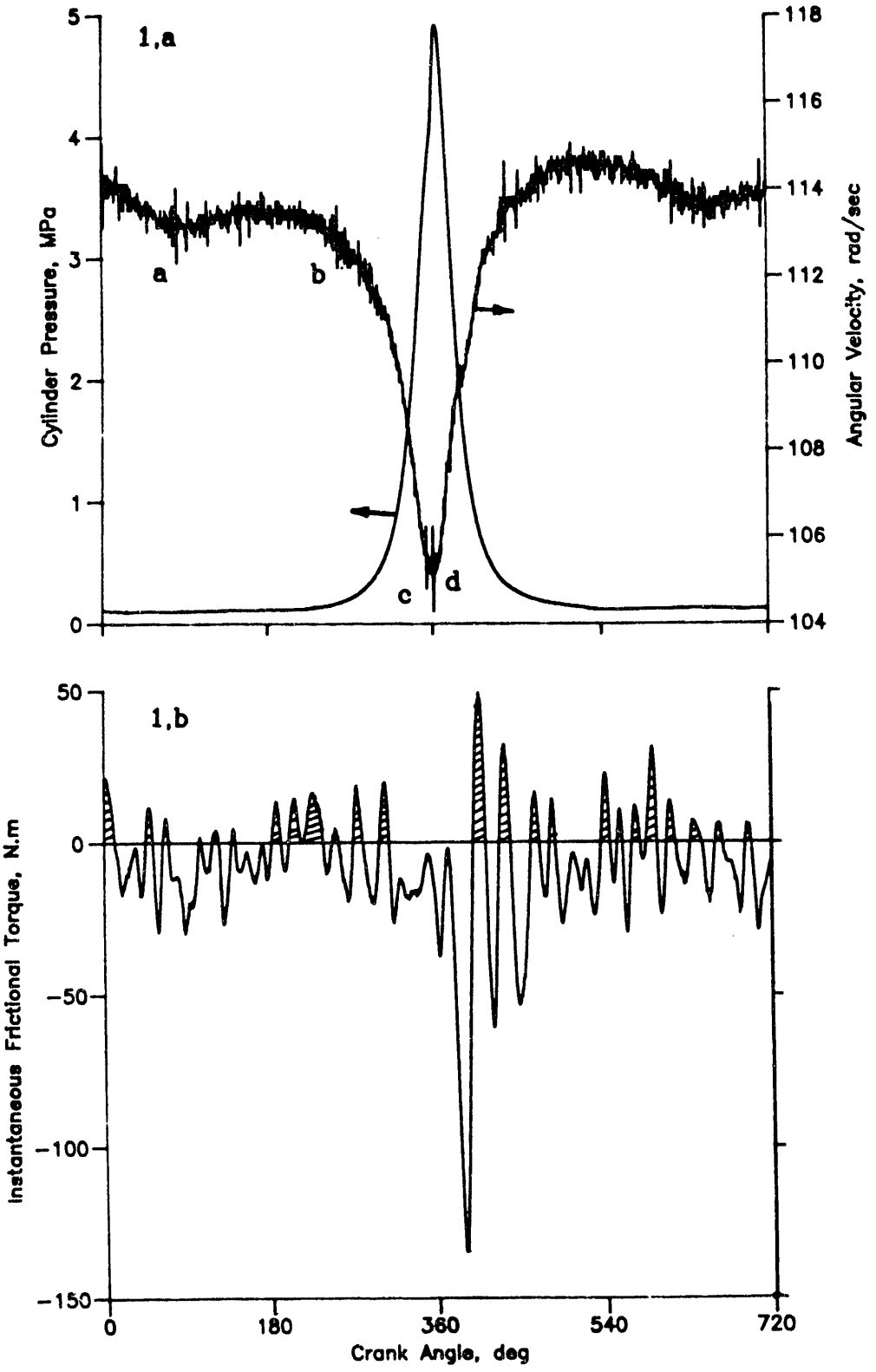

Figure 4.1. Sample of the angular velocity , cylinder gas pressure and IFT over one cycle

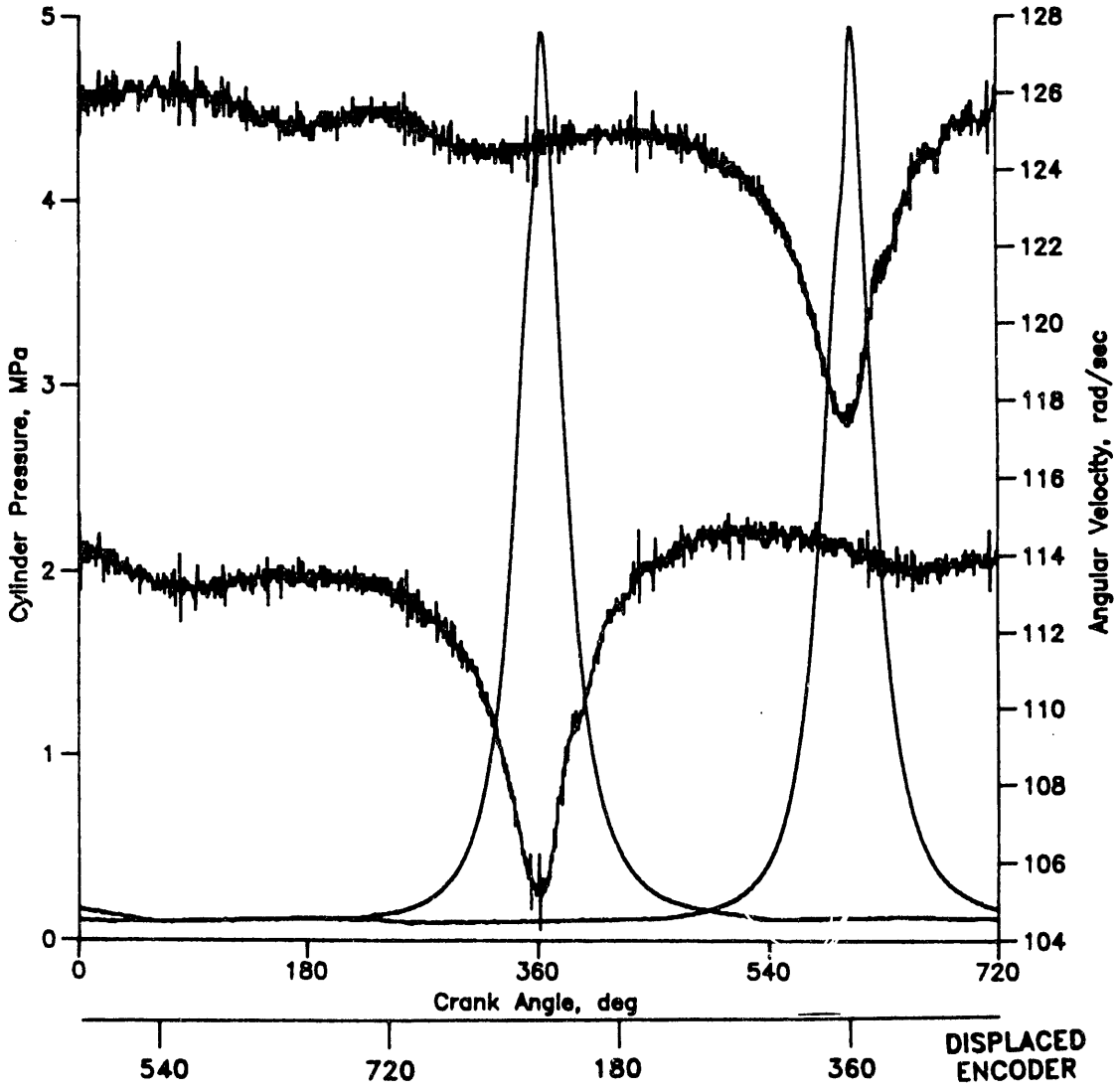

Figure 4.2. Effect of angular displacement of shaft encoder disc on the position of the sudden oscillation in ω with respect to TDC

ω' was calculated from ω traces with least-squares cubic splines, from $\Delta\theta$ according to equation (4.2)

$$\omega' = \frac{\Delta\omega^2}{2\Delta\theta} \tag{4.2}$$

4.2 ANGULAR VELOCITY ERROR ANALYSIS

Equation 4.1 indicates that the error incorporated in calculating ω can be due to an error in the measurement of $\Delta\theta$ as well as an error in the measurement of Δt.

The error given in ω is given by ref [17],[18]

$$\omega_\omega = \sqrt{\left(\frac{\partial\omega}{\partial\Delta\theta}\omega_{\Delta\theta}\right)^2 + \left(\frac{\partial\omega}{\partial\Delta t}\omega_{\Delta t}\right)^2} \tag{4.3}$$

From equation (4.1)

$$\omega_\omega = \sqrt{\left(\frac{\omega_{\Delta\theta}}{\Delta t}\right)^2 + \left(\frac{\Delta\theta}{\Delta t^2}\omega_{\Delta t}\right)^2} \tag{4.4}$$

where $\omega_{\Delta\theta}$ is the error in $\Delta\theta$ of the encoder or flywheel teeth, and $\omega_{\Delta t}$ is the error due to the time resolution of the counters. Formally the above statements are written as:

$$\omega_{measured} = \omega_{actual} \pm \omega_{\Delta\omega} \tag{4.5}$$

$$\Delta\theta_{measured} = \Delta\theta_{actual} \pm \omega_{\Delta\theta} \tag{4.6}$$

$$\Delta t_{measured} = \Delta t_{actual} \pm \omega_{\Delta t} \tag{4.7}$$

In the instrumentation the error in Δt is equivalent to one count and is equal to $\pm ((12)10^6)^{-1}$ sec.

Figure 4.3 shows the results of the above analysis carried out for different values of $\Delta\theta$ and rotational speed. ω_ω increases with the angular velocity ω and with the decrease in $\Delta\theta$. An error of 0.05 degrees produces 5 percent error in ω, if the $\Delta\theta$ is 1 degree. This error is appreciable because the engine speed varies only from 5 to 15 percent during the cycle, as shown in figures 4.1 and 4.2. ω_ω decreases with the decrease in $\omega_{\Delta\theta}$.

4.3 ERRORS IN $\Delta\theta$

Errors in $\Delta\theta$ may be due to manufacturing or installation. The manufacturing errors may be in the allowable tolerances in the divisions within the encoder or the teeth of the flywheel gear. Errors in $\Delta\theta$ can also be caused by misalignment within one encoder or the flywheel gear. The installation errors may be caused by misalignment between the encoder shaft and the driving shaft, and between the flywheel and the crankshaft.

4.4 EXPERIMENTAL APPARATUS AND PROCEDURE

The errors in ω were investigated by using a simplified engine mechanism. The effects of the cylinder gas pressure, and the inertia of the reciprocating parts were eliminated by removing the piston and connecting rod. In addition, all the valve train and auxiliaries except the oil pump were removed. The mechanism used is shown in Figure 4.4.

The crankshaft was motored by an electric starter to a speed of about 900 RPM. The starter was then turned off and the crankshaft decelerated to a complete stop. The data for ω were recorded from the beginning of motion of the crankshaft to its

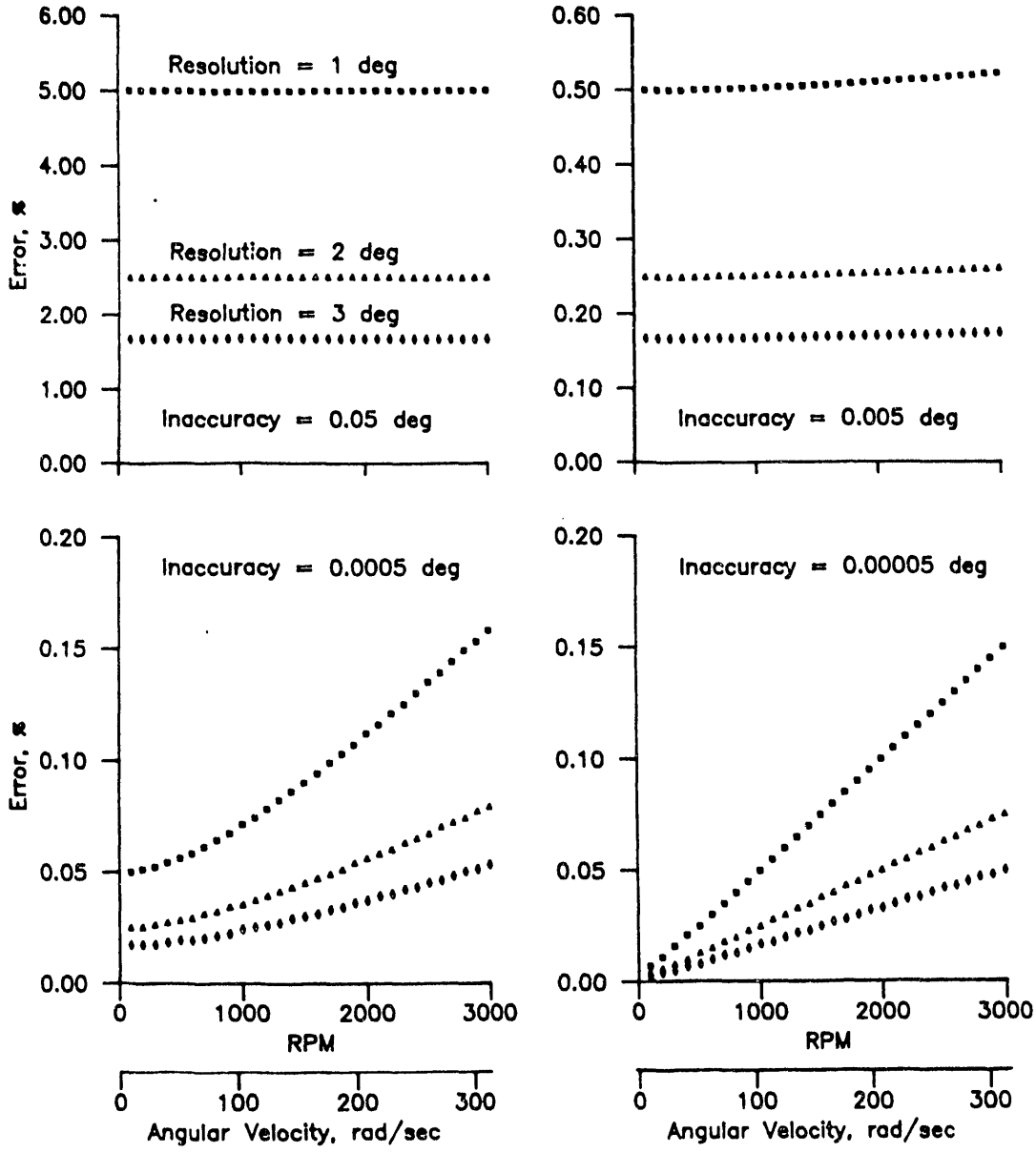

Figure 4.3. Effect of speed and $\Delta\theta$ on the error in ω

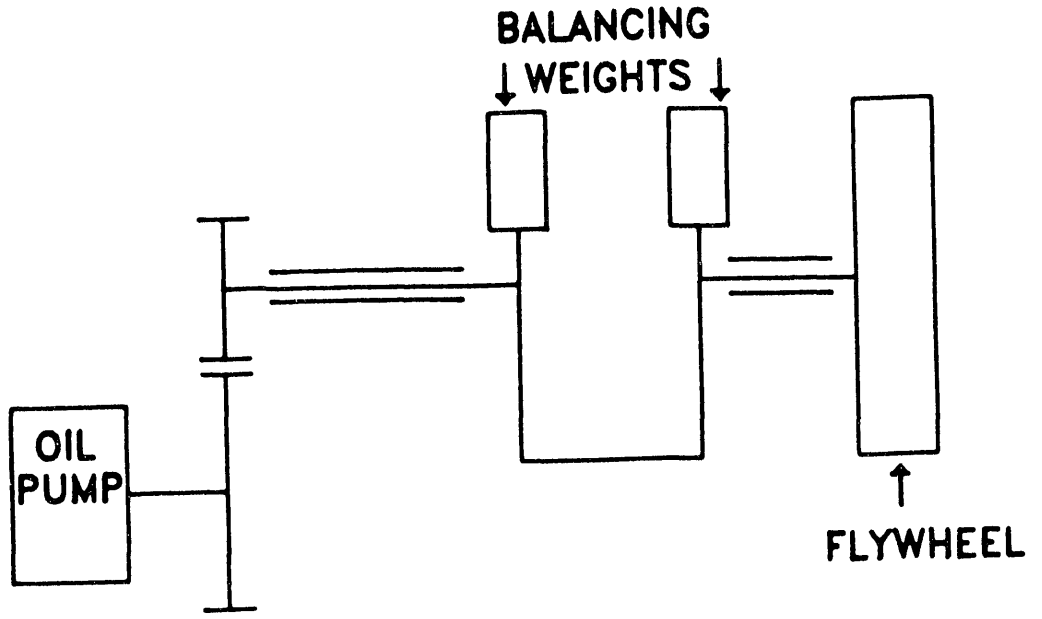

Figure 4.4. Mechanism for error analysis in shaft encoders

complete stop. The results and analysis presented in this paper are for data taken 5 to 10 revolutions after the disengagement of the starter to avoid any residual effects of the starter torque on the dynamics of the system.

Experiments were conducted with four different shaft encoders and with the flywheel gear teeth. The terms flywheel-mounted and front-mounted refer to the location of the encoder as being on the flywheel or on the front end of the crankshaft. The encoder was rigidly fitted in its position on the engine frame. A rigid coupling was used between the encoder shaft and the crankshaft. The digital pulses in the shaft encoder were produced by an on-off action of an infrared light emitter-collector system installed on the optical disk of the encoder.

The measurement of ω from the flywheel gear teeth was accomplished by installing a magnetic pick-up on the flywheel housing opposite to the teeth. The pick-up produced a digital pulse every time a gear tooth passed by it. Two 12 MHz counters were used alternately for measuring the time between consecutive pulses produced by the pick-up. The output of the magnetic pick-up was fed into a data acquisition system, which was specifically designed for this work. The time between consecutive pulses was recorded and stored in the memory and later in the hard disk of a 16 bit 80286 based micro computer. The computer interfaced with the acquisition system.

4.5 EXPERIMENTAL RESULTS AND DISCUSSIONS

4.5.1 EFFECT OF ENCODER-TO-ENCODER VARIATIONS

Figure 4.5 shows ω traces obtained while the engine was decelerating, by using three different encoders and the flywheel gear teeth. Encoder A-1 and A-2 showed sudden oscillations in ω.

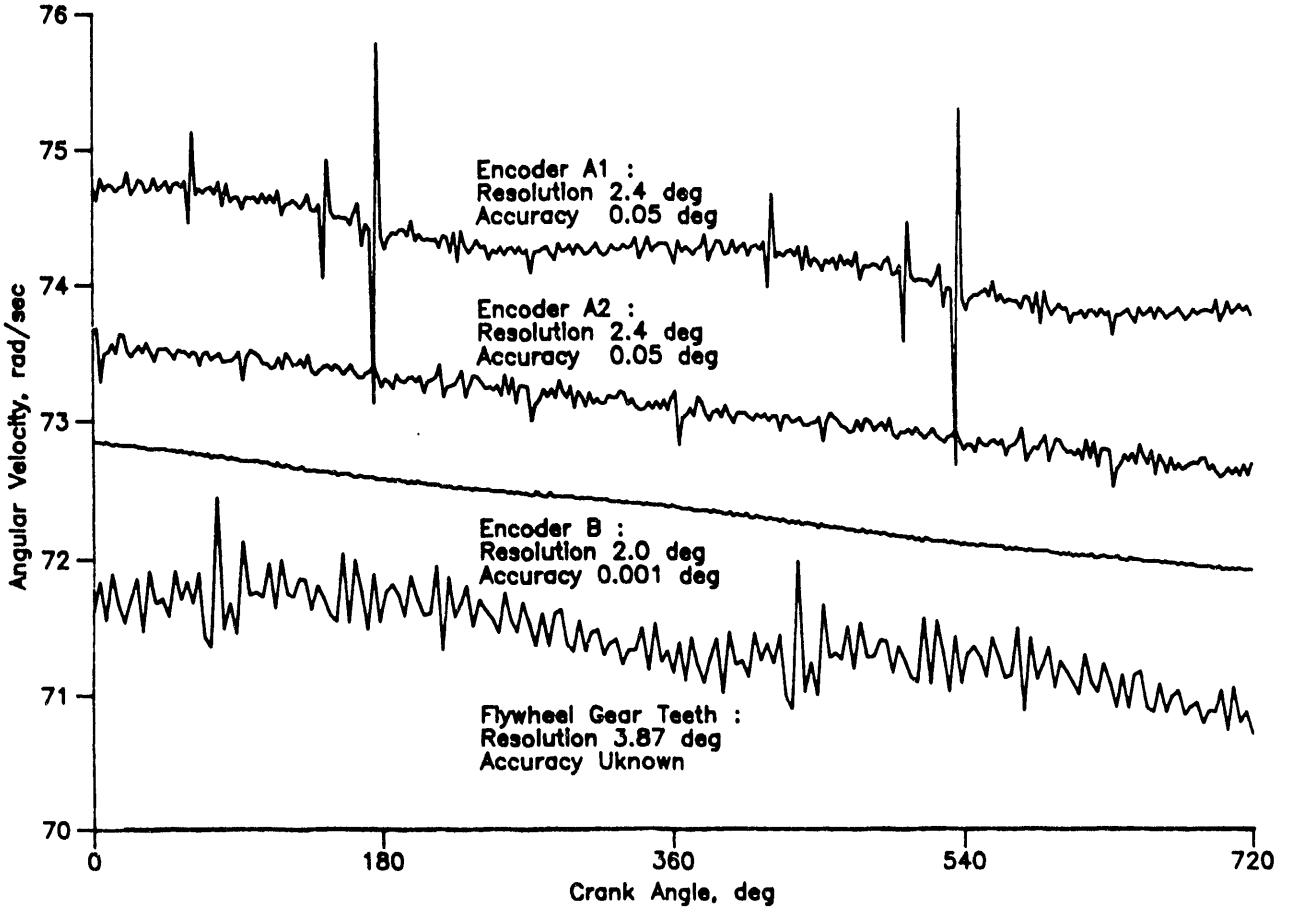

Figure 4.5. Effect of encoder-to-encoder and flywheel gear tooth-to-tooth variations on error in ω

A low frequency sinusoidal wave is riding on trace A-1, and does not exist in trace A-2. Encoder B produced a good signal with little noise. The flywheel produced a signal with a lot of noise. All the traces in figure 4.5 were taken on the flywheel side of the engine and the encoders were properly aligned.

Figure 4.6 shows the results of the time-dependent frictional torque in the two main bearings and oil pump while the crankshaft was decelerating. The ω data for figure 4.6 are from figure 4.5 for encoder A-1. The numbers on the curves indicate the cycle number after turning on the starter switch. Figure 4.6 shows positive frictional torque around the TDC of the high speed cycles. This is an indication of errors in measuring ω. Figure 4.7 is similar to figure 4.6 for the shaft encoder A-2. A-2 encoder produced better results than A-1 encoder. Figure 4.8 for shaft encoder B appears to produce the best results for instantaneous friction torque. The sinusoidal shape of the curves is caused by the variation in the loading on the bearings caused by the centrifugal force of the balancing weights in absence of the piston and connecting rod. Note that A-2 and B encoders produce close results for instantaneous friction torque at the very low speeds, where the errors are not as significant as they are at the high speeds.

Figure 4.9 shows results obtained with encoders A-1, A-2 and C, all mounted on the front of the engine. Encoder C produced a high frequency, low amplitude sinusoidal oscillation at 200 Hz superimposed on the main signal. The sinusoidal oscillation is not related to the crankshaft rotation. This was proved when the encoder was mounted on an electric drill and produced exactly the same oscillation.

4.5.2 EFFECT OF ROTATIONAL SPEED

The traces obtained for ω after the crankshaft decelerated and

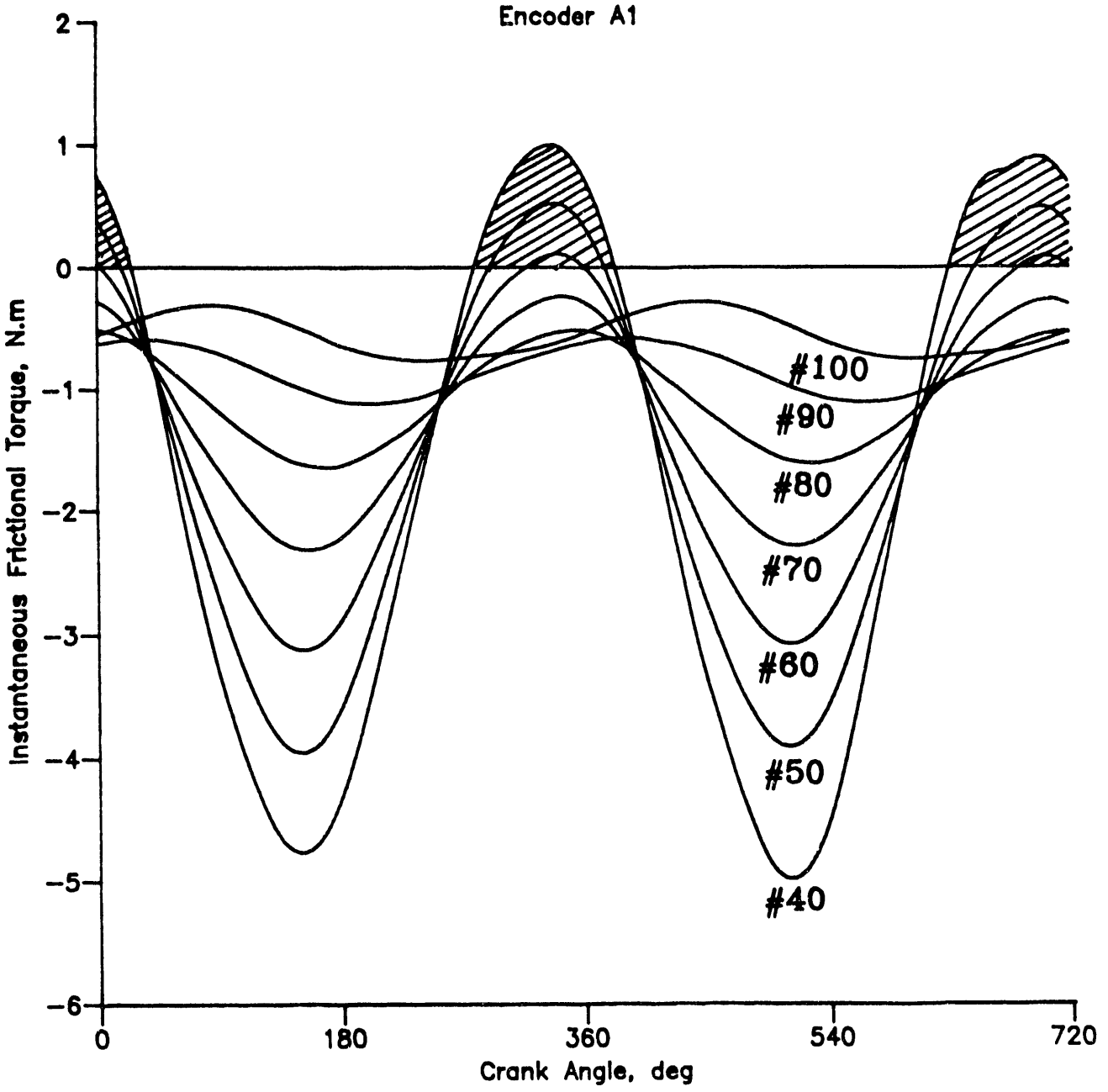

Figure 4.6. Effect of errors in shaft encoder A-1 on time-dependent frictional torque

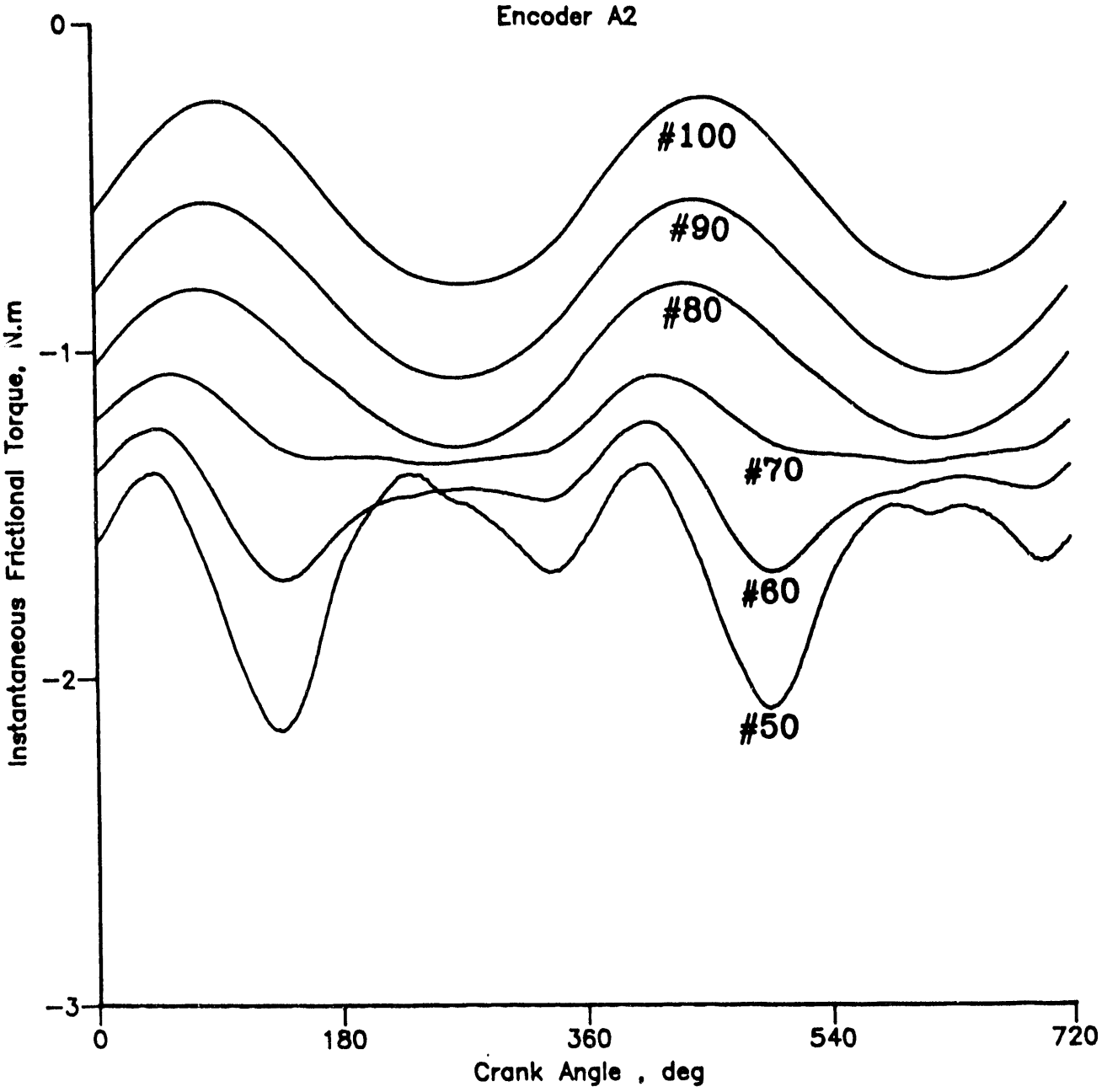

Figure 4.7. Effect of errors in shaft encoder A-2 on time-dependent frictional torque

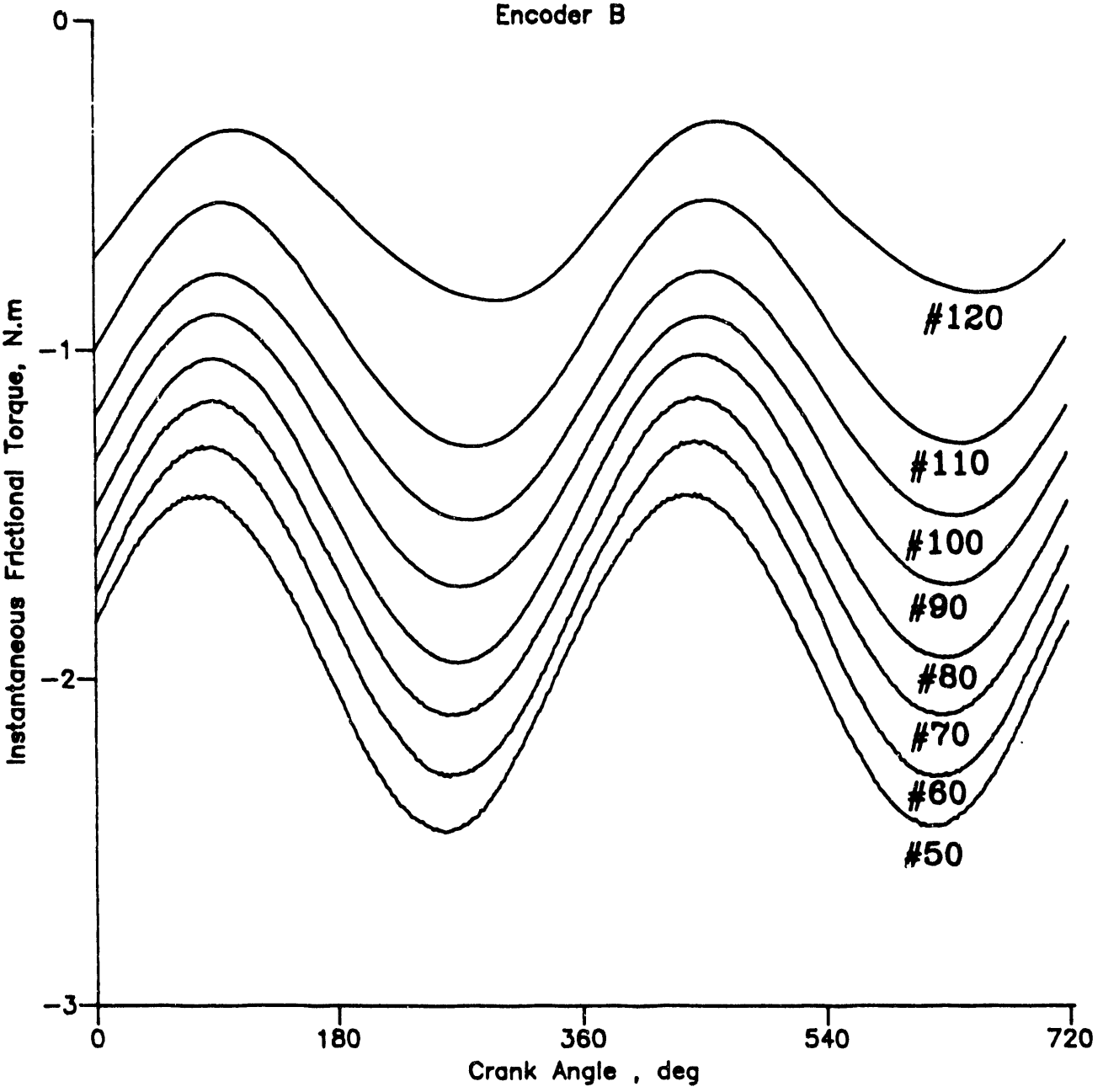

Figure 4.8. Time dependent frictional torque determined from shaft encoder B

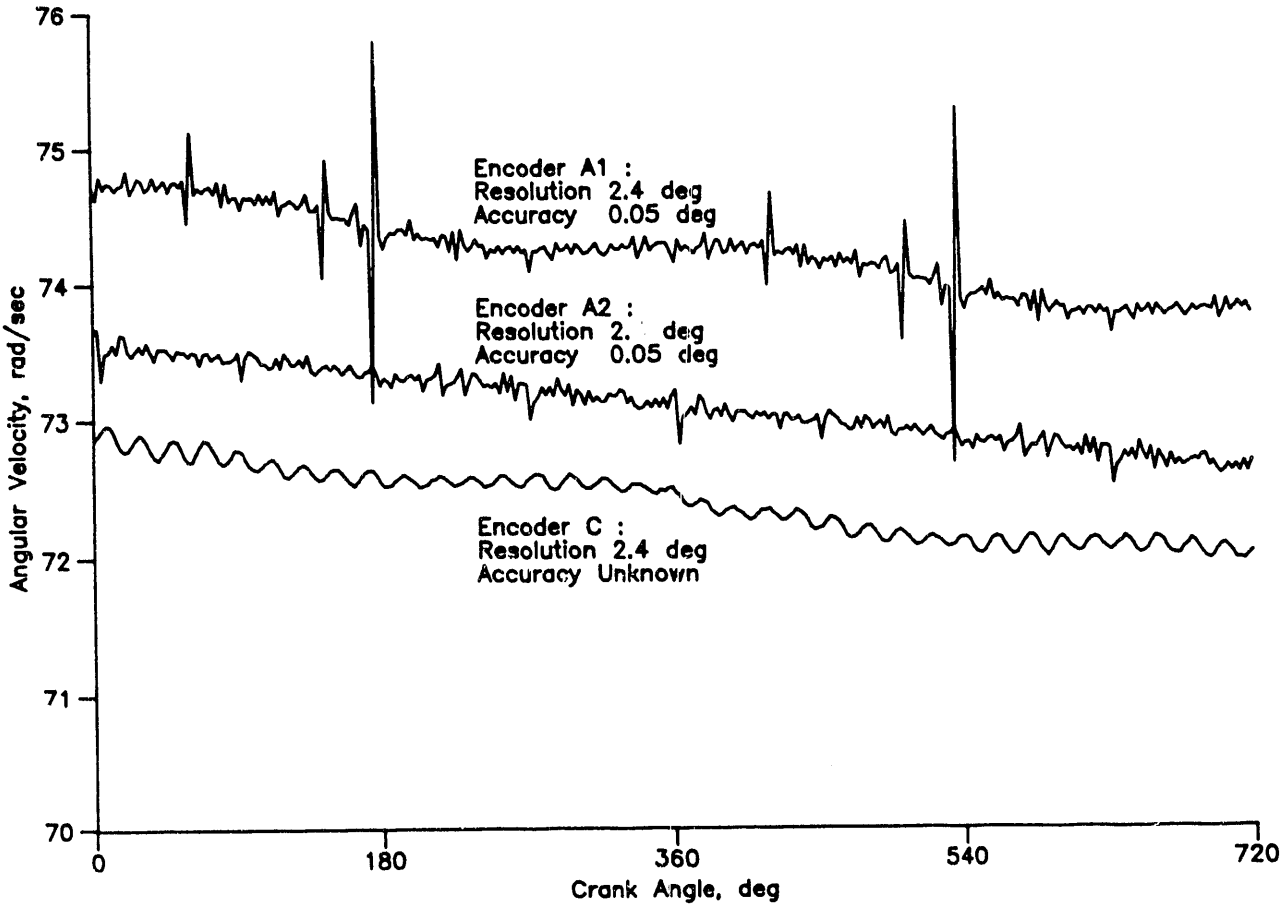

Figure 4.9. ω traces from shaft encoders A-1, A-2 and C

reached low rotational speeds are shown in figure 4.10. The high speed traces for the same run are those shown in figure 4.5. The noise level dropped appreciably at the lower speeds as discussed earlier in the theoretical analysis. The very low frequency sinusoidal oscillations at the low speed of figure 4.10 were found to be caused by the gravitational force of the crankshaft balancing weights. These weights are unbalanced in the absence of the reciprocating masses of the piston, pin and connecting rod. The contribution of the gravitational forces in the dynamics of this mechanism increases as the speed decreases.

4.5.3 EFFECT OF $\Delta\theta$

Figure 4.11 shows the effect of $\Delta\theta$ in encoder B on ω. Different values for $\Delta\theta$ were obtained by controlling the data acquisition system to obtain the data at intervals of 1, 2, 4 and 8 degrees. As $\Delta\theta$ decreases the error increases in agreement with the theoretical analysis.

4.5.4 EFFECT OF MISALIGNMENT

Another source of errors in the measurement of ω is the misalignment of the shaft encoder and the engine shaft. The types of misalignment are shown in figure 4.12. End-float misalignment does not effect the ω measurement. Parallel misalignment might cause angular misalignment. Angular misalignment produces distortions in the ω trace. To investigate the effect of the misalignment angle β on the measured ω, the two shafts were considered to be joined by the Hooke's joint. The ratio of the measured and actual ω can be given [19]

$$\frac{\omega_{measured}}{\omega_{actual}} = \frac{\cos\beta}{1-\sin^2\beta\ \sin^2\theta_{actual}} \qquad (4.8)$$

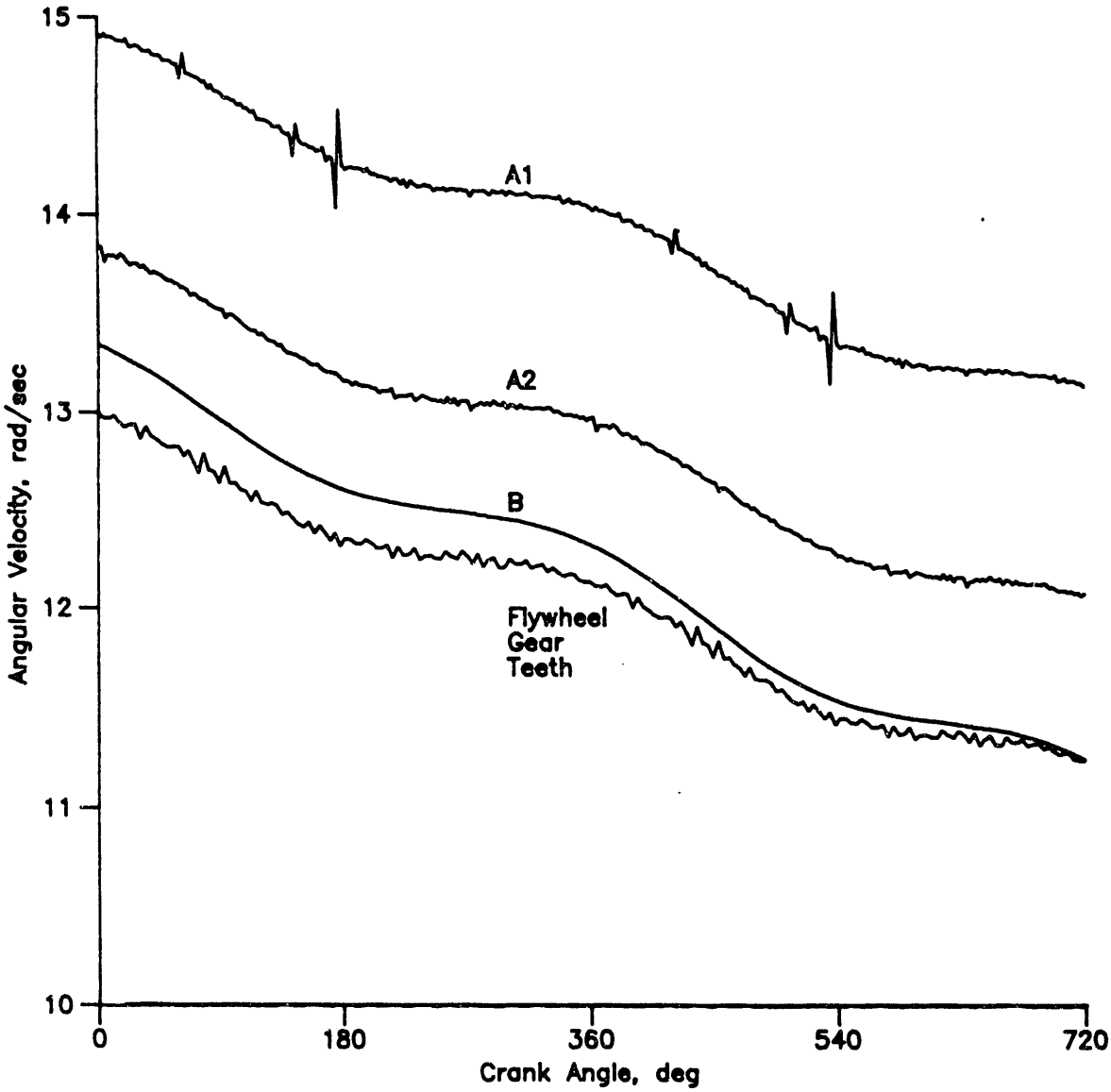

Figure 4.10. ω traces from shaft encoders A-1, A-2, B and flywheel gear teeth at very low speed

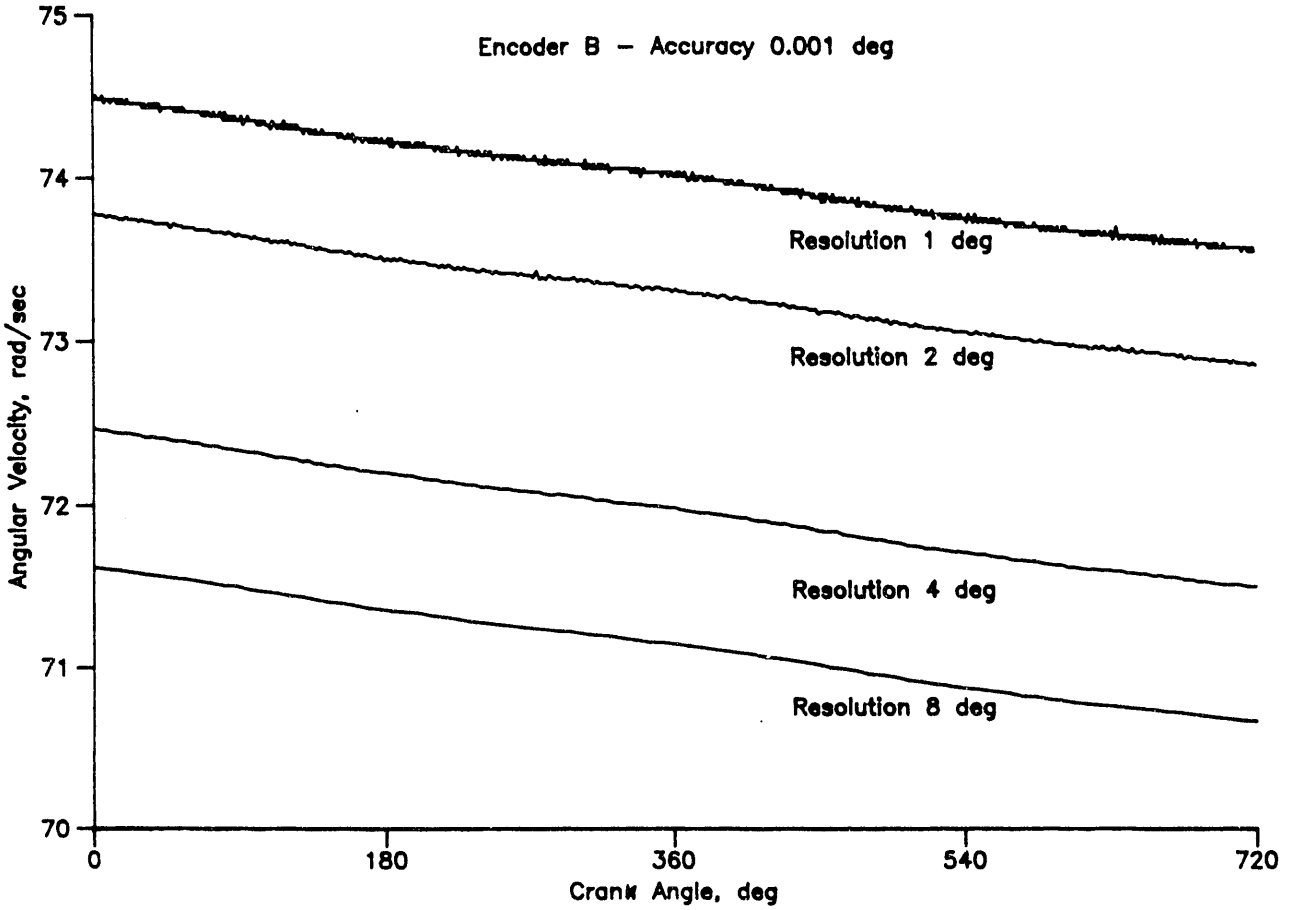

Figure 4.11. Effect of $\Delta\theta$ in shaft encoder B on the ω trace

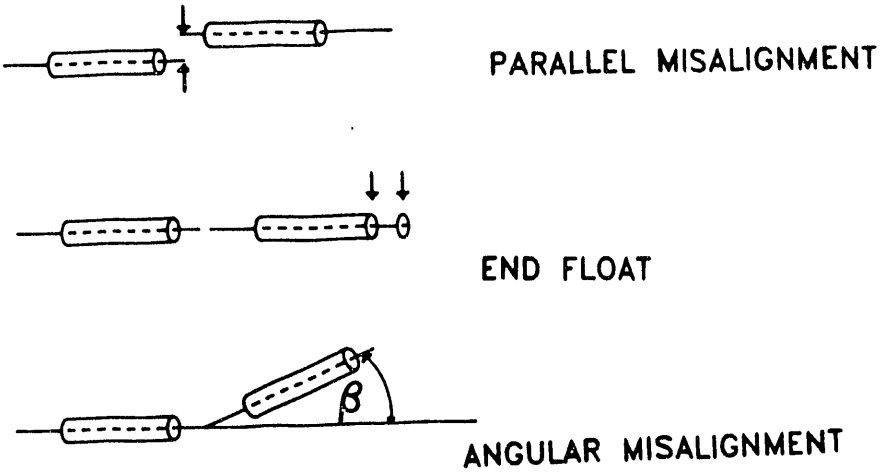

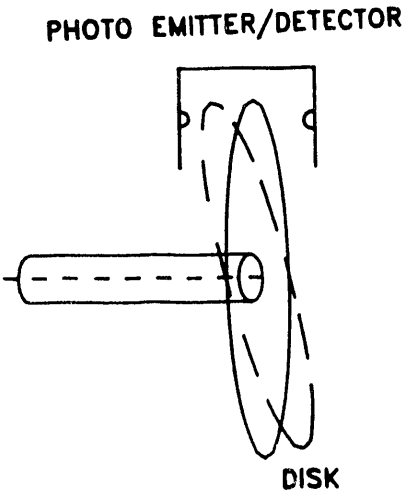

Figure 4.12. Types of misalignment in shaft encoders

Fig 4.13 shows the above ratio calculated for a complete revolution of the crankshaft, assuming a constant angular velocity of the crankshaft system and misalignment angles of 1° and 2°. The error is sensitive to the increase in the misalignment angle ß.

Figure 4.14 shows results obtained with encoder B, properly aligned and misaligned. This distortion in the ω trace is reproducible from one revolution to another. A closer look at the trace shows low frequency high amplitude waves within one revolution resembling the traces of figure 4.13. Exact agreement is not expected, since the Hooke's joint approach to error analysis is not meant as an exact representation of the complex motion imposed on the shaft encoder due to its angular misalignment with the crankshaft. An alarming observation in the misaligned trace is that of the sharp acceleration modes in a decelerating system.

The above analysis may explain some error in earlier figures. The traces in figure 4.5 for encoder 1 and the flywheel gear teeth produce accelerating and decelerating modes at the high rotational speeds. At these speeds the sinusoidal oscillations should not appear because the gravitational forces are negligible compared to the centrifugal forces. Accordingly encoder A-1 appears to have internal misalignment associated with its manufacturing. The flywheel gear teeth were examined and found to be eccentric with the crankshaft. These two systems were the ones used in the initial stage of this investigation to produce the traces in figure 4.1(a). This analysis may explain the reason for the 'positive' friction produced by the (P-ω) method in figure 4.1(b) of this paper and figure 4.6 and figure 4.8 of the previous work published in Reference [12].

4.5.5. EFFECT OF CRANKSHAFT-DRIVEN COMPONENTS

Another source of error in the measurement is that due to components driven by the crankshaft, i.e. gears. Figure 4.15 shows

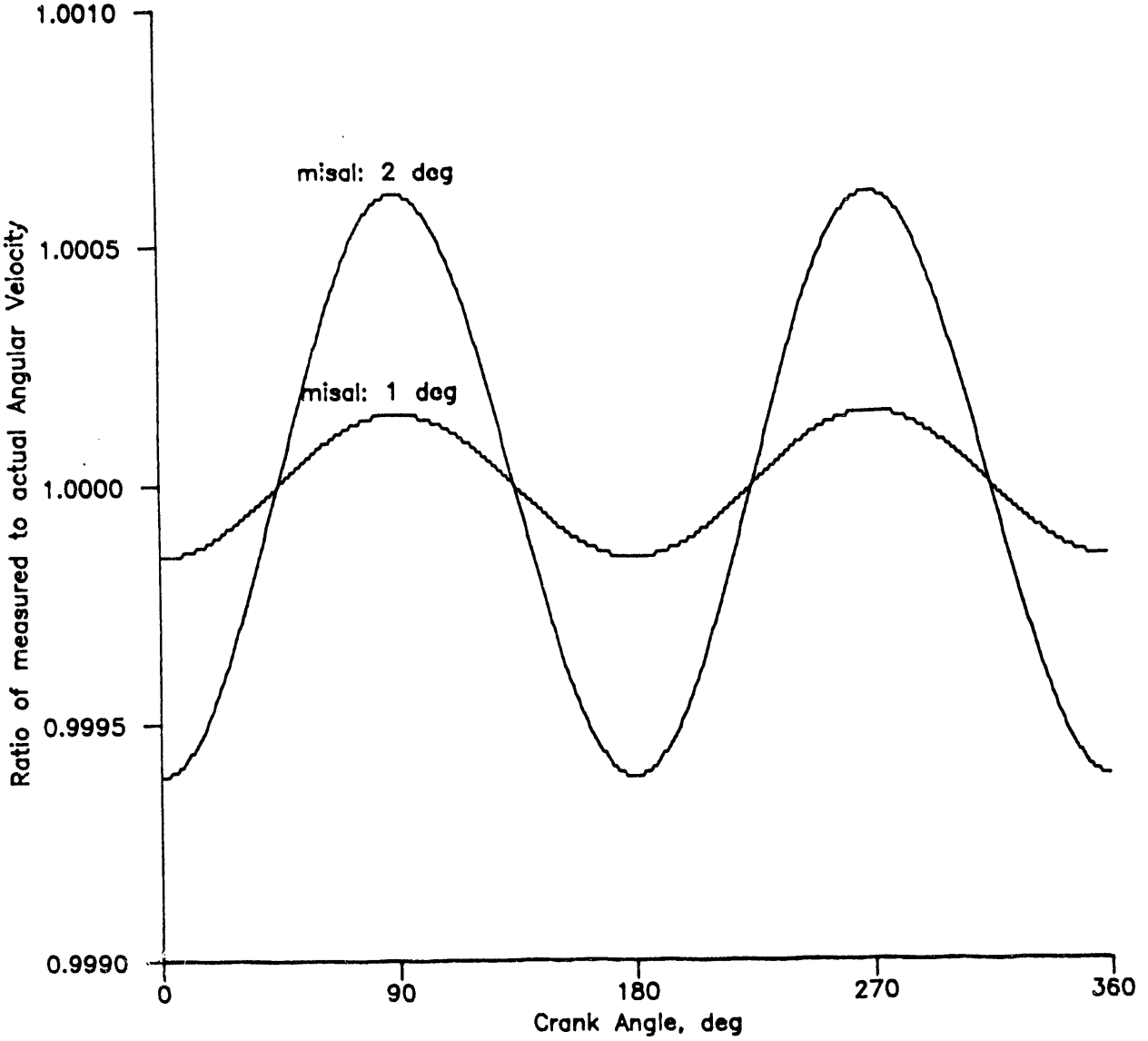

Figure 4.13. Effect of angular misalignment on ω

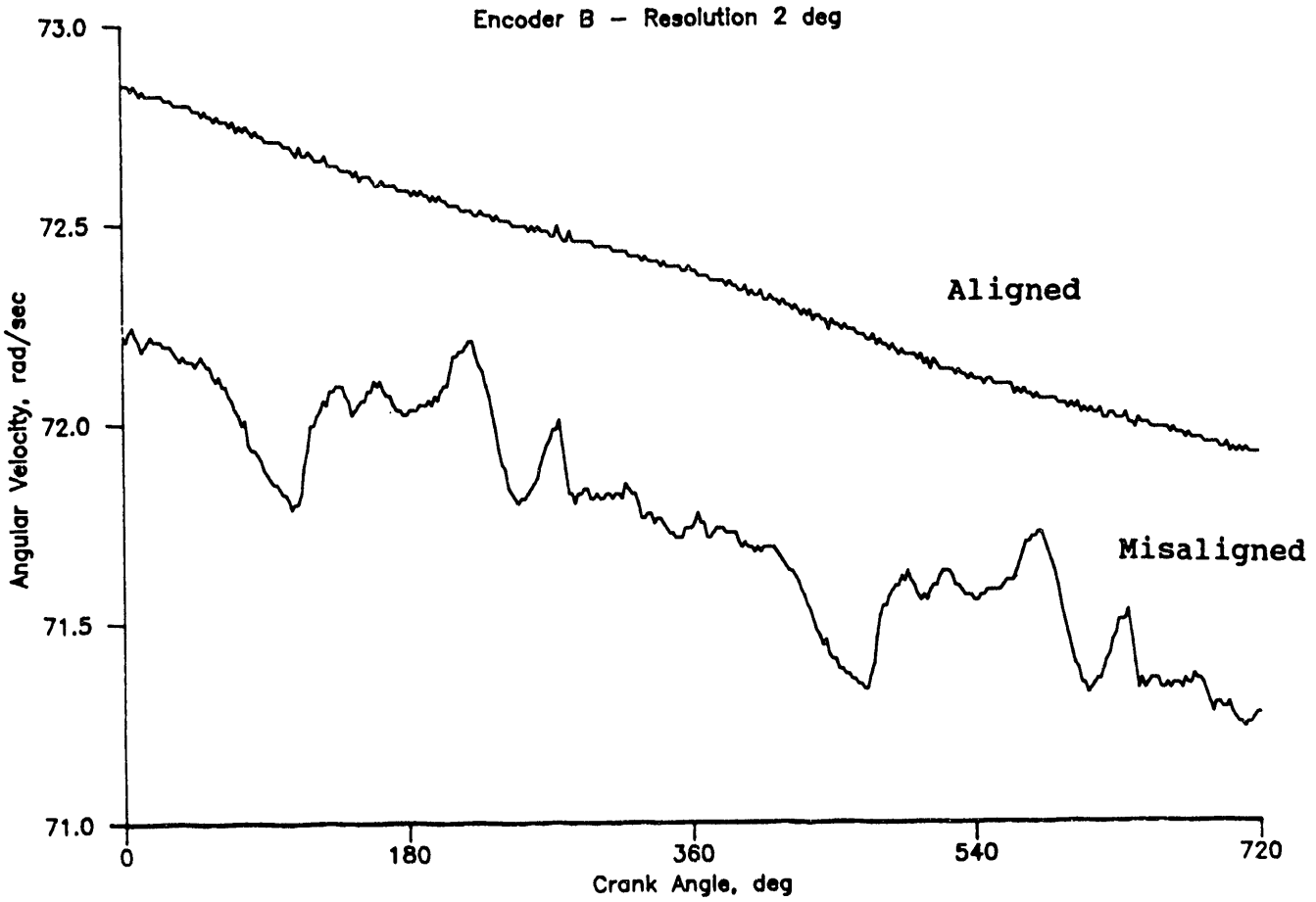

Figure 4.14. Effect of angular misalignment of encoder B on ω

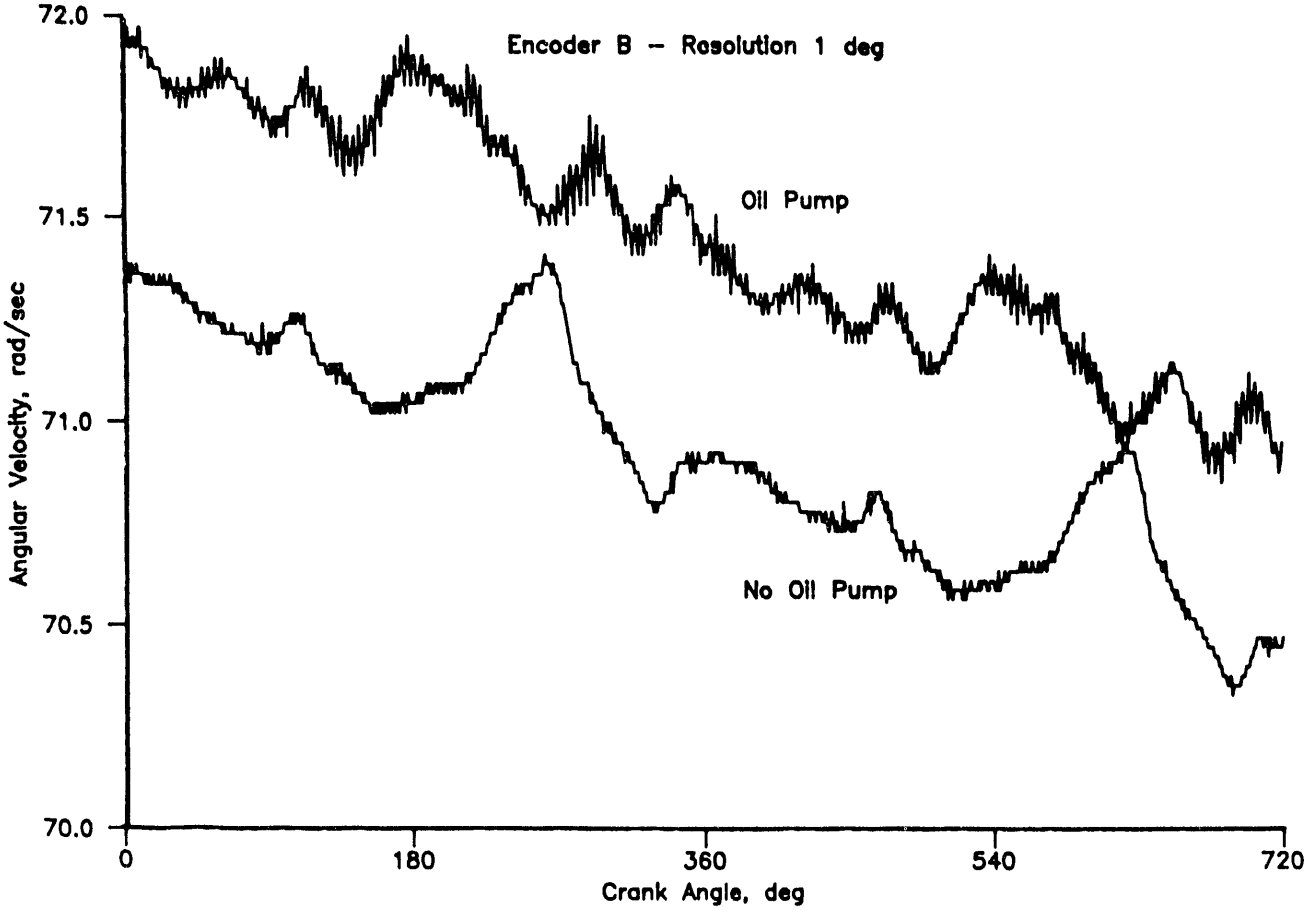

Figure 4.15. Effect of angular misalignment of encoder B and driving the oil pump on ω

angular velocity traces obtained with encoder B misaligned in two different ways, one with the oil pump engaged and the other with the pump disengaged. The $\Delta\theta$ used for both runs was 1 degree. The oil pump gear produced noise in the trace believed to be caused by shocks on the crankshaft gear by the oil pump gear. The trace without the oil pump has a much lower noise level.

To avoid the noise produced from driven auxiliaries, the shaft encoder should be positioned on the end of the crankshaft far from the auxiliary drives. Figure 4.16 shows ω measurements with encoder B positioned on the flywheel, and at the front end of the crankshaft, with the oil pump engaged. The flywheel trace has a much lower noise level than the front end trace. This makes the flywheel end of the crankshaft a much better location for ω measurement for the system described above.

Another problem found to affect the measurements is shown in the experimental results of Figure 4.17. The connecting rod-piston mechanism was installed on the crankshaft along with the balancing shaft and the camshaft. The top traces show the measured angular velocities, with and without the valve mechanism and the fuel injection pump. The bottom trace shows the measured torque on the camshaft, for identification of the engine events. The measured angular velocity, without valves and fuel pump, shows small noise bands 30 to 40 degrees after the TDC positions. It was found that this was the effect of the balancing shaft's gear teeth, which change contact side every time the balancer passes through TDC.

The trace obtained with the valve and fuel pump systems installed on the engine shows relatively large amplitude and long duration noise bands incorporated in the angular velocity during parts of the three distinct events. These events are identified by observation of the torque measured on the cam. Clearly the intake valve is responsible for the first noise band, the fuel pump for the second, and the exhaust valve for the last two. Measurements of the static radial position of the shaft encoder, with the engine

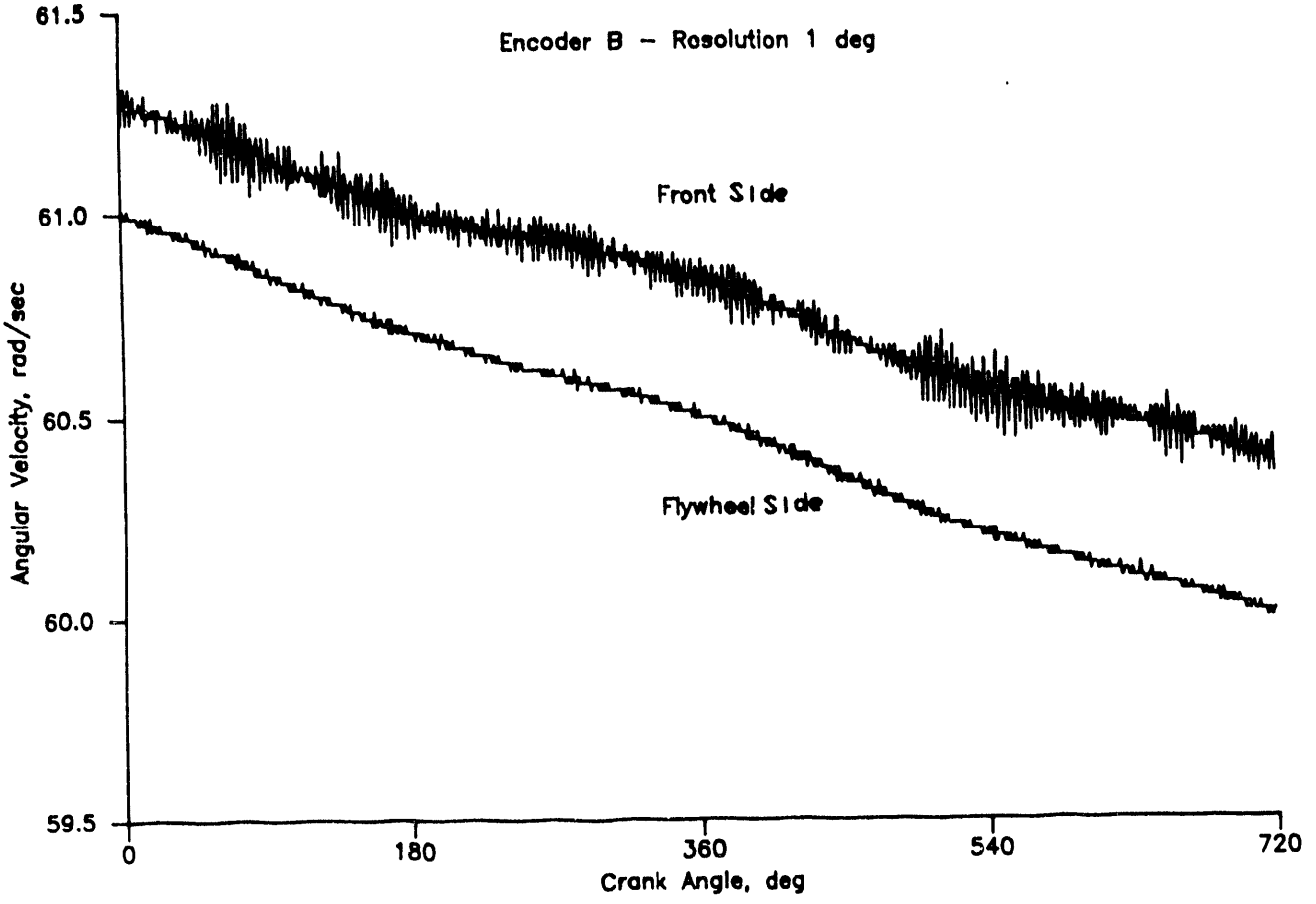

Figure 4.16. Effect of the location of encoder B with respect to oil pump drive on ω

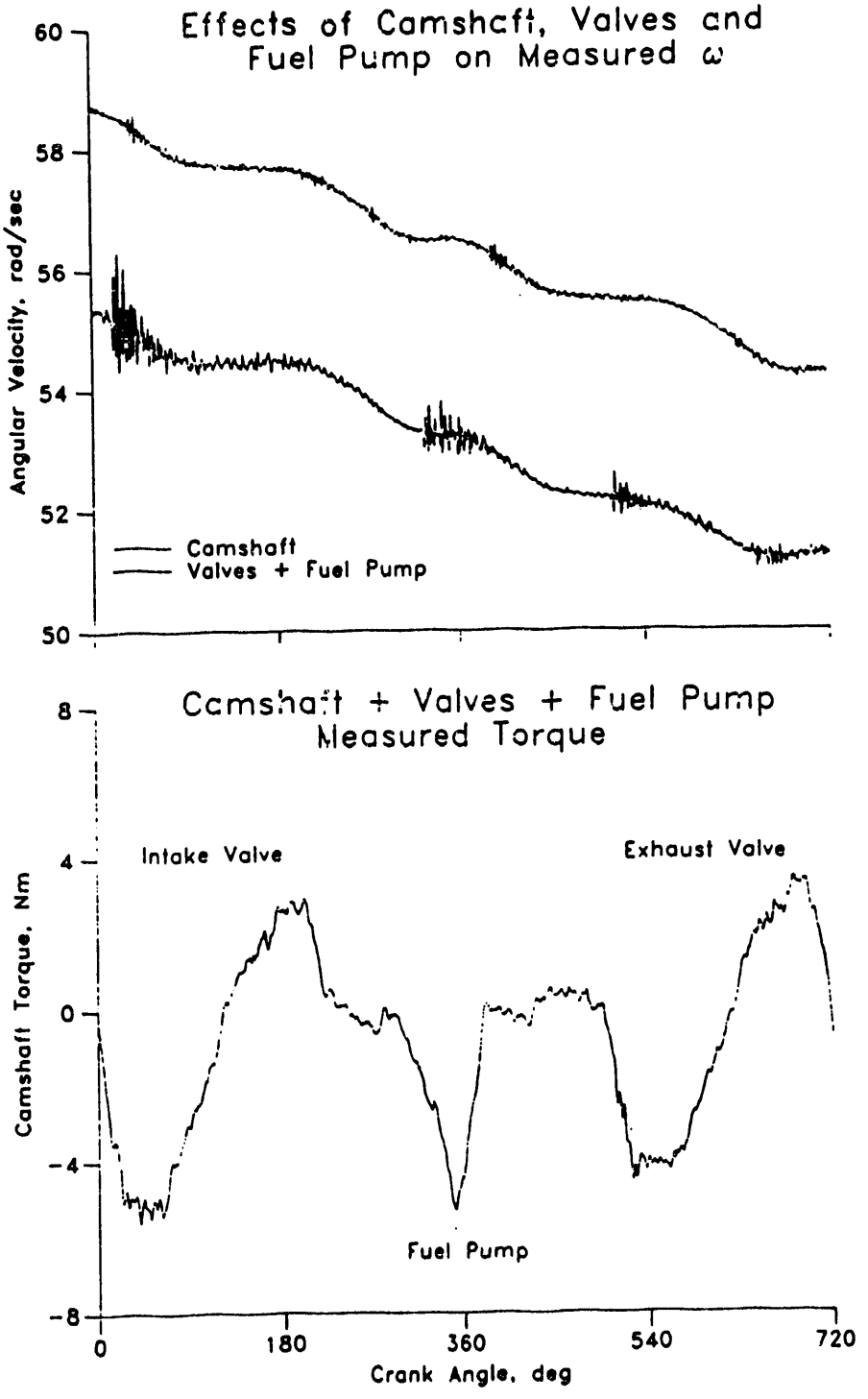

Figure 4.17. Effect of balancer and cam shaft assembly

rotated through small intervals by hand, showed that misalignments exist exactly at the same locations with the measured noise bands. After observation of the camshaft's movements, it was concluded that the changes on the loading of the cam were responsible for this noise, since these movements are transferred to the encoder's shaft, as shocks. There was nothing that could be done about this, but the measurements on the flywheel side dampened this noise tremendously as it will become apparent latter.

4.6 ANGULAR VELOCITY AND ACCELERATION COMPUTATIONS

The angular acceleration is computed, as mentioned earlier, by the following : $\alpha \equiv d\omega/dt = \omega d\omega/d\theta$. Clearly the angular velocity controls the acceleration's errors, which are actually amplified. Even in the cases of extreme smoothness of the ω trace, the trace is itself a collection of discrete points, which make its derivative a very noisy signal. A technique was required to 'smooth' these discrete points, so that a continuous curve could be developed describing the angular velocity, from which the acceleration could be obtained.

A number of different smoothing schemes were developed and tested along with the Fast Fourier Transform treatment of the signal, but all of them had major problems and the FFT approach specifically produced ringing after its filtering action.

A different approach, based on cubic spline theory introduced by Reinsch [20], proved very successful in the smoothing of the angular velocity. Let $g(x_i)$ be the desired smoothing function, and y_i the measured quantities defined at the points x_i, $i=0,1,...n$. The objective is then to minimize the following summation :

$$\sum_{i=0}^{n} \left(\frac{g(x_i) - y_i)}{\delta y_i} \right)^2 \leq S \qquad (4.9)$$

with $\delta y_i>0$ and $S\geq 0$ given. If the relative weights δy_i^{-2}, are given as the standard deviations of y_i, then $N-(2N)^{1/2} \leq N \leq N+(2N)^{1/2}$, $N=n+1$, is the natural choice for S. The above theorem was applied to the angular velocity trace, with some modifications introduced by this author, to allow for the localized problem of noise induced by the gear set. The major modification is the way that these weights are calculated, with the calculation based on the 'local errors' of every trace.

The cubic spline approach was applied in the crank angle-time domain, (θ,t), or in the angular velocity-crank angle domain, (ω,θ). The application in the $(\omega-\theta)$ domain required the angular velocity to be calculated by a central difference scheme applied to the data in the $(\theta-t)$ domain. Namely, the angular velocity was calculated by : $\omega_i=2\Delta\theta/(\Delta t_i+\Delta t_{i+1})$, with Δt_i defined as the time interval recorded by the time counters between crank angle markers i-1 and i. The application of the smoothing technique to the (θ,t) domain was accomplished by the generation of two functions, one for the crank angle and the other for the time by the summations of the respective measured increments, ie $\theta_i=\Sigma\Delta\theta$, $\theta_o=0$ and $t_i=\Sigma\Delta t_j$, $t_o=0$.

4.6 SUMMARY

This investigation indicated the following:

1. Errors in ω were found to be caused by:

   a) $\Delta\theta$-to-$\Delta\theta$ variations within one encoder or the flywheel gear teeth.
   b) Encoder-to-encoder variations.
   c) Misalignment within the encoder itself or between the encoder shaft and the driving shaft or between the flywheel gear teeth and crankshaft.

2. The theoretical investigation and the experimental results

indicated that the magnitude of the error is a function of the crank angle increment, $\Delta\theta$, and the rotational speed.

3. Driving the oil gear pump produced detectable noise in the ω trace.

A shaft encoder which showed essentially no errors was used in all the tests conducted in this program.

CHAPTER 5: ERROR ANALYSIS OF GAS PRESSURE MEASUREMENTS

5.1 BACKGROUND

Errors in the measurements of cylinder gas pressure result in errors in calculating the frictional losses and other performance parameters in combustion engines. Frictional losses can be determined by five different methods, three of which do not account for the effect of load and therefore are not sensitive to these errors. The only two methods which account for load are the mean effective friction pressure (FMEP) method and the (P-ω) method which determines the instantaneous frictional torque (IFT) of the engine [11].

In combustion engines the gas pressure is measured by using piezoelectric quartz crystal transducers which have been found to be superior to other types of transducers [21]. Errors in pressure measurements can be intrinsic to the transducer or operational. The intrinsic errors have been found to be due to nonlinearity, hysteresis, thermal stresses, mechanical stresses due to mounting, or inertia effects due to the impact of different forces on the cylinder head [21, 22, 23]. The sensitivity of the transducer output to each of the error sources depends to a large extent on the quartz cut [21], whether it is ordinary or polystable, the piezoelectric effect whether it is longitudinal or transverse, the diaphragm design whether it is made of sheet metal, machined or double ring [21], and other design and construction parameters of the transducer. The operational errors are related to calibration of the transducer and charge amplifier, the use of clean drift free cable connections, external noise and phasing of the pressure signal with respect to crank angle [22, 23].

The cylinder gas pressure is calculated from the output voltage of the charge amplifier by using a calibration constant. This constant is determined by measuring the voltage output for

different static pressures produced by a dead-weight tester [22, 23]. The calibration is usually made while the transducer is in thermal equilibrium with its mounting at normal room temperature. In an actual engine the transducer and its mounting, usually the cylinder head, are at a much higher temperature than the normal room temperature. In addition, in an engine, the transducer surface temperature fluctuates during the thermodynamic cycle. The thermal stresses resulting from the high steady state temperature and the unsteady cyclic temperature variations may cause errors in the output.

Most of the previous investigations on pressure errors have been made to improve the accuracy of IMEP for engines running at steady rotating speeds. One of the features of the (P-ω) method is that it can determine the IFT in the engine under the transient modes of acceleration and deceleration as well as under steady state. Under the transient conditions many of the errors may be magnified.

In this section a comparison is made between the IFT and FMEP obtained by using five pressure transducers of different makes and designs. The effects of different sources of errors are investigated.

5.2 EXPERIMENTAL SETUP AND PROCEDURE

A single cylinder Deutz diesel engine is used. All tests were conducted with combustion under no-load conditions at various speeds.

* TRANSDUCERS TESTED

The following five types of transducers were used. They are of two makes, different quartz cuts, with and without water

cooling.

1-	8QP505c:	AVL with cooling and heat shield
2-	12QP250ck:	AVL with cooling, and specially selected temperature compensation
3-	QC41B-X:	AVL gold plated with temperature shock compensated diaphragm, and specially selected thermoshock compensation and linearity < ± 0.2%
4-	6121:	Kistler with polystable quartz element, double diaphragm with ceramic front plate and without water cooling
5-	7063:	Kistler with polystable quartz element and thermal shield and water cooling

The specifications are given in table 5.1.

The calibration of the transducers was done together with the charge amplifiers and connecting cables on a dead-weight tester at normal room temperature, according to recommendations made by the manufacturers, Brown [22] and Lancaster et. al [23].

5.3 EXPERIMENTAL RESULTS

5.3.1 EFFECT OF TRANSDUCER-TO-TRANSDUCER VARIATIONS ON IFT AND FMEP

Five transducers were mounted in the cylinder head, two at a

Table 5.1
Specification for Transducers

	1 8QP505c	2 12QP250ck	3 QC41B-X	4 6121	5 7063
Dynamic Range, bar	0-180	0-120	0-200	0-250	0-200
Calibrated Partial Range, bar				0-25	0-20
Sensitivity, pC/bar	≈ 20	≈ 70	≈ 68	≈ 14	≈ 80
Natural Frequency, kHZ	100	67	50	>55	>30
Linearity, %FSO	<±0.4	<±0.2	≤±0.2	≤±1.0	≤±0.8
Acceleration Sensitivity, bar/g	0.002	0.002	0.003	<0.003 Axial <0.0002 Trans	<.005
Insulation Resistance at 20°C, Ω	$>10^{13}$	$>10^{13}$	$>10^{13}$	$>10^{13}$	$>10^{13}$
Shock Resistance, g				2000	2000
Damping log. decrement	0.35	0.30	0.30		
Capacitance, pF	3.8	21	18		10
Hysteresis, %FSO				<1.0	≤±0.5
Temperature Coefficient of Sensitivity 20....50°C % 20...100°C % 20...350°C % 200± 50°C %	±0.015	±0.015	±0.015	 <±0.5 <±3 <±1	 ≤±1 ≤±3.5 ≈±1
Thread M or Diaphragm Diameter Φ, mm	M10	M14	M14	Φ6	M14
Water cooling	Yes	Yes	Yes	No	Yes
Mass/Weight, g	14	30.4	34	9.5	30
Mounting Torque, Nm	15	20	20	4-6	25
Features			Gold Plated		

time. The two transducers were located close to each other, midway between the inlet and exhaust valves. Interchanging the location of the two transducers showed very minor changes in the outputs. This may be attributed to the change in wall temperature in the two locations. Transducer No. 1 was common to all the tests. The tests for all the transducers were conducted under steady state conditions at no load and 600 RPM. The cylinder pressure was measured and the friction parameters were determined and compared with the other four transducers. Figure 5.1 and 5.2 show samples of the (IFT-θ) for transducers No. 1 and 4. The main difference between the two traces is in the period between IVC and EVO. IVC is at 63° ABDC and EVO is at 63° BBDC. A summary of the different friction parameters for the five transducers is given in table 5.2. The peak IFT during compression varied from +7% to +14%. The peak IFT during expansion varied from -5% to -9%. The integrated IFT during the whole cycle varied from -5% to +7%. The IMEP varied from -6% to +7%. The variations between the transducers may be related to the differences between their construction, linearity and their response to the thermal stresses. The test-to-test variations in the results of transducer No. 1 may be attributed to small variations in the ambient temperature, lubricating oil temperature and engine speed.

5.3.2 COMPARISON BETWEEN THE LINEARITY OF THE TRANSDUCERS AT NORMAL AMBIENT TEMPERATURE

Figure 5.3 shows the difference between the pressure applied by the dead-weight tester and that indicated by each of the five transducers. In the range of the cylinder pressures encountered in the current investigation, 0-1000 psia (0-6895 kPa), the variations in the linearity varied from - 0.2% to + 0.4% FSO.

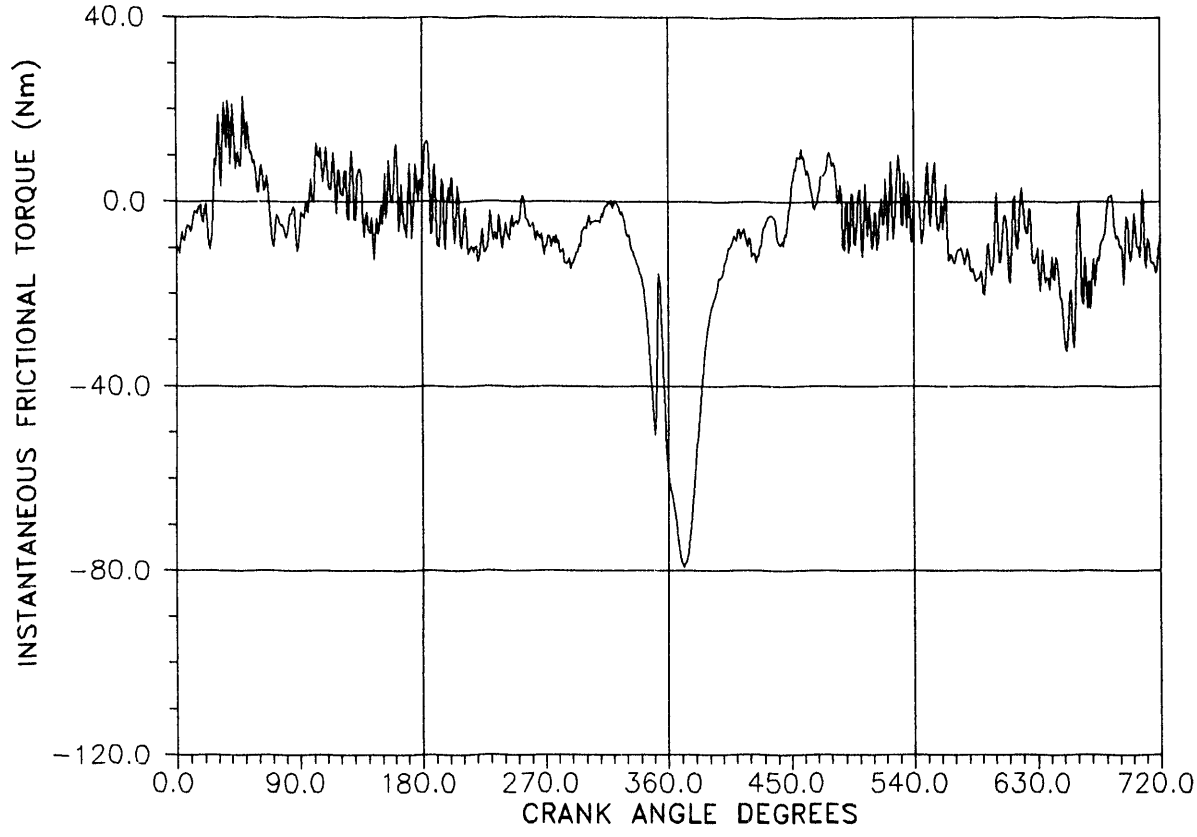

Figure 5.1. IFT determined by using transducer No. 4

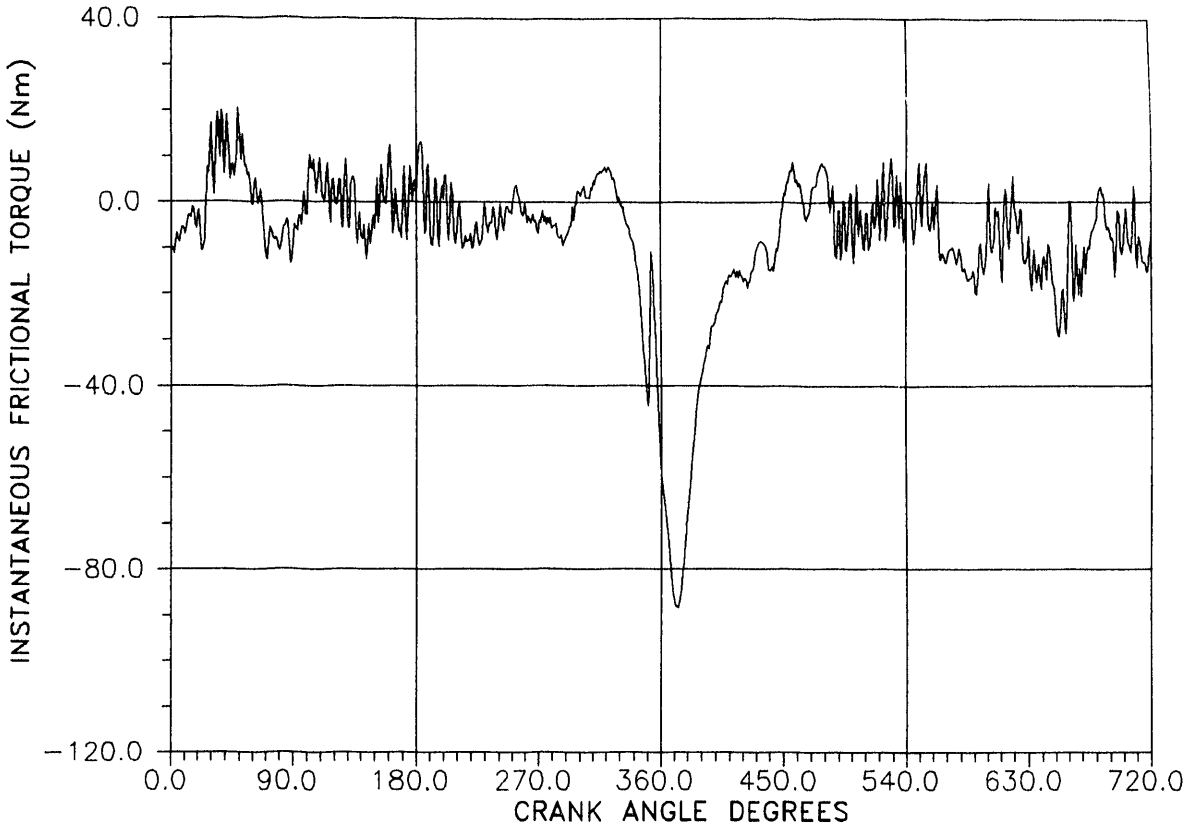

Figure 5.2. IFT determined by using transducer No.1

Table 5.2
Comparison between Friction Parameters Computed
from Data of Transducer No.1 and Four Other Transducers

	1 8QP505C	2 12QP250ck	3 QC41B-X	4 6121	5 7063
Peak IFT	-44			-50	
Compression	-39		-42		
Nm	-52				-56
	-45	-48			
Peak IFT	-88			-80	
Expansion,	-77		-70		
Nm	-88				-80
	-78	-74			
$\int$IFT dθ,	-98.6			-93.4	
	-100.0		-106.6		
Nm Rad	-111.7				-106.7
	-111.7	-99.2			
FMEP, kPa	127.7			120.5	
	130.3		139.5		
	149.0				150.6
	137.2	134.4			

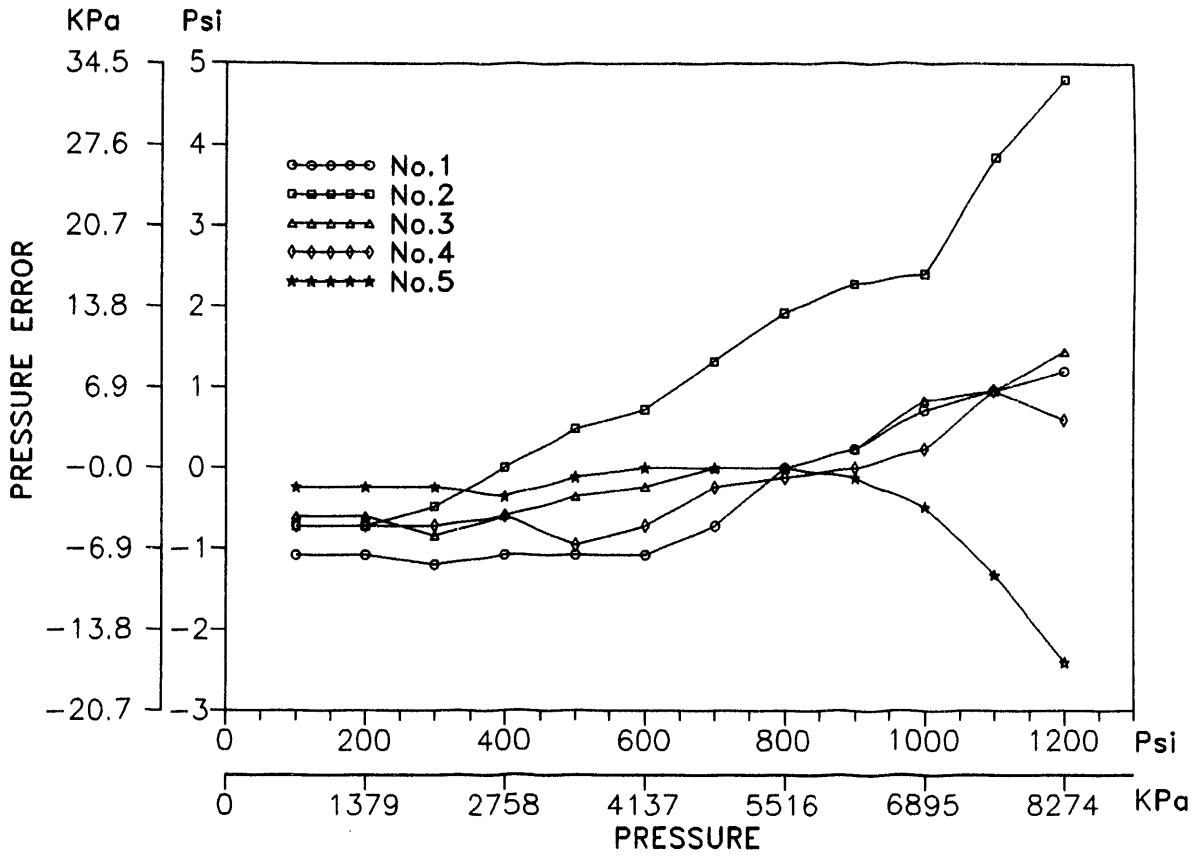

Figure 5.3. Comparison between the linearity of transducers at normal room temperature

5.3.3 ERRORS DUE TO ZERO DRIFT CAUSED BY HEATING AT A FAST RATE DUE TO ACCELERATION

The effect of heating at a fast rate was determined by mounting the transducer in the cylinder head and accelerating the engine. The signal from transducer No. 4 was recorded simultaneously with the surface temperature as shown in Figure 5.4. As the surface temperature started to rise, the transducer drifted to a lower pressure at a rate of 6.5 kPa/°C. A drop in surface temperature caused by deceleration, starting at point (b), resulted in a very slight drift. It appears that an upward drift compensated for most of the downward drift. A second acceleration resulted in an increase in surface temperature, accompanied by a drift to a much lower pressure. Similar tests were conducted on transducers No. 3 and No. 1 and the results are shown in figure 5.5 and 5.6.

Figure 5.5 shows that the transducer produced no drift during acceleration and deceleration which are indicated by the rise or fall in the peak pressure respectively. Figure 5.6 shows that the transducer produced a small drift to a lower pressure during acceleration and a drift to a higher pressure during deceleration. Under steady state conditions there was no drift.

5.3.4 ERRORS DUE TO ZERO DRIFT CAUSED BY TRANSIENT COOLING AT A FAST RATE DUE TO DECELERATION

The engine was decelerated and the pressure traces from transducer No. 4 and 3 were recorded, as shown in figure 5.7 and 5.8. Engine deceleration caused cooling of the cylinder head and the transducers. Transducer No. 4 drifted to a higher pressure, while transducer No. 3 had almost zero drift. It should be noted that transducer 4 is uncooled and has a diameter of 6 mm. Transducer No. 3 was chosen for the rest of the investigation.

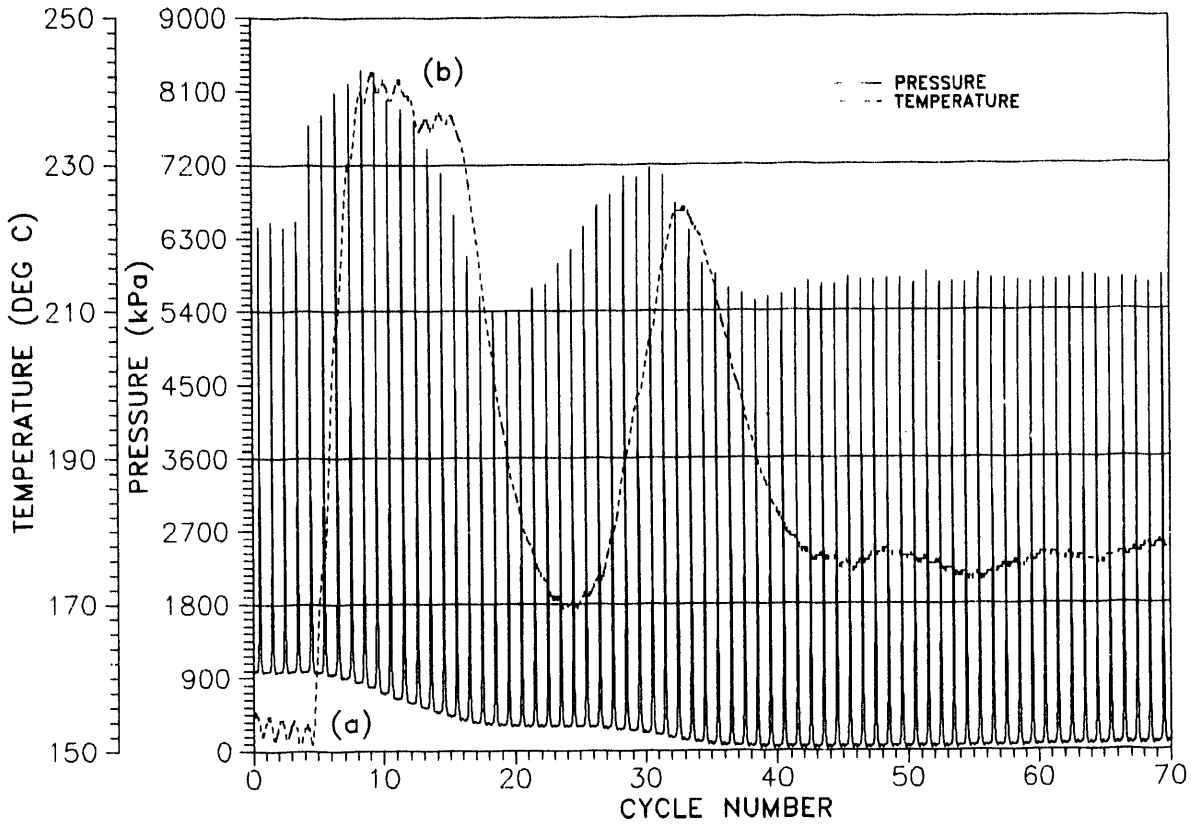

Figure 5.4. Zero drift of transducer No.4 due to acceleration

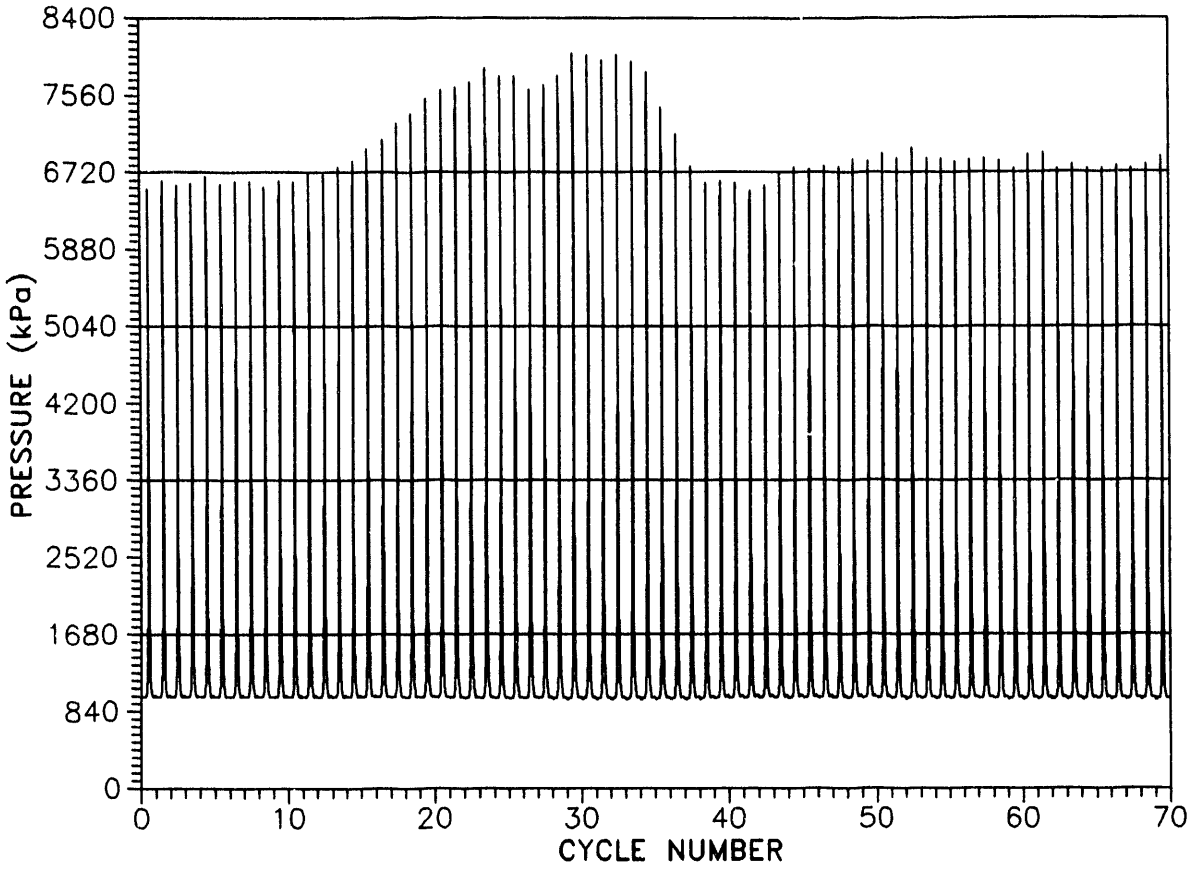

Figure 5.5. Zero drift of transducer No.3 due to acceleration

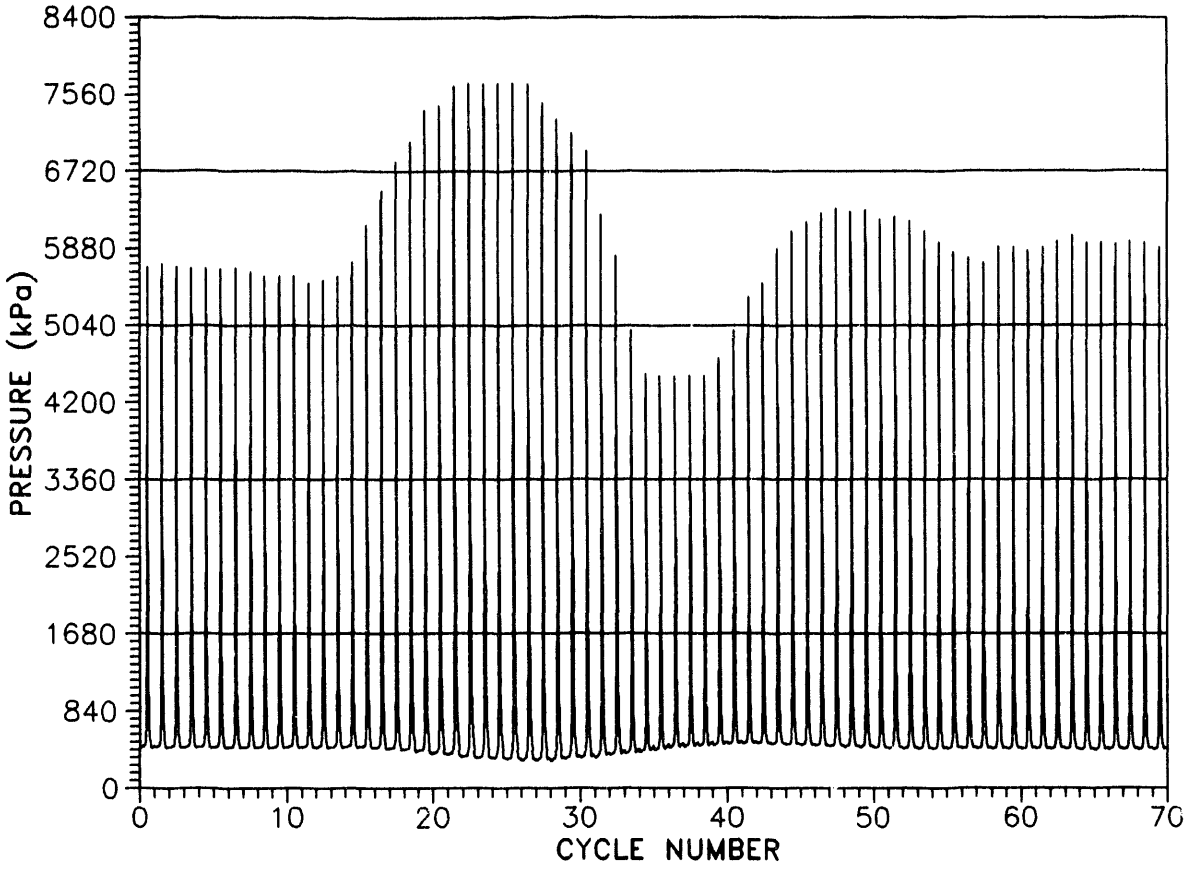

Figure 5.6. Zero drift of transducer No.1 due to acceleration

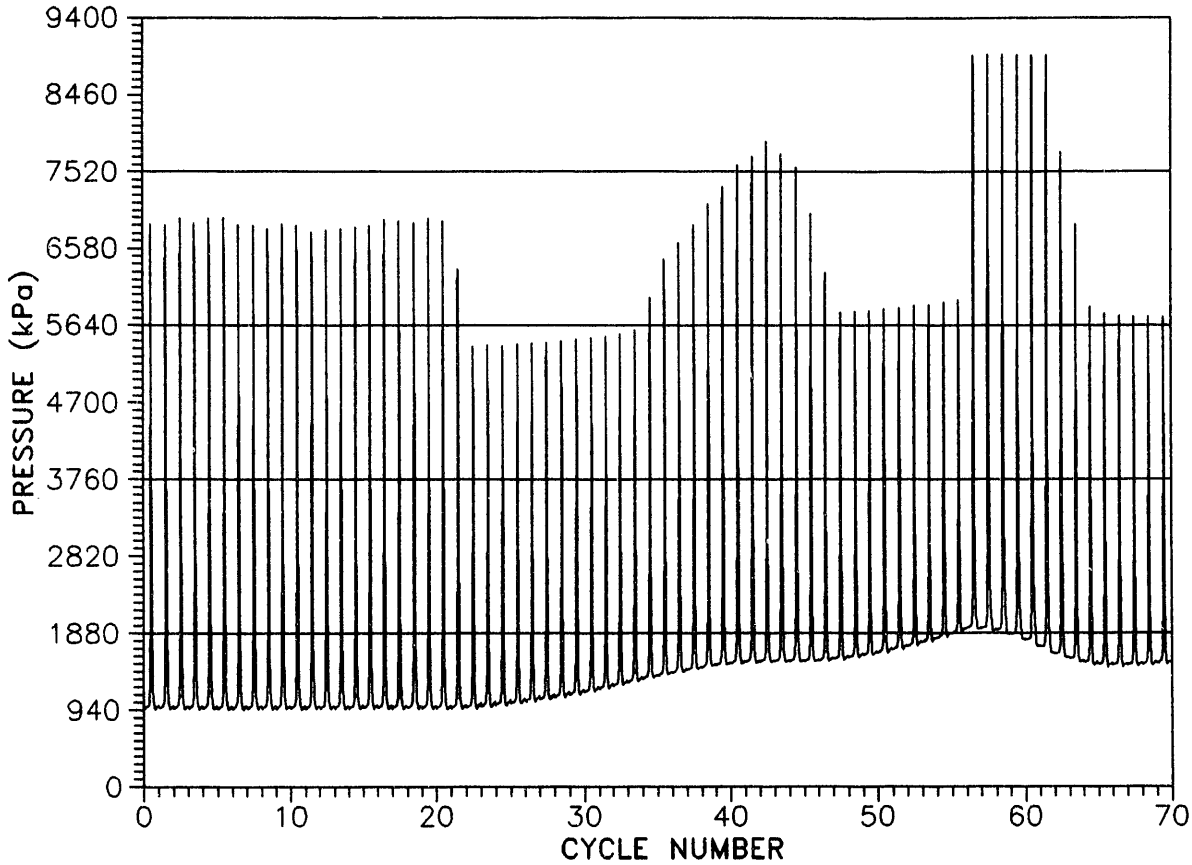

Figure 5.7. Zero drift of transducer No.4 due to deceleration

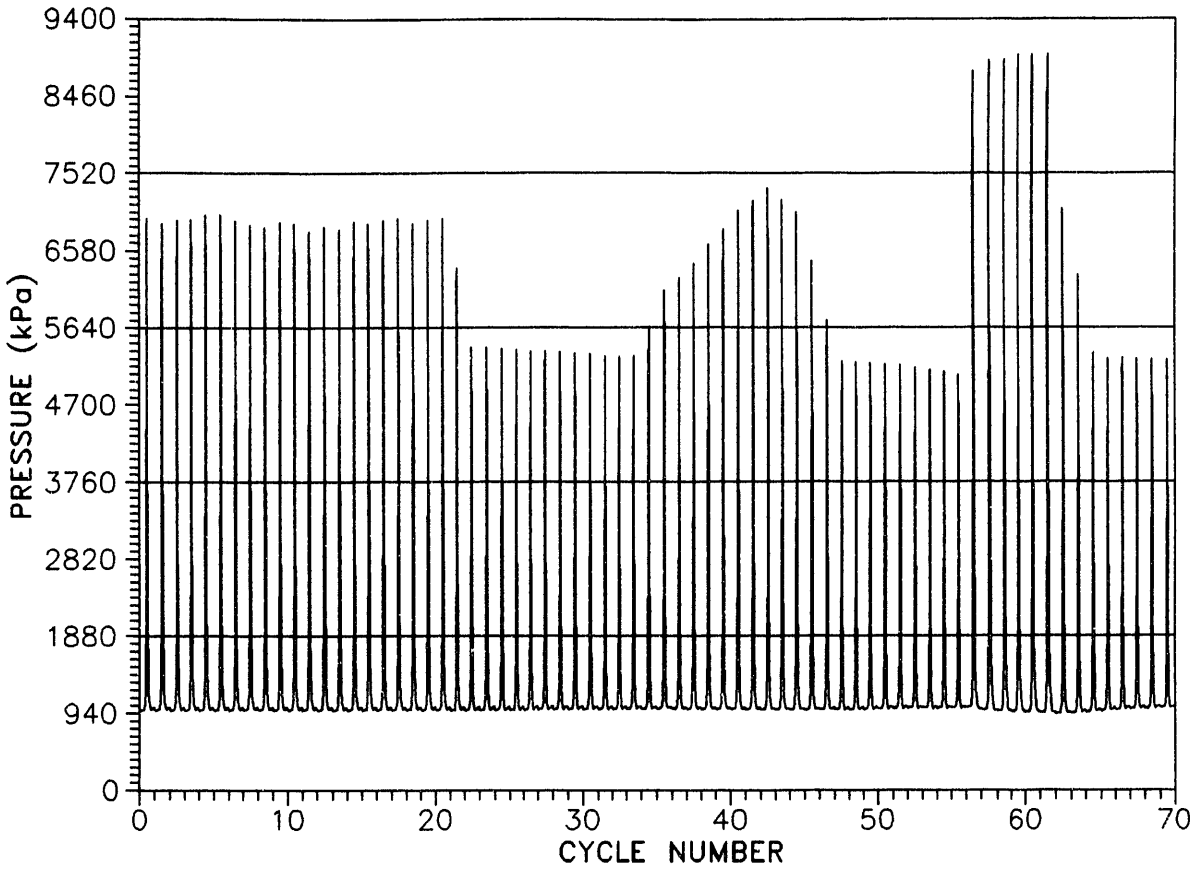

Figure 5.8. Zero drift of transducer No.3 due to deceleration

5.3.5 ERROR DUE TO SURFACE COOLING AT A SLOW RATE

The transducer No. 3 was mounted in the cylinder head away from the engine, and the whole surface was exposed to a steady heat flux in atmospheric air till the temperature reached a steady 90°C. Cool air was then blown on the surface of the cylinder head at a uniform rate, and the surface temperature and the transducer pressure signal were recorded. Figure 5.9 shows that cooling the surface resulted in a pressure signal which increased as the cooling continued. A temperature drop of 14°C produced a signal equivalent to a pressure of 103 kPa. The cooling process was at a rate of 0.28°C/sec. This is a very slow rate compared to the engine cyclic and transient operating modes.

It appears that the slow rate cooling caused the diaphragm to shrink causing an additional pressure on the quartz crystal in addition to the increase in the piezoelectric effect.

5.3.6 EFFECT OF CALIBRATION AT STEADY ELEVATED TEMPERATURE

In engines, the transducer is in thermal equilibrium with the cylinder head where it is mounted. The diaphragm, the quartz crystal and the other parts of the transducer are at a temperature higher than the normal room temperature at which the transducer is usually calibrated. To investigate this effect, transducer No. 3 was calibrated on the dead-weight tester with its bulk and mounting heated to different steady temperatures. Figure 5.10 shows that the sensitivity changed and produced a higher pressure signal at the higher temperatures. The nonlinearity resulted in a higher error at the low pressures. This may be attributed to the variation of the piezoelectric effect with temperature and the differences in the coefficients of expansion of the materials in the transducer and its mounting or of the quartz crystal and the

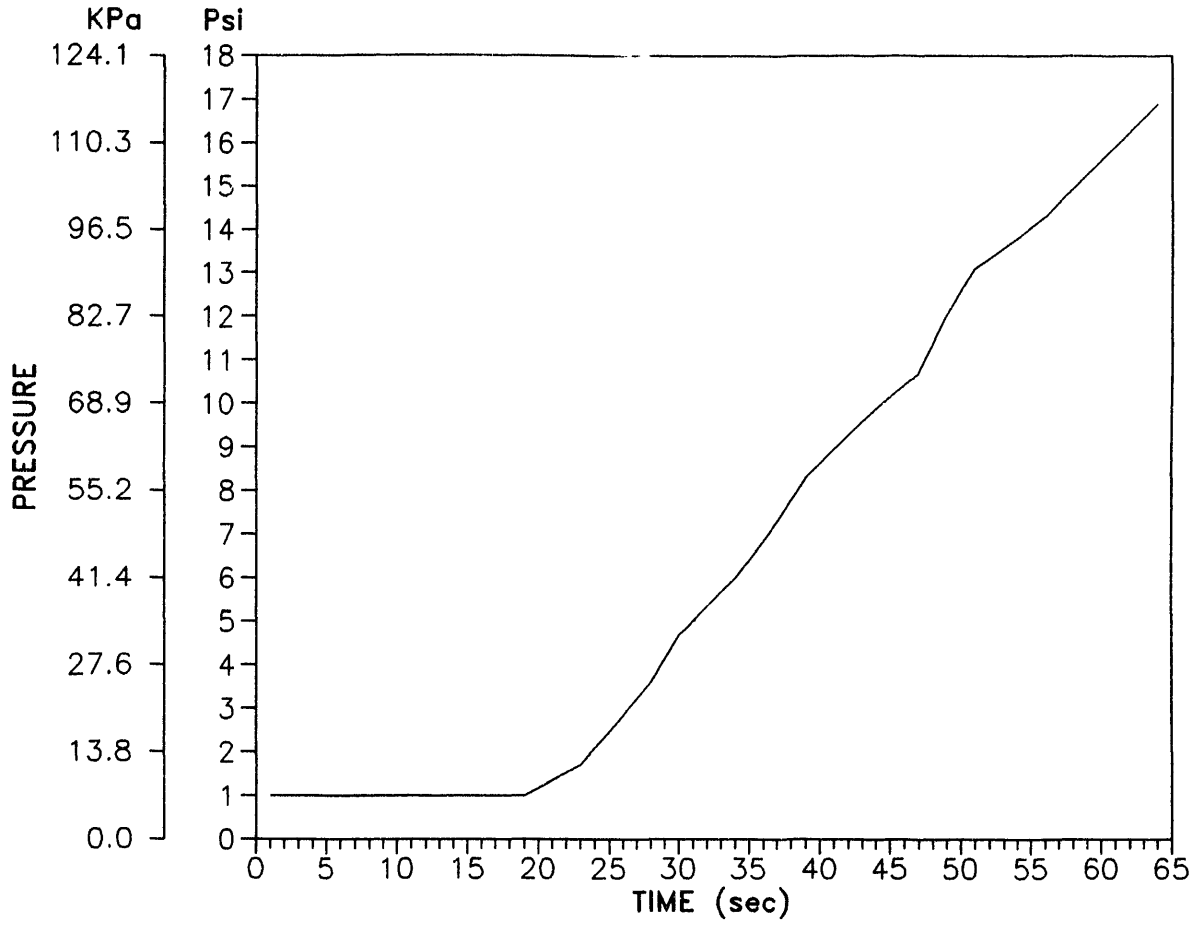

Figure 5.9. Effect of surface cooling at slow rate

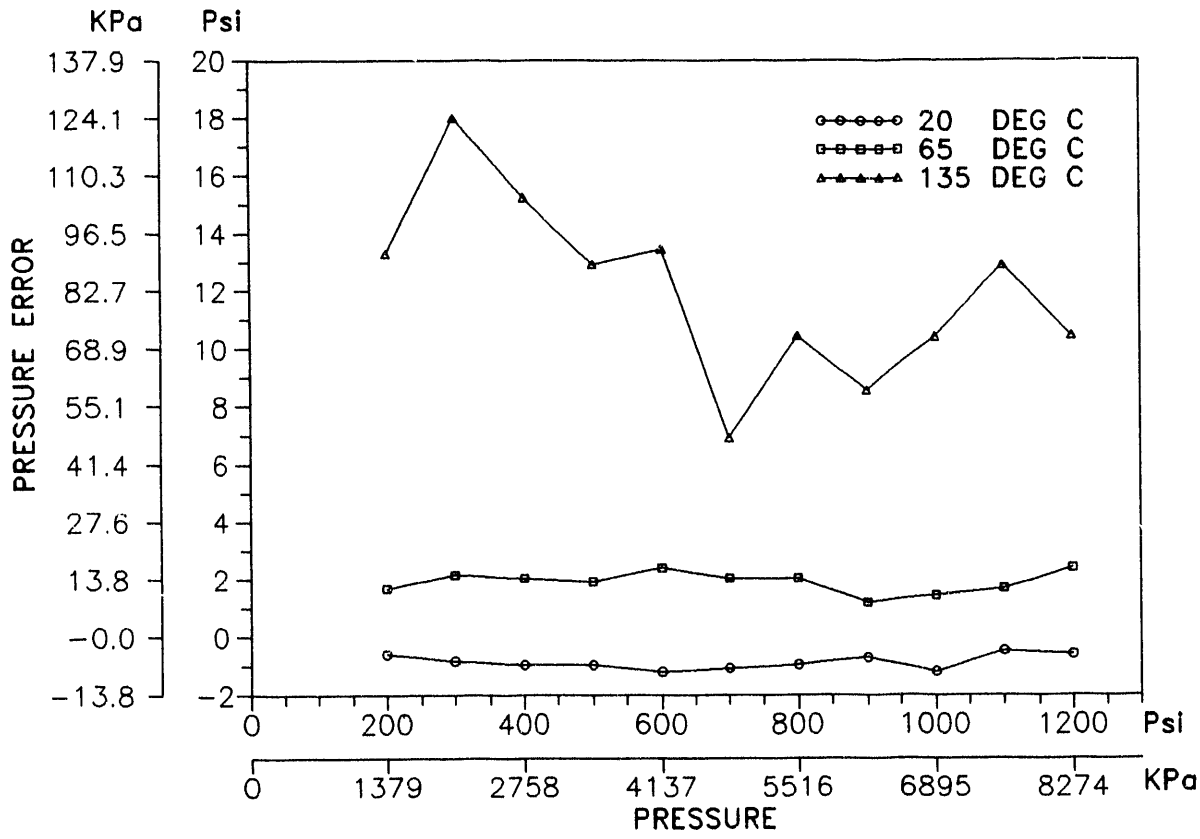

Figure 5.10. Comparison between the linearity of transducer No.3 at temperatures of 20°C, 65°C and 135°C

body of the transducer. Any changes in the radial or axial stresses on the transducer may affect the stresses on the crystal and its output.

5.3.7 EFFECT OF CYCLIC VARIATION OF THE SURFACE TEMPERATURE

Transducer No. 3 was mounted in the cylinder head and exposed to an intermittent flame at a frequency corresponding to the engine speed, following the procedure developed by Brown [22]. The effect on the transducer output was found to be less than 7 kPa (1 psia).

5.3.8 EFFECT OF ELEVATED TEMPERATURE CALIBRATION ON IFT AND FMEP

The calibration of transducer 3 at 135°C was used to calculate the cylinder gas pressure, IFT and FMEP. The slope of the best fitting straight line was used as a calibration constant. The calibration showed nonlinearity ranging from -0.83% to 1.08% FSO. Figure 5.11 shows the IFT calculated from the high temperature calibration constant compared with that from the normal room temperature calibration constant shown in figure 5.12. The differences are in the period between IVC and EVO. The friction parameters for the two calibration constants are given in table 5.3.

5.4 SUMMARY

1- Errors in cylinder pressure measurements affect the IFT and FMEP, which are the only two methods to measure the friction in engines under load. The FMEP can be obtained from the integration of IFT.

2- The error in IFT and FMEP caused by errors in the cylinder gas pressure measurements may be reduced if the

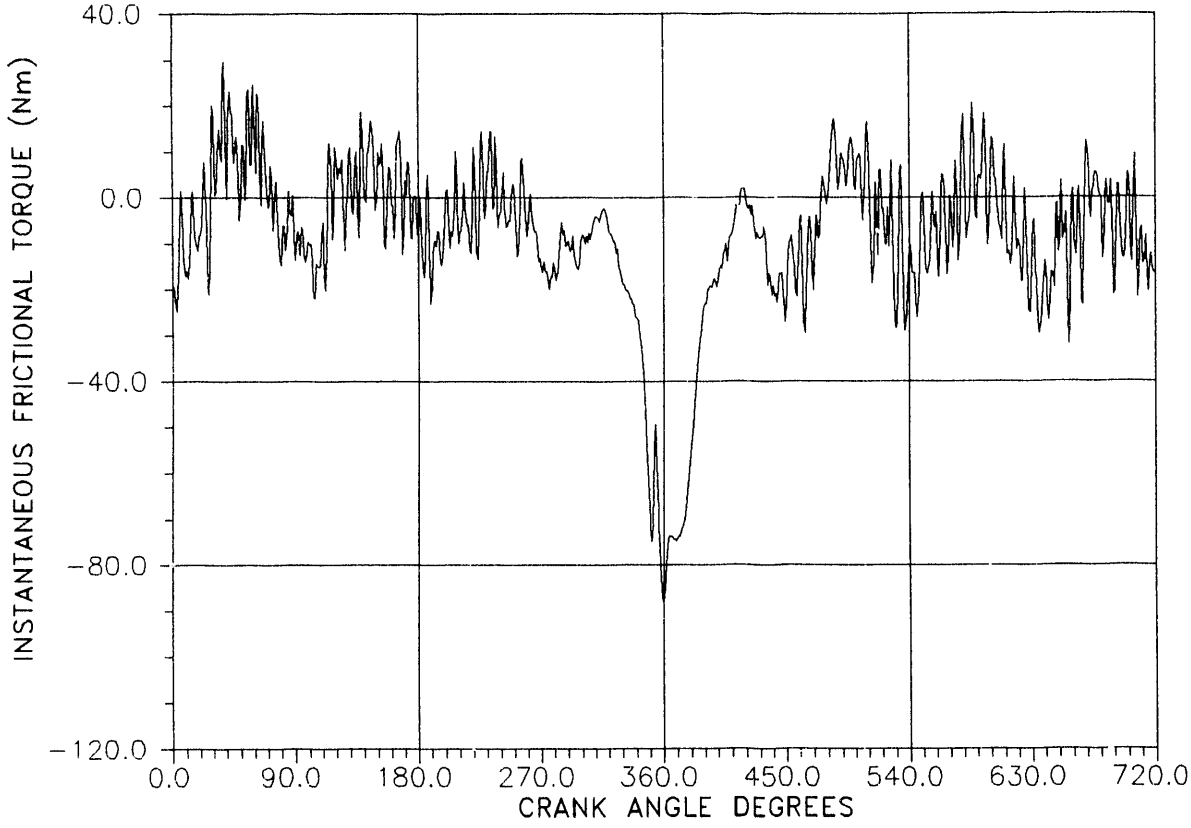

Figure 5.11. IFT from the high temperature calibration constant

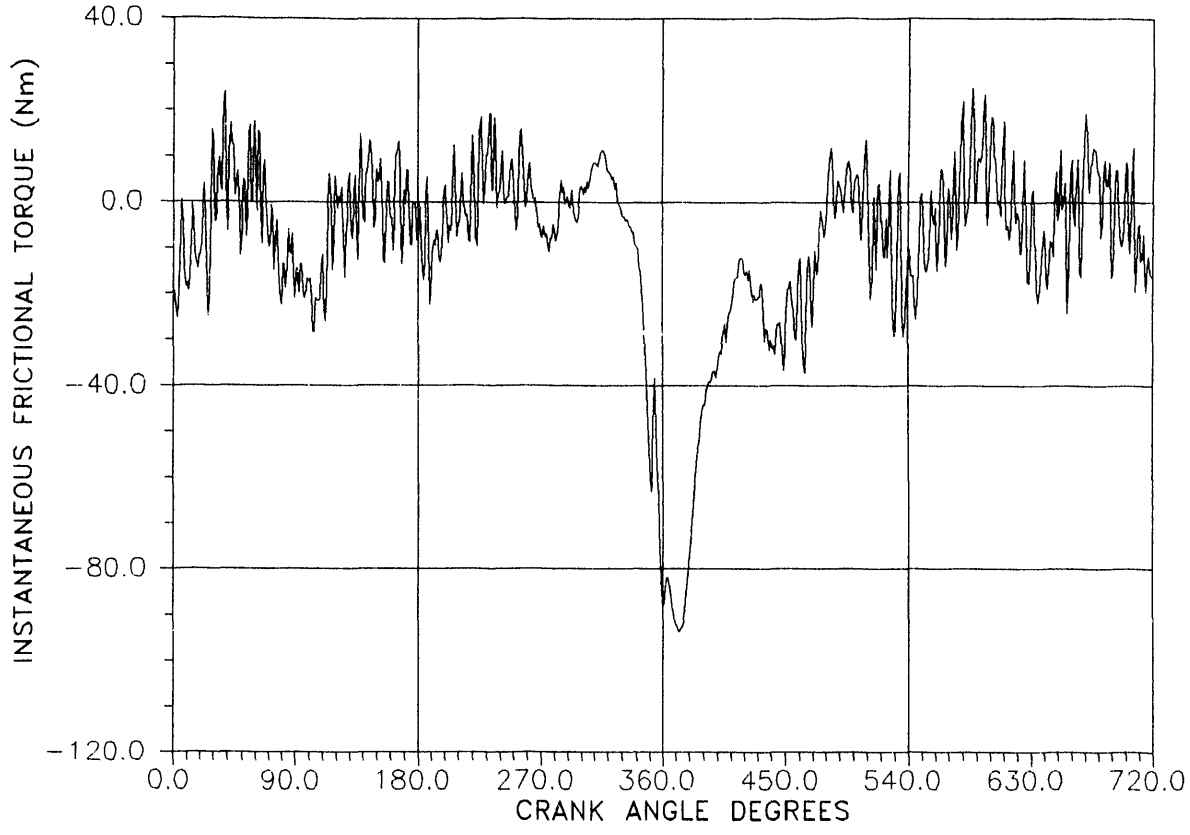

Figure 5.12. IFT from the normal room temperature calibration constant

Table 5.3
Effect of Transducer calibration at an Elevated Temperature (135°C) on Friction Parameters

	Room Temperature Calibration	Elevated Temperature Calibration	% Error
Peak IFT Compression,Nm	-63.0	-75.4	+16.4%
Peak IFT near TDC, Nm	-88.6	-89.1	+0.6%
Peak IFT Expansion, Nm	-93.7	-74.9	-25.1%
$\int$IFT $d\theta$	-117.4	-112.0	-4.8%
FMEP	164.7	157.0	-4.9%

calibration is conducted while the transducer bulk and its mounting are heated to a steady state temperature. The calibration constant should be determined as a function of temperature and calculated at the surface temperature in the combustion chamber.

3- The error due to the cyclic change in temperature under simulated engine conditions was found to be much less than that due to the steady state thermal stresses.

4- The steady state heating produced a positive pressure error, while transient heating produced an opposite effect. The steady state heating affects all the transducer components, while the transients affect the diaphragm only.

The quartz crystal transducers used in this investigation were chosen after being tested and found to produce no zero drift. Their calibration was made on the modified heated dead-weight tester developed at Wayne State University.

CHAPTER 6: EFFECT OF OPERATING PARAMETERS ON INSTANTANEOUS FRICTIONAL TORQUE OF THE ENGINE

6.1 BACKGROUND

Frictional losses in engines depend on many design and operating variables. The method which is widely used to measure engine friction is the motoring test, explained in chapter 1. During motoring, many operating conditions do not duplicate the actual conditions of running engines. For example the cylinder pressures during motoring are much lower than those during firing. Even during firing the cylinder gas pressures increase with the load and speed of the engine. Accordingly, there are errors in the frictional losses determined by the motoring test.

The goal of this chapter is to determine the IFT and the mean frictional torque during the cycle under different operating conditions and compare it with the results of the motoring test. The effects of the following operating variables are presented:

i) engine load
ii) oil temperature
iii) oil grade
iv) engine speed

The engine used in this investigation is the single cylinder Duetz diesel engine.

6.2 EXPERIMENTAL SETUP AND PROCEDURE

A layout of the experimental setup is shown in figure 6.1. The engine was loaded by a low inertia water dynamometer, through a flexible coupling.

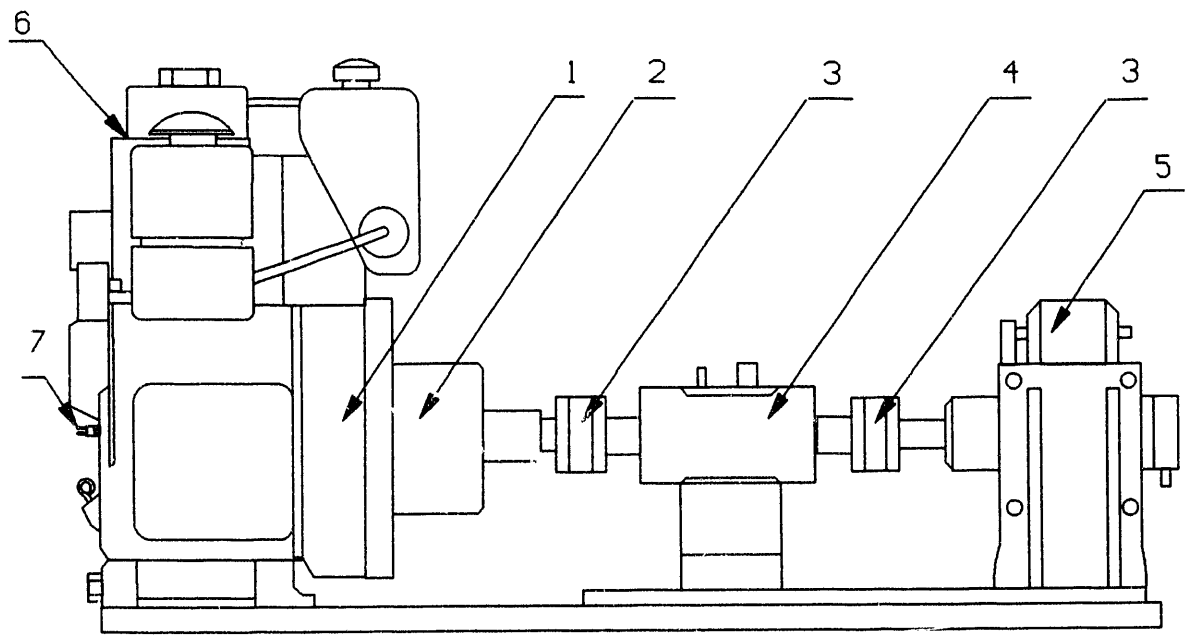

1. DEUTZ ENGINE F1L 210 D
2. INCREMENTAL SHAFT ENCODER
3. LOW INERTIA SHAFT COUPLINGS
4. TORQUE SENSOR
5. LOW INERTIA HYDRAULIC DYNOMOMETER
6. CYLINDER PRESSURE TRANSDUCER
7. CRANKCASE PRESSURE TRANSDUCER

Figure 6.1. Experimental setup

The cylinder gas pressure was measured by an AVL water-cooled, quartz crystal transducer and charge amplifier. The crankcase pressure was measured by using a Kistler Piezotrone® transducer. The cylinder pressure transducer together with the charge amplifier and the connecting cable were calibrated by using a modified dead-weight tester, in which the bulk of the transducer and its surroundings were heated to elevated temperatures representative of actual working temperatures in the engine [14]. The instantaneous angular velocity of the crankshaft was measured by using a BEI hollow shaft encoder, mounted on the flywheel. The instantaneous load torque was measured by a torque meter mounted between the flywheel and the water dynamometer. The signals from the pressure transducers, torque meter, shaft encoder and a TDC indicator were fed to a data acquisition system. The data were recorded every crank angle degree for one or more cycles.

The frictional torque under motoring conditions was determined by applying the (P-ω) method to a few engine cycles when the fuel flow was interrupted while the engine was idling at the same speed. In the present setup the engine could not be motored by the dynamometer.

6.3 EXPERIMENTAL RESULTS

Figure 6.2a shows a sample of the (P-θ), (ω-θ),(M_L-θ) traces obtained at 980 RPM, 11.3 Nm torque, with oil at a sump temperature of 57°C. The oil used was SAE 30. The cylinder pressure reached 6.6 MPa (958 psia). The instantaneous angular velocity dropped from a peak of 101 rad/sec to 87 rad/sec near the end of the compression stroke. The load torque reached a peak of 19 Nm at 420 CAD and fluctuated during the cycle. The fluctuations in the load torque may be attributed to the change in the angular velocity of the engine and the corresponding effect on the water dynamometer.

Figure 6.2b shows also the computed instantaneous torques due

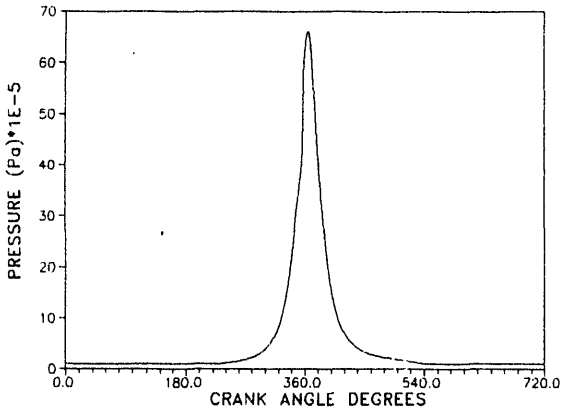

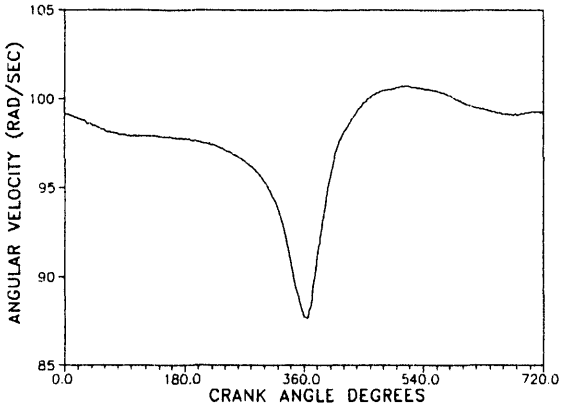

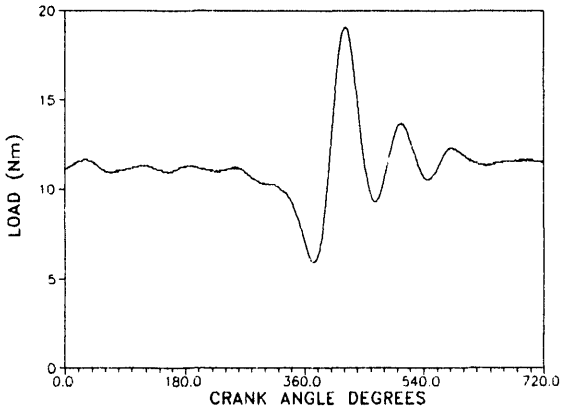

Figure 6.2a

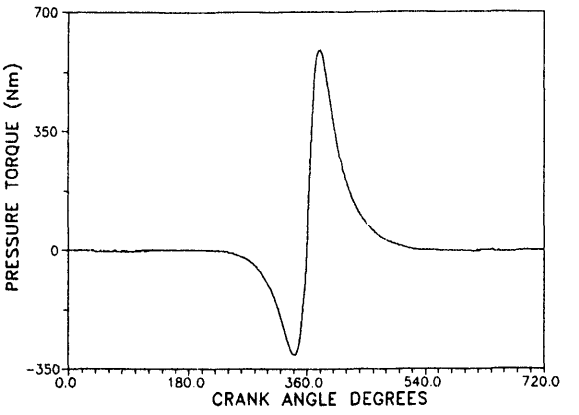

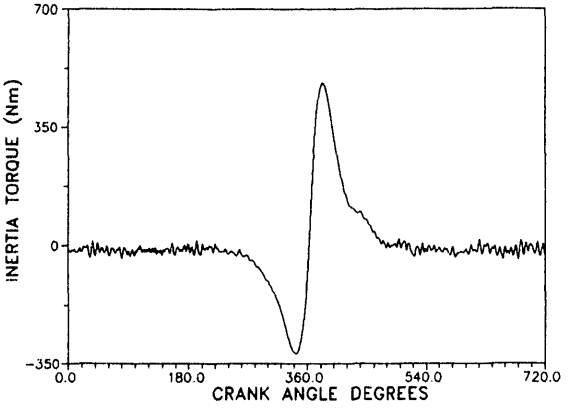

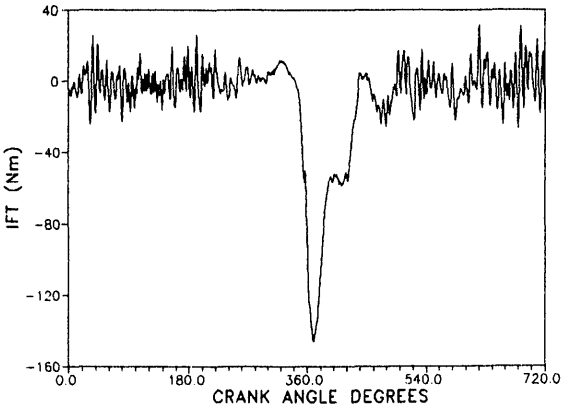

Figure 6.2b

Figure 6.2. Sample of experimental data and corresponding IFT results

to the cylinder gas pressure, the inertia of the moving parts and the instantaneous frictional torque. IFT reached its maximum absolute value during the expansion stroke, shortly after TDC. This will be referred to in this paper as the peak IFT. The reason for the positive apparent IFT, particularly during the compression stroke, is still under investigation. The cycle average frictional torque was -9.1 Nm.

6.3.1 EFFECT OF LOAD ON IFT

Figure 6.3 shows the ($P-\theta$), ($\omega-\theta$) and ($M_L-\theta$) traces for the engine at no-load and two different loads. The engine speed was 980 RPM, the sump oil temperature was 57°C.

The corresponding IFT for the compression and expansion strokes at different loads is shown in figure 6.4. The main effect of load on IFT is during the expansion stroke. The cycle-average IFT increased from -7.6 Nm at no load to -9.1 Nm at 11.3 Nm load.

Figure 6.5 shows the corresponding total integrated IFT from the beginning of the cycle to any crank angle degree, as a percentage of the total integrated IFT over the whole cycle. A large percentage of the frictional losses occurred near TDC due to the sharp increase in the cylinder pressure caused by combustion. It is noticed that the contribution of the frictional losses during the intake, compression and exhaust strokes is small compared to the contribution of the expansion stroke, at all the loads.

The effect of load on the maximum absolute value of IFT is shown in figure 6.6. IFT increased almost linearly with the load. This reflects the increase in the frictional losses in the piston-ring assembly and the main bearings of
the engine, due to the high pressures reached in the expansion stroke.

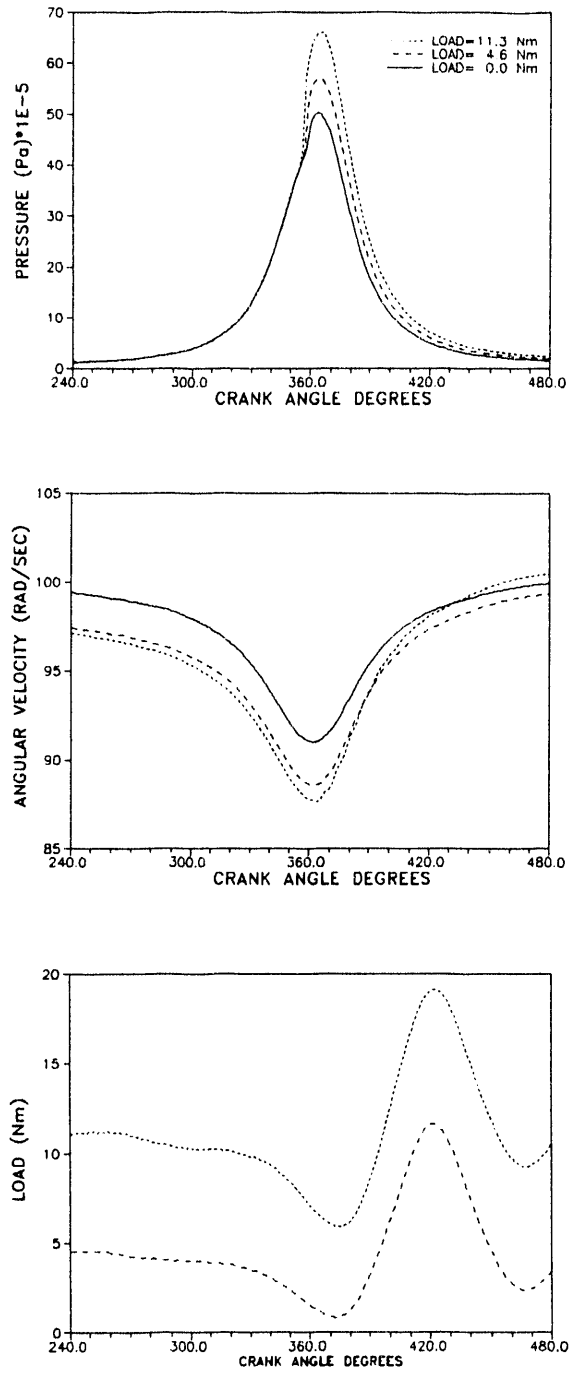

Figure 6.3. Sample of experimental data at three different loads

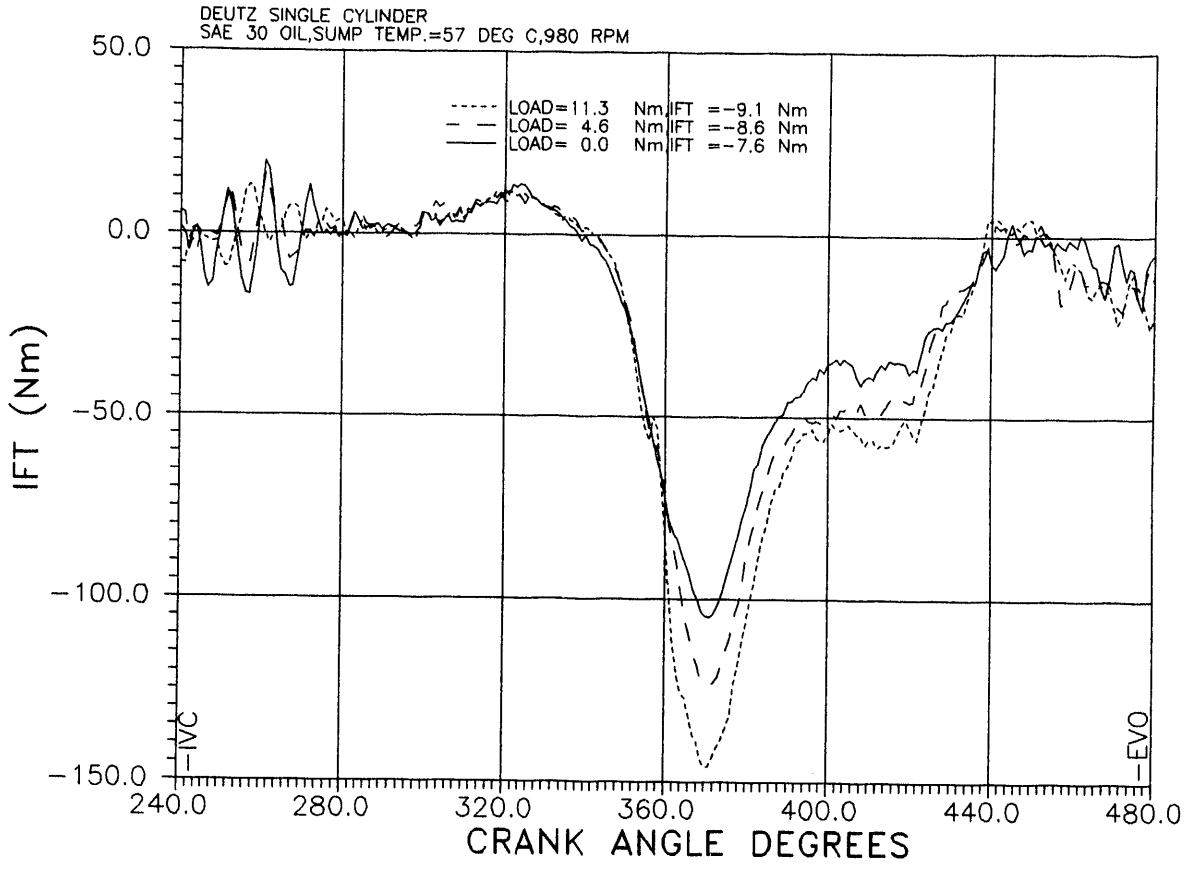

Figure 6.4. Effect of load on IFT

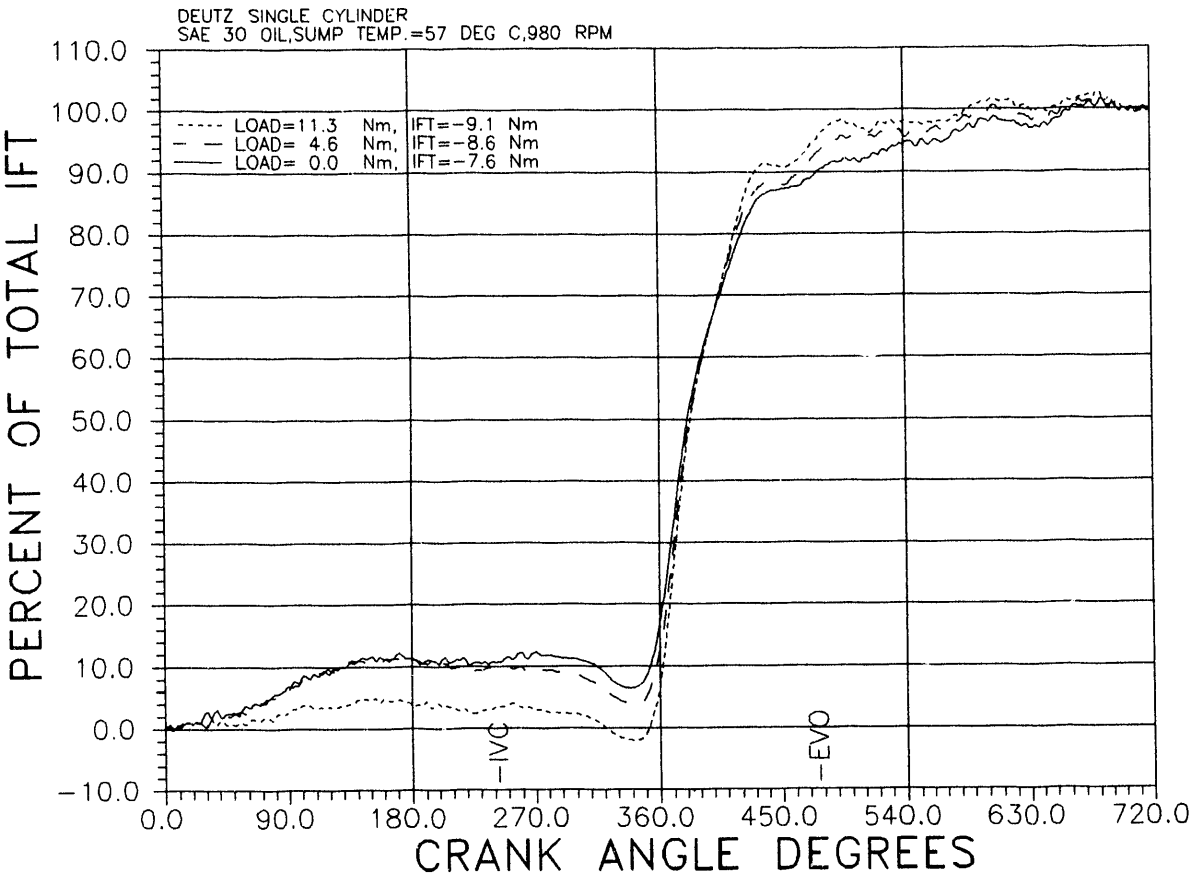

Figure 6.5. Effect of load on integrated IFT over the cycle

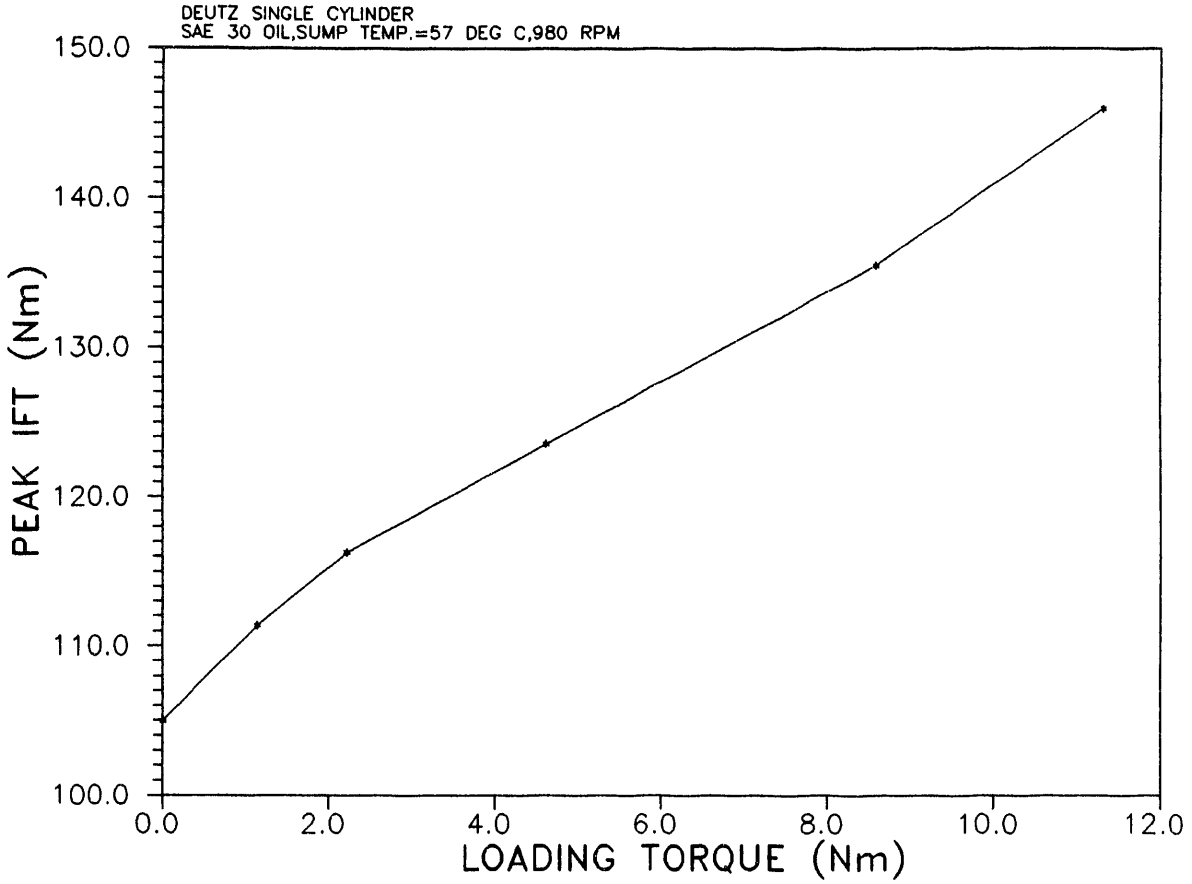

Figure 6.6. Effect of load on peak IFT

Figure 6.7 shows the peak IFT and the average IFT per cycle plotted versus the peak cylinder gas pressure. Points n and n1 are for the peak and the cycle-average IFT when the engine was running at no load under steady state conditions. Points m and m1 are the corresponding points when the fuel was momentarily shut-off. Points m and m1 represent the motoring run. The relationship between the peak IFT, cycle-averaged IFT and the peak cylinder gas pressure is essentially linear.

The relationship between the cycle-averaged IFT and the peak cylinder gas pressure may be given by

$$\overline{IFT}=0.9P_{peak}+3.3 \qquad \textbf{(6.1)}$$

The relationship between the peak IFT and peak cylinder gas pressure may be given by

$$(IFT)_{peak}=27P_{peak}-32 \qquad \textbf{(6.2)}$$

It is clear that the motoring frictional torque does not represent the frictional torque under firing conditions. The error in the measurement of the frictional torque by using the motoring test varies from 12.5% at no load, to 31.4% at full load.

Figure 6.8 shows the variation of the IFT during the compression and expansion strokes for the no-load and motoring conditions. The two curves correspond to points n and m respectively in figure 6.7. The main difference between the two curves is during the later part of the compression stroke and during the expansion stroke. The maximum difference is shortly after TDC in the expansion stroke.

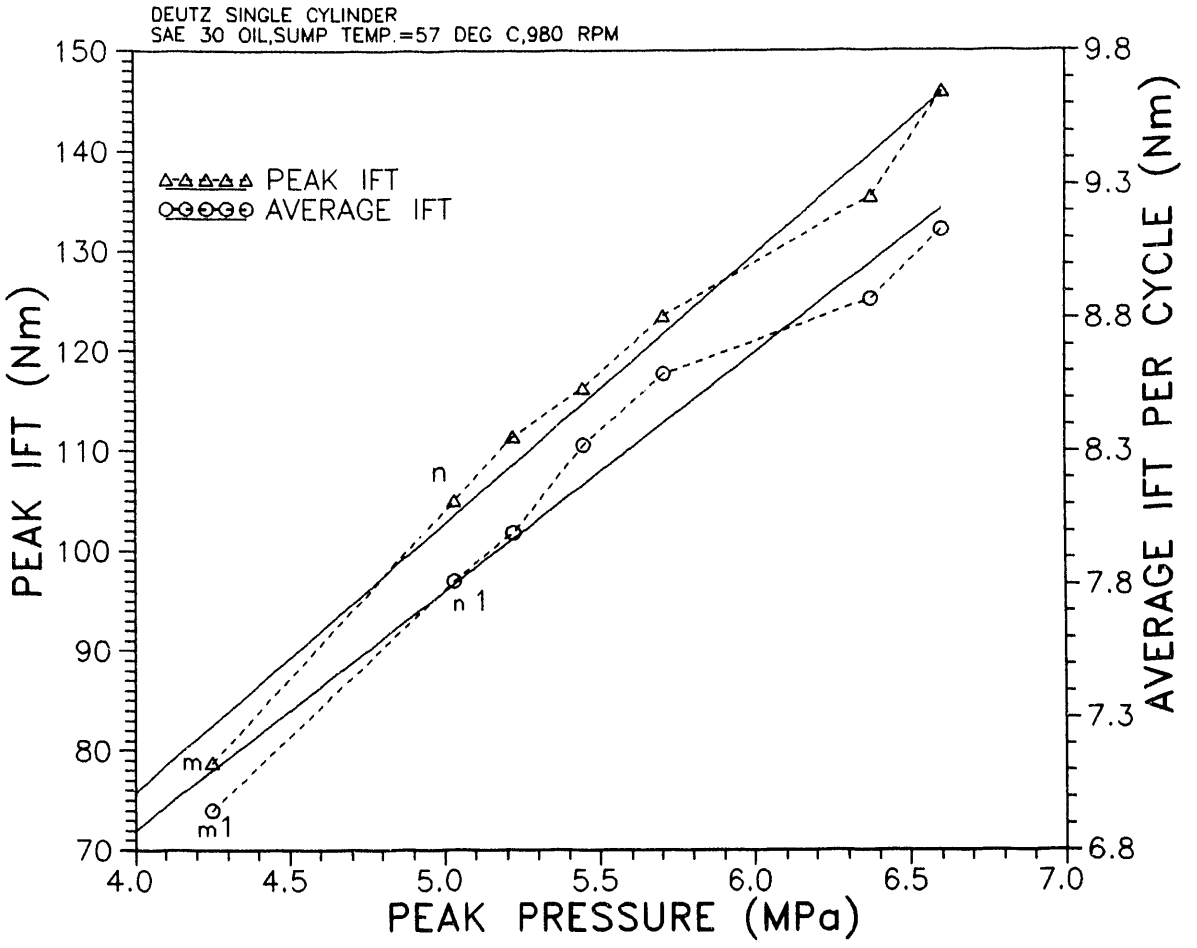

Figure 6.7. Effect of peak cylinder pressure on peak IFT

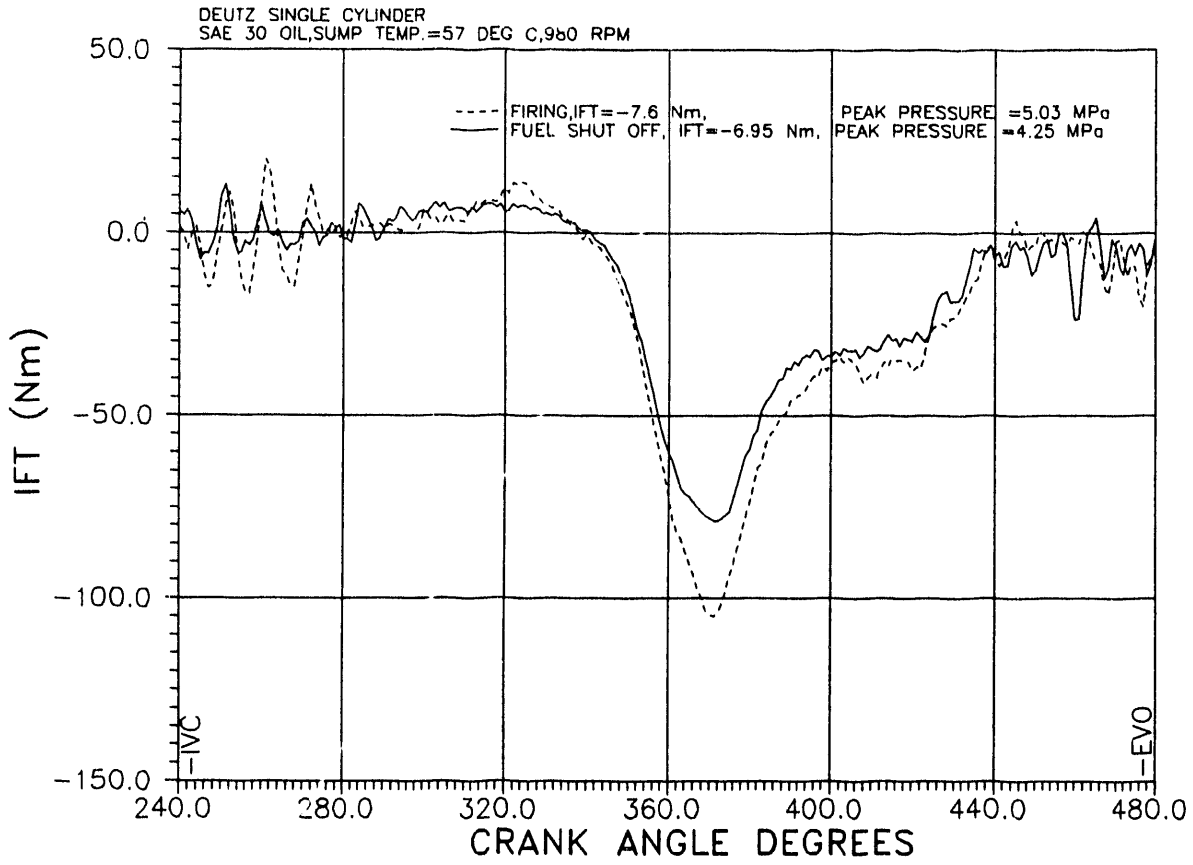

Figure 6.8. IFT for engine under no-load and motoring

6.3.2 EFFECT OF OIL TEMPERATURE ON IFT

Figure 6.9 shows the IFT for the engine, under no-load at two different oil temperatures: 20°C and 45°C. The oil used was SAE 30. For these runs the static injection timing was advanced by 15 CAD, relative to the injection timing of the previous figures. By comparing figure 6.9 with figure 6.4 it is clear that advancing the injection timing produced a peak in IFT during the compression stroke.

The corresponding average frictional torque for the whole cycle is shown in figure 6.10. An increase of 25°C in the sump oil temperature caused a drop of 30% in the cycle frictional losses. The corresponding decrease in oil viscosity is 80%.

During motoring the sump oil temperature is usually lower than during firing. This would also contribute to the errors in using the results from motoring tests to represent the firing operation.

6.3.3 EFFECT OF OIL GRADE ON IFT

Two oil grades, SAE 30 and SAE 50, were used at the same sump temperature of 57°C, speed of 980 RPM and approximately equal loads. Figure 6.11 shows that the lighter oil produced less frictional torque as expected. The difference between the two traces is not significant but the averaged IFT over the whole cycle changed from -9.1 Nm for SAE 30 oil to -10.9 Nm for the SAE 50 oil. The difference in viscosities of these oils at 57°C is 50%.

The corresponding effect of oil viscosity on the cycle-averaged IFT is shown in figure 6.12. The contribution of the frictional losses during the intake, compression and exhaust in the total cycle friction increased with the increase in oil viscosity. This reflects the increase in the contribution of hydrodynamic lubrication with the increase in oil viscosity.

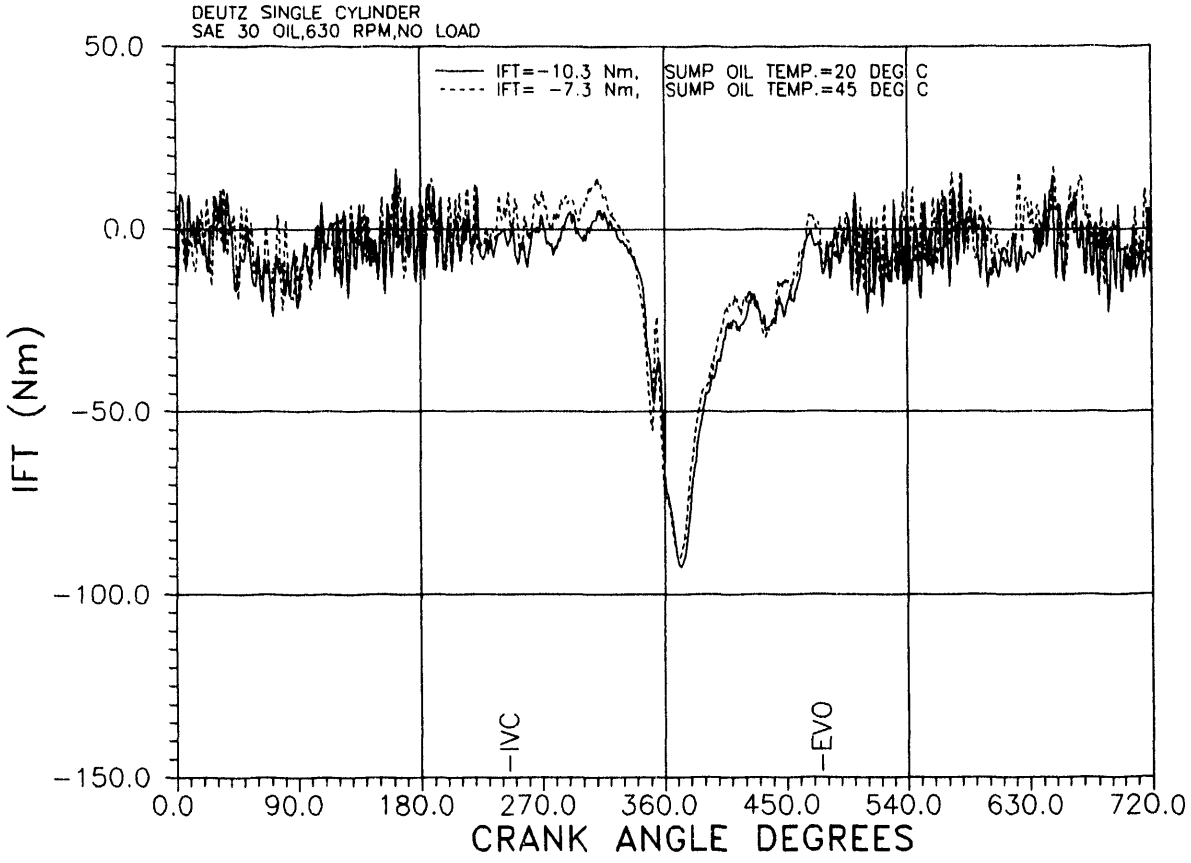

Figure 6.9. Effect of oil sump temperature on IFT

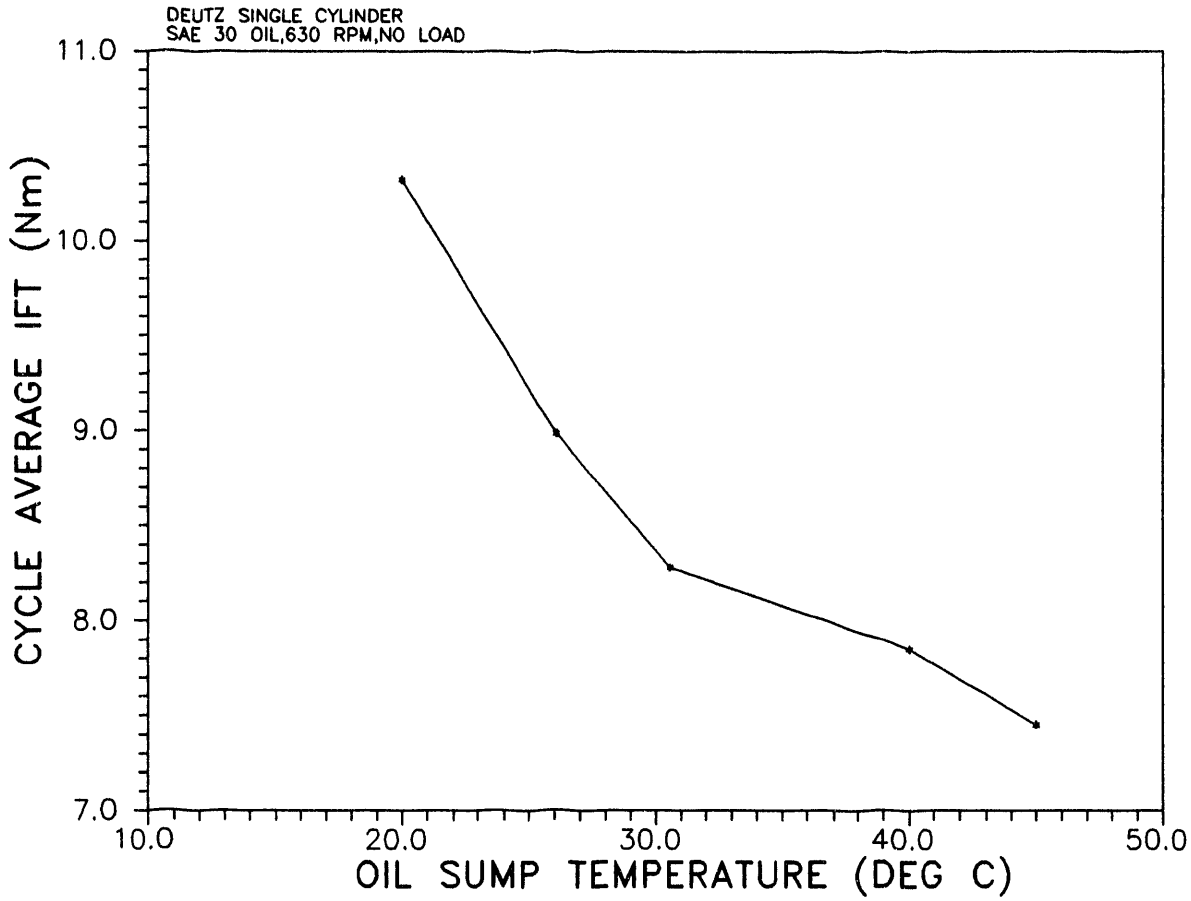

Figure 6.10. Effect of oil sump temperature on cycle averaged IFT

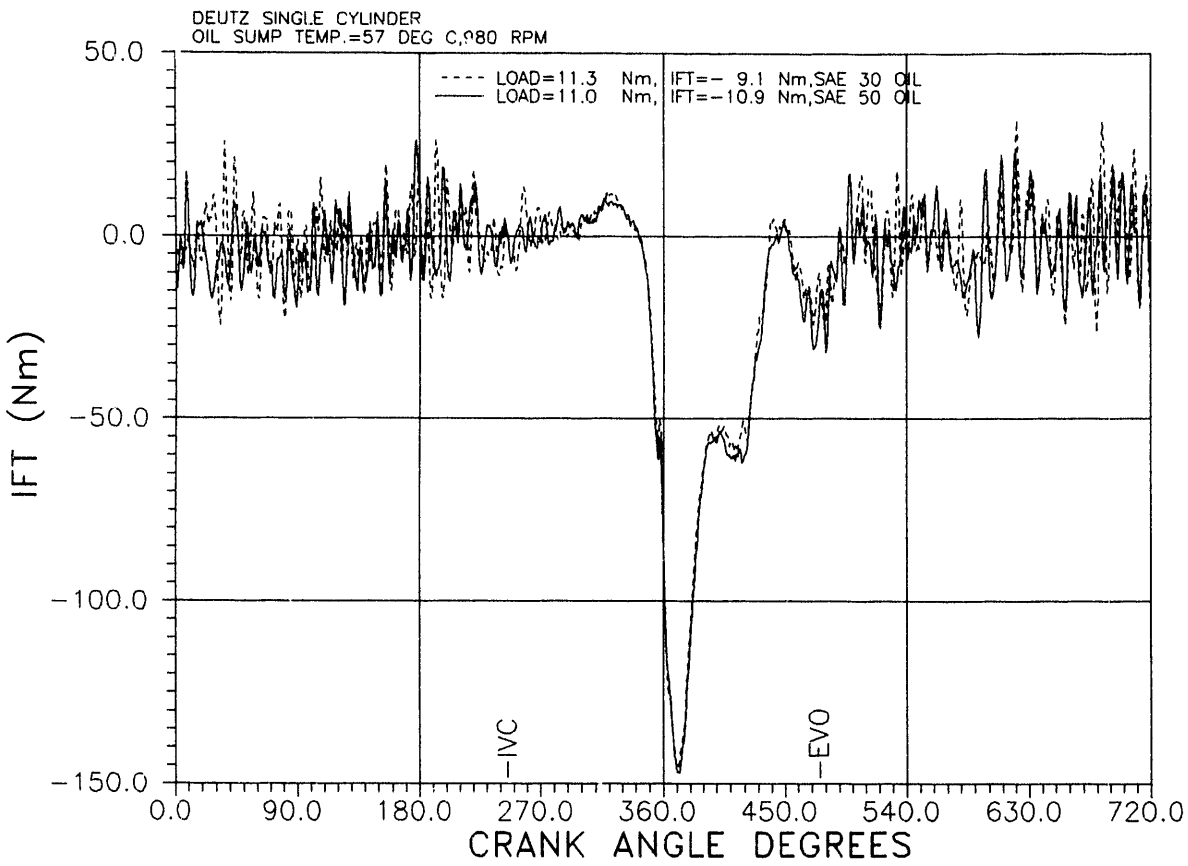

Figure 6.11. Effect of oil grade on IFT

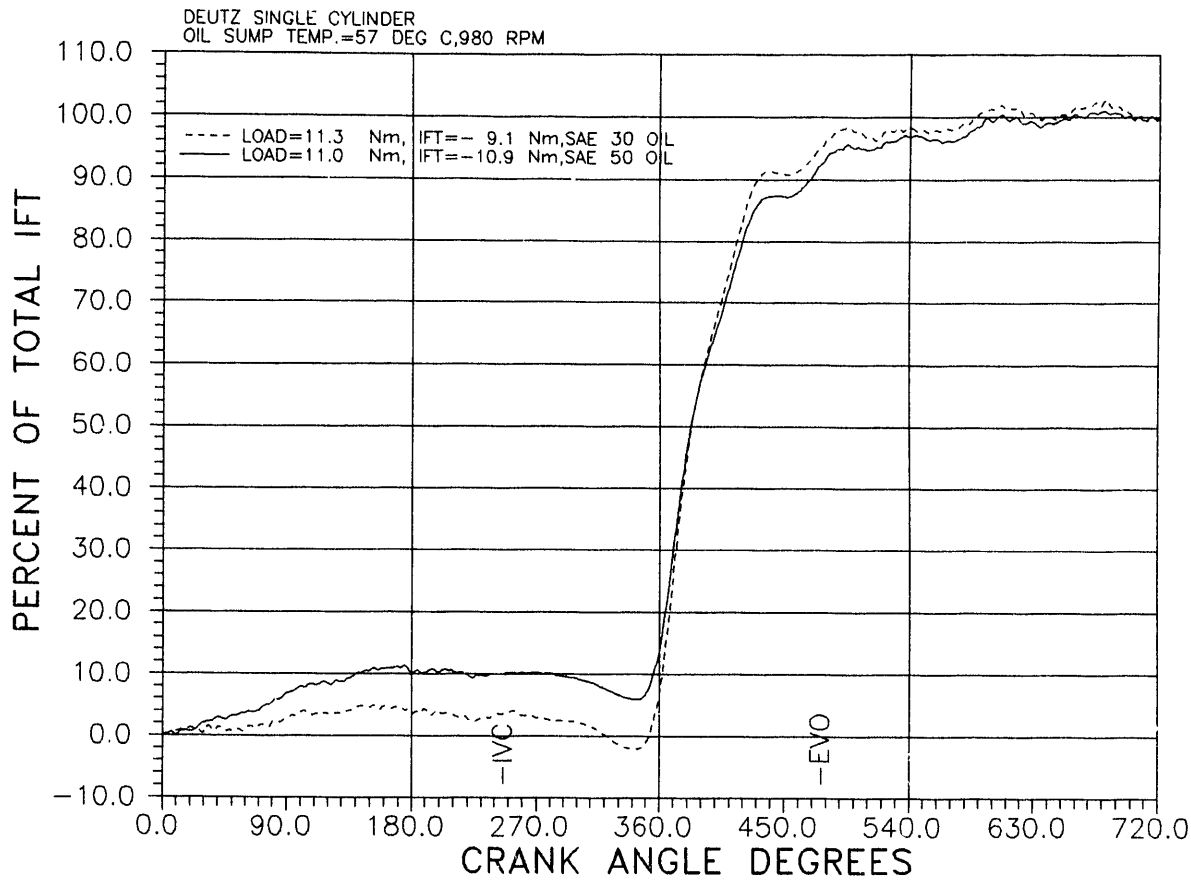

Figure 6.12. Effect of oil grade on integrated IFT

6.3.4 EFFECT OF ENGINE SPEED AT CONSTANT LOAD

The engine was tested at three different speeds of 717 RPM, 1588 RPM and 2598 RPM, and at a constant load torque of 6.6 - 6.7 Nm. The oil used was SAE 30 at a sump temperature of 58°C. The variation in cylinder gas pressure, instantaneous angular velocity and instantaneous load torque, for each of the three speeds is given in figure 6.13. Notice the small cyclic variations in the instantaneous angular velocity and load-torque, at the higher speeds.

The variation in the IFT for 717 RPM and 1588 RPM runs is shown in figure 6.14. The contribution of the frictional losses during the intake, compression and exhaust strokes in the total cycle frictional losses increased with speed. This reflects the increase in the friction due to hydrodynamic lubrication. The corresponding effect of speed on the total cycle friction is shown in figure 6.15. It is clear that the friction increases almost linearly with speed.

6.4 SUMMARY

1- The peak and cycle-averaged IFT are strongly dependent on the load on the engine. At higher loads more fuel is injected and higher pressures are reached. There is a linear relationship between the peak and cycle-averaged frictional torque and the peak cylinder gas pressure.

2- The motoring frictional torque does not represent the frictional torque under firing conditions because of the low pressures reached. The error was 12.5% at no load and 31.4% at full load.

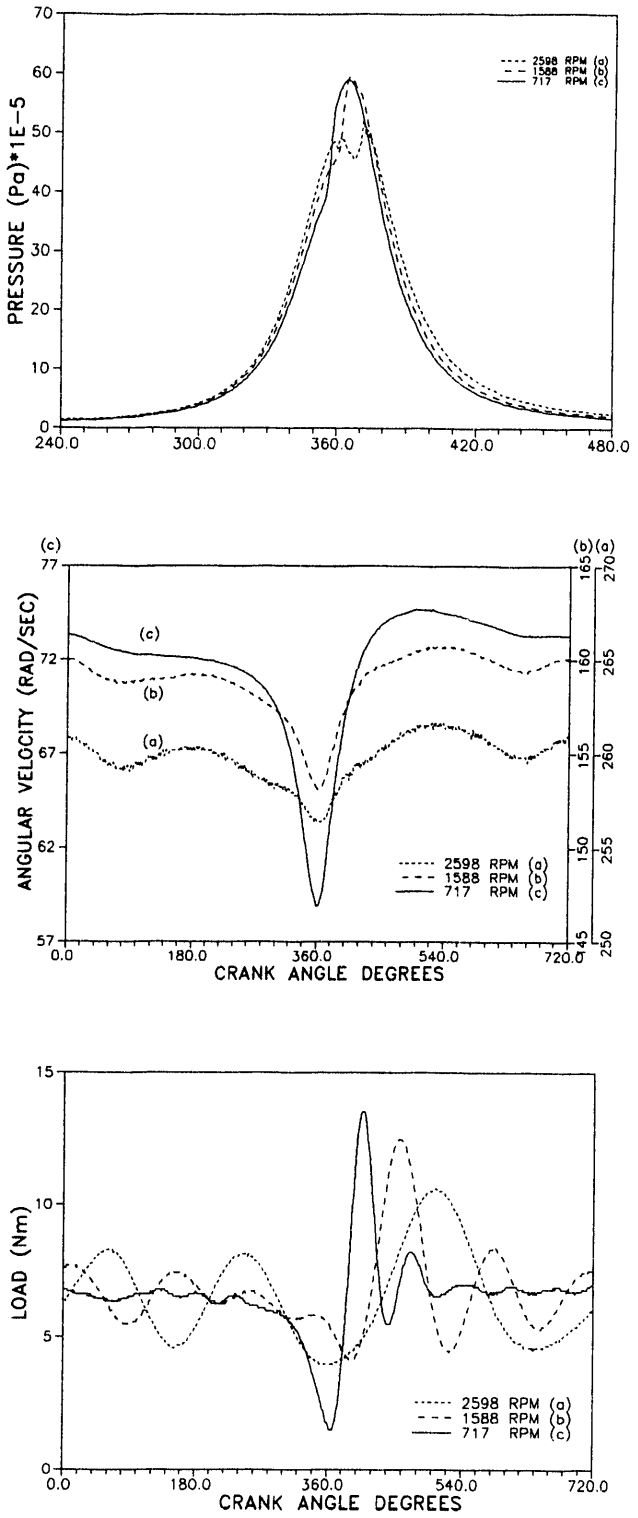

Figure 6.13. Sample of experimental data for three different speeds

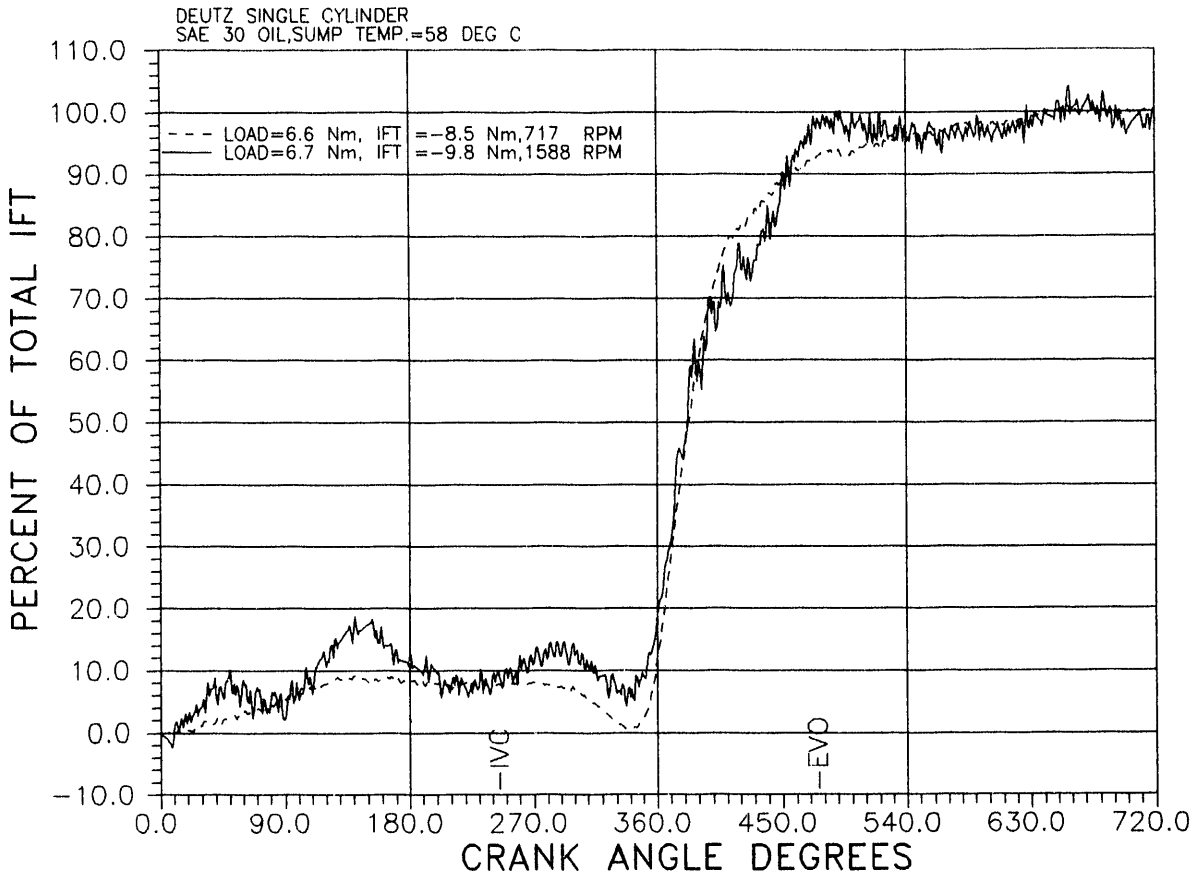

Figure 6.14. Effect of speed on integrated IFT

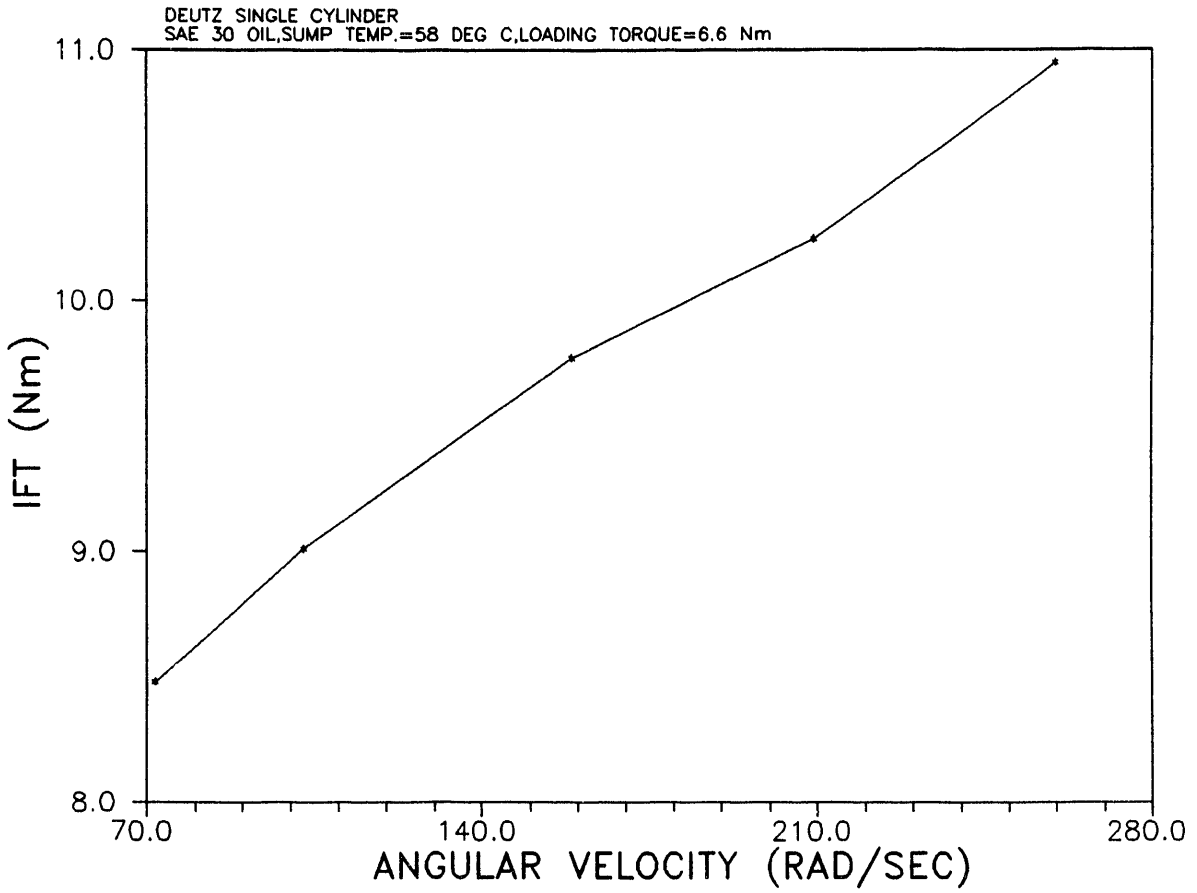

Figure 6.15. Effect of speed on cycle averaged IFT

3- The peak and cycle-averaged IFT decreased with the drop in oil viscosity caused by temperature increase or by using a lighter oil.

4- The contribution of the hydrodynamic lubrication during the inlet, compression and exhaust strokes in the total cycle friction increased as the oil viscosity increased.

5- The cycle-averaged frictional torque increased linearly with speed, at a constant load. The contribution of the hydrodynamic lubrication friction in the total cycle friction increased with speed.

CHAPTER 7: COMPONENTS OF ENGINE INSTANTANEOUS FRICTIONAL TORQUE (WITHOUT THE CYLINDER HEAD)

7.1 BACKGROUND

Frictional losses in reciprocating combustion engines are of concern to engine designers. Incremental reductions in frictional losses in different components can add up to appreciable savings in fuel consumption and an increase in the power output of the engine.

Many researchers have investigated the breakdown of the time averaged frictional losses in different engine components [4, 24-27]. In some investigations the individual contribution of each component was determined by selective removal or addition of the component in a motoring test. While the tests did not duplicate the engine normal running conditions, or even the conditions when the whole engine is motored, the results reflected roughly the relative contribution of each component in the overall frictional losses under the test conditions. An extrapolation of the results might help in estimating the relative contribution of some components such as the piston and bearings under the actual thermodynamic conditions, by including the effects of the high pressures and temperatures on the component friction. The friction in other components such as the valve train, fuel injection pump and some accessories is not greatly affected by the actual gas pressure and temperature in the cylinder.

Whitehouse and Metcalf [24] measured the power losses due to each component in a 1.5 liter gasoline engine, at speeds ranging from 1500 rpm to 4000 rpm. The components are the crankshaft, oil pump, piston and connecting rod, piston rings and valve train. Analysis of their data indicated that the relative contributions of the valve train and oil pump increased at lower speeds.

Cleveland and Bishop [25] reported the contribution of the

components as a function of the vehicle speed. Analysis of their data indicated that the contribution of the piston-ring assembly and the valve train increased at the lower speeds while the contribution of the other components decreased.

Kovach et al [4] determined the friction components for a four stroke, four cylinder gasoline engine at speeds ranging from 1000 rpm to 4000 rpm. Analysis of their data indicated that the contribution of all the components dropped except that of the valve train.

The literature review indicates the following:

i) all the results for the friction components were time averaged values over one cycle or over a period of time.

ii) the piston-ring assembly was the largest contributor in total engine friction under the motoring test without the cylinder head. Under actual engine conditions this contribution increases .

iii) the valve train contribution in total friction increased with the drop in speed.

The (P-ω) method was used to determine IFT of different engine components by considering the different torques and the resulting acceleration. In this investigation the IFT of the components was determined by adding one component at a time. The base unit consisted of the crankshaft with the flywheel and the oil pump.

7.2 EXPERIMENTAL WORK

The Deutz single cylinder direct injection diesel engine was used in the experimental work. The torques on each of the starter shaft and the camshaft were measured by using strain gages bonded

to each of the shafts in a Wheatstone bridge configuration. The outputs from the wheatstone bridges were amplified and recorded as functions of the crank angle, viewed on an oscilloscope screen and recorded by the data acquisition system. The details of the experimental setup are given in reference [28].

The engine was disassembled and rebuilt in steps. In each step one component was added and its effect on the frictional torque was determined. The frictional torque in each of the configurations was determined during a coast-down mode, after the crankshaft was accelerated to about 900 rpm by the electric starter. During coast-down the torques acting on the crankshaft were due to the inertia forces of the moving parts, the gravitational forces and the frictional forces.

The instantaneous frictional torque was determined for the basic configuration which consisted of the crankshaft with flywheel rotating in the two main bearings while driving the oil pump. The effect of adding each of the following components on the instantaneous frictional torque was determined:

1- balancer shaft
2- balancer shaft and camshaft
3- piston without rings
4- piston with different ring combinations
5- valve train
6- fuel injection pump

7.3 EXPERIMENTAL RESULTS AND DISCUSSIONS

7.3.1 IFT FOR BASIC CONFIGURATION: CRANKSHAFT WITH FLYWHEEL AND OIL PUMP

This configuration is given in figure 7.1. The upper part of

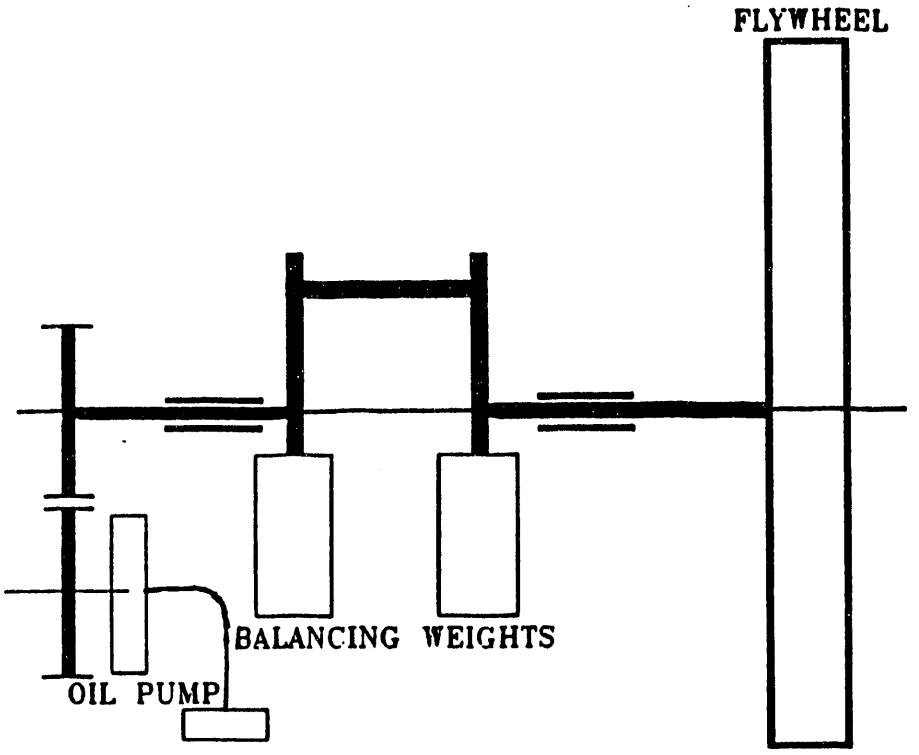

Figure 7.1. Basic system configuration

Figure 7.2 shows the instantaneous angular velocity during coast-down, for 2 consecutive revolutions, from which the frictional torque was calculated. The frictional torque was due to bearing frictional forces, oil pump and windage losses. The lower part of Figure 7.2 gives the instantaneous frictional torque for many cycles during the coast-down process. The numbers on each curve are for the order of the cycle from the time the starter was turned on. It is noticed that as the rotating speed decreased the cycle averaged cycle frictional torque decreased. The variation in IFT during each cycle was due to the variations in the instantaneous angular velocity caused by the change in the net torque acting on the crankshaft. The torque due to the gravitational forces of the crankshaft, balancing weight (which is unbalanced in this configuration) varied with the crankangle. The variation in the energy lost in friction as a function of the cycle averaged angular velocity is shown in figure 7.3. The energy lost in friction was calculated from

$$E = \int_0^{720} M_{IFT} d\theta \qquad (7.1)$$

The energy lost in friction decreased linearly as the speed dropped from 90 rad./sec. to 25 rad./sec. At lower speeds the energy lost decreased at a fast rate till the shaft stopped. The nonlinear behaviour at the low speeds is believed to be caused by the change in the eccentricity in the bearings and the contribution of the oil pump.

7.3.2 EFFECT OF ADDING THE BALANCER SHAFT

This configuration is represented in figure 7.4. The additional frictional losses are due to the balancer shaft bearings and gear. The loss in energy, with and without the balancer shaft is shown in figure 7.5.

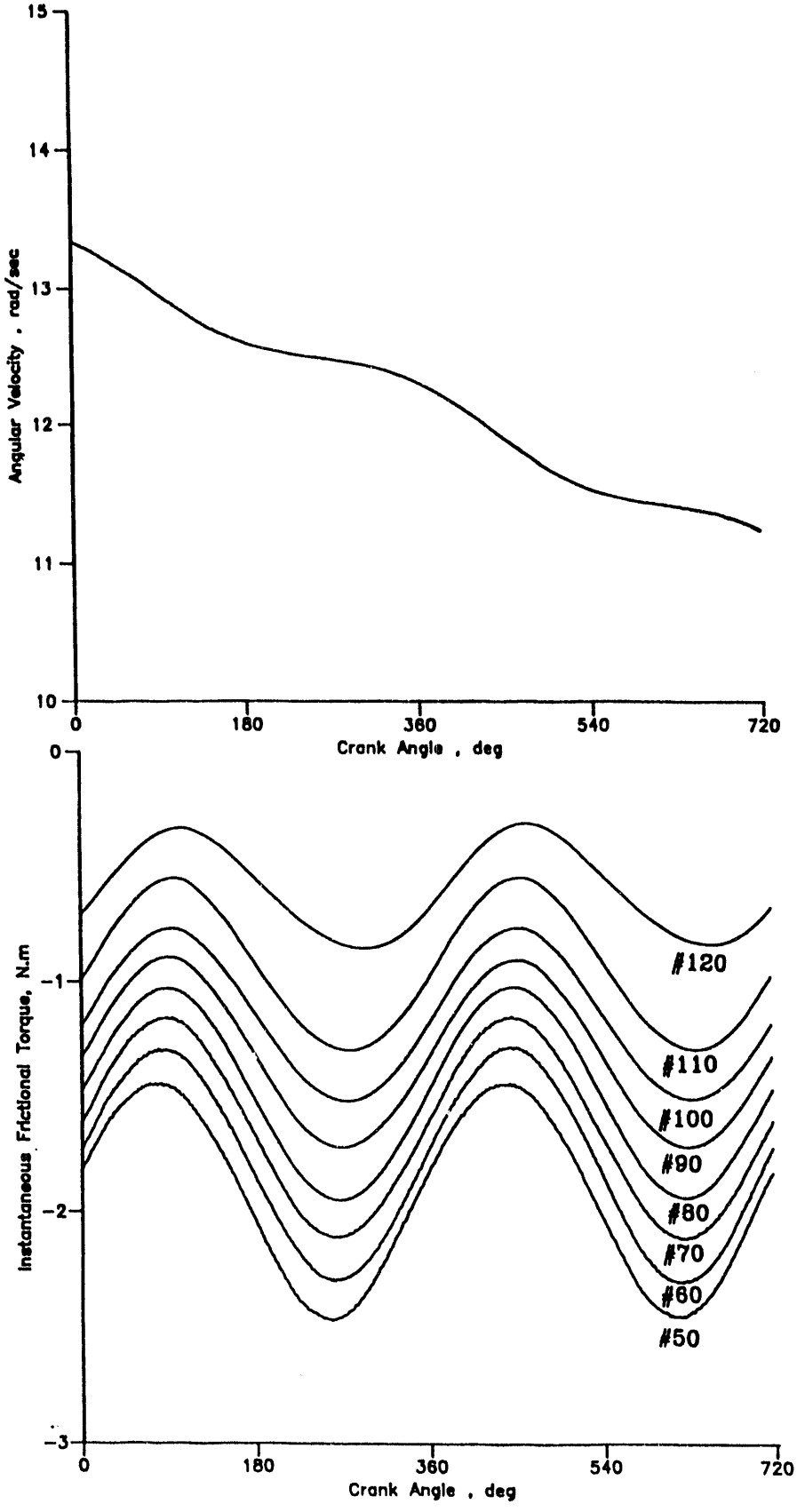

Figure 7.2. Angular velocity and IFT during coast-down of the basic system

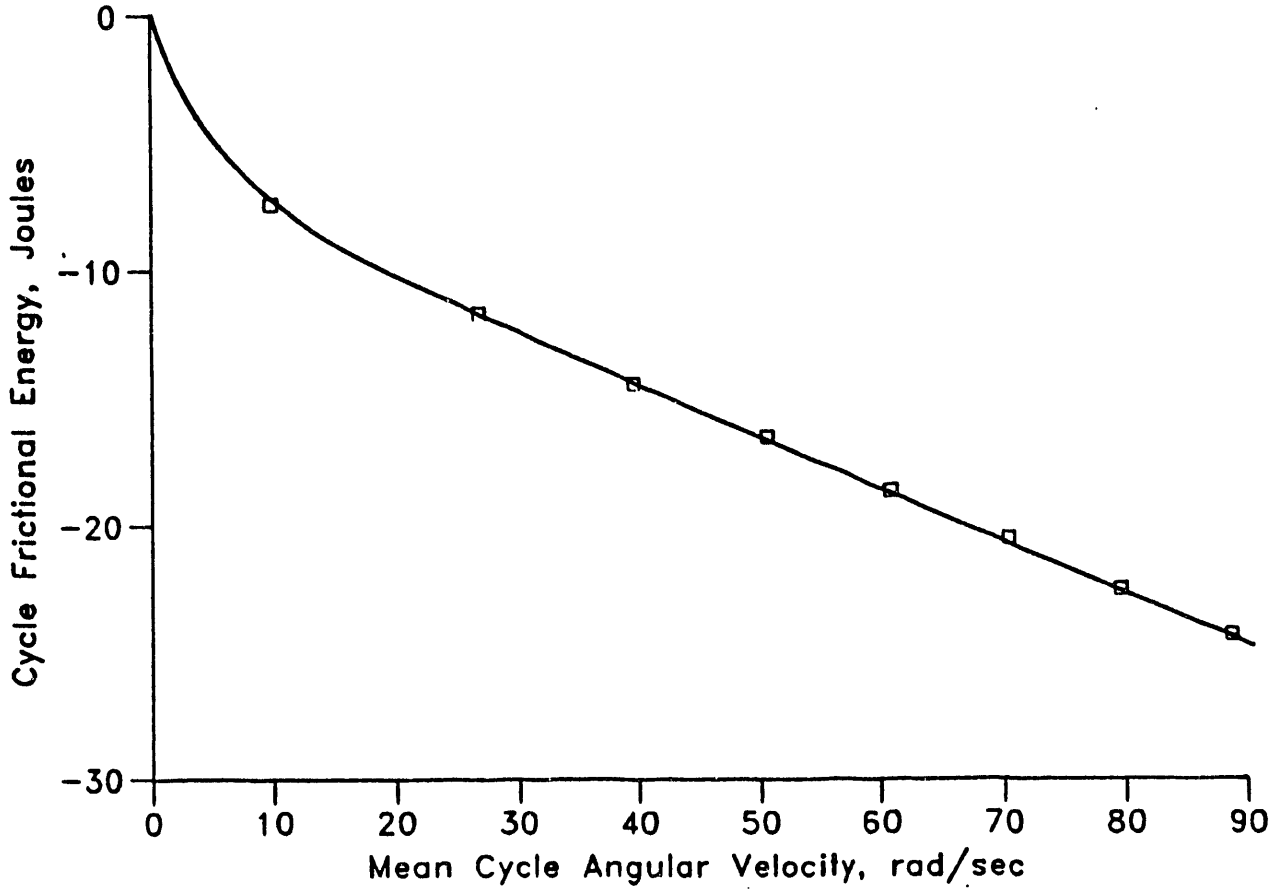

Figure 7.3. Effect of angular velocity on energy lost in friction of the basic system

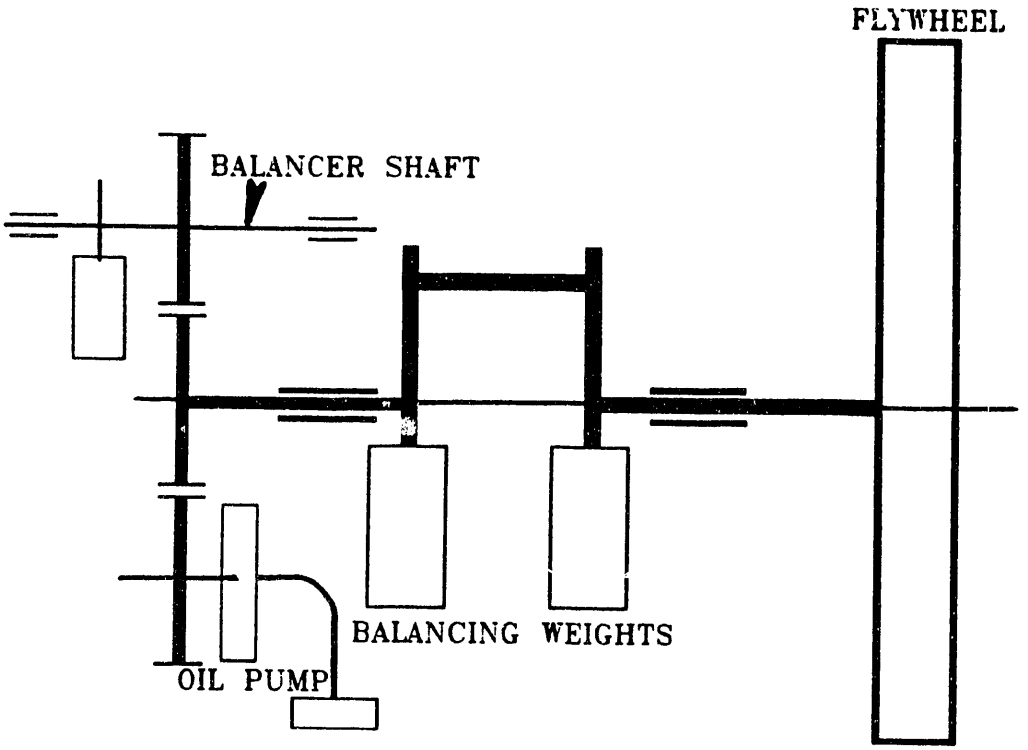

Figure 7.4. Configuration with the balancer shaft

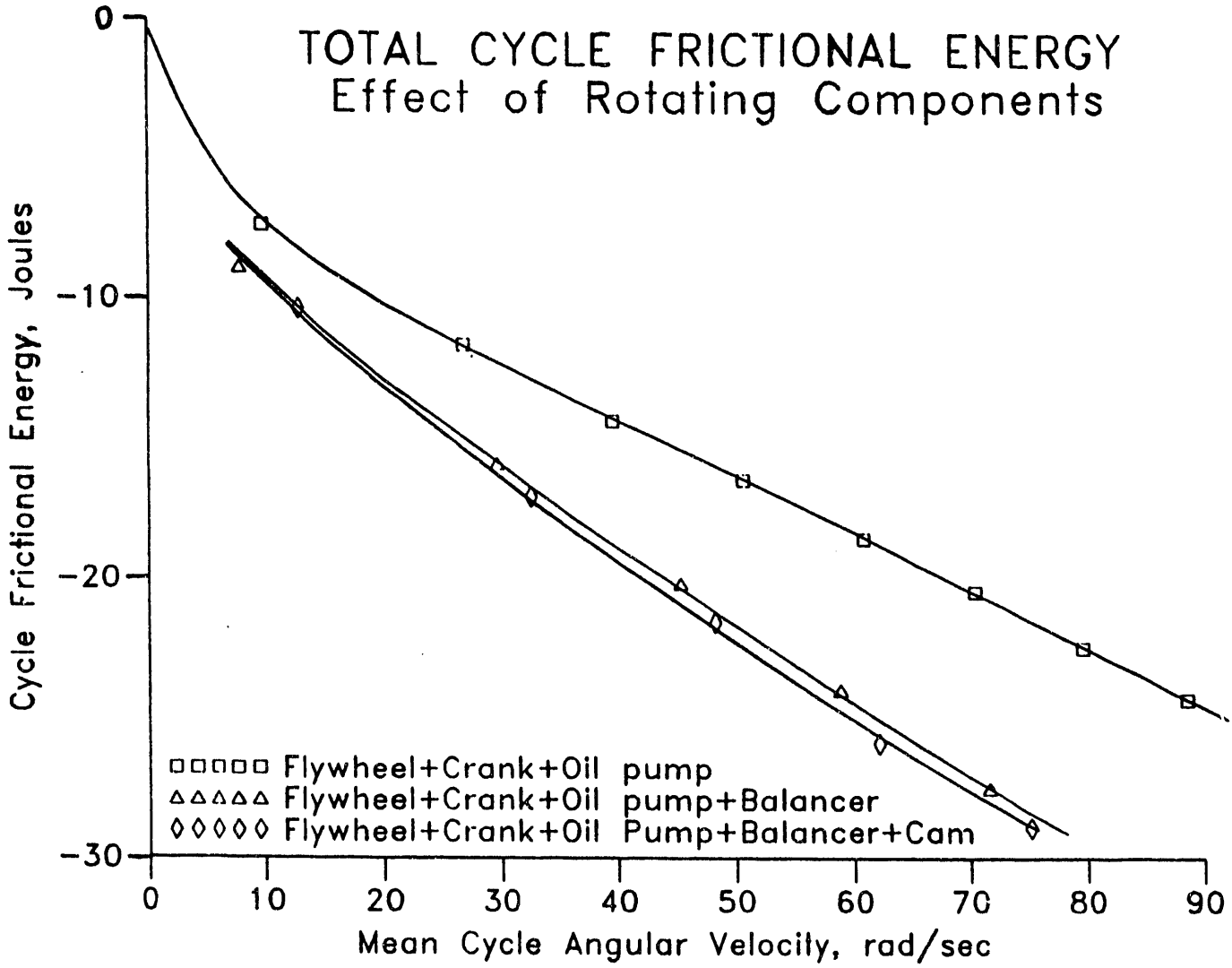

Figure 7.5. Effect of angular velocity on energy lost in friction

7.3.3 EFFECT OF ADDING THE CAMSHAFT (NO VALVES)

The crankshaft-drive is shown in figure 7.6. The additional frictional losses are in the gear drive of the camshaft and its two bearings. The results, shown in figure 7.5, indicate small additional frictional losses. The relatively small additional frictional losses resulted from the use of a new camshaft and driving gear. Meanwhile the balancer shaft gear and the crankshaft gear were used and not in a good condition. If the balancer shaft and gear were in good condition the frictional losses would have been less.

7.3.4 EFFECT OF RECIPROCATING PARTS

This configuration consisted of the crankshaft with flywheel, oil pumps, connecting rod and piston (without rings), as shown in figure 7.7. The frictional losses are in the two main bearings, oil pump, crankpin bearing, small end bearing and between piston and cylinder. Figure 7.8 shows the IFT for the piston without rings, at two different speeds. The IFT increased at the higher speed at all crankangles. The variation of IFT during the different strokes was mainly due to changes in the instantaneous piston speed, which reached a maximum near midstroke, and the resulting change in the lubricating film thickness. The mode of lubrication of piston without rings is mainly hydrodynamic and the film thickness and the relative speed played a big role in frictional losses. In addition, the change in film thickness along the length of the skirt might have contributed to the changes in IFT. The clearance between the piston and cylinder was a function of the piston tilt. Also the piston slap, which could be heard during the experiment, played a role in the IFT, particularly at the higher speed.

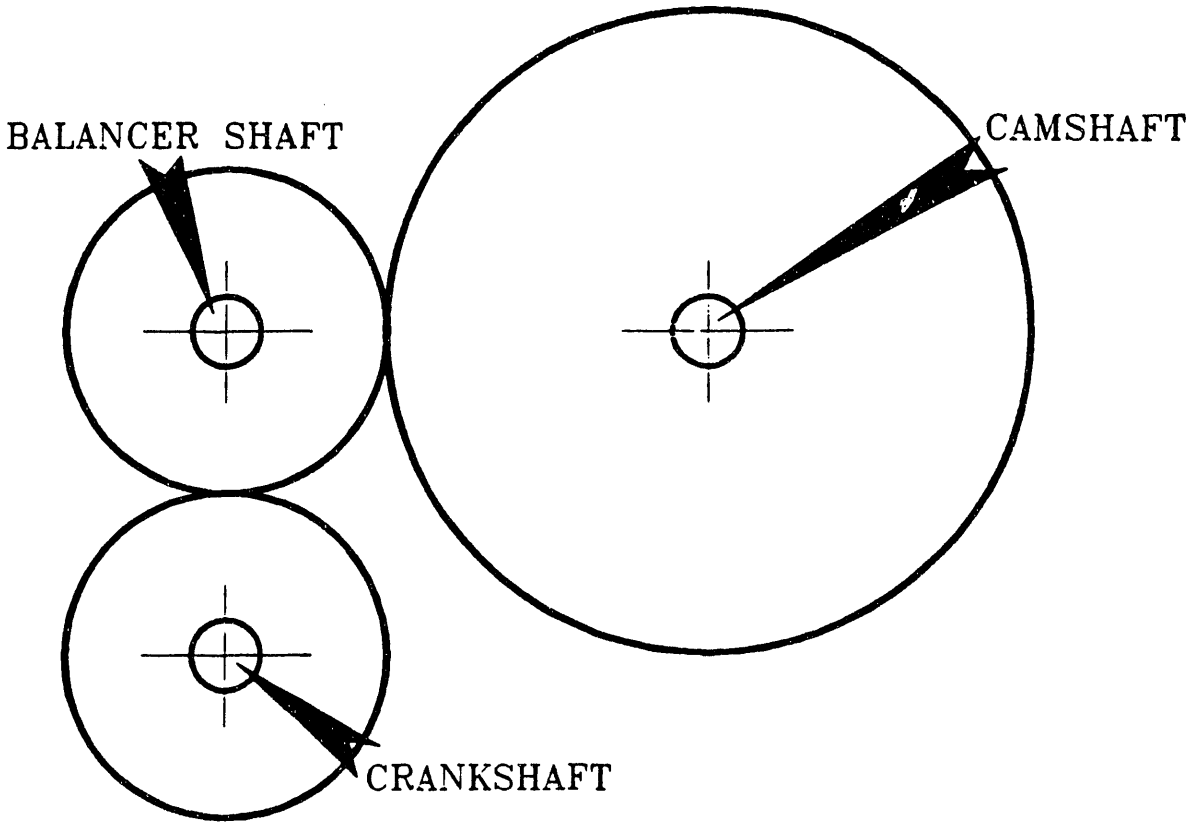

Figure 7.6. Cam shaft drive

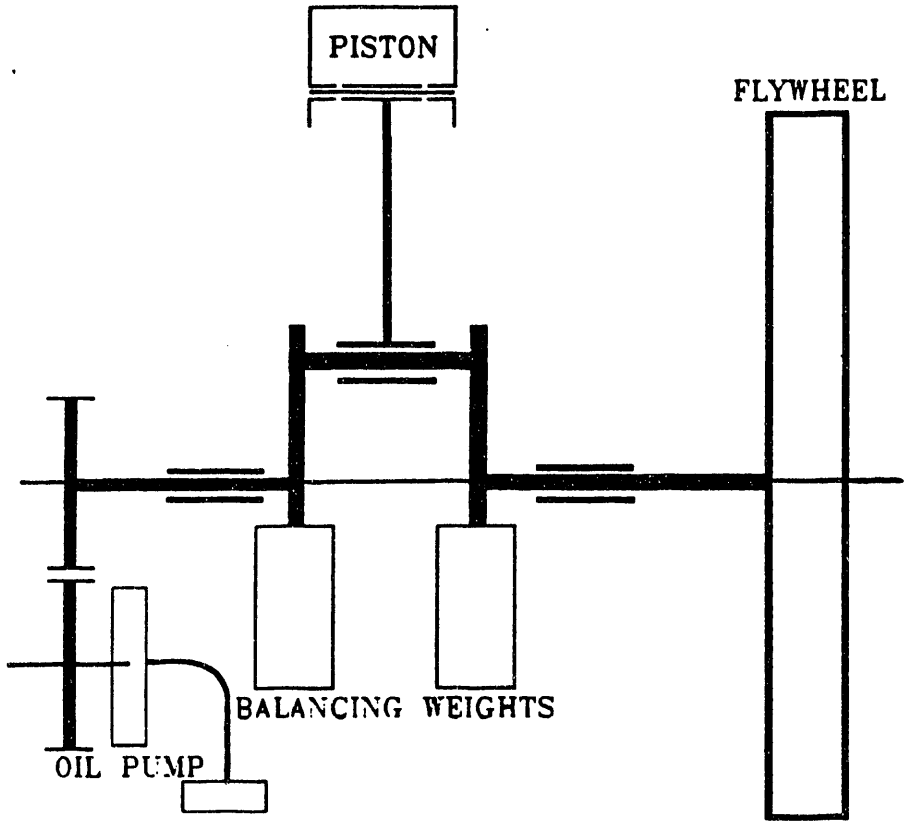

Figure 7.7. Configuration with the reciprocating parts

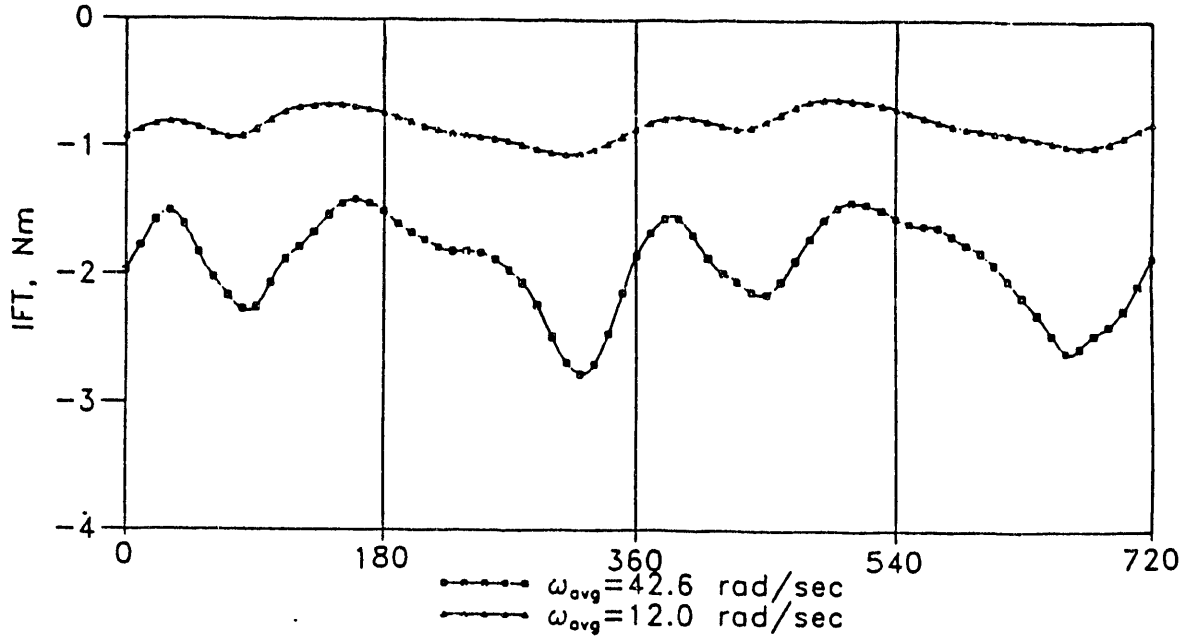

Figure 7.8. Effect of speed on IFT of the basic system with reciprocating parts

7.3.5 EFFECT OF RING PACK

Different combinations of piston rings were installed and the IFT measured. Figure 7.9 shows the coast-down IFT of the different combinations. The cycles chosen had very close average velocities, as indicated in the figure. The IFT for the basic configuration is shown for comparison. The shape of the curves indicates that the mode of lubrication away from the dead canters, is hydrodynamic and is dependent on speed. Near the dead canters the lubrication appears to be mixed. The oil ring contribution in IFT is higher than any of the compression rings. The combinations of the oil ring with any one of the two compression rings resulted in an increase in IFT. The increase in IFT due to the top compression ring is slightly more than that of the second compression ring. This is caused by the slightly higher elastic tension of the top ring when compared with the second ring. The contribution of the piston skirt small-end bearing and big-end bearing is less than that of the oil ring.

Figure 7.10 shows results similar to figure 7.9 but at a lower average angular velocity. By comparing the two figures it is clear that the IFT for any combination increased with the speed.

The total energy lost in friction for all the above engine configurations is plotted as a function of the cycle averaged speed in figure 7.11. The contribution of the oil ring is more than any of the two compression rings. The contribution of the reciprocating parts and the connecting rod in the total friction is more than that of all the other components.

7.3.6 EFFECT OF VALVE TRAIN

Figure 7.12 shows the variation in the angular velocity and IFT for the system with piston, balancer shaft and camshaft without the valve train, at two different average speeds. Figure 7.13 is

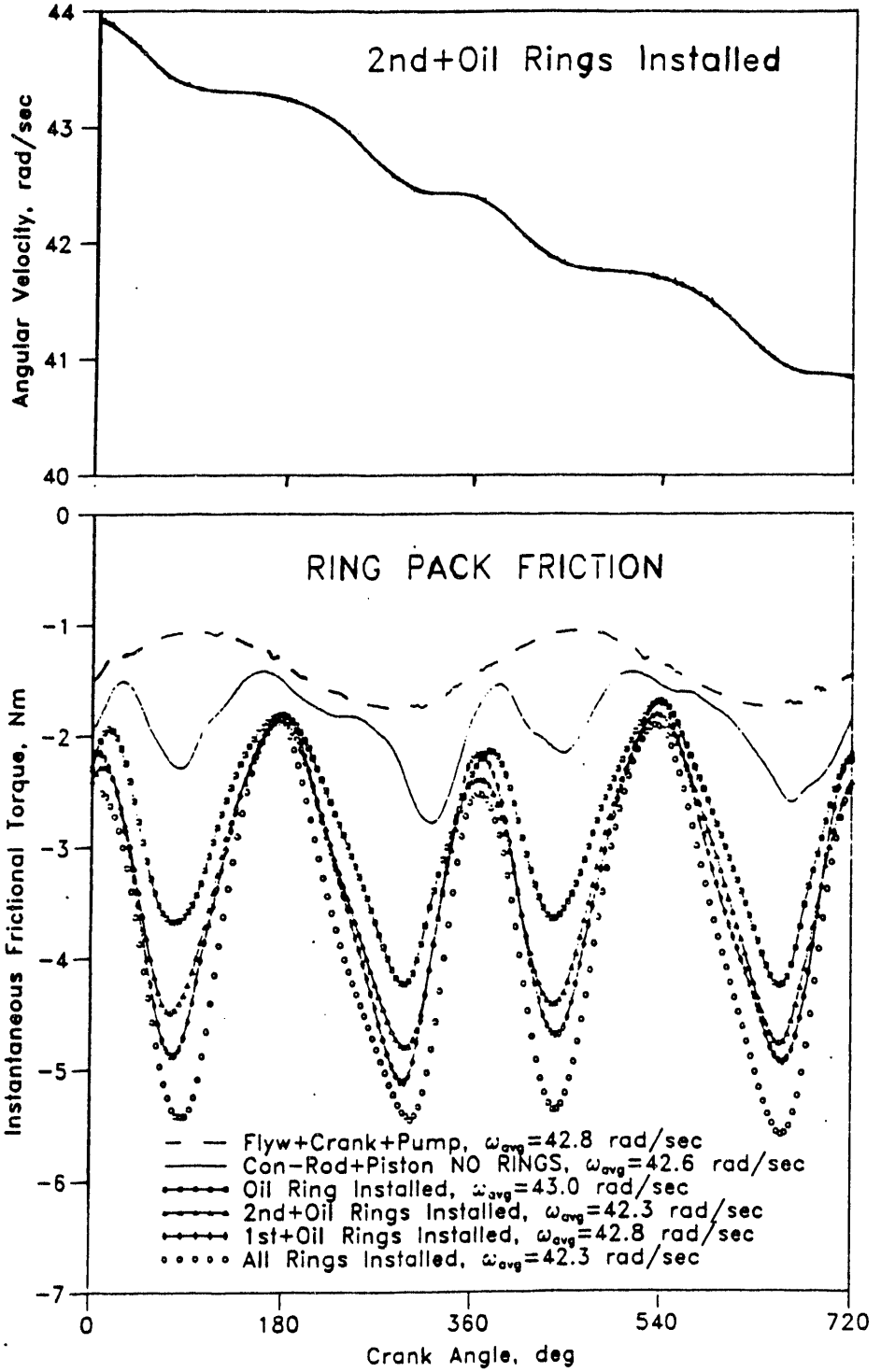

Figure 7.9. IFT due to different combustion of piston and ring at 42.5 rad/sec.

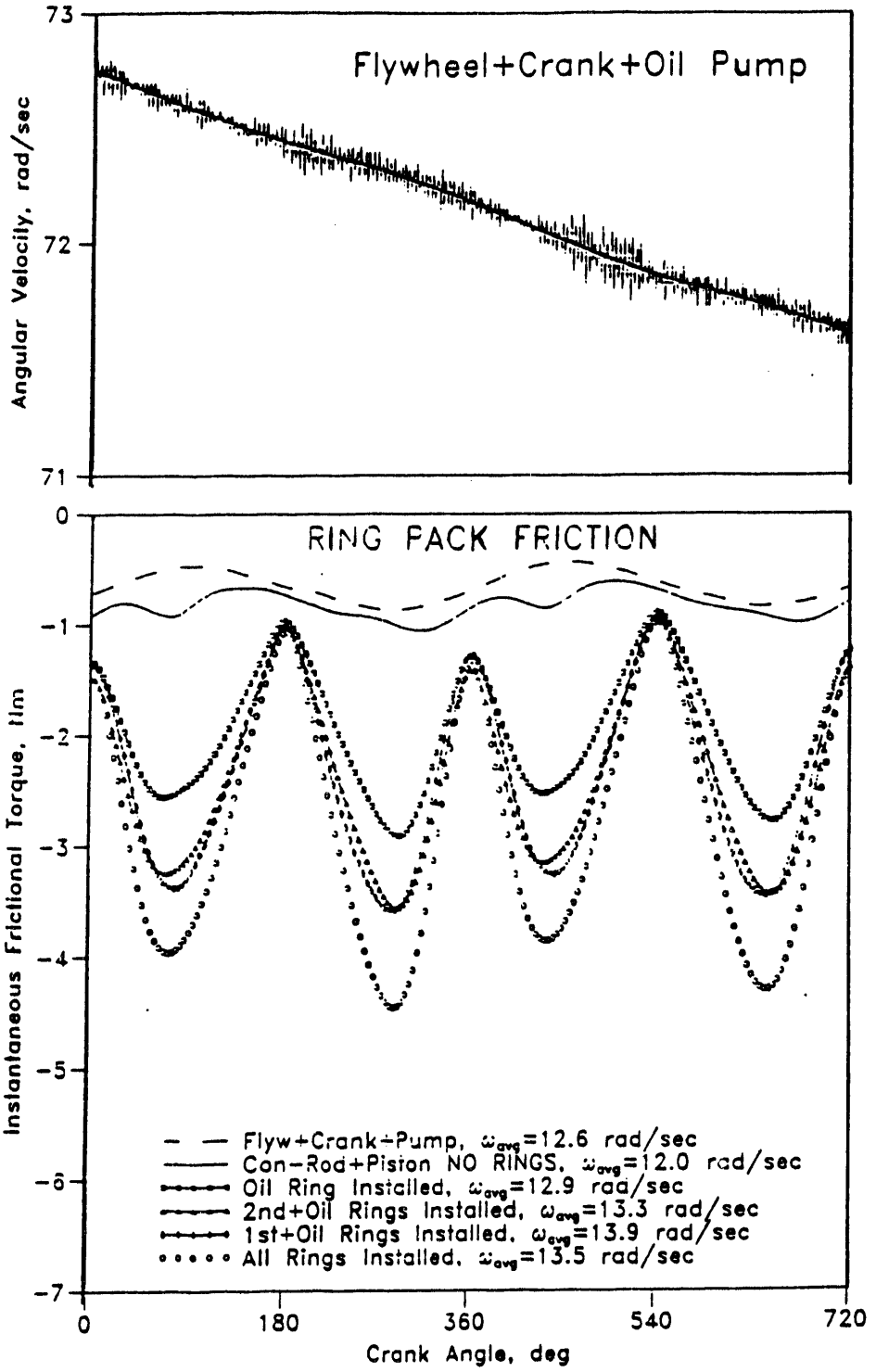

Figure 7.10. IFT due to different combustion of piston and rings at 13 rad/sec.

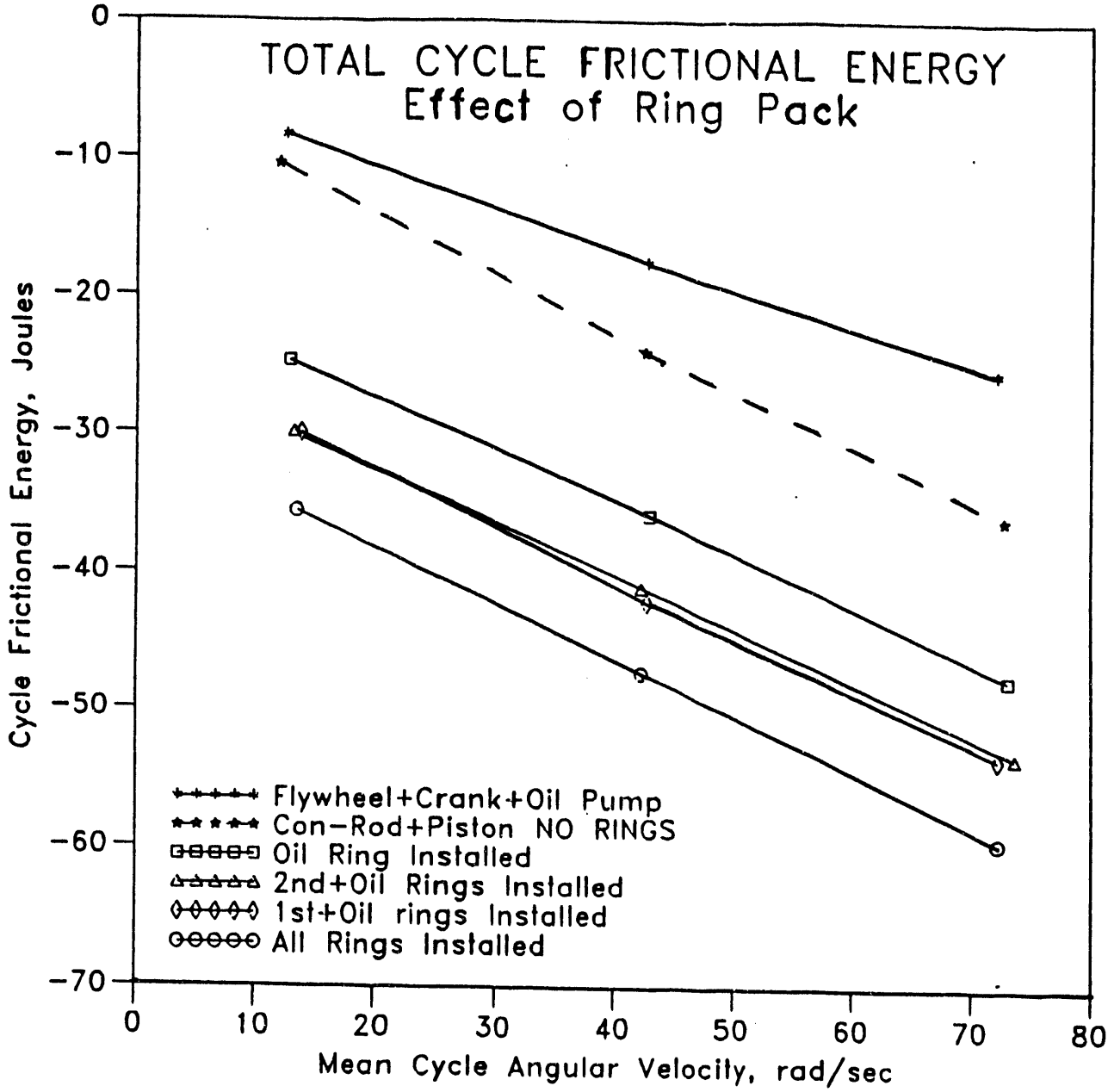

Figure 7.11. Effect of speed on energy lost in different components

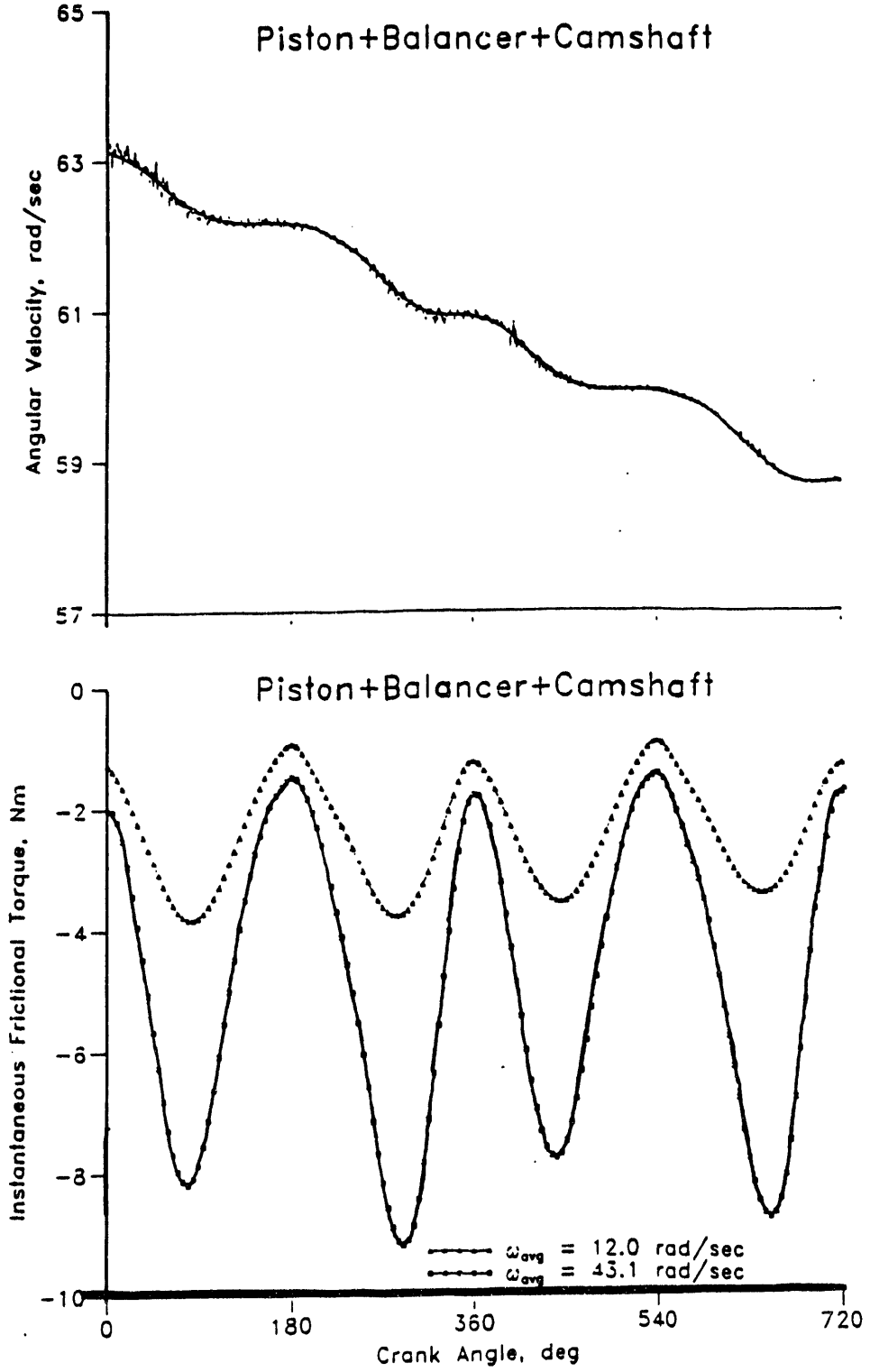

Figure 7.12. IFT for reciprocating parts, balancer shaft, without valves

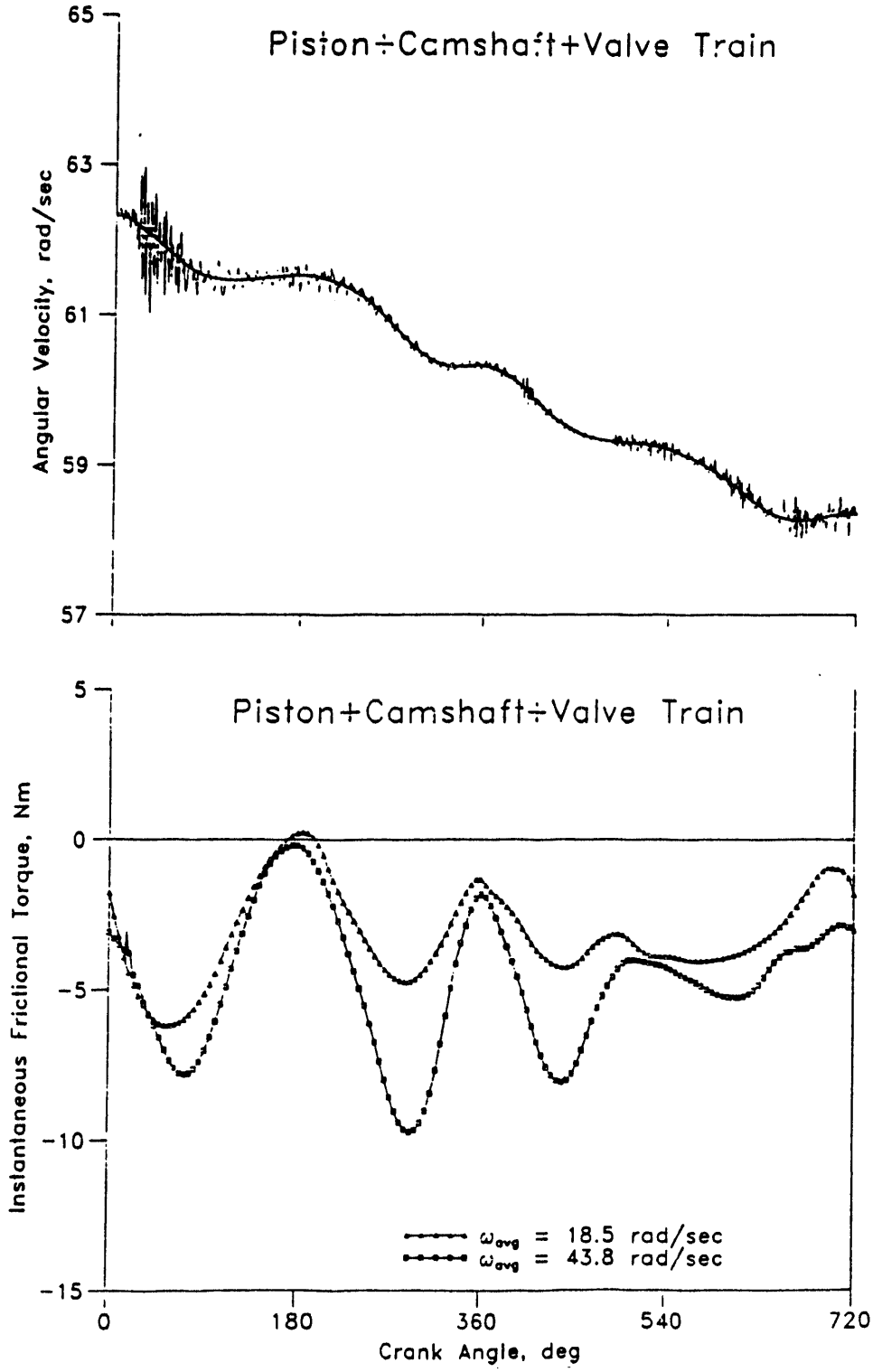

Figure 7.13. Effect of valve train on IFT

for the angular velocity and IFT when the valve train was added. The difference between the IFT in figures 7.12 and 7.13 shows the effect of adding the valves. When the two valves are closed, from 240° to 480°, the two figures show similar results. The contribution of the valves was investigated by using experimental data obtained from the torque meter installed on the camshaft.

Figure 7.14 shows the torque acting on the camshaft. It is clear that each of the two valves absorbs energy during its opening and releases part of it during its closing. The variation in the torque with speed is not very clear in the figure, but a close examination of the traces indicates that the torque decreased at the higher speeds. This finding agrees with the data reported by Whitehouse [24], Cleveland [25], Kovach [4], Armstrong et al. [29] and Staron et al. [30]. This indicates that the mode of lubrication of the valve train is elastohydrodynamic. At the low rotating speeds the release of the valve energy may result in positive net friction for the system as shown near BDC in figure 7.13 when the inlet valve closed.

7.3.7 EFFECT OF FUEL INJECTION PUMP

The effect of driving the fuel injection pump on IFT with and without fuel injection is shown in figure 7.15. The fuel injection process required a much higher torque than any of the valves. This is clear from the corresponding torque curves shown in figure 7.16. Figure 7.16 shows that the injection pump did not release any energy to the engine during the plunger return, as reported by reference [31]. The energy lost in friction and the contribution of the fuel injection pump are shown in figure 7.17.

It should be noted that the above results were obtained during a coast-down mode without compression and combustion. In an actual engine the frictional losses of some components are different from the present results due to the gas pressure in the cylinder. These

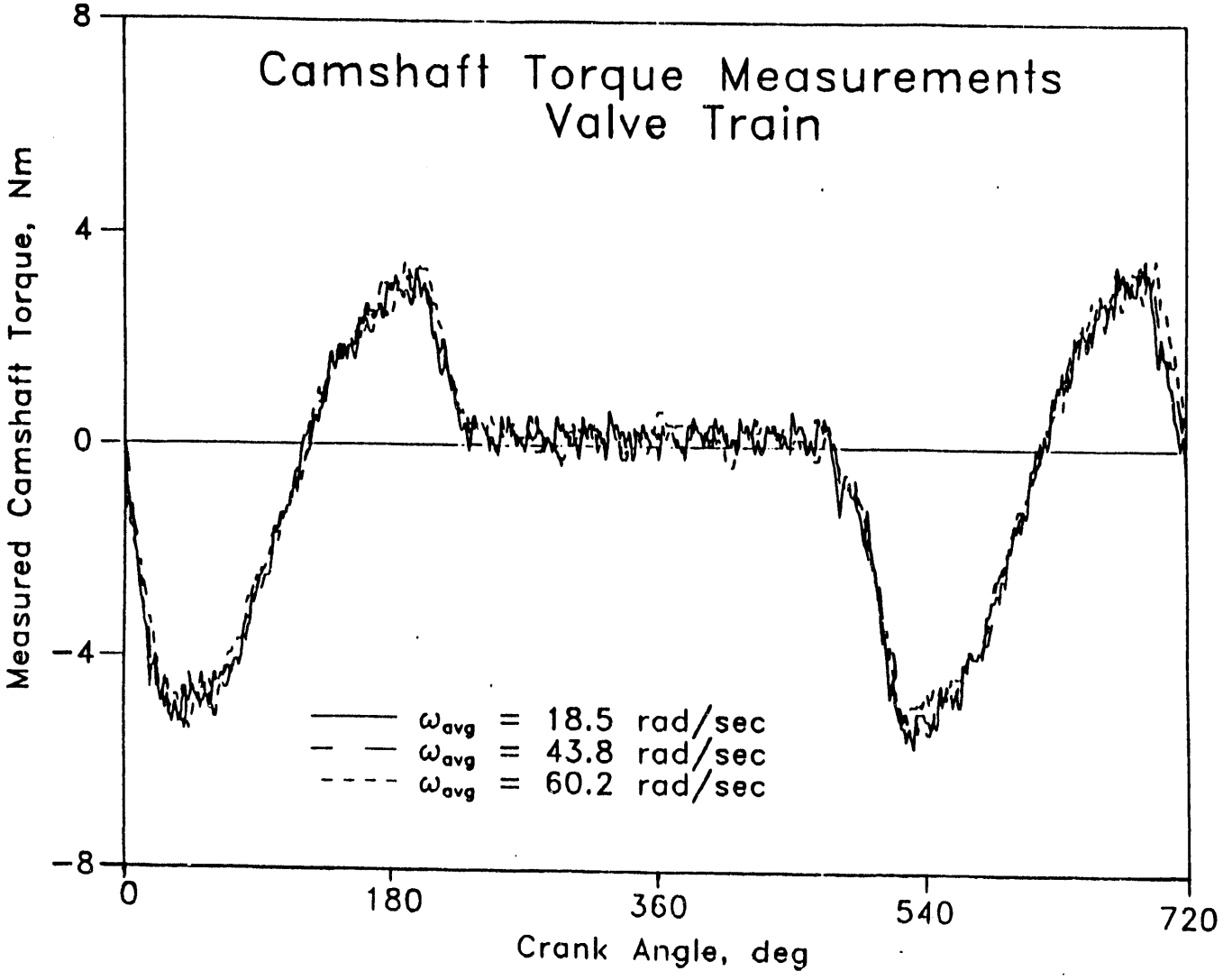

Figure 7.14. Torque on cam shaft with valve train

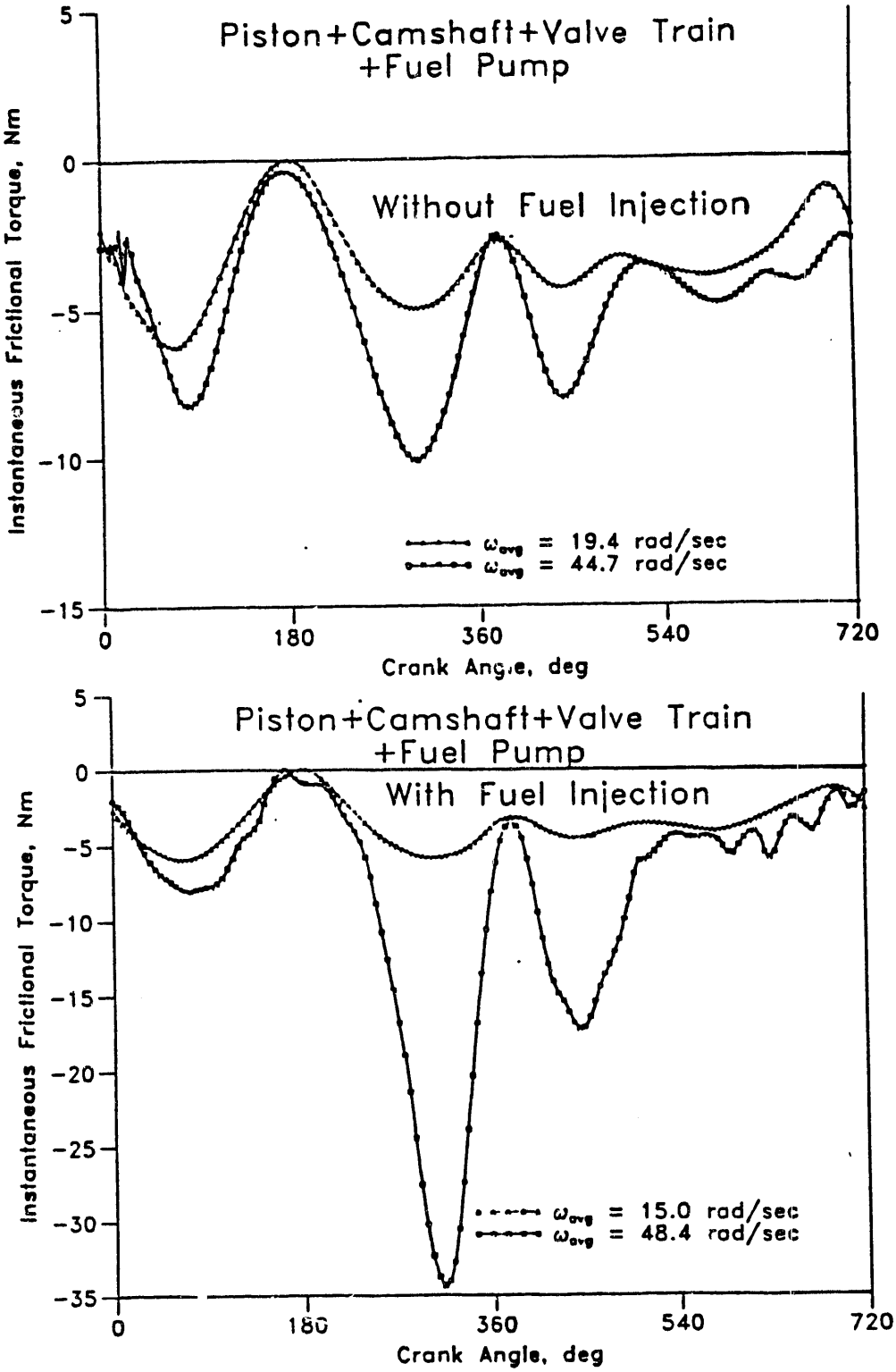

Figure 7.15. Effect of fuel injection on torque on cam shaft

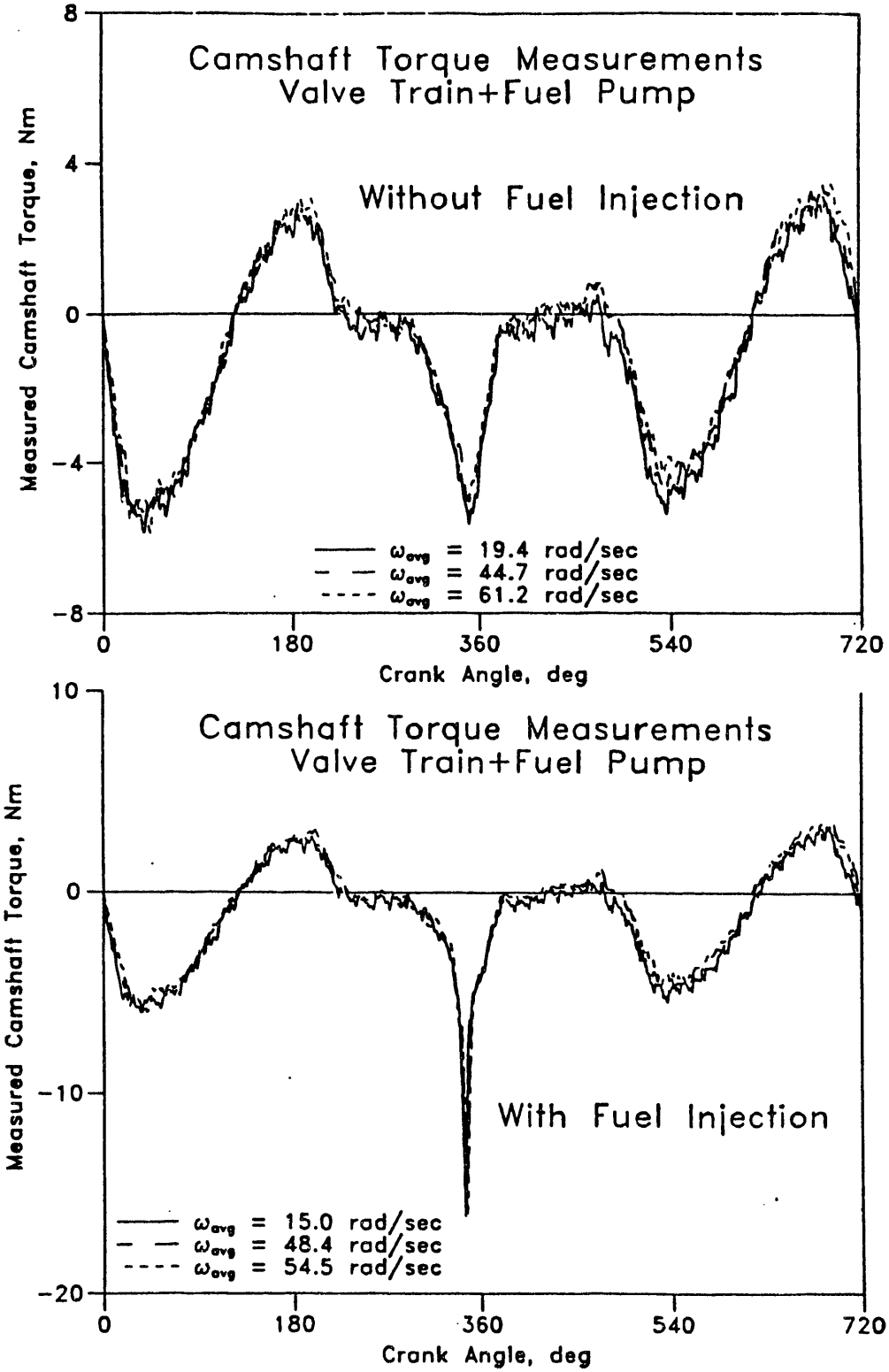

Figure 7.16. Effect of fuel injection on torque on cam shaft

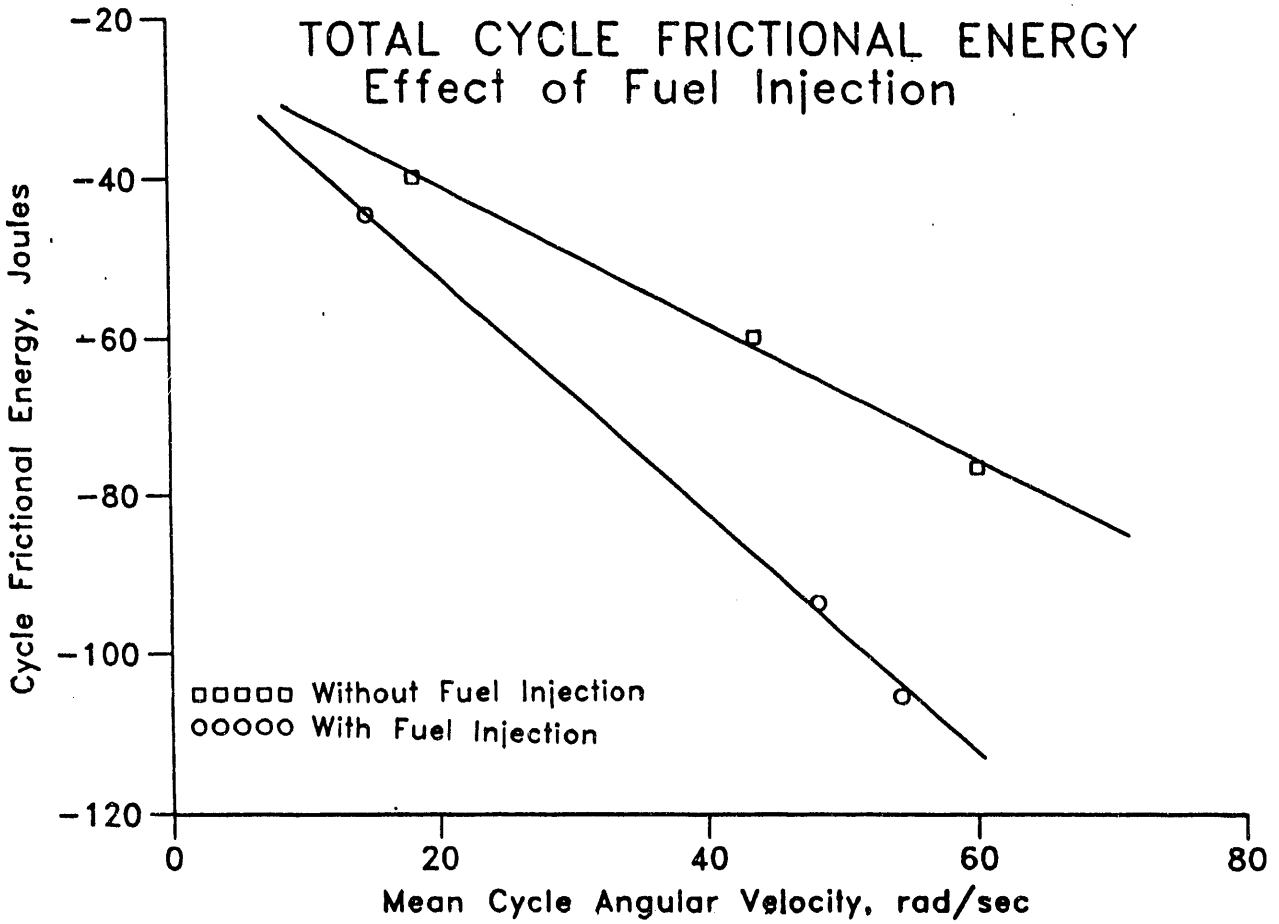

Figure 7.17. Effect of speed on energy lost in friction with and without fuel injection

components are the piston assembly and main bearings during compression and expansion. The valve train friction in an actual engine will be slightly different from the present results because of the difference between the actual cylinder gas pressure and the atmospheric pressure used in this investigation. The actual frictional loses in the fuel pump should be close to the results of the present investigations, except for the effect of temperature on the injection process. The difference between the oil temperature in an actual engine and the present investigation is another factor which affects the frictional loses.

7.4 SUMMARY

The following are the results obtained in this investigation for the frictional torque on different components of a single cylinder diesel engine. The components were added one at a time to the basic crankshaft / lubricating oil pump system. The instantaneous friction was determined during a coast-down mode, after the crankshaft was accelerated to about 900 rpm with an electric starter.

1. The instantaneous frictional torque on each component can be determined by using the same method known as (P-ω) method developed earlier for the whole engine as a system.

2. The piston-ring assembly is the largest contributor in the total frictional losses, even under the atmospheric conditions of the present experiments.

3. The valve train frictional torque decreased at higher speeds.

4. Torque measurements on the camshaft indicated that the valve springs release some energy to the engine during valve closing.

5. The fuel injection pump required a much higher torque than any of the valves, and did not release any energy back to the engine.

CHAPTER 8: EFFECT OF COATING RINGS ON PISTON ASSEMBLY FRICTION

8.1 BACKGROUND

The results discussed in previous chapters indicate that the majority of the engine frictional losses occur near top dead center during the last part of the compression stroke, after the start of combustion, and during the expansion stroke before the exhaust valve opens. The two major engine components which contribute in the sharp rise in frictional losses near top dead center are the piston assembly and the main bearings. Many efforts have been made to reduce the frictional losses produced by the piston assembly. Coating of piston rings is one of the approaches which are seriously considered to reduce piston assembly friction. The ring coating, for this investigation, has been made at Argonne National Laboratory.

The engine used is the Deutz Diesel, air cooled, four stroke engine. A comparison has been made between 4 sets of rings.

Two types of tests are made:

1- Without cylinder head

2- With cylinder head and combustion

8.2 TESTS WITHOUT THE CYLINDER HEAD

8.2.1 EXPERIMENTAL SETUP AND PROCEDURE

The tests were conducted without the cylinder head, the camshaft and balancing shaft. Under these conditions the friction was mainly due to the piston-ring assembly and the main bearings.

The forces acting on the piston-crank mechanism were due to the following:

i- difference between the atmospheric pressure acting on top of the piston, and the crankcase pressure acting on the lower side of the piston

ii- the inertia forces of the moving parts

iii- the frictional forces

The pressure in the crankcase was measured by a pressure transducer type AVL QC41B-X. The engine was accelerated by the electric starter to the maximum possible speed and then allowed to decelerate till it stopped. A battery charger was attached to the battery all the time to ensure the full charge of the battery.

The following signals were recorded.

1) crankcase pressure
2) oil sump temperature
3) crank angle degrees signal
4) TDC signal

The following five ring sets were tested.

1) An old set of rings which had been used for at least 100 engine hours
2) A new set of rings
3) A new set of coated rings, type 900 613
4) A new set of coated rings, type 900 614
5) A new set of improved coated rings

8.2.2 RESULTS AND DISCUSSIONS OF TESTS ON THE FIRST FOUR SETS OF RINGS

The engine was accelerated by the electric starter to the maximum possible speed and then allowed to decelerate till it stopped. Figure 8.1 shows a sample trace for the instantaneous angular velocity of the crankshaft as a function of cycle number. Counting of the cycles started at the moment the starter switch was turned on. Each cycle contains 720 points. It can be noticed from this figure that the starter was disengaged during cycle number 41. Thereafter, the engine decelerated until it stopped during cycle number 65.

To compare between the different sets of rings, the oil sump temperature was held as constant as possible to maintain the same running conditions for all rings. During the experiment it was noticed that coating from the top ring was peeling off probably due to the chromium-electroplated surface. To avoid accounting for the effect of peeling of the coatings of the top ring in sets 900613, and 900614, the early runs, when the coating was intact, were chosen. Figure 8.2 shows such a comparison between the cycle averaged IFT of the different rings. The following is noticed:

1- In general the coated-ring sets produced less friction than the new-ring set. The drop in friction for ring set No. 900613 ranged from 16% at 16 rad/sec, to 5% at 76 rad/sec.

2- The coated-ring set No. 900614 reduced the friction losses by 10% at 16 rad/sec and 3% at 76 rad/sec.

The old set behaved differently. Although it had the lowest friction at low speeds, it had the highest friction at high speeds. The behaviour of the old set can be attributed to the fact that it has a different design than the others. Figure 8.3 shows cross-sectional views of the new and old sets of rings.

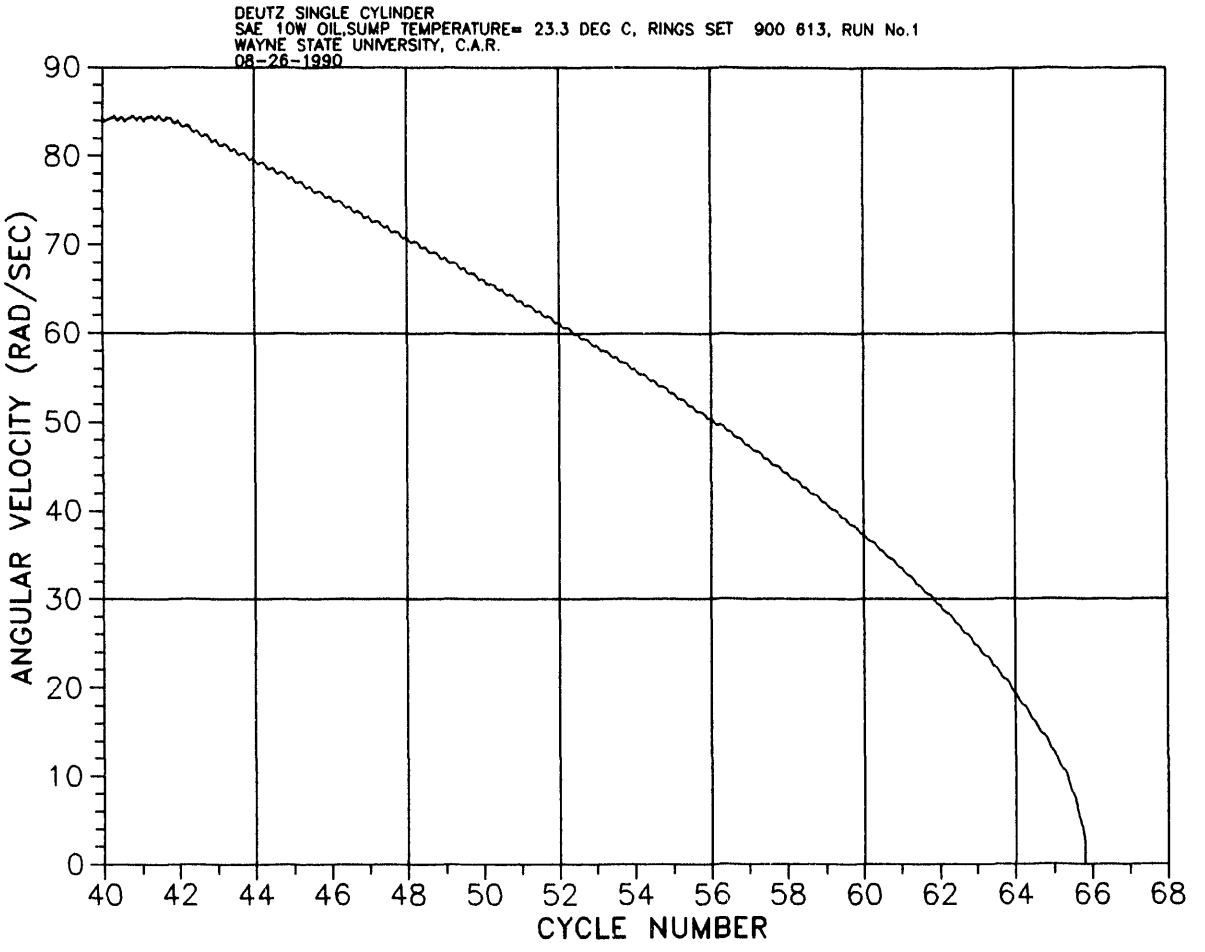

Figure 8.1. Angular velocity versus cycle number during engine deceleration

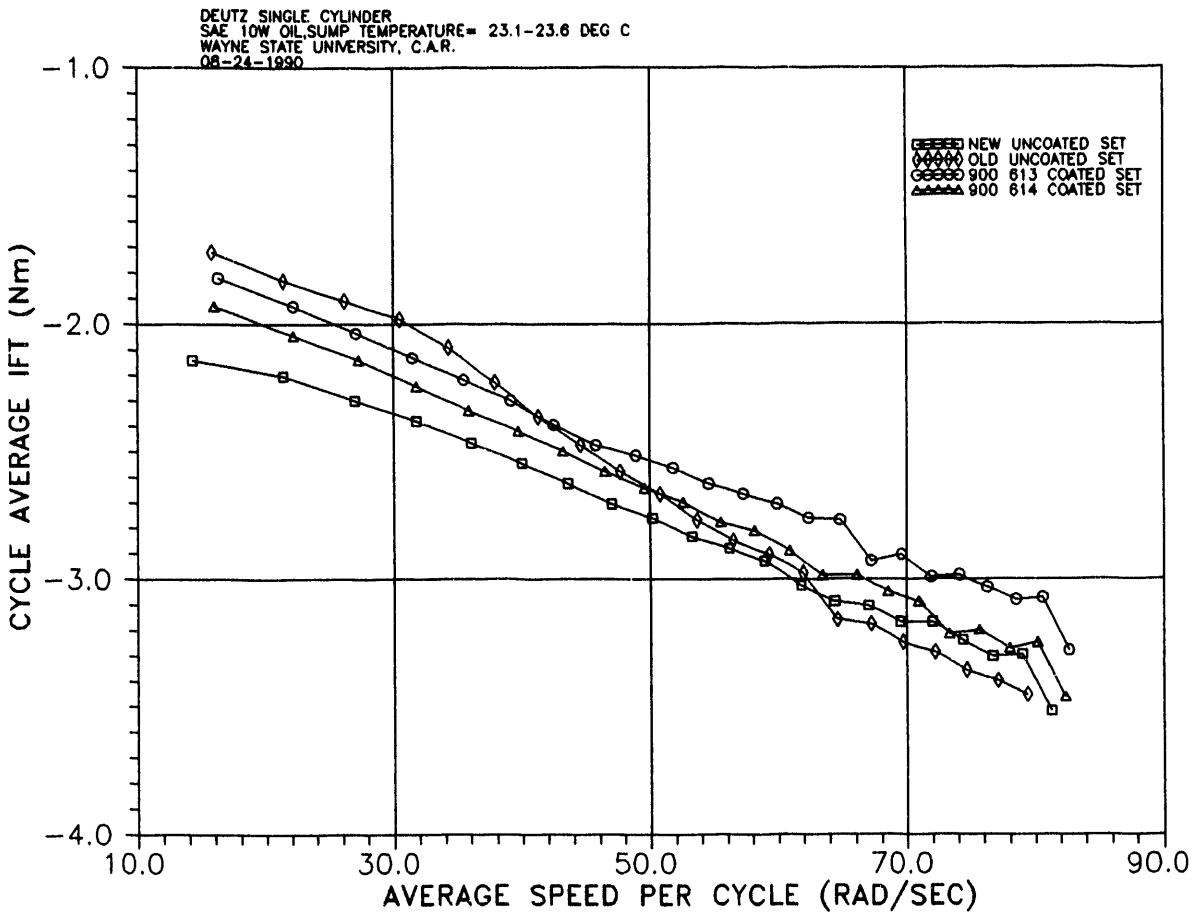

Figure 8.2. Comparison between the different types of ring sets

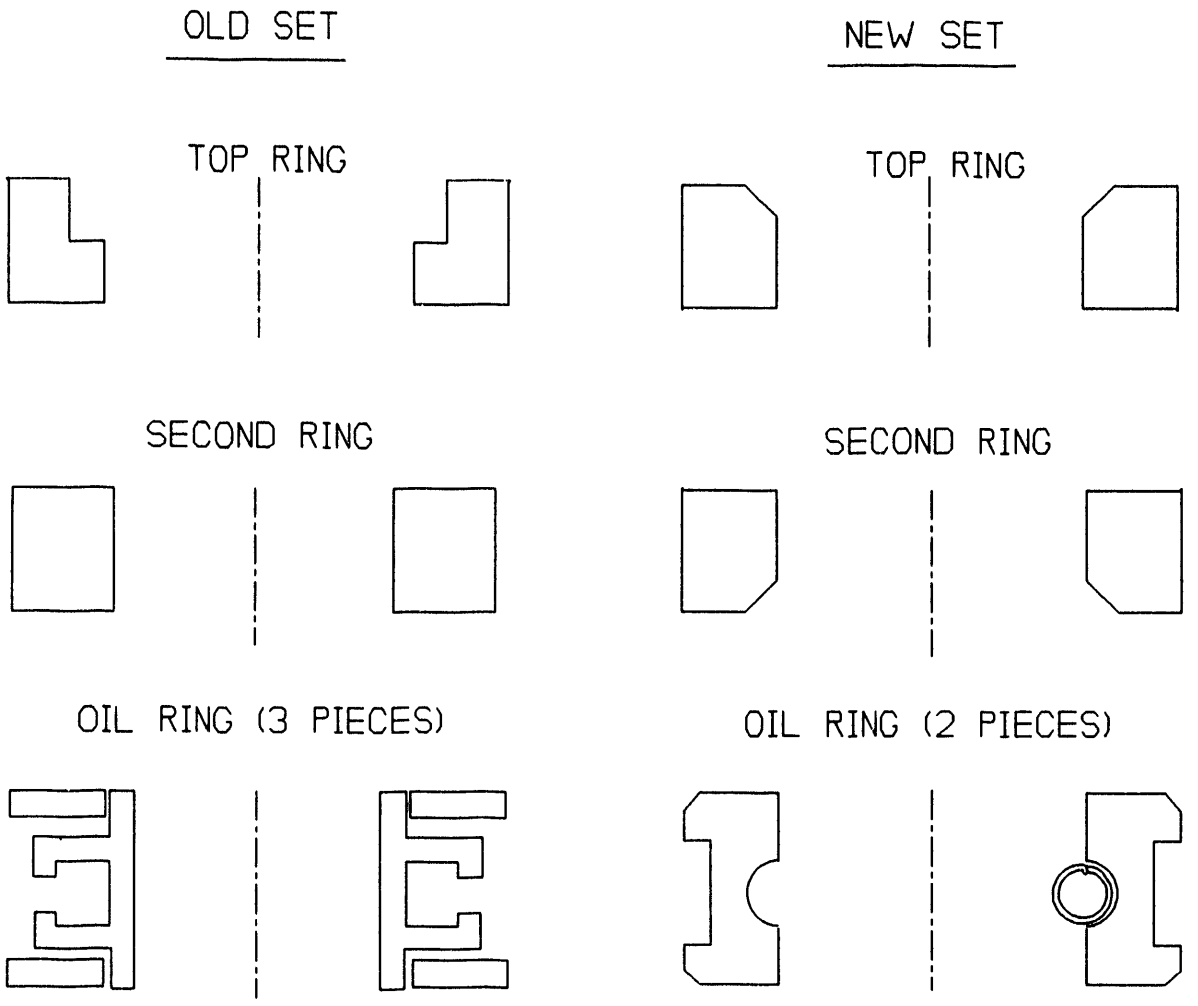

Figure 8.3. Cross section of the old and new sets of rings

8.2.3 SUMMARY OF TEST RESULTS FOR THE FIRST FOUR SETS OF RINGS

1- Coating the new ring-set reduced the frictional losses by up to 16% at 16 rad/sec and 5% at 76 rad/sec.

2- Different coatings reduced the friction by different degrees.

3- The coating peeled after the first few runs of the chrome-plated top compression ring.

8.2.4 RESULTS AND DISCUSSIONS OF TESTS ON THE IMPROVED SET OF COATED RINGS

Piston rings with improved coating were tested again on the same engine setup. For this set the pressure in the crankcase was measured by a low range pressure transducer KISTLER Model 206 PIZOTRON® instead of AVL QC41B-X which was used in the previous sets. The low range pressure transducer gave more accurate results. Figure 8.4 shows a comparison between the friction results of the new coated set of rings, new uncoated set of rings and the piston without rings.

The piston without rings produced the lowest cycle averaged IFT, followed by the coated rings. The uncoated set of rings resulted in more frictional losses.

8.3 TESTS WITH THE CYLINDER HEAD AND COMBUSTION

Coated piston rings were tested under normal fired engine operating conditions. Measurements of the frictional force on the piston-rings assembly was made by using an instrumented connecting rod. The details of the instrumentation and necessary engine modifications were described in chapter 3.

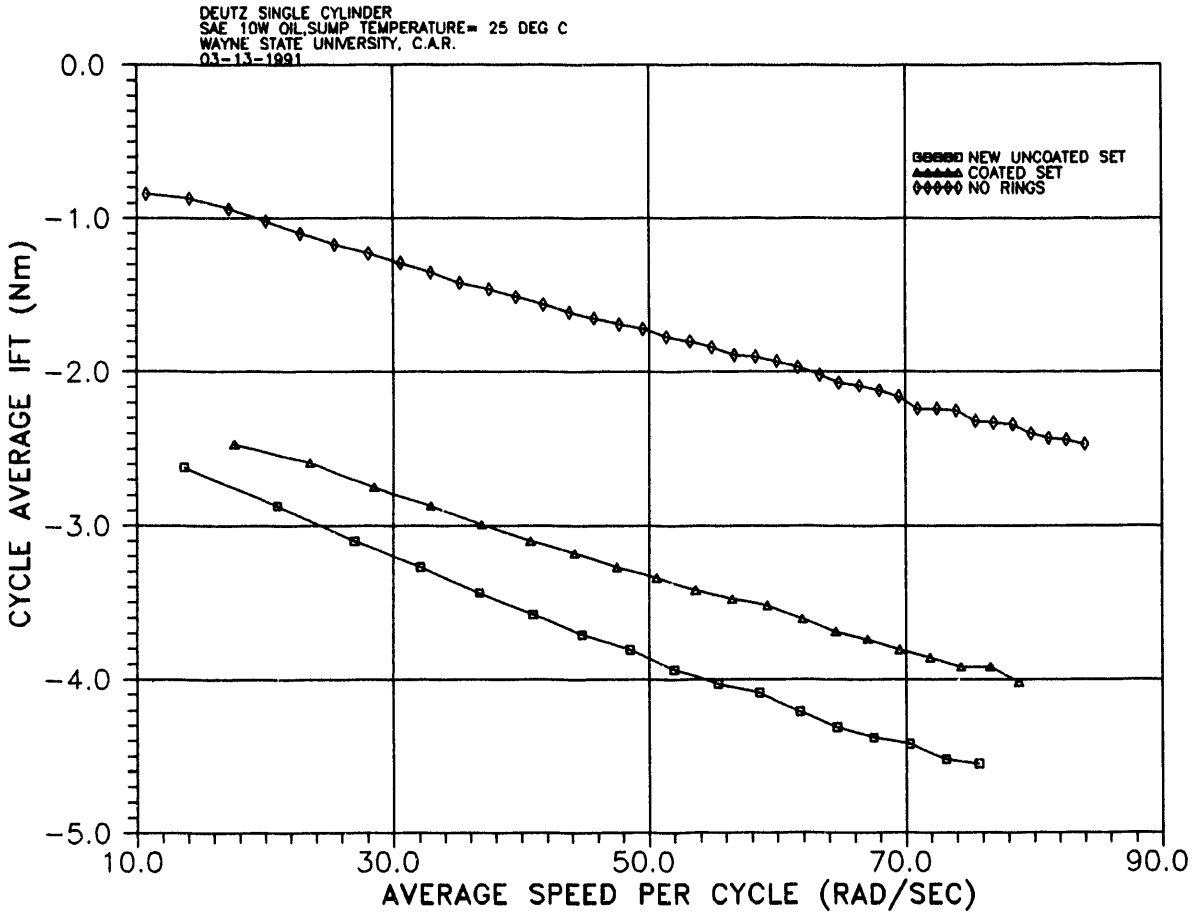

Figure 8.4. Comparison between the different types of ring sets

Calculation of friction force between the piston assembly and the cylinder liner requires simultaneous measurements of:

1- connecting rod force
2- cylinder pressure
3- crankcase pressure
4- crankshaft position, angular velocity and acceleration

The signal from the strain gage was analyzed and the corresponding connecting rod force was calculated. Figure 8.5 shows a sample of the strain gage signal converted into connecting rod force.

Piston-rings assembly friction is calculated by using data of the connecting rod force, the traces for the pressure, the load and angular velocity. Figure 8.6 shows a sample of the piston assembly friction corresponding to the trace of the figure 8.5.

Two sets of piston rings were tested at different operating conditions: coated rings and a new uncoated set. Table 8.1 shows a summary of the results of 10 different runs. For comparison purposes between coated and uncoated rings, runs with similar operating conditions of speed and oil sump temperature were chosen. All runs were at no load condition.

Figure 8.7 shows piston-rings assembly frictional force for uncoated rings and figure 8.8 for coated rings, at 563 RPM and 40.5°C sump oil temperature. Figure 8.9 and 8.10 are for 987 rpm and 42.8 deg C.

Columns A, B and C of table 8.1 show that the ring coating resulted in a reduction in the instantaneous frictional torque of the whole engine, averaged over the whole cycle, of 1.15% to 17.28%. The corresponding reduction in the piston assembly friction was 14.42% and 7.8% respectively. Column D shows that the increase in the sump oil temperature from 34.4 deg C to 45 deg C

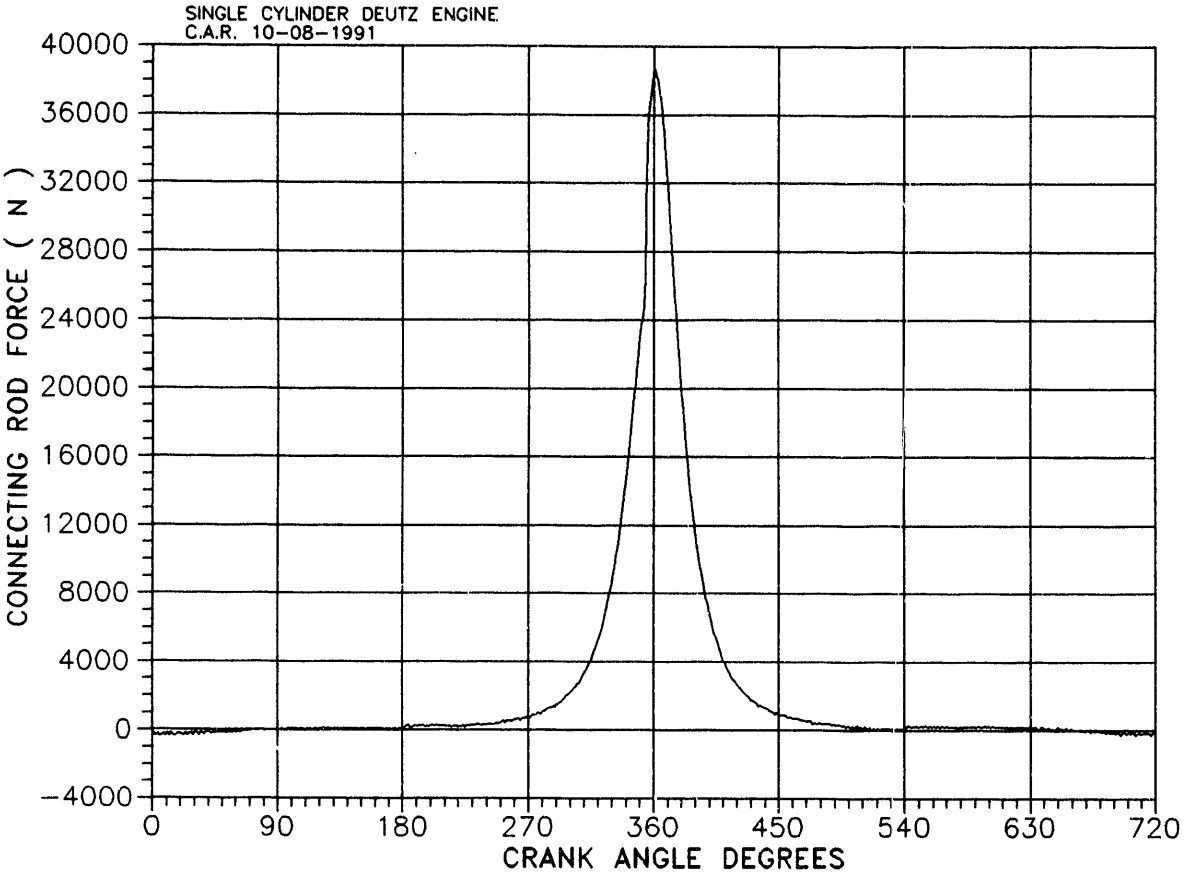

Figure 8.5. Sample of connecting rod force trace

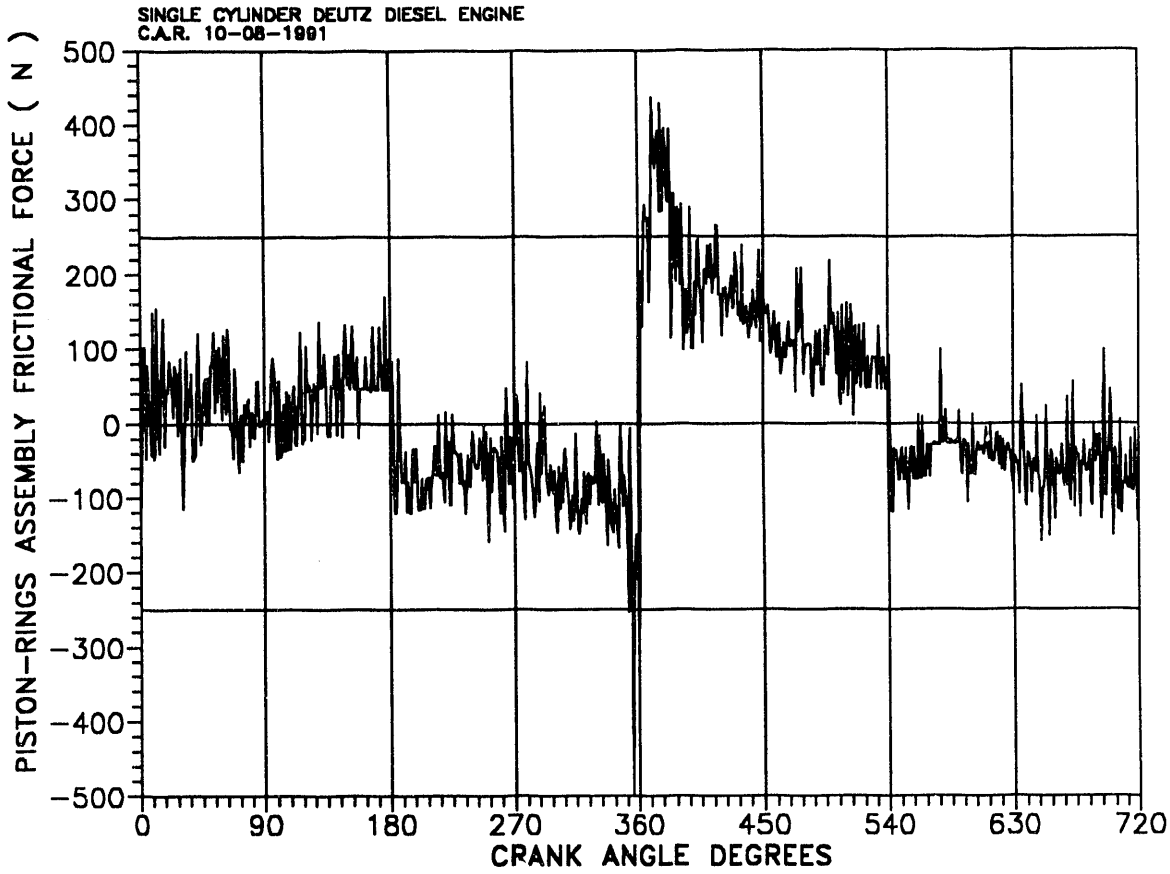

Figure 8.6. Sample of piston-rings assembly frictional force

Table 8.1*
Effect of piston Ring Coating on Friction Deutz Engine

	A		B		C	
	1a	2a	1b	2b	1c	2c
Piston Ring Type	Not Coated	Coated	Not Coated	Coated	Not Coated	Not Coated
Oil Sump Temperature, (°C)	31.1	31.1	40.5	40.5	42.8	42.8
RPM	532	532	563	563	987	987
Cycle Integral of IFT, (Nm Rad)	-86.6	-85.6	-95.5	-79.0	- 90.9	-79.7
Cycle Averaged IFT, (Nm)	-6.89	-6.81	-7.60	-6.29	-7.23	-6.34
Integral of Piston-Ring Frictional Force,(N Rad)	1047	896	1193	1100	1293	1257
Average of Piston-Ring Frictional Force, (N)	83.32	71.30	94.94	87.54	102.89	100.03
% Change in Cycle Averaged IFT	-1.15		-17.28		-12.32	
% Change in Piston-Ring Friction	-14.42		-7.8		-2.78	

* Continued on next page

Table 8.1 (continued)
Effect of piston Ring Coating on Friction Deutz Engine

	D		E	
	1d	2d	1e	2e
Piston Ring Type	Coated	Coated	Coated	Coated
Oil Sump Temperature, (°C)	34.4	45.0	29.4	29.4
RPM	980	980	703	1411
Cycle Integral of IFT, (Nm Rad)	-93.7	-78.0	-95.2	-116
Cycle Averaged IFT, (Nm)	-7.46	-6.21	-7.58	-9.23
Integral of Piston- Ring Frictional Force,(N Rad)	1228	1284	1145	1341
Average of Piston-Ring Frictional Force, (N)	97.72	102.18	91.12	106.71
% Change in Cycle Averaged IFT	-16.76		+21.85	
% Change in Piston- Ring Friction	+4.56		+17.12	

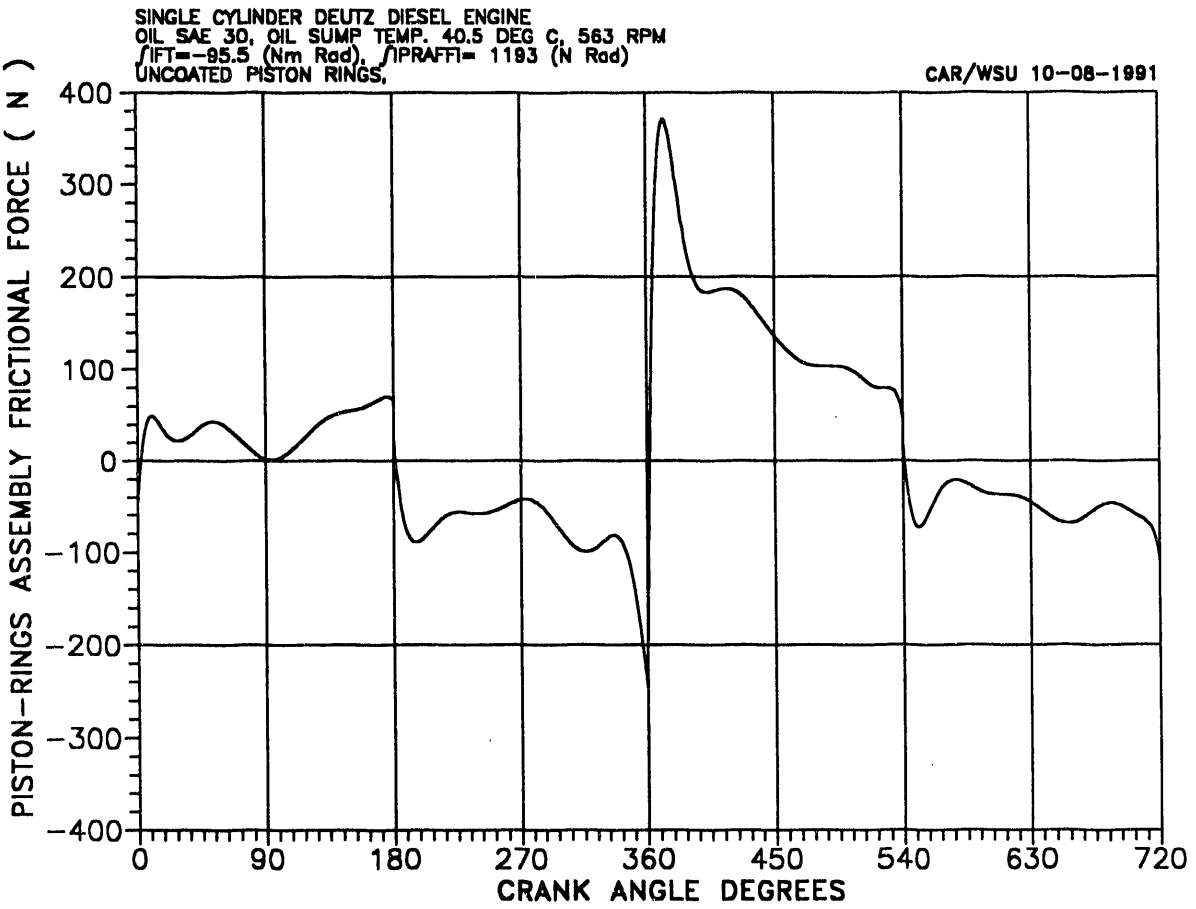

Figure 8.7. Piston-rings assembly frictional force for uncoated set of rings at 563 RPM

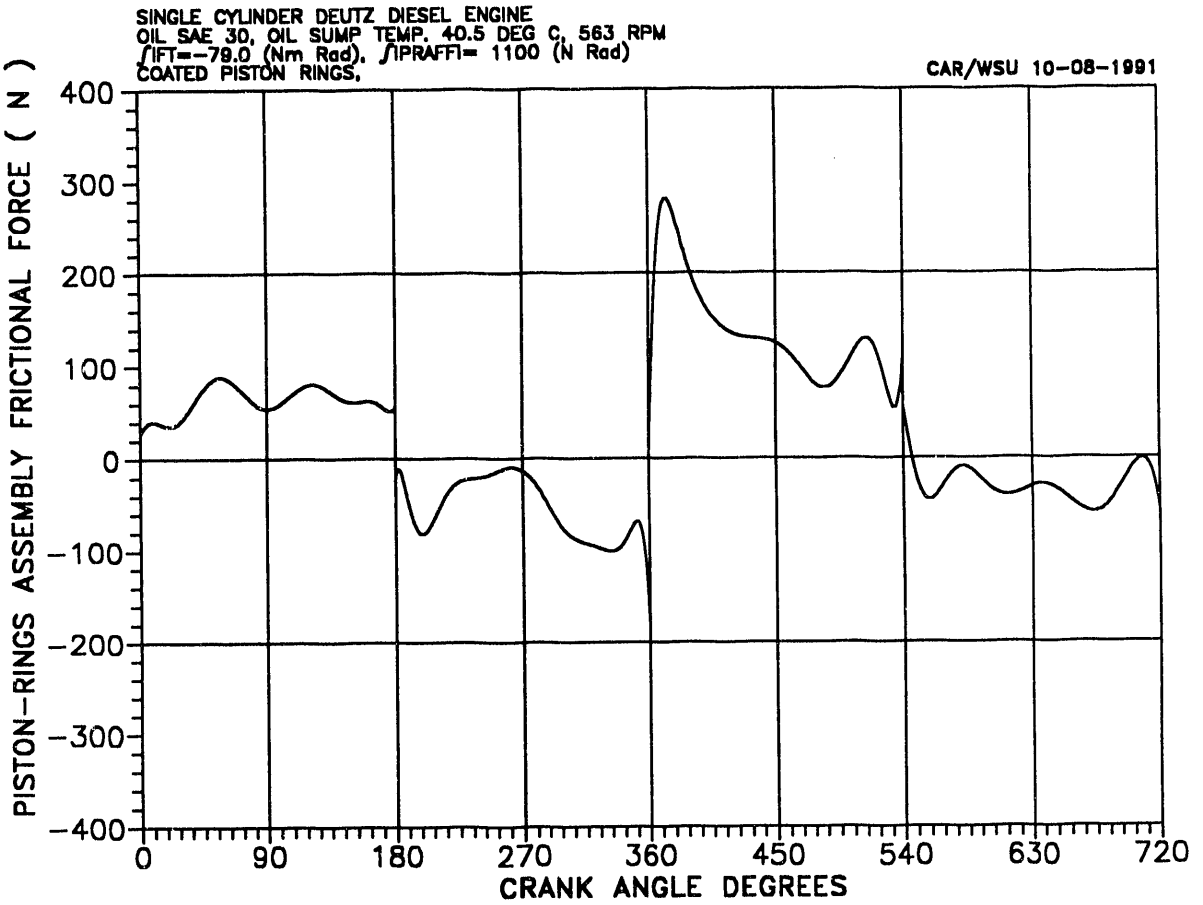

Figure 8.8. Piston-rings assembly frictional force for coated set of rings at 563 RPM

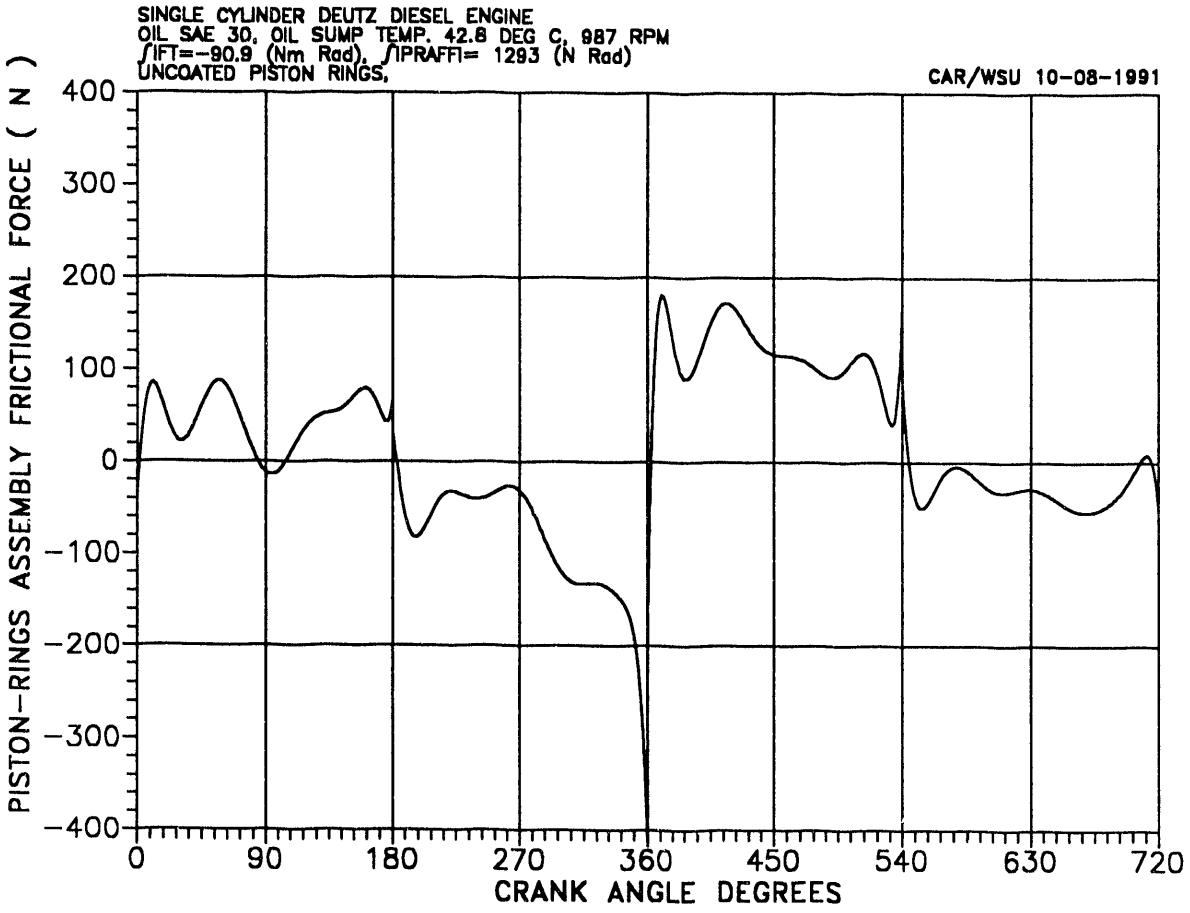

Figure 8.9. Piston-rings assembly frictional force for uncoated set of rings at 987 RPM

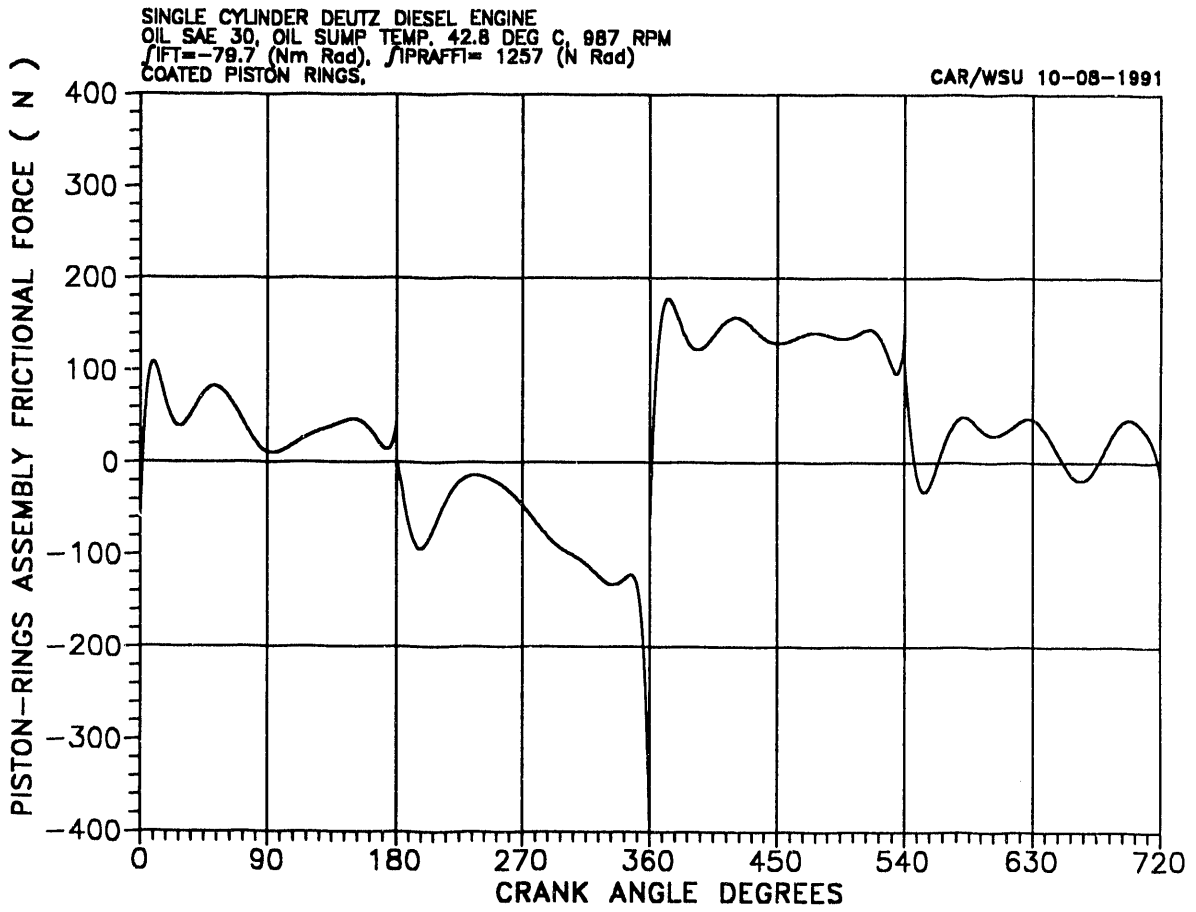

Figure 8.10. Piston-rings assembly frictional force for coated set of rings at 987 RPM

resulted in a drop in the cycle averaged torque of 16.76%, but an increase of 4.56% in the piston assembly friction. This increase needs to be investigated, and may be explained in terms of the drop in oil viscosity while the lubrication was in the mixed regime on the Streibeck's diagram. Column E showed that the increase in speed from 703 RPM to 1411 RPM resulted in an increase of 21.85% in the cycle averaged friction and 17.12% in the piston assembly friction.

Figures 8.11 and 8.12 show accumulated piston-rings assembly frictional force for two types of ring sets at 563 RPM and a sump oil temperature of 40.5 deg C.

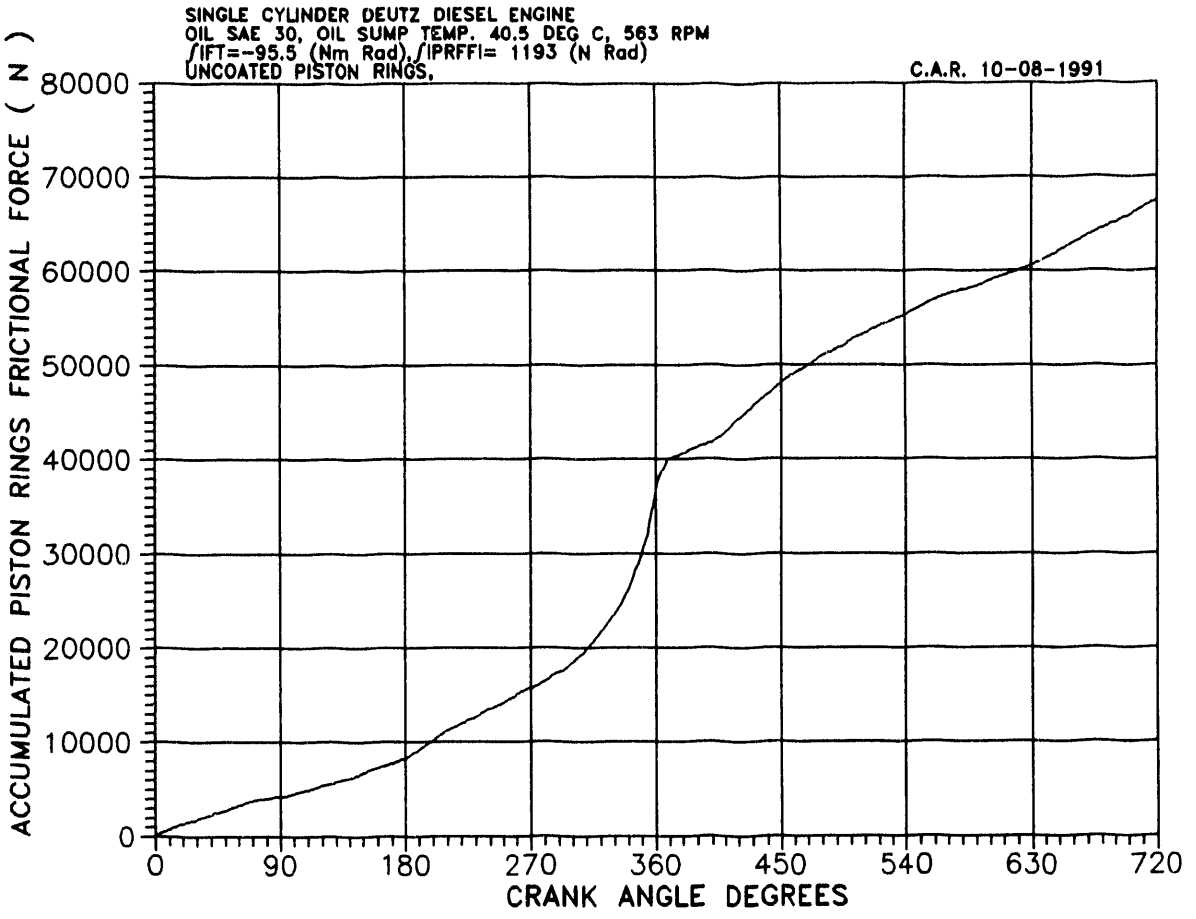

Figure 8.11. Accumulated piston-rings assembly frictional force for uncoated set of rings

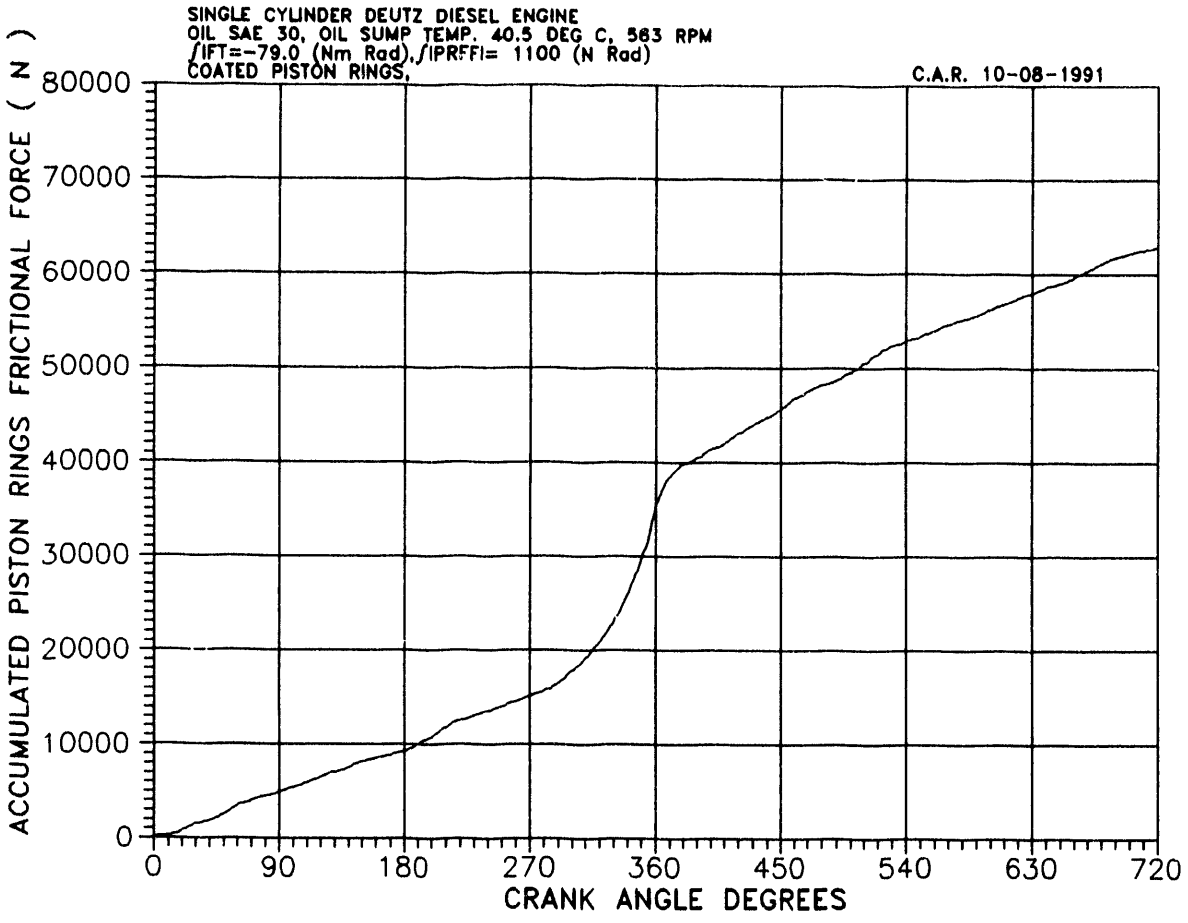

Figure 8.12. Accumulated piston-rings assembly frictional force for coated piston rings

CHAPTER 9: COMPARISON BETWEEN IFT OF DIESEL AND GASOLINE ENGINES

9.1 BACKGROUND

There are differences between the cylinder gas pressures in diesel engines and gasoline engines. In diesel engines the compression pressures are much higher than those in gasoline engines because of the higher compression ratios used in the diesel engines. Also, the rates of pressure rise and the peak pressure in diesel engines are higher than in gasoline engines.

Since the frictional losses are directly related to the cylinder gas pressure, one would expect some differences between the two engines in this respect.

The goal of this chapter is to give the results of the instantaneous frictional torque determined for the Honda single cylinder gasoline engine and compare it with the Deutz single cylinder diesel engine. The specifications of the engines are given in Chapter 3.

9.2 EXPERIMENTAL RESULTS

The IFT is affected by the net gas force acting on the piston, the angularity of the crank, the inertia of the reciprocating parts and coefficient of friction, which depends on the lubrication regime. The net gas force is the result of the cylinder gas pressure acting on top of the piston and the crankcase gas pressure acting on the bottom of the piston. Figure 9.1 shows these two gas pressures at an engine speed of 1175 RPM. The cylinder gas pressure is lower than the crankcase pressure during the intake and the first part of the compression stroke. In diesel engines this difference in pressure is much smaller than that in gasoline engines because of the absence of the throttle valve. The peak

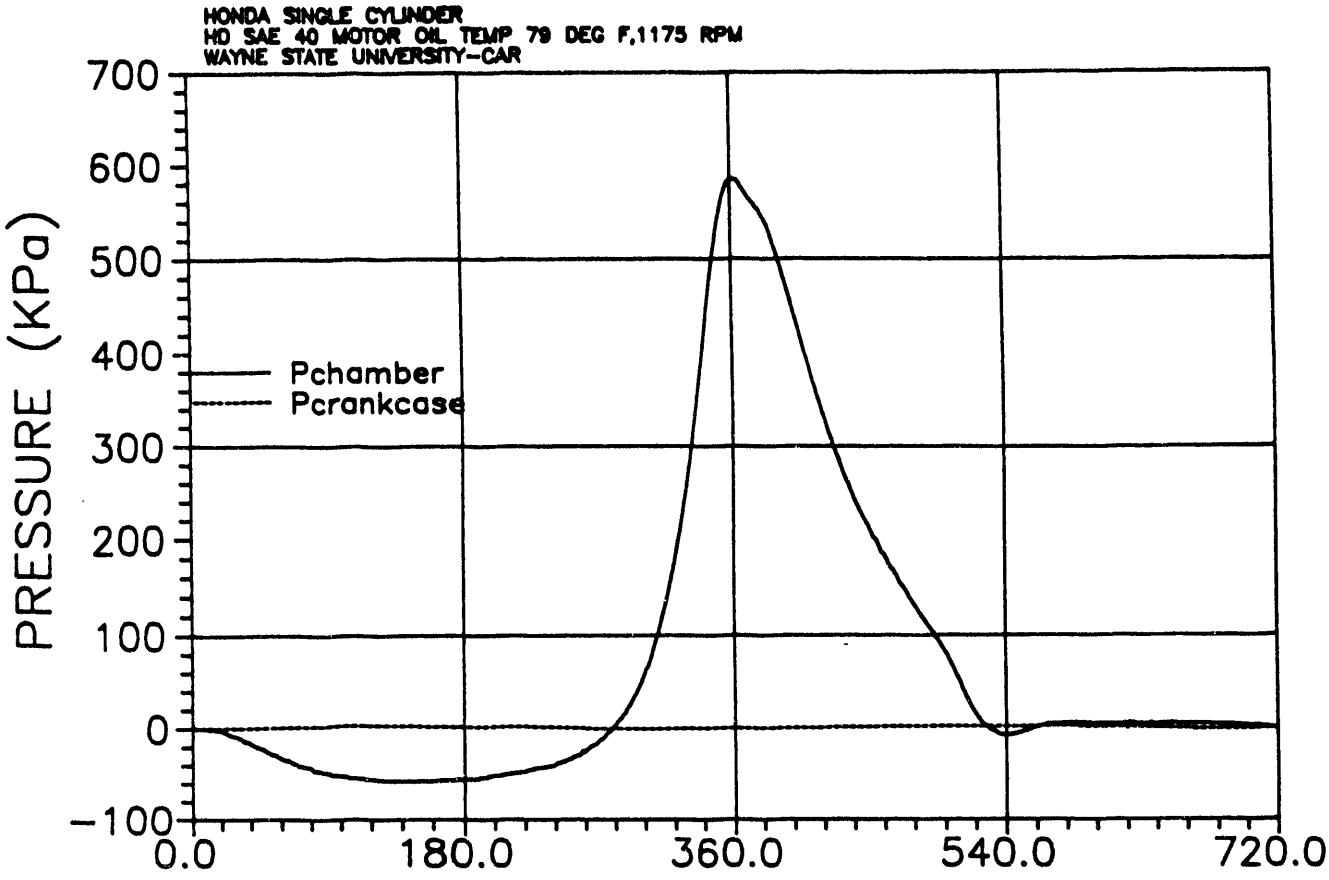

Figure 9.1. Pressure in combustion chamber and in crankcase

pressure reached in the cylinder is 0.580 MPa. This is much lower than the peak pressure reached in the diesel engine. Figure 4.1 shows that the peak cylinder gas pressure reached 5 MPa in the Deutz engine. This is about 8.6 times the peak pressure reached in the gasoline engine. Both engines were running at no load, and at approximately the same speed.

Figure 9.2 shows the different torques acting on the crankshaft. The net gas torque is negative during the intake stroke because the gas pressure in the crankcase is higher than that on top of the piston. The gas torque during the first portion of the compression stroke is positive because the net gas force is in the direction of motion. It becomes negative near the end of the compression stroke, and positive during the expansion stroke. The torque due to the inertia of the reciprocating parts fluctuates from positive to negative during each stroke. The torque due to the inertia of the rotating parts reaches a minimum during the later part of the compression stroke. It reaches a maximum during the expansion stroke. The load torque is not shown because the engine was under no load.

9.2.1 EFFECT OF SPEED

Figures 9.3 and 9.4 show the different torques acting on the crankshaft at 1770 RPM and 2665 RPM respectively. Figure 9.5 shows the angular velocity, cylinder gas pressure and IFT for the engine at 1175, 1770 and 2265 RPM. It is noticed that during the intake and compression strokes, where the contribution of the gas pressure is small, IFT reaches it highest value near the middle of the stroke where the piston reaches its maximum speed. This is an indication that lubrication is in the hydrodynamic regime. The IFT is highest during the expansion stroke and increases with speed.

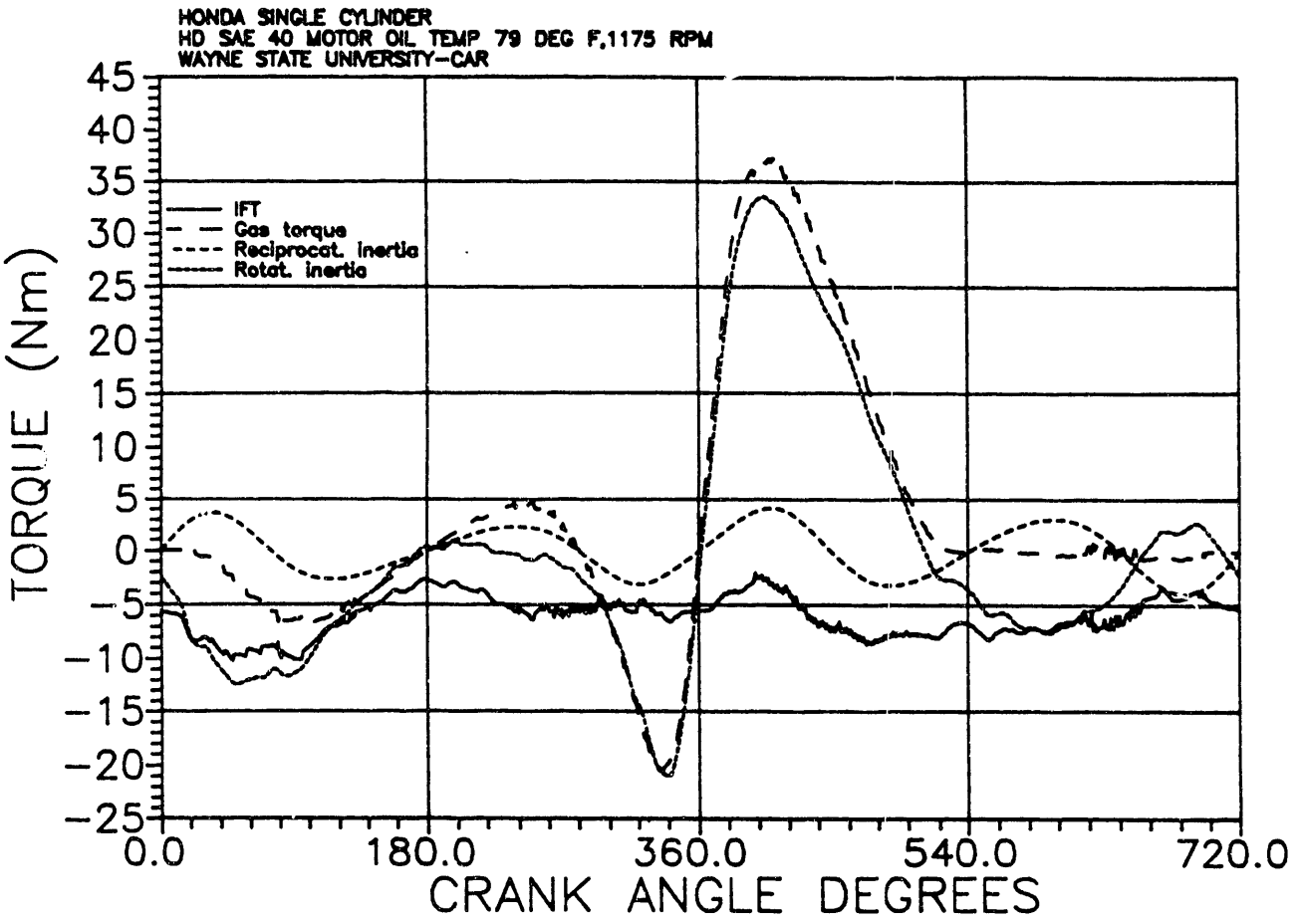

Figure 9.2. Gas torque, inertia torque and IFT versus crank angle

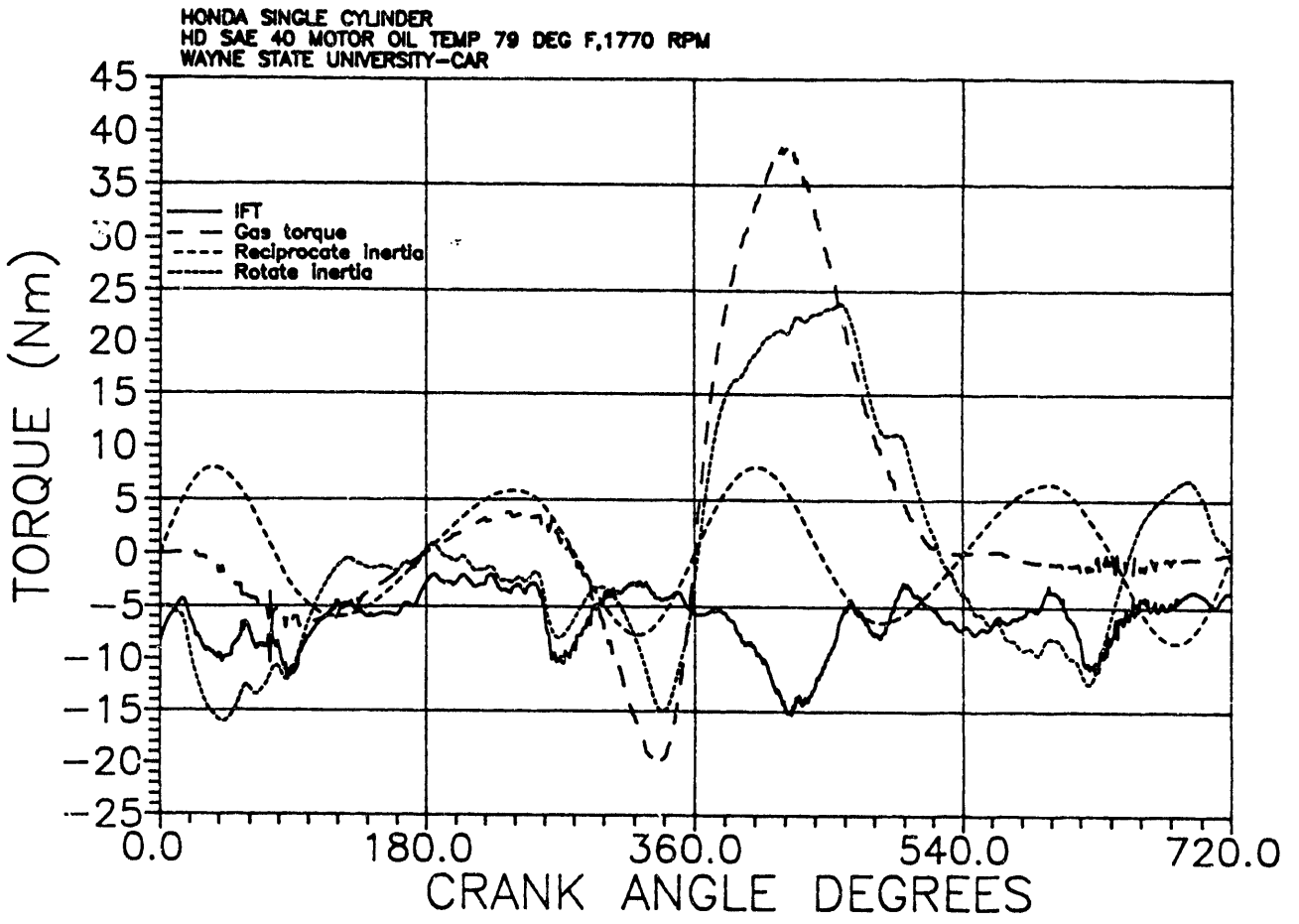

Figure 9.3. Gas torque, inertia torque and IFT versus crank angle

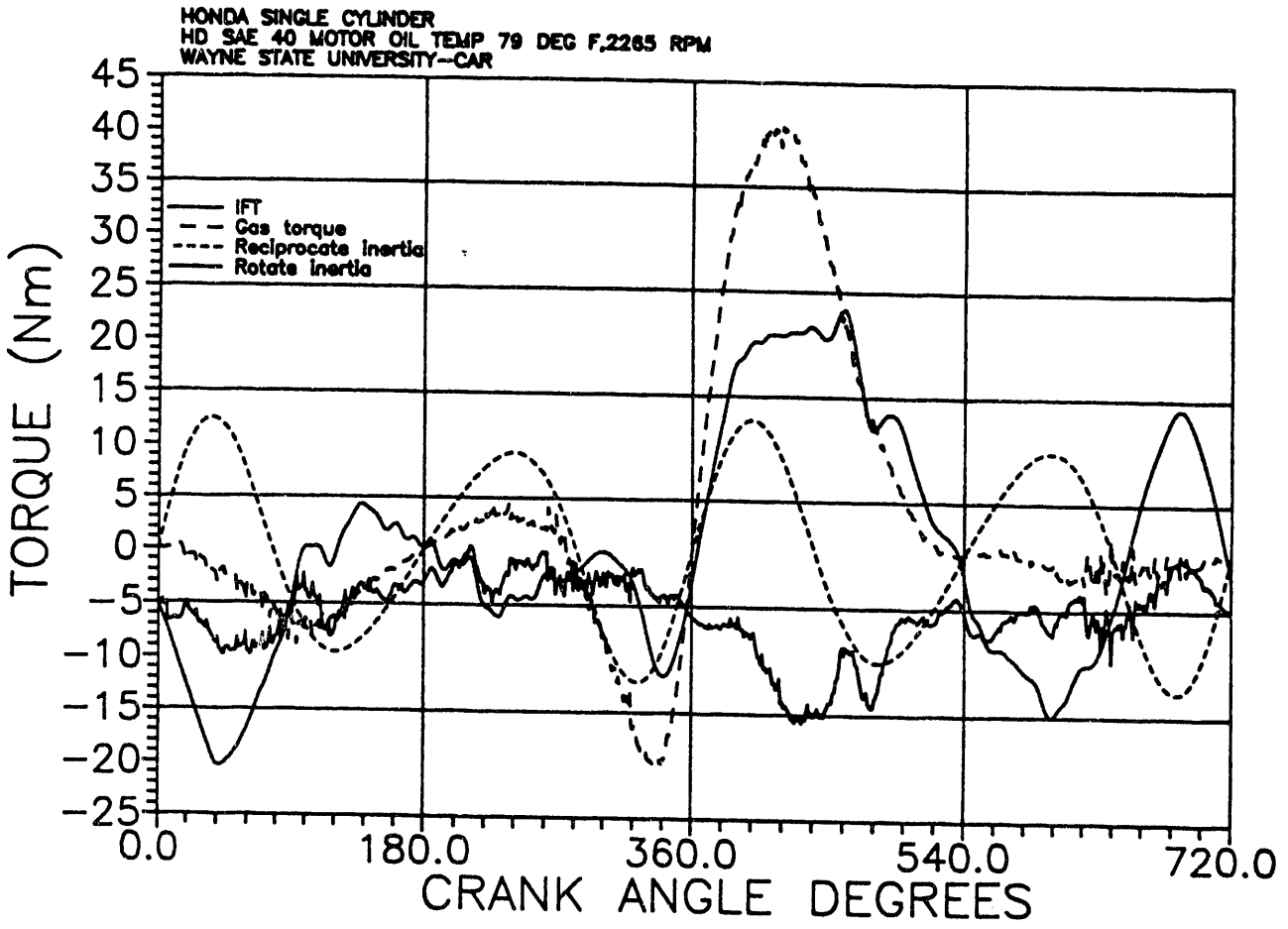

Figure 9.4. Gas torque, inertia torque and IFT versus crank angle

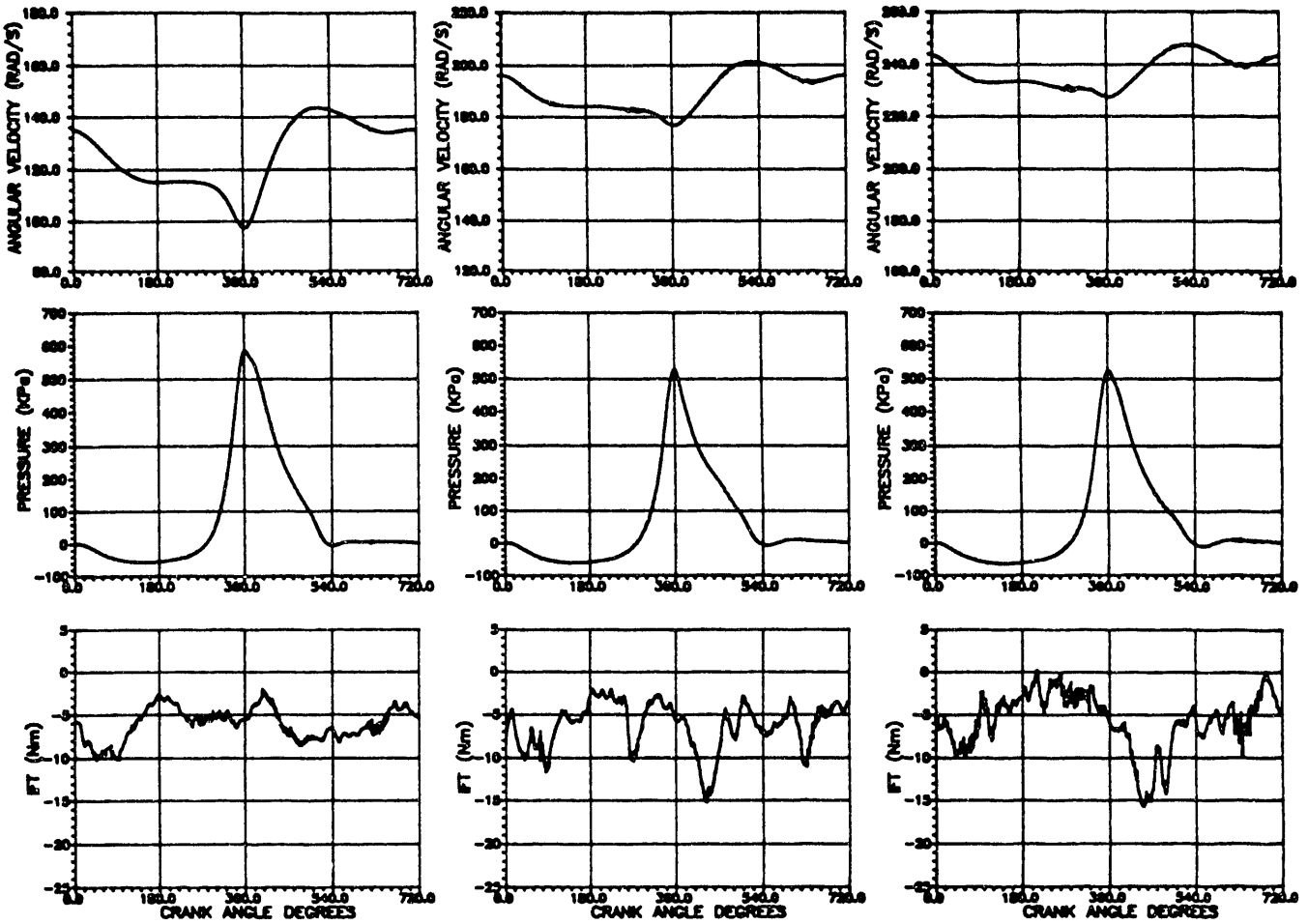

Figure 9.5. Engine dynamics at 3 different speeds at sump oil temperature 79 °F

9.2.2 EFFECT OF SUMP OIL TEMPERATURE

Figure 9.6 and 9.7 are for sump oil temperatures of 45° C (113° F) and 60.6° C (141° F) respectively.

Figure 9.8 shows the effect of sump oil temperature on cycle-averaged IFT at three speeds. Average IFT increases with speed and with the increase in oil viscosity.

9.2.3 DISTRIBUTION OF IFT OVER THE WHOLE CYCLE

Figure 9.9 shows the percent of total IFT over the whole cycle at three speeds. The contribution of the forces at TDC decreases as the speed increases.

9.2.4 COMPARISON BETWEEN IFT IN GASOLINE AND DIESEL ENGINES

Figure 9.10 shows a comparison between percentage IFT over the whole cycle for the gasoline (Honda) and the diesel (Deutz) engine. The contribution of the forces acting on the engine near TDC is very significant for the diesel engine. In the diesel engine the period from -20° BTDC to +50° ATDC contributed 60% of the total cycle friction, compared with 8% in the gasoline engine.

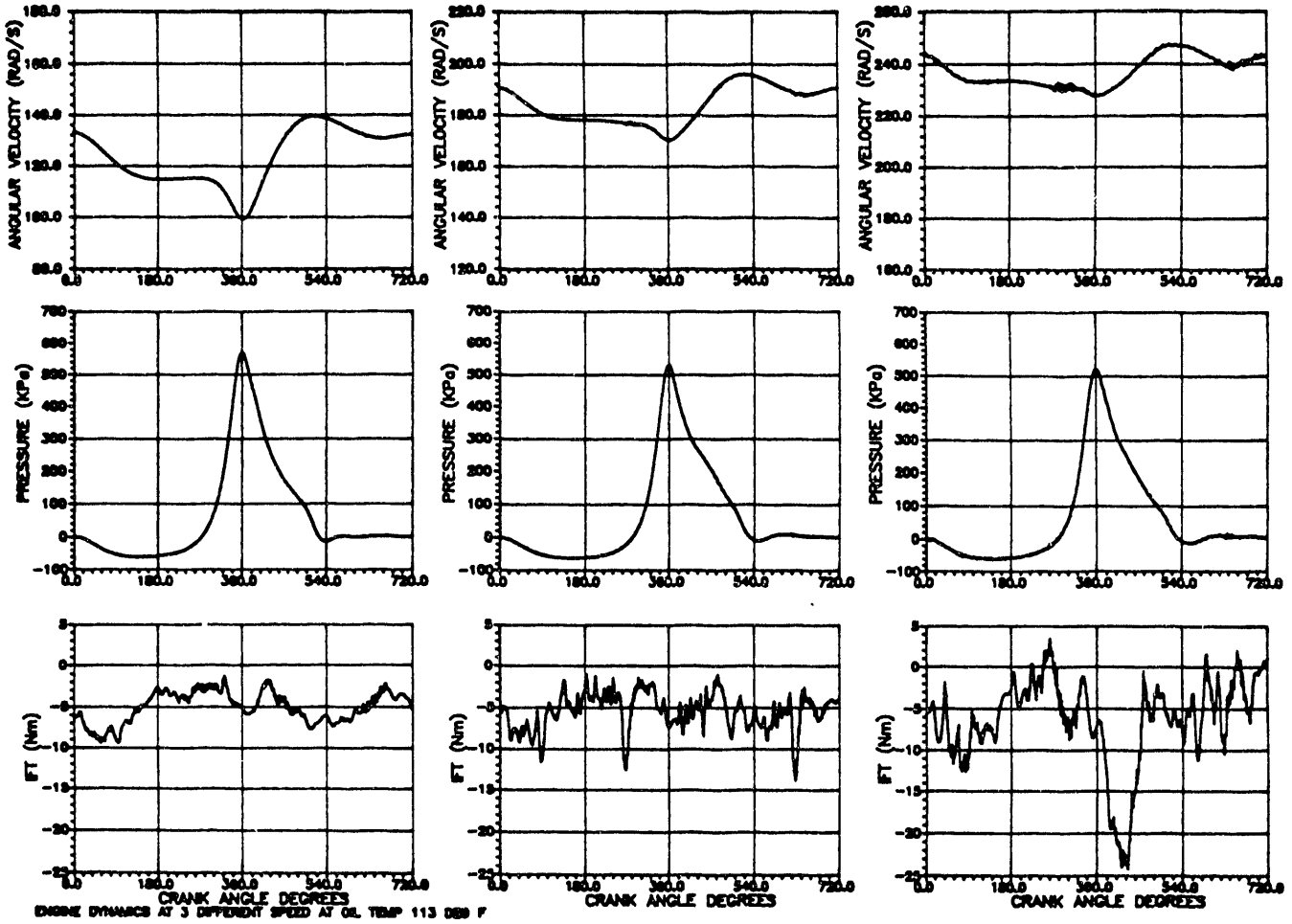

Figure 9.6. Engine dynamics at 3 different speeds at sump oil temperature of 45°C

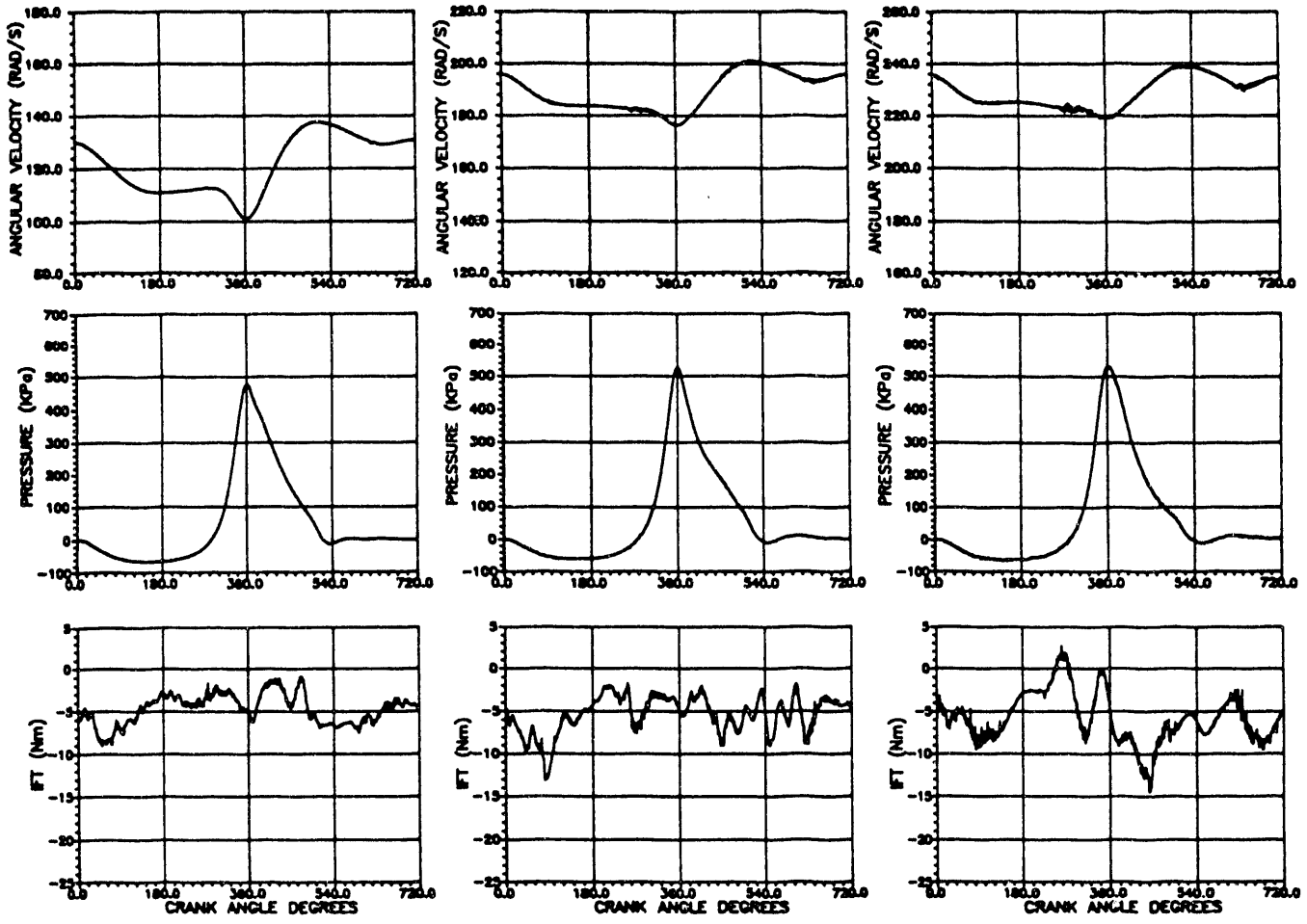

Figure 9.7. Engine dynamics at 3 different speeds at sump oil temperature of 60.6°C

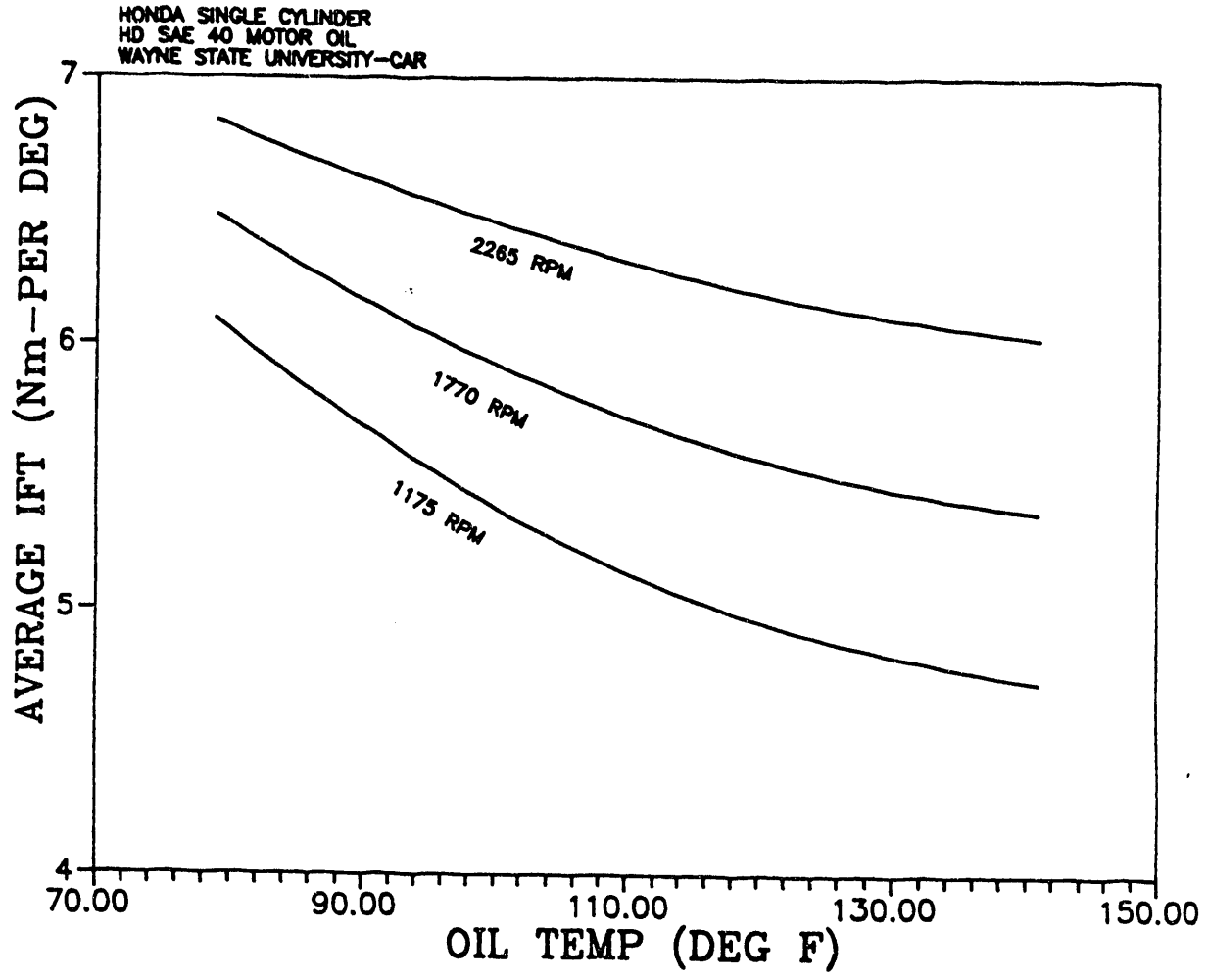

Figure 9.8. Effect of sump oil temperature

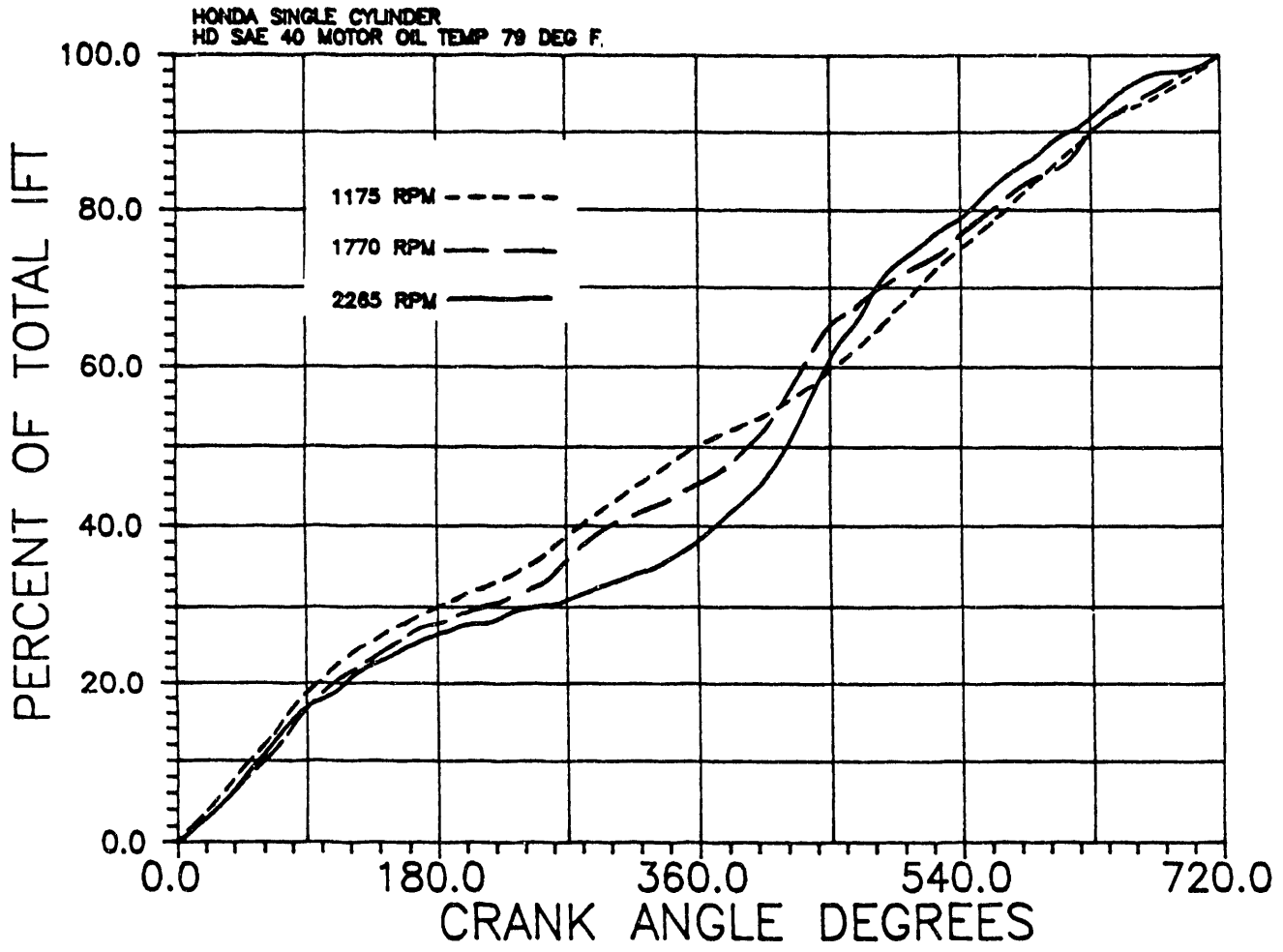

Figure 9.9. Effect of crank angle on integrated IFT, Honda gasoline engine

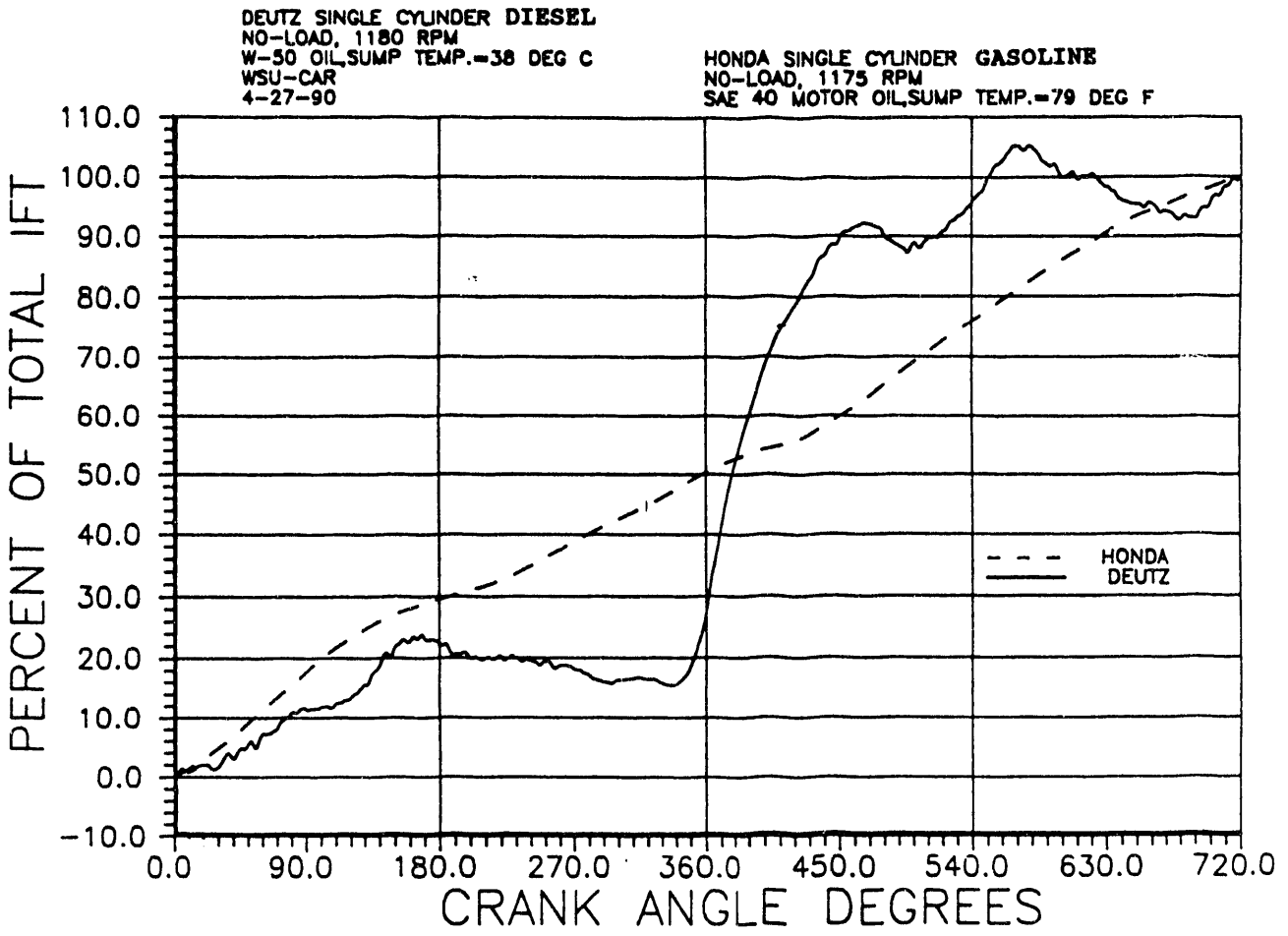

Figure 9.10. Comparison between the distribution of IFT over the whole cycle in a Diesel and a gasoline engine

CHAPTER 10: CONCLUSIONS AND RECOMMENDATIONS

10.1 CONCLUSIONS

1. The (P-ω) method developed to determine the instantaneous frictional torque of the engine has the following advantages:

   a- It is the only method to determine IFT in reciprocating engines used in land transportation, power generation, marine applications and some airplanes.

   b- It is the only method to determine IFT in reciprocating compressors used for compressed air, gas and refrigerants.

   c- It determines IFT non-invasively.

   d- It determines IFT under different loads and speeds with the engine operating under steady state.

   e- It is the only method to determine IFT under the transient states of acceleration and deceleration.

   f- Its accuracy is not subject to errors caused by cycle-to-cycle variations, which are common in gasoline engines.

2. The accuracy of the (P-ω) method in determining IFT of the engine improves if the following errors in measuring the angular velocity are reduced.

   a- $\Delta\theta$-to-$\Delta\theta$ variations within one encoder or the flywheel gear teeth.

   b- Encoder-to-encoder variations.

c- Misalignment within the encoder itself or between the encoder shaft and the driving shaft or between the flywheel gear teeth and the crankshaft.

3. The accuracy of the (P-ω) method in determining IFT of the engine improves if the following errors in measuring cylinder gas pressure are reduced.

a- Calibration at normal atmospheric temperature. The dead-weight tester used in this investigation was modified to reduce this error by heating the transducer, the oil and the mounting to high temperatures.

b- Transducer zero-drift during the transients. This can be accomplished by testing different transducers and choosing a transducer with no drift. Transducers with gold plated diaphragms have been found to produce no zero-drift.

4. The effect of load and other operating variables on IFT have been determined, for the first time. The peak and cycle-averaged IFT decreased with the reduction in load, drop in oil viscosity caused by increasing temperature or by using a lighter oil, or running the engine at lower speeds.

5. The motoring frictional torque, which is widely used in engine testing, does not represent the frictional torque under firing conditions because of the low pressures reached. The error in the motoring frictional torque was 12.5% at no load and 31.4% at full load.

6. The components of the instantaneous frictional torque of the

Deutz engine were determined without gas pressure (without cylinder head). The engine components were added one at a time to the basic crankshaft-lubricating oil pump system. The IFT was determined during a coast-down mode, after the crankshaft was accelerated to about 900 RPM with an electric starter. The investigation indicated the following:

a- The valve-train frictional torque decreased at higher speeds. This indicates that the mode of lubrication was elastohydrodynamic.

b- The piston-ring assembly is the largest contributor in the total frictional losses in diesel engines, even under the atmospheric conditions of these experiments.

c- The torque measured on the camshaft indicated that the valve springs release some energy during valve closing.

d- The fuel injection pump required a much higher torque than any of the valves, and did not release any energy back to the engine.

7. The coating of the piston rings (made at Argonne National Laboratory) reduced the piston-rings assembly friction in two types of tests. The first is under atmospheric conditions (without the cylinder head) during a coast-down mode. The second is under firing at different speeds, without load.

8. A comparison between IFT' in the Deutz diesel engine and the Honda gasoline engine over the whole cycle showed that the contribution of the combustion process in the total cycle friction is much higher in the diesel engine. Both tests were conducted at no-load.

10.2 RECOMMENDATIONS

1. Develop techniques, both experimental and analytical, to reduce the noise in the angular velocity traces at high engine speeds. This would improve accuracy of the (P-ω) method when determining the instantaneous frictional torque at high speeds.

2. Improve the accuracy of the (P-ω) method by considering the elastic behaviour of the engine components, particularly the connecting rod and crankshaft.

3. Apply the method to measure the instantaneous frictional torque of multicylinder transportation engines. All the tests conducted so far have been an single cylinder engines.

4. Investigate the effect of coating the piston rings with advanced materials on rings assembly friction.

5. Investigate the effect of coating the inside surface of the cylinder with advanced materials on piston-rings assembly friction.

6. Develop the wear probe to measure the microscopic and macroscopic wear in the cylinder bore at the top-ring-reversal point. Correlate the wear measurements with the friction measurements.

REFERENCES

1- "Oil and Competition in World Market," Chicago Fed Letter, Federal Reserve Bank of Chicago, Chicago, IL, No. 39, Nov. 1990.

2- Bishop, I.N., "Effect of Design Variables on Friction and Economy," SAE Paper 812A, 1964.

3- Furuhama, S., Takiguchi, M., Tomizawa, K., "Effect of Piston and Piston Ring Designs on the Piston Friction Forces in Diesel Engines", SAE Paper 810977, 1981.

4- Kovach, J.T., Tsakiris, E.A., Wong, L.T., "Engine Friction Reduction for Improved Fuel Economy," SAE Paper 820085, 1982.

5- Rosenberg, R.C., "General Friction Considerations for Engine Design," SAE Paper 821576, 1982.

6- Roberts, D.C., Tournier, M., "The influence of Engine Oil Formulation on the Prevention of Valve Train Wear in Modern European Passenger Cars," SAE Paper 810328, 1981.

7- Irwin, R.F., Fernandez, F., "Energy-Conserving Engine Oils-Techniques and Technology," SAE Paper 830164, 1983.

8- Clevenger, J.E., Carlson, D.C., Kleiser, W.M., "The Effects of Engine Oil Viscosity and Composition on Fuel Efficiency," SAE Paper 841389, 1984.

9- Gauthier, A., Constants, B., Perrin, H., Roux, F., "Lubricants Effects on Piston/Rings/Liner Friction in an Instrumented Single Cylinder Diesel Engine," SAE Paper 872034, 1987.

10- Willermet, P.A., Pieprzak, J.M., Dalley, D.P., "Friction

Reduction in Valve Trains: The Influence of Friction Reducing Oil Additives," SAE Paper 890725, 1989.

11- Rezeka, S. F., Henein, N.A., "A New Approach to Evaluate Instantaneous Friction and Its Components in Internal Combustion Engines," 1984 SAE Transactions Paper No. 840179, 1984.

12- Henein, N.A., Fragoulis, A.N., Nichols, A.H., "Time-Dependent Frictional Torque in Reciprocating Internal Combustion Engines," Lubr. Eng., 44, 4, pp313-318, 1988.

13- Fragoulis, A.N., Nichols, A.H., Henein, N.A., "Error Analysis of Time-Dependent Frictional Torque in Reciprocating Engines: Effect of Angular Velocity,"Lubrication Eng., 45, 7, pp493-499, 1989.

14- Henein, N.A., Marek, S.L., Fragoulis, A.N, "Error Analysis of Time-Dependent Frictional Torque in Reciprocating Engines: Effect of Cylinder Gas Pressure," Paper presented at ASME/STLE Tribology Conference, Toronto, Canada, October 7-10, 1990.

15- Marek, S.L., Henein, N.A., Bryzik, W., "Effect of Load and other Parameters on Instantaneous Friction Torque in Reciprocating Engines," SAE Paper No.910752, 1991.

16- Henein, N.A., Fragoulis, A.N., Bryzik, W., "Instantaneous Frictional Torque Components in a Diesel Engine," SAE Paper No.890241, 1989.

17- Kline, S.J. and McClintock, F.A., "Describing Uncertainties In Single-Sample Experiments," Mech. Eng., Jan. 1953.

18- Moffat, R.J., "Contributions to the Theory of Single-Sample Uncertainty Analysis," ASME Trans., 104,1882.

19- Ramachandra, S.K, "Theoretical Analysis for Practical Design of Universal Joint Trunnion Bearings," SAE Paper 860387, 1986.

20- Reinsch, C.H., "Smoothing by Spline Functions," Numerische Mathematik 10, pp 177-183, 1967.

21- Dubendorfer, U., Wolfer, P., "State-of-the-Art Pressure Measurements in Combustion Engines," ISA Trans, 24, 2, pp34-45, 1985.

22- Brown, W.L., "Methods for Evaluating Requirements and Errors in Cylinder Pressure Measurements," SAE Automotive Engineering Congress,Paper No. 670008, 1967.

23- Lancaster, D.R., Krieger, R.B., Lienesch, J.H., "Measurement and Analysis of Engine Pressure Data," SAE Paper No. 750026, 1975.

24- Whitehouse, J.A., Metcalf, J.A., "The Mechanical Efficiency of I.C. Engines," The Motor Industry Research Association (MIRA), Research Report 1958/5, Warwickshire, England, 1958.

25- Cleveland, A.E., Bishop, I.N., "Several Possible Paths to Improved Part-Load Economy of Spark-Ignition Engines," SAE Paper 150A, 1958.

26- Millington, B.W., Hartles, E.R., "Frictional Losses in Diesel Engines," SAE Paper 680590, 1968.

27- Walder, C., "Problems in the Design and Development of High Speed Diesel Engines," SAE Paper 978A, 1965.

28- Fragoulis, A.N., "Instantaneous Frictional Torque of Reciprocating Combustion Engines, Ph.D. Dissertation, Wayne State University, 1988.

29- Armstrong, W.B. and Buuck, B.A., "Valve Gear Energy Consumption: Effect of Design and Operation Parameters," SAE Paper 810787, 1981.

30- Staron, J.T. and Willermet, P.A., "An Analysis of Valve Train Friction in Terms of Lubrication Principles," SAE Paper 830165, 1983.

31- Ball, B.F. et al., "The Friction of a 1.6 Litre Automotive Engine-Gasoline and Diesel," SAE Paper 860418, 1986.

DATE
FILMED
6/15/93